

JSCSEN 78(11)1633–1836(2013)

ISSN 1820-7421(Online)

Journal of the Serbian Chemical Society

ersion
lectronic

VOLUME 78

No 11

BELGRADE 2013

Available on line at



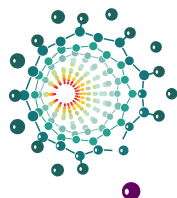
www.shd.org.rs/JSCS/

The full search of JSCS
is available through

DOAJ DIRECTORY OF
OPEN ACCESS
JOURNALS

www.doaj.org

Publication of this issue is financially co-supported by



University of Belgrade

**FACULTY OF
PHYSICAL CHEMISTRY**

www.ffh.bg.ac.rs





CONTENTS

<i>Preface: 110 years of Physical Chemistry at the University of Belgrade</i>	1635
<i>S. Macura, P. K. Mishra, J. D. Gamez and I. Pirko: NMR microscopy of tissue in organic and mixed solvents</i>	1641
<i>N. O. Juranić, K. A. Jones, A. R. Penheiter, T. J. Hock and J. H. Streiff: Halothane binds to druggable sites in the [Ca²⁺]₄-calmodulin (CaM) complex, but does not inhibit [Ca²⁺]₄-CaM activation of kinase</i>	1655
<i>T. Jovanović-Talisman and V. Vukojević: Super-resolution fluorescence imaging and correlation spectroscopy: principles and examples of application (Review)</i>	1671
<i>J. Snyder, N. M. Marković and V. R. Stamenković: Single crystalline thin films as a novel class of electrocatalysts</i>	1689
<i>M. N. Krstajić, M. D. Obradović, B. M. Babić, V. R. Radmilović, U. Č. Lačnjevac, N. V. Krstajić and S. Lj. Gojković: Electrochemical oxidation of methanol on Pt/(Ru_xSn_{1-x})O₂ nanocatalyst</i>	1703
<i>B. Šljukić, D. Micić, N. Cyjetičanin, G. Ćirić-Marjanović: Nanostructured materials for sensing Pb(II) and Cd(II) ions: manganese oxohydroxide versus carbonized polyanilines</i>	1717
<i>A. Radu, T. Radu, C. McGraw, P. Dillingham, S. Anastasova-Ivanova and D. Diamond: Ion selective electrodes in environmental analysis (Authors' Review)</i>	1729
<i>I. A. Pašti, N. M. Gavrilov and S. V. Mentus: Fluorine adsorption on transition metal surfaces – A DFT study</i>	1763
<i>M. Etinski, M. Petković and M. M. Ristić: A study of the low-lying singlet and triplet electronic states of chlorophyll <i>a</i> and <i>b</i></i>	1775
<i>A. M. Abramyan, Z. Liu and V. Pophristic: An <i>ab-initio</i> study of pyrrole and imidazole arylamides (Short communication)</i>	1789
<i>N. M. Dimitrijević: Investigation of the charge-transfer in photo-excited nanoparticles for CO₂ reduction in non-aqueous media</i>	1797
<i>A. Janošević, B. Marjanović, A. Rakić and G. Ćirić-Marjanović: Progress in conducting/semiconducting and redox-active oligomers and polymers of arylamines (Review)</i>	1809

Published by the Serbian Chemical Society
Karnegijeva 4/III, 11000 Belgrade, Serbia
Printed by the Faculty of Technology and Metallurgy
Karnegijeva 4, P.O. Box 35-03, 11120 Belgrade, Serbia



EDITORIAL

This issue of the *Journal of the Serbian Chemical Society* is dedicated to the celebration of the 110th anniversary of Physical Chemistry teaching at the University of Belgrade. Dean of the Faculty of Physical Chemistry – University of Belgrade and Guest Editor of the issue, together with the Editor in Chief of the *Journal*, invited some of their distinguished colleagues from different institutions, most of which are located outside of Serbia, to contribute to the issue in their respective scientific areas. The invited authors, including several young scientists from the Faculty of Physical Chemistry, are former students of the University of Belgrade. Through the papers contributed to this special issue, the influence of Physical Chemistry on the development of the University of Belgrade could be recognized.

The selected papers by invited authors cover a variety of contemporary research topics. The issue includes a Preface, 3 review papers, 8 research papers and 1 short communication.

The Guest Editor of this special issue of the *Journal* would sincerely like to thank all authors who accepted the invitation to submit their valuable contributions for this issue and to the expert reviewers for their efforts and valuable and important contributions to the evaluation process. The Guest Editor also wishes to express his profound gratitude to the Editor in Chief Branislav Nikolić and to the Technical Editors of the *Journal of the Serbian Chemical Society* for their support in the process of compiling this special issue devoted to the celebration of the of the 110th anniversary of Physical Chemistry teaching at the University of Belgrade.

Slobodan K. Milonjić
Guest Editor



PREFACE

110 years of Physical Chemistry at the University of Belgrade



This issue of the *Journal of the Serbian Chemical Society* is dedicated to the celebration of the 110 years of Physical Chemistry at the University of Belgrade. To commemorate this special occasion, we have asked some of our distinguished colleagues to contribute to this issue in their respective subfields of Physical Chemistry. We attempted to ensure that these contributions spanned a range of different institutions, most of which are situated outside of Serbia. The contributions were submitted by former students of the University of Belgrade. A portion of the space in this issue was reserved for contributions from several young authors from the Faculty of Physical Chemistry. I take this opportunity to thank sincerely all the contributors on behalf of the Faculty of Physical Chemistry.

As a discipline, Physical Chemistry started to mature in the second half of the 19th century. In fact, Physical Chemistry was first mentioned in 1752 in Lomonosov's lectures to the students of St. Petersburg University entitled "A Course in True Physical Chemistry" («Курс истинной физической химии» in Russian), but its modern concepts date back to the second half of the 19th century, when the first articles on chemical kinetics and thermodynamics commenced appearing in scientific journals. Around the same time, some of the classical terms in Physical Chemistry, such as chemical potential and phase rule, were introduced. Key researchers in the area at that time were J. W Gibbs, K. K. Onnes, S. A. Arrhenius, J. H van't Hoff and W. Ostwald. In 1887, Ostwald founded the first scientific journal in the area of Physical Chemistry, *Zeitschrift für physikalische Chemie*. This early history of Physical Chemistry should also include the studies that contributed to the discovery of radioactivity – initiated in France by H. Becquerel in 1896 and later followed by Pierre and Marie Curie. Some authors would argue that these contributions would better fit into the history of nuclear chemistry, but at the University of Belgrade, nuclear chemistry

was traditionally considered a part of Physical Chemistry – in fact, as its most important component during several decades.

Physical Chemistry is a science whose unique conception combines knowledge of chemistry, physics, and mathematics, with the overarching goal of answering some of the very basic questions of chemistry: how and why do chemical reactions occur, or what is the structure of matter.

Belgrade's Great School, as the University of Belgrade was called until 1905, included enough visionaries to realize the importance of this young scientific discipline, and Physical Chemistry was included in the *Curriculum* as early as 1903. In 1903, Dr. Miloje Stojiljković, who obtained his doctorate at the University of Geneva, was elected as a Docent of Physical Chemistry in the Section for Natural Sciences and Mathematics of the Faculty of Philosophy at Belgrade's Great School. Since then, instruction and research in Physical Chemistry have continued uninterrupted to the present day. Initially, the home for physical chemists was the Faculty of Philosophy, then the Faculty of Natural Sciences and Mathematics, and finally, since 1990, the Faculty of Physical Chemistry as the home institution. During the academic year 1925/26, the Section for Technology of the Technical Faculty (today the Faculty of Technology and Metallurgy) elected Panta S. Tutundžić to be a Docent of Physical Chemistry and Electrochemistry. In 1926, he founded the Laboratory of Physical Chemistry and Electrochemistry, which still exists today. A significant contribution to the instruction in Physical Chemistry has also been provided by the Faculty of Pharmacy. Since 1939, Pavle Savić taught physical chemistry at what was then the Section of Pharmacy of the Faculty of Medicine. The University of Belgrade also constituted a nucleus for the development of physical chemistry at other universities in Serbia and Yugoslavia.



Prof. Miloje Stojiljković



Academician Pavle Savić



Academician Panta Tutundžić

Many of us best know Mihajlo Pupin for his invention of the so-called Pupin solenoid, which allowed improved transmission of telephone signals. Much less known is the fact that he was the first physical chemist from the Balkans; in 1889, he defended his doctoral dissertation in Physical Chemistry on the topic of osmotic pressure in Berlin under the supervision of Herman von Helmholtz.

One of the key figures in the development of Physical Chemistry, especially in the period after World War II, was certainly Prof. Pavle Savić. In the 1930s, working in Paris with Irène Joliot-Curie, who by then was already a Nobel Laureate, he made a key contribution to one of the most significant scientific discoveries in history – nuclear fission. He taught Physical Chemistry (at the Faculty of Medicine before World War II, and at the Faculty of Natural Sciences and Mathematics after it), he founded the Vinča Institute of Nuclear Sciences, and acted as the president of the Serbian Academy of Sciences and Arts (SASA) between 1971 and 1981. As Physical Chemistry was traditionally oriented towards fundamental research, a number of physical chemists were always members of SASA at any given time in its history. In addition to Pavle Savić, whose focus in teaching and research was nuclear chemistry, Professors Milenko Šušić (electrochemistry and general physical chemistry) and Slobodan Ribnikar (chemistry of isotopes and spectrochemistry) from the Faculty of Physical Chemistry were also Academy members. Furthermore, Professors Panta Tutundžić, Aleksandar Despić and Dragutin Dražić, all from the Faculty of Technology and Metallurgy, also worked on and made significant contributions to Physical Chemistry, with particular focus on electrochemistry. Professor Aleksandar Despić was also the president of SASA between 1994 and 1998. The establishment and development of individual subfields of physical chemistry owes much also to Professors Slobodan Ristić (spectrochemistry) and Slobodanka Veljković (chemical kinetics



Academician Milenko
Šušić



Academician Aleksandar
Despić



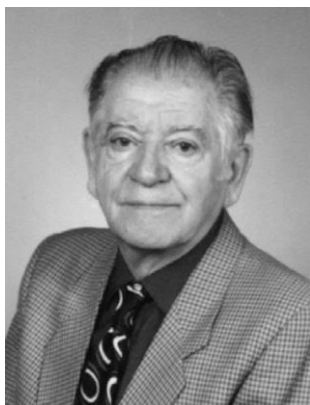
Academician Slobodan
Ribnikar

and reaction mechanisms). Outstanding contributions are also made by Professor Ivan Draganić, whose work in the field of radiation chemistry at the Vinča Institute of Nuclear Sciences resulted in very significant contributions to the radiation chemistry of water.

During the past decades, Physical Chemistry at the University of Belgrade has developed in parallel under the auspices of several institutions. The Faculty of Physical Chemistry is the main teaching venue and is active in research spanning the fields of electrochemistry, nuclear chemistry, quantum chemistry, chemical kinetics, thermodynamics, spectrochemistry, biophysical chemistry, environmental physical chemistry, *etc.* The traditional strengths of the Faculty of Technology and Metallurgy are the fields of electrochemistry and the physical chemistry of materials (especially macromolecules). For more than six decades, the Vinča Institute of Nuclear Sciences has been developing physical chemistry through research in the fields of isotope chemistry, spectrochemistry, mass spectrometry, radiochemistry, radiation chemistry, chemistry and analysis of nuclear materials, surface chemistry, energy conversion, *etc.* Significant contributions to the teaching and science of Physical Chemistry are also being made at the Faculty of Pharmacy, mainly in the areas of interest to pharmaceutical studies, and most directly through the work at the Center for Physical Chemistry and Instrumental Methods.

The mission of the Faculty of Physical Chemistry, University of Belgrade, is to provide the highest possible quality of instruction for its students at BSc, MSc and PhD levels, including training in the specialized areas of forensic science, radioecology, instrumental analysis, biosystems and radiation. Our goal is to create graduates whose quality is globally recognized. We are delighted to see the success of this strategy as graduates from the Faculty of Physical Chemistry, University of Belgrade, can be found in the most established world laboratories at the Universities of Oxford, Bonn, Heidelberg, Berlin, Eindhoven, Moscow State University, UC Berkeley, UC Santa Barbara, Argonne National Laboratory, University of Dnjepropetrovsk, CWRU Cleveland, Brookhaven National Laboratory, Mayo Clinic, Karolinska Institute, École Central Paris, as well as numerous other institutions in the USA, Germany, France, Russia, Spain, Portugal, Brazil, and around the world.

What is our vision for the future? To ensure that the instruction in Physical Chemistry follows the modern trends of increased use of new technologies in the analyses of processes, chemical composition, and the structure of matter. Furthermore, there is also a tendency to combine several disciplines – chemistry, physics, mathematics, geology, biology, astronomy, hydrology – in an attempt to provide the best possible understanding of natural phenomena. Quick adoption and development of new knowledge is facilitated by new information technologies. In the future, Faculty of Physical Chemistry must follow and contribute to these tendencies, while keeping their importance in context – as new graduates



Prof. Ivan Draganić



Prof. Slobodan Ristić



Prof. Slobodanka Veljković



Academician Dragutin Dražić

should be able to not only adopt and apply modern technological discoveries, but also to develop them within our own local environment. The planning of teaching curricula will continue to learn from positive experiences in other countries, and following these worldwide trends will be facilitated by nurturing the contacts established with numerous physical chemists around the world. Their contributions to this issue of JSCS are an excellent illustration of this practice.

ŠĆEPAN S. MILJANIĆ, Dean
Faculty of Physical Chemistry
University of Belgrade



J. Serb. Chem. Soc. 78 (11) 1641–1654 (2013)
JSCS–4524

NMR microscopy of tissue in organic and mixed solvents

SLOBODAN MACURA^{1*}, PRASANNA K. MISHRA¹, JEFFREY D. GAMEZ²
and ISTVAN PIRKO²

¹Department of Biochemistry and Molecular Biology and ²Department of Neurology,
Mayo Clinic, Rochester, Minnesota, 55905, USA

(Received 8 October 2013)

Abstract: The use of organic and mixed solvents for nuclear magnetic resonance microscopy of fixed tissue is proposed as a means for improving image information content. NMR properties of some standard solvents (methanol, acetone or DMSO) and solvents in use for tissue processing in pathology (xylenes, paraffin, “Clearify”) have been measured, reviewed and analyzed. It was found that DMSO and paraffin are very useful solvents that provide images of better quality than those obtained in water (neutralized formalin buffer). This is illustrated on formalin-fixed mouse brain sections imaged at 16.4 T (700 MHz).

Keywords: NMR, MRI, MRM, nuclear magnetic resonance, NMR imaging, NMR microscopy, magnetization transfer, cross-relaxation.

INTRODUCTION

Nuclear magnetic resonance (NMR) imaging,^{1,2} in clinical settings known as magnetic resonance imaging (MRI),³ is an indispensable tool in medicine providing non-invasively a detailed picture of tissues and organs in the human body. When performed on small samples with high spatial resolution, NMR imaging is frequently referred to as NMR microscopy.⁴

Proton (nucleus of hydrogen, ¹H) is most widely used nucleus in imaging because of its sensitivity and because of its abundance in tissue (water, carbohydrates, lipids and proteins). In most NMR images, only protons from water are observed since the human body is comprised of ≈60 % water. This translates into a water proton concentration of ≈65 M, whereas the concentration of any other proton (except fat) is below 1 M. In addition, protons built into macromolecules (proteins and carbohydrates) are not detectable under routine imaging conditions. Besides water, a strong proton signal can be detected from the aliphatic part of lipid chains (fat) but this can easily be suppressed (when needed) so that almost all clinical images are based on the detection of protons from tissue water.

* Corresponding author. E-mail: macura@mayo.edu

doi: 10.2298/JSC131108108M

Source of contrast in MRI

Compared to other imaging modalities (X-ray, ultrasound, positron emission, *etc.*), NMR has an extensive assortment of contrasting means, most of which are based on the molecular properties of water and their sensitivity to fine changes in molecular environment. For example, the T_1 relaxation rate of water is very sensitive to the presence of natural (deoxyhemoglobin) or artificial (paramagnetic ions, Gd^{3+} , Mn^{2+} and stable free radicals) paramagnetic centers. Paramagnetism of deoxyhemoglobin is the principal source of contrast in functional NMR imaging (fMRI), whereas the paramagnetism of different ions (Gd^{3+} and Mn^{2+}) represents the basis for the development of various contrast agents.⁵ Similarly, the water T_2 relaxation depends on molecular mobility and the T_2^* relaxation on the local magnetic susceptibility gradients. This dependence of water properties on local physicochemical environment led to the creation of dozens of NMR imaging methods that emphasize selected properties. The main purpose of developing new ways of imaging contrast is to discriminate different tissues (*e.g.*, gray matter *vs.* white matter in the brain) or normal from diseased tissue (cancer, necrosis, plaques, *etc.*) in a unique and unambiguous way. However, the main problem is that under certain experimental conditions, contrast depends on several different properties simultaneously, which makes it difficult to attribute it to a single disease condition. Thus, it is desirable to understand the source of NMR contrast at the molecular level, which, due to interplay among numerous water/tissue interactions, is rather difficult.

Although the most important aspect of MRI is its application *in vivo*, NMR imaging of tissue or organs *ex vivo* is also of great value. The most obvious advantage of *ex vivo* imaging, compared to *in vivo*, is that it can be performed in more details due to the absence of motion and time restriction (typically less than an hour in human subject imaging). Imaging *ex vivo* could be performed with higher resolution and better contrast, and most importantly, could be correlated with other types of tissue analysis (histology) and thus could serve as a guide for interpreting *in vivo* images. *Ex vivo* imaging is performed on either fresh tissue (surgical specimens), or thawed tissue earlier preserved by deep freezing, or formalin-fixed (FF) tissue. In all cases, protons are detected from tissue water and thus, most of the ambiguities present *in vivo* are still present in *ex vivo* imaging. For example, spin echo attenuation of water protons depends simultaneously on water diffusion, chemical exchange with labile protons from tissue (proteins, polysaccharides or small metabolites), the presence of paramagnetic species *etc.*, and individual contributions of various effects can be deduced only after a series of experiments.

Formalin-fixed (FF) tissue most frequently is subsequently embedded in paraffin for further histology (optical microscopy) analysis. In this process, tissue is exposed to a series of organic solvents (most frequently ethanol, xylenes) until it

is completely dehydrated. In clinical settings this is realized on almost every surgical specimen requiring histology analysis; thus, having tissue in an organic solvent is not a rarity. In this work, whether imaging tissue in an organic solvent has any advantages over imaging in water was investigated. The main expectation was that interactions of organic solvents with FF tissue are much simpler and that they could be influenced by the solvent composition. This could help to understand better the contribution of tissue water to contrast in different experiments. In addition, it is conceivable that suitable solvents or their mixture could selectively emphasize various tissue properties.

Water/tissue interactions

By interacting in various ways with structures and components of living systems, water acts as a solvent, reactant, lubricant, adhesive, transporter, *etc.* Thus, it is not surprising that the interaction of water with tissue was one of the first applications of NMR in biological systems.⁶ For MRI and magnetic resonance spectroscopy (MRM), only fast interactions that affect the properties of bulk water are of interest. Then, the observed macroscopic property, R_{obs} (chemical shift, relaxation rates, diffusion rate, *etc.*), is an ensemble average of the properties of individual components, free R_f , and bound, R_b :

$$R_{\text{obs}} = f_f R_f + \sum_j (f_b R_b)_j \quad (1)$$

where f_f and f_b represent free and bound fractions, respectively, and

$$f_f + \sum_j (f_b)_j = 1$$

The summation goes over all species that represent water molecules in assumed bound states. For example, based on relaxation dispersion studies,⁷ at least four different waters in proteins, *i.e.*, surface, cavity, cleft, and metal water, could be identified. Water in each site may have its own mobility (rotational or translational) and may exchange protons within the site, among different sites, with bulk water or labile protein protons. Due to rapid exchange with bulk water,⁸ all these sites and processes mediate properties of the observable bulk phase.⁹ Thus, it is rather difficult to explain, on a molecular level, the principal sources of contrast in imaging experiments. For example, transverse relaxation of water in tissue can be equivalently described by two physically different models. One emphasizes the role of diffusion in a weak gradient of the magnetic field, and the other a chemical exchange between two proton sites in slightly different fields.¹⁰ As both processes are likely to occur in water, it is hard to determine their individual contributions in any given case. However, the processes could be easily delineated if one could be quenched, which is feasible when water is replaced by a solvent without labile protons.

Organic solvent–tissue interaction

Tissue in an organic solvent is encountered quite frequently in research and clinical settings. Namely, for long-term preservation, tissue is treated with formalin and for pathology analysis treated with a series of solvents until it is finally embedded in paraffin. One reason for the present study was the wide availability of tissue in organic solvents. The other, perhaps more interesting, was the possibility of interpreting solvent tissue interactions on a molecular level. Most organic solvents neither dissociate nor react with tissue (after the tissue has been fixed), which significantly reduces the number of possible interactions. In addition, scanning the same specimen in different solvents could help better characterize NMR tissue properties relevant for imaging contrast.

Organic solvent–tissue interactions most likely depend on both the type of tissue and the solvent. A non-polar solvent may not interact with a tissue at all, whereas a polar solvent may interact preferentially with a polar fragment of tissue (polar protein side chains, polysaccharides, hydrophilic part of lipids, *etc.*), potentially distinguishing different types of tissue in a specimen.

Mixed solvent–tissue interaction

Preferential solvation, frequently observed in mixed solvent systems, is the preferential accumulation of one solvent component around a specific solute. Obviously, the degrees of solvation depend on all components involved. In the case of tissue imaging, preferential solvation could potentially serve as an additional means of contrasting: water could accumulate in hydrophilic regions whereas organic components could preferentially solvate the hydrophobic regions. In general, preferential solvation occurs on the molecular scale (one or more molecular layers) but in a highly packed tissue matrix, it is possible that it occur on a larger scale amenable to MRM. Moreover, mixed solvents could be useful for monitoring tissue–solvent interactions *via* the interligand nuclear Overhauser effect (ILOE).¹¹ The ILOE is observed if two ligands (in the present case solvent molecules) reside on the macromolecular surface (in the present case tissue) in close proximity longer than one nanosecond (for a process to be within the spin-diffusion limit¹²).

Solvent influence on the signal to noise ratio in MRM

The best image is the one that reveals a specimens microstructure without artifacts and maximal contrast and sensitivity. Besides the applied external magnetic field strength, B_0 , hardware and method design, the quality of NMR images strongly depends on the chemical environment of the observed spins. Here, the properties of the imaging medium that could affect the image parameters are of most interest.

The signal to noise ratio (*SNR*) is proportional to the spin concentration N , and depends on the transverse relaxation time of the solvent, T_2^* , and the imaginary part of the dielectric permittivity, ϵ'' as follows:¹³

$$SNR \propto N \sqrt{\frac{T_2^*}{\epsilon''}} \quad (2)$$

The *SNR* also depends on the real part of the dielectric permittivity, ϵ' , but in a more complex way, with the general rule that the smaller the permittivity, the better is the *SNR*.¹³ Thus, for a given tissue specimen, the *SNR* could be improved by selecting the solvent with the highest spin density, the longest T_2^* relaxation time and smallest dielectric permittivity.

Similarly, an estimate of the experimental time, t_T , as a function of the desired signal to noise ratio SNR_D , and T_1 and T_2^* relaxation times of the imaging medium can be obtained from the following equation:¹⁴

$$t_T \propto SNR_D^2 \frac{T_1}{T_2^*} \quad (3)$$

Thus, the experimental time is proportional to the ratio of the longitudinal T_1 and the effective transverse relaxation time T_2^* of the imaging medium within the tissue. With all other conditions the same, an image with a desired signal to noise ratio could be obtained faster if T_1 is shorter and T_2^* is longer.

Heterogeneity of tissue samples induces large random intrinsic magnetic field gradients,¹⁵ which directly affects the effective transverse relaxation time and consequently, both the *SNR* and resolution.^{15,16} The influence of the intrinsic field gradient can be expressed over the susceptibility gradient across the voxel $\Delta\chi$ ($\Delta\chi = \chi_{tis}^{loc} - \chi_{solv}$) as $\gamma B_0 \Delta\chi$ where γ is the gyromagnetic ratio and B_0 the external magnetic field. Then, the effective transverse relaxation rate is the sum of the intrinsic transverse relaxation rate $1/T_2$ (signal dephasing due to homogeneous line broadening) and the signal dephasing caused by the susceptibility gradients:

$$\frac{1}{T_2^*} = \frac{1}{T_2} + \gamma B_0 \Delta\chi \quad (4)$$

The additional relaxation rate term represents signal broadening across the voxel due to the differences in the magnetic susceptibilities between the tissue and the solvent and is equivalent to inhomogeneous broadening of the spectral line. The phase of the signal from individual spins varies with the spin location within a voxel, which leads to partial signal cancellation. Obviously, on the microscopic level, the magnetic susceptibilities of various tissue components are different and it is conceivable that diverse solvents with their own susceptibility could selectively modulate $\Delta\chi$ across the specimen.

Diffusion of spins within the susceptibility induced magnetic field gradient produces additional effects which depend on the diffusion rate¹⁷ but which are of concern only at a resolution below 10 $\mu\text{m pixel}^{-1}$.⁴ Here, the effects of a linear field gradient, G , applied during the imaging sequences are of more interest. Random motion (diffusion) of the spin in this gradient leads to spin dephasing which ultimately can be expressed with an additional term in the transverse relaxation rate:³

$$\frac{1}{T_{2\text{diff}}^*} = \frac{1}{T_2^*} + kG^2D \quad (5)$$

where D is the diffusion coefficient of the medium and k is a constant that encompasses the parameters of the specific method used to measure the relaxation (gradient echo *vs.* spin echo *vs.* CPMG). Combining expressions (2)–(5), an estimate can be obtained of the influence of the solvent properties (T_1 , T_2 , D and ϵ'') on the sensitivity per unit time in a spin echo type of experiment:

$$SNR_t = \frac{SNR}{t_T} \propto N \frac{1}{\epsilon''^{1/2}T_1} \left(\frac{T_2}{1 + kG^2DT_2} \right)^{3/2} \quad (6)$$

Thus, the best imaging solvent is the one with the highest spin concentration (number of equivalent spins per unit volume) N , the longest T_2 , the shortest T_1 ($T_1 \geq T_2$), smallest diffusion coefficient D , and the smallest imaginary part of the dielectric permittivity, ϵ'' .

EXPERIMENTAL METHODS

Mouse brain tissue preparation

Throughout this work, formalin-fixed paraffin-embedded (FFPE) mouse brain, prepared earlier in a standard manner was used. Briefly, mice were perfused *via* intracardiac puncture with 50 mL of 10 % neutral-buffered formalin (NBF). The brains were removed and post fixed for 24–48 h in 10 % NBF. Uniform 1 mm coronal cuts of the brain were made using brain matrix, resulting in 6 pieces that were embedded in paraffin. Mid-section (A3) was removed from the paraffin block by melting the paraffin away. The sections were deparaffinized with xylenes or Clearify (both from Electron Microscopy Sciences, Hatfield, PA) by dipping them twice into a 50 fold larger volume of the deparaffinization solvent for an hour at 60 °C. Deparaffinized specimens were similarly treated with fresh solvent and subsequently transferred into custom-made rectangular glass cuvettes, 10 mm×8 mm×1.5 mm suitable for mounting on a surface coil. For DMSO, the specimens were allowed to swell in the solvent overnight before the scanning. Solvents at hand were used: methanol, acetone and DMSO (all from Sigma) and solvents used for tissue processing for histology paraffin, xylenes and “Clearify” (all from Electron Microscopy Sciences, Hatfield, PA). The xylenes used were an *o*-, *m*- and *p*-xylene mixture, which showed two distinct groups of lines at ≈ 2.2 ppm (methyls) and 7 ppm (aromatics) in high-resolution ¹H-NMR spectra. Separation of ≈ 5 ppm is enough to excite selectively only one group, in this study, the methyls. Clearify is a mixture of aliphatic hydrocarbons that is used for tissue deparaffinization. In the ¹H-NMR spectra, three distinct groups of lines corresponding to CHs, CH₂s and CH₃s at ≈ 0.9 , 1.3 and 1.5 ppm are visible.

Thus, the “Clarify” point spread function could be approximated with a Gaussian distribution with an intrinsic width of ≈ 0.6 ppm, *i.e.*, 420 Hz at 16.4 T. In solution, the paraffin $^1\text{H-NMR}$ spectrum consists of 2 sharp singlets, CH_3s at ≈ 0.9 ppm and CH_2s at 1.3 ppm with the ratio 1:6, which corresponds to the linear aliphatic chain $\text{CH}_3-(\text{CH}_2)_{24}-\text{CH}_3$. Although the paraffin point spread function seems to have an intrinsic width of ≈ 0.4 ppm, *i.e.*, 280 Hz at 16.4 T, due to the overwhelming CH_2 signal, it behaves like a real delta function (width below 10 Hz). For reference, the brain slices were also scanned while in 10 % neutral buffered formalin (NBF), which is routinely used for tissue preservation.

Magnetic resonance microscopy

A 16.4 T vertical bore spectrometer (Avance III, Bruker-Biospin, Billerica, MA) equipped with micro-imaging accessories and a temperature controlled probe head with a 10 mm surface coil was employed. The experiments were performed with a gradient coil core temperature of 21 °C, except for the paraffin studies. In the paraffin experiments, the specimen temperature was maintained at 70 °C by a stream of hot air using a temperature controller built into the spectrometer and driven by the manufacturer’s software (TopSpin 2.0). The mouse brain specimens were 1–2 mm thick and were scanned with a spin-echo method using parameters optimized separately for each experiment (given in the captions of presented figures), providing 3D images with isotropic resolution of 25–64 $\mu\text{m pixel}^{-1}$ for a total scanning time of 4 to 16 h.

Parametric images, T_1 and T_2 , were reconstructed from a series of single slice 2D RARE scans, recorded with variable repetition and echo times, respectively. Image reconstruction was performed by curve fitting (pixel by pixel) of a respective series of images using the same software package as for the data collection (ParaVision 5.1, Bruker-Biospin).

RESULTS AND DISCUSSION

The relevant properties of the solvents used in this work are listed in Table I. The bulk solvent values were measured from the region of interest (ROI) placed into the solvent, whereas the tissue values are average values across the tissue. The solvents are listed by their polarity. Notable are the extremely low dielectric losses (ϵ'') in non-polar solvents, which are especially important at higher fields as dielectric losses scale with the cubic power of the resonance frequency.¹³ For example, dielectric losses in water increase ten-fold on going from 500 to 950 MHz.¹³ Thus, finding a suitable solvent would be of great value for high field MRM. From this point of view, the most promising solvents are hydrocarbons (paraffin, “Clarify” and xylenes) and, to some extent, acetone.

Diffusion coefficients are apparently unrelated to dielectric properties, as can be seen in Table I. The slowest diffusion was in the paraffin melt, “Clarify” and DMSO. The water signal attenuation due to diffusion is appreciable when the imaging resolution approaches 50 $\mu\text{m pixel}^{-1}$. According to Eq. (6), the signal attenuation (reciprocal of SNR_I) scales with the third power of the gradient, thus it rapidly increases with increasing resolution. As it also scales with $D^{3/2}$, slowing the diffusion at a given resolution could appreciably reduce the attenuation. For example, substituting water with DMSO could reduce the attenuation five times and with paraffin, almost twenty times, Eq. (6). Thus, paraffin and DMSO

are expected to give stronger signal than water at the highest possible resolution (25 $\mu\text{m pixel}^{-1}$ in the present case).

TABLE I. NMR properties of some organic solvents

Solvent	Polarity	ϵ^a	ϵ'^a	$D / 10^9 \text{ m}^2 \text{ s}^{-1}$	T_1 / ms neat/tissue ^b	T_2 / ms neat/tissue	N^c mol L ⁻¹
Paraffin ^d	Apolar	2 ^e (1.9) ^f	0.001	0.32	1210/1210	220/35	128
“Clearify”	Apolar	2 ^e	0.001	0.71	1180/1200	73/25	na
Xylenes	Apolar	na (2.4) ^f	na	2.3	4230/2000	40/15	49
Acetone	Polar aprotic	2	0.03	4.6	> 6000/na	na/na	81
CH ₃ OH	Polar protic	31	0.38	2.2	4930/2600	54/22	74
DMSO	Polar aprotic	47	0.24	0.73	2240/1500	160/20	85
NBF (H ₂ O)	Polar protic	79	0.2	2.3	2450/1500	16/12	111

^aAt 930 MHz¹³; ^bat 16.4 T (700 MHz); ^cproton spin concentration (mol/L) of neat solvent; ^dmelt at 70 °C; ^ethe *n*-hexane value; ^fCRC Handbook of Chemistry and Physics

Table I shows that all solvents have T_1 relaxation times within a factor 2 of the water (in NBF) value except for acetone, for which T_1 is impractically long. Paraffin and “Clearify” relax twice as fast as water, while DMSO has a very similar relaxation time to water; hence, from this point of view, all three solvents are good candidates.

It is well known that the water relaxation is highly accelerated by internal water chemical exchange and it is not surprising that all solvents have longer T_2 relaxation times than water. Notable is the ten-fold longer T_2 relaxation time of DMSO and the even longer one of paraffin, which puts these solvents ahead of others in terms of relative sensitivity per unit time, Eq. (6).

Finally, the last column in Table I shows molarity of equivalent spins in neat solvents. Only paraffin has somewhat higher proton concentration than water. In other solvents, concentrations are lower partly because of the lower densities of the solvents (apart from DMSO) and partly because of the much lower proton contribution to molecular mass.

The apparent superior properties of paraffin compared to water (significantly lower dielectric losses, slower diffusion, longer T_2 , shorter T_1 and higher proton spin concentration) do not guarantee that it would be a better imaging solvent. Increased *SNR*, as provided by such properties, is unrelated to the image contrast that is essential for high quality images. NMR contrast originates from the local variability of NMR parameters, which in turn is caused by the tissue–solvent interaction. A simple way to estimate the strength of interactions is to compare NMR properties of neat solvents and the solvent within tissue. Such a comparison is made in Table I for the T_1 and T_2 relaxation times. Equality of the paraffin and “Clearify” T_1 relaxation times in bulk and tissue indicates the absence of an interaction between the tissue and these aliphatic solvents. Thus, T_1 contrast is negligible in these cases. However, in xylenes and methanol, the T_1 relaxation

times in tissue are half of the values in bulk solvents. Shortening of T_1 was observed also in water and DMSO, although somewhat smaller. Any reduction of the relaxation time indicates solvent–tissue interaction, which in the framework of Eq. (1) points to the presence of one or more new solvent fractions. Similarly, shortening of T_2 relaxation times, observed in all cases, points to the existence of local field fluctuation that could range from real solvent–tissue interaction (spin exchange or molecular binding) to unrestricted motion of the solvent spins in the local field gradient. In any case, the change in the relaxation time is an indicator of potential contrasting.

Representative slices from 3D T_2 -weighted images in various solvents are shown in Fig. 1. The imaging conditions were different mostly because attempts were made to optimize the parameters for each solvent independently. Panel A shows a single slice of the mouse brain in water (NBF) with $32 \mu\text{m pixel}^{-1}$ isotropic resolution. Clearly visible are the dorsal hippocampus, thalamus, hypothalamus and cortex. The mice used in this study were infected with the Theiler murine encephalitis virus (TMEV), a murine multiple sclerosis (MS) model. Intracerebral TMEV infection results in chronic-progressive demyelination in susceptible mouse strains. The dark areas above the hippocampus (and below on the right) are from hemorrhages from intracerebral injections.

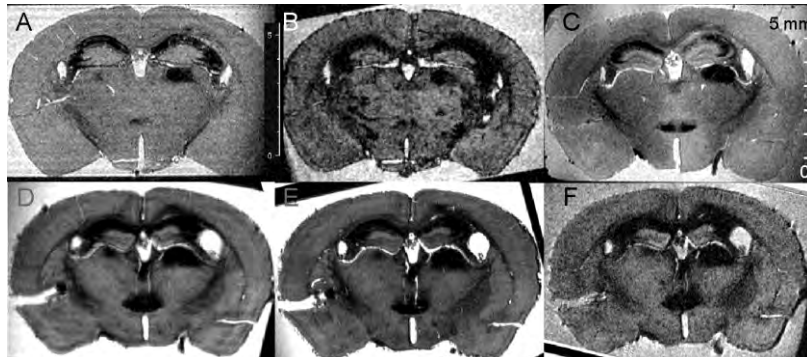


Fig. 1. Slices from 3D RARE (spin echo) scans of mouse brain in different solvents. A) H_2O (NBF): TE_{eff} 26, EncMTX $333 \times 176 \times 78$, FOV $12.8 \times 8 \times 3.2$, MTX $400 \times 256 \times 100$, RareFactor 4, TR 2100, ScanTime 12 h, SpatResol $32 \mu\text{m pixel}^{-1}$ (isotropic); B) CH_3OH : TE_{eff} 26, EncMTX $166 \times 88 \times 50$, FOV $12.8 \times 8 \times 3.2$, MTX $200 \times 128 \times 64$, RareFactor 4, TR 2200, ScanTime 4 h, SpatResol $64 \times 63 \times 50 \mu\text{m pixel}^{-1}$; C) DMSO: TE_{eff} 11, EncMTX $333 \times 176 \times 78$, FOV $12.8 \times 8 \times 3.2$, MTX $400 \times 256 \times 100$, RareFactor 1, TR 3000, ScanTime 11.5 h, SpatResol $32 \mu\text{m pixel}^{-1}$ (isotropic); D) “Clarify”: TE_{eff} 26, EncMTX $333 \times 176 \times 100$, FOV $10.2 \times 6.4 \times 3.2$, MTX $400 \times 256 \times 128$, RareFactor 4, TR 2200, ScanTime 16 h, SpatResol $25 \mu\text{m pixel}^{-1}$ (isotropic); E) paraffin: TE_{eff} 26, EncMTX $333 \times 176 \times 100$, FOV $10.2 \times 6.4 \times 3.2$, MTX $400 \times 256 \times 128$, RareFactor 4, TR 2200, ScanTime 16 h, SpatResol $25 \mu\text{m pixel}^{-1}$ (isotropic); F) xylenes: TE_{eff} 31, EncMTX $426 \times 220 \times 100$, FOV $12.8 \times 8 \times 3.2$, MTX $512 \times 320 \times 128$, RareFactor 4, TR 2400, ScanTime 14.7 h, SpatResol $25 \mu\text{m pixel}^{-1}$ (isotropic). The brightness was adjusted for each panel separately.

The methanol image, panel B, shows much better contrast but, although recorded with half the resolution, has a much lower *SNR* (owing to the longer T_1) than the water image. On the other hand the DMSO image, panel C, exhibits a much better *SNR* and contrast than the water image, most likely due to the slower diffusion and shorter T_1 .

The aliphatic hydrocarbon images (D – “Clearify”, E – paraffin) show superior sensitivity and contrast compared to the polar solvent images, mostly because of their much longer T_2 values. In addition, their lower diffusion coefficients enabled scanning at the even higher resolution of $25 \mu\text{m pixel}^{-1}$. A moderate blurring in the Clearify image caused by a relatively poor point spread function should be noted. With effective spectral width of 50–100 kHz and readout size of 400 points, the Clearify signal spreads over a few pixels introducing noticeable blurring compared to the paraffin image. The xylenes image, panel F also exhibits excellent contrast, but due to long T_1 suffers from a poor *SNR. The acetone image (not shown) was of rather poor quality partly because of an extremely long T_1 (very low *SNR*) and partly because of the volatility of the solvent (artifacts caused by the change of the sample volume (solvent is lost due to the evaporation)).*

Figure 2 shows T_1 parametric images of the mouse brain slices in the indicated solvents. In polar solvents (A – water, B – methanol, C – DMSO) there is noticeable variation of T_1 within the tissue and between tissue and the solvent,

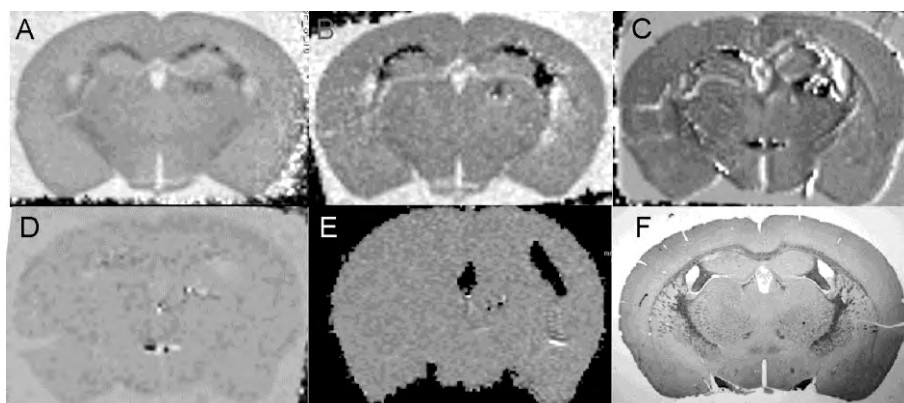


Fig. 2. Parametric T_1 images of the mouse brain slice in different solvents. A) H_2O (NFB), B) CH_3OH , C) DMSO, D) “Clearify”, E) paraffin and F) optical image ($1.25\times$) of a $5 \mu\text{m}$ slice taken from a formalin-fixed, paraffin-embedded mouse brain slice. The observed contrast depends on the tissue–solvent interaction. Notable is the complete absence of an interaction (uniform T_1 parametric image) between tissue and paraffin, panel E. The brain contour is visible because the specimen was mounted “dry” on the surface coil; otherwise, due to T_1 s in tissue and bulk solvent being the same (lack of contrast), the slice would completely merge with the solvent background signal. In all other cases, the solvent T_1 was longer than the tissue T_1 .

but in aliphatic hydrocarbon solvents these variations are either minimal (D – “Clarify”) or nonexistent (E – paraffin). There is no background in panel E because the specimen was mounted “dry” on the surface coil. Otherwise, when immersed in paraffin, the tissue signal fuses completely with the surrounding solvents signal. This uniformity of T_1 clearly indicates that paraffin molecules do not interact with any of the tissue components, which actually could help in the interpretation of the T_2 relaxation of the paraffin in tissue (*vide infra*). Interestingly, the xylenes T_1 parametric image (not shown) is uniform within the tissue, like the paraffin image, but has an intensity distinctly different from that of the surrounding solvent.

For reference, Fig. 2F shows an optical image of a 5 μm thick paraffin-embedded slice. The NMR images can hardly match the optical ones in resolution and contrast but they are obtained from the intact paraffin block while the slice must be physically cut for optical microscopy. This opens an interesting prospect for MRM of paraffin-embedded tissue as NMR images could be used to guide sectioning of ROIs for subsequent specimen cutting for histological analysis.

Mouse brain T_2 parametric images in various solvents are shown in Fig. 3. Notable are the differences between the tissue and solvent signal in all cases. Again, the background signal in the paraffin image, panel E, is absent because the specimen was mounted “dry” on the surface coil. However, traces of bulk solvent are visible as very bright spots in the specimen cracks. Large differences in signal intensity between the solvent and tissue for hydrocarbon solvents (D – “Clarify”, E – paraffin, F – xylenes) mean that the major source of contrast is the local field gradients. For polar solvents, in addition to local gradients, other

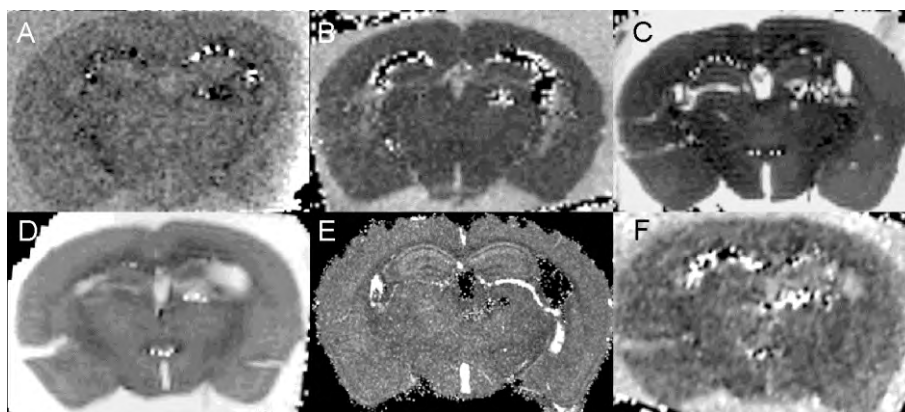


Fig. 3. Parametric T_2 images of the mouse brain slice in different solvents. A) H_2O (NFB), B) CH_3OH , C) DMSO, D) “Clarify”, E) paraffin and F) xylene. Notable are the differences between the tissue solvent and bulk solvent intensities. In panel E, the background is black because the specimen was mounted ‘dry’; neat solvent is visible only in the tissue pockets (white areas).

interactions may exist, such as chemical exchange with tissue labile protons (water, methanol) or binding (adsorption, absorption and intercalation) of solvent molecules in the tissue matrix (water, methanol and DMSO).

One way to test the existence of an interaction between the solvent and tissue is to monitor magnetization exchange between the two components of the solvent mixture. In high resolution spectroscopy this experiment is known as ILOE¹¹ and in NMR imaging as magnetization transfer (MT).¹⁸ Both experiments are based on incoherent magnetization exchange (chemical exchange and cross-relaxation^{12,19,20}), the only difference being whether the transferred magnetization is used to modulate the image or high resolution spectrum. Briefly, while a resonance line at one frequency is observed, the other frequency or frequency band is irradiated. Irradiation saturates the lines at the selected resonances. In the presence of magnetization exchange, this saturation is transferred to exchanging partners causing a signal decrease at the observed line. Intermolecular chemical exchange involves labile protons and is not of concern here. More interesting is cross-relaxation which depends on both the geometry and mobility of the interacting nuclei.¹² At the spin-diffusion limit ($\omega_0\tau_c > 1$, ω_0 – resonance frequency, τ_c – correlation time), the cross-relaxation rate is proportional to the correlation time: the longer the correlation time, the higher the rate. At the other limit, extreme narrowing ($\omega_0\tau_c < 1$,) results in cross-relaxation being significantly lower and of the opposite sign.¹² Thus, strong intermolecular cross-relaxation indicates that the observed spin pair is in the spin diffusion regime, which at 700 MHz would mean that the two spins are in close proximity for longer than 0.3 ns. This time interval is about three orders of magnitude longer than the correlation time in free liquids (≈ 1 ps). In other words, observation of strong intermolecular magnetization transfer between small molecules indicates their binding on a common substrate. In the present case, observation of MT in a mixed solvent would indicate solvent–tissue interaction. To test for solvent–tissue interaction, a mixture of water and DMSO was selected. From the ¹H-NMR spectrum of DMSO around the tissue (not shown), it was found that the solvent contained ≈ 20 % water (the water signal was ≈ 15 % of the total magnetization and ≈ 900 Hz downfield from the DMSO signal); thus the original DMSO specimen without any changes was used as a mixed solvent system.

The Z-spectrum obtained by systematic irradiation of the 8 kHz range around the DMSO resonance, in increments of 200 Hz, is shown in Fig. 4. A single slice FLASH image was generated by selective excitation and detection of the DMSO line was conducted where, in a series of experiments, the irradiation frequency was systematically changed from one experiment to another. Three ROIs were selected: within the tissue (thalamus), within the solvent (bulk) and outside tissue and solvent (the noise floor). The frequency offset was counted from the DMSO resonance that was solely detected. In the bulk solvent, only

direct saturation around zero offset exists: the observed resonance line is hit directly by the saturating field that resulted in a massive signal reduction. Thus, in neat mixed solvent, no MT was detected. However, within the tissue manifest MT between water and DMSO was observed. A minimum at ≈ 1 kHz (water resonance) showed that the DMSO signal is significantly reduced when the water line is saturated, indicating strong cross-relaxation between the water and DMSO proton spins. Strong cross-relaxation could be observed only if both molecules reside within the tissue for longer than 0.3 ns, which could be interpreted as solvent binding. In the present case, the MT effect was uniform across the tissue and besides binding no new information was added. However, it is conceivable that in different solvent mixtures and in a different tissue, the ILOE could exhibit regional selectivity, which could be an additional useful contrasting tool.

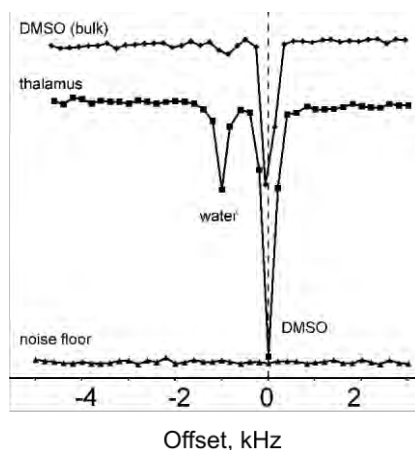


Fig. 4. The Z-spectrum of the DMSO–water system. Magnetization transfer was performed in a series of 41 2D FLASH experiments with MT offsets from -5000 to $+3000$ Hz (in 200 Hz increments). The offset was measured from the DMSO resonance that was selectively detected and used to generate the images. In a single experiment, saturation was performed with a series of 20 Gaussian pulses, 10 ms with MT time 200 ms and 1 μ T amplitude, which kept a saturation bandwidth of 275 Hz. The points represent the signal integral from the indicated region of interest at a given offset.

CONCLUSIONS

It was shown that the MRM of tissue in organic and mixed solvents is a promising approach for improvement of image quality and for a better understanding of tissue–solvent interactions. The employment of organic solvents for MRM at high fields is particularly promising because aliphatic solvents eliminate some of the problems encountered in standard imaging using water. The properties of an ideal MRM solvent were briefly discussed and a few available in the lab were tested experimentally. It was found that the most promising of these were paraffin (at 70 °C) and DMSO, but, with certainty, there are some further options that could be even better. In addition, the use of mixed solvents was proposed, and experimentally demonstrated, as a means to test the residence time of solvent molecules on the tissue surface.

Acknowledgement. We thank Mr. David Hinton for critical reading of the manuscript.

ИЗВОД

NMR СЛИКАЊЕ ТКИВА У ОРГАНСКИМ И МЕШОВИТИМ РАСТВОРАЧИМА

SLOBODAN MACURA¹, PRASANNA K. MISHRA¹, JEFFREY D. GAMEZ² и ISTVAN PIRKO²¹*Department of Biochemistry and Molecular Biology* и ²*Department of Neurology, Mayo Clinic, Rochester, Minnesota, 55905, USA*

У овом раду разматрана је употреба органских и мешовитих растварача за нуклеарно-магнетно-резонантну микроскопију фиксираних ткива, као средства за побољшање информационог садржаја NMR слике. NMR својства неких стандардних растварача (метанол, ацетон и диметил-сулфоксид (DMSO)) и растварача који се користе за обраду ткива у патологији (ксилен, парафин и „Clearify“) измерени су, прегледани и анализирани. Утврђено је да су DMSO и парафин веома корисни растварачи који пружају слике бољег квалитета од оних добијених у води (неутралном формалинском пуферу). Ово је илустровано на узорцима формалином фиксираних мишићног мозга сликаног на 16,4 T (700 MHz).

(Примљено 8. октобра 2013)

REFERENCES

1. P. C. Lauterbur, *Nature* **242** (1973) 190
2. A. Kumar, D. Welti, R. R. Ernst, *J. Magn. Reson.* **18** (1975) 69
3. E. M. Haacke, *Magnetic resonance imaging: physical principles and sequence design*. Wiley, New York, 1999.
4. P. T. Callaghan, *Principles of nuclear magnetic resonance microscopy*. Oxford University Press/Clarendon Press, Oxford (England)/ New York, 1991
5. P. Caravan, J. J. Ellison, T. J. McMurry, R. B. Lauffer, *Chem. Rev.* **99** (1999) 2293
6. T. M. Shaw, R. H. Elskens, *J. Chem. Phys.* **21** (1953) 565
7. K. Venu, V. P. Denisov, B. Halle, *J. Am. Chem. Soc.* **119** (1997) 3122
8. B. Halle, *Magn. Reson. Med.* **56** (2006) 60
9. P. S. Belton, *Cell. Mol. Life Sci.* **57** (2000) 993
10. R. A. Brooks, F. Moiny, P. Gillis, *Magn. Reson. Med.* **45** (2001) 1014
11. D. Li, E. DeRose, R. London, *J. Biomol. NMR* **15** (1999) 71
12. S. Macura, R. R. Ernst, *Mol. Phys.* **41** (1980) 95
13. T. Horiuchi, M. Takahashi, J. Kikuchi, S. Yokoyama, H. Maeda, *J. Magn. Reson.* **174** (2005) 34
14. S. Blackband, D. Buckley, J. Bui, M. I. Phillips, *MAGMA* **9** (1999) 112
15. R. J. Kurland, F. Q. H. Ngo, *Magn. Reson. Med.* **3** (1986) 425
16. J. A. Glasel, K. H. Lee, *J. Am. Chem. Soc.* **96** (1974) 9
17. R. P. Kennan, J. Zhong, J. C. Gore, *Magn. Reson. Med.* **31** (1994) 9
18. S. D. Wolff, R. S. Balaban, *Magn. Reson. Med.* **10** (1989) 135
19. S. Macura, R. R. Ernst, *Period. Biol.* **83** (1981) 87
20. S. Macura, W. M. Westler, J. L. Markley, *Methods Enzymol* **239** (1994) 106.



J. Serb. Chem. Soc. 78 (11) 1655–1670 (2013)
JSCS–4525

Halothane binds to druggable sites in the $[Ca^{2+}]_4$ -calmodulin (CaM) complex, but does not inhibit $[Ca^{2+}]_4$ -CaM activation of kinase

NENAD O. JURANIĆ^{1*}, KEITH A. JONES², ALAN R. PENHEITER¹,
THOMAS J. HOCK² and JOHN H. STREIFF²

¹Mayo College of Medicine at Rochester, U.S.A. and

²University of Alabama at Birmingham, U.S.A.

(Received 23 May 2013)

Abstract: The mechanism(s) of volatile anesthetics (VAs) are poorly understood. High-resolution NMR spectroscopy was used to determine the structure of the halothane- $[Ca^{2+}]_4$ -calmodulin ($[Ca^{2+}]_4$ -CaM) complex, and it was found that halothane molecules bind in the druggable sites. Then it was examined whether VAs binding to druggable sites in calmodulin would affect the $[Ca^{2+}]_4$ -CaM dependent activity of myosin light chain kinase. Fluorescence assays were used to determine that VA mediate $[Ca^{2+}]_4$ -CaM activation of smooth-muscle-myosin-light-chain-kinase (smMLCK), but do not alter significantly the K_d of $[Ca^{2+}]_4$ -CaM binding to skeletal-myosin-light-chain-kinase-peptide recognition sequence (skMLCKp). The results suggested that VAs do not alter $[Ca^{2+}]_4$ -CaM dependent MLCK activity *via* direct interactions with $[Ca^{2+}]_4$ -CaM.

Keywords: volatile anesthetic, calmodulin, halothane, drugs, protein structure.

INTRODUCTION

Volatile anesthetic (VA) drugs are used extensively with little knowledge of their cellular targets or mechanisms. The targets likely include proteins because anesthetic effects ultimately manifest as changes in protein function. This is further supported by the observation that the bioluminescent protein luciferase is inhibited *in vitro* by direct interaction with a variety of anesthetic agents.¹

Calmodulin (CaM) is a ubiquitous Ca^{2+} second messenger that regulates many anesthetic sensitive systems. CaM has two EF hands, Ca^{2+} -binding domains that can bind up to 2 Ca^{2+} ions each. The EF hands are located at the N- and C- termini and are separated by a flexible central helix. The main difference between calcium-free CaM (apoCaM) and $[Ca^{2+}]_4$ -CaM is the interhelical angle

* Corresponding author. E-mail: juranic.nenad@alumni.mayo.edu

doi: 10.2298/JSC130523090J

between the Ca^{2+} binding domains, which increases upon Ca^{2+} binding and exposes large hydrophobic pockets in each termini to the aqueous environment.² These hydrophobic pockets are critical for the interaction of $[\text{Ca}^{2+}]_4\text{-CaM}$ with many proteins and hence the regulation of numerous enzymatic pathways. The Ca^{2+} dissociation constant (K_d) of $[\text{Ca}^{2+}]_4\text{-CaM}$ is decreased by ligands, peptides, and proteins to the extent that they reduce the effective hydrophobic surface of $[\text{Ca}^{2+}]_4\text{-CaM}$ exposed to an aqueous environment.³ In other words, Ca^{2+} signaling through CaM is partially tuned by the target.

$[\text{Ca}^{2+}]_4\text{-CaM}$ antagonists bind in the hydrophobic pockets of $[\text{Ca}^{2+}]_4\text{-CaM}$,⁴ with a concomitant decrease in the Ca^{2+} K_d of $[\text{Ca}^{2+}]_4\text{-CaM}$,⁵ and inhibition of $[\text{Ca}^{2+}]_4\text{-CaM}$ activation of enzyme activity.⁶ Short chain *n*-alcohols also bind to the hydrophobic pockets of $[\text{Ca}^{2+}]_4\text{-CaM}$,⁷ and decrease the Ca^{2+} K_d of $[\text{Ca}^{2+}]_4\text{-CaM}$.⁸

It was found and verified that the VAs halothane and isoflurane decrease the Ca^{2+} K_d of $[\text{Ca}^{2+}]_4\text{-CaM}$.^{9,10} It was shown that VAs bind to $[\text{Ca}^{2+}]_4\text{-CaM}$, but not to apoCaM.¹⁰ This suggests that VAs bind to sites in $[\text{Ca}^{2+}]_4\text{-CaM}$ that are either not present or not accessible in apoCaM. Together, these findings suggest that VAs bind to the hydrophobic pockets of $[\text{Ca}^{2+}]_4\text{-CaM}$. This was supported by docking studies that indicated that the VAs halothane, isoflurane, and sevoflurane bind within the hydrophobic pockets in both the N- and C-termini.^{10,11} Thus, it was posited that VAs, as alcohols, would inhibit $[\text{Ca}^{2+}]_4\text{-CaM}$ dependent enzymes and might directly antagonize $[\text{Ca}^{2+}]_4\text{-CaM}$.

The objective of this work was to verify that VAs bind to the hydrophobic pockets in $[\text{Ca}^{2+}]_4\text{-CaM}$ and determine whether they antagonize the $[\text{Ca}^{2+}]_4\text{-CaM}$ -dependent myosin light chain kinase (smMLCK) activity. This work is significant because it will test whether the effects of VAs on protein function could arise from low affinity ligand binding to druggable sites.

EXPERIMENTAL

Proteins and peptides

Human calmodulin cDNA was sub-cloned into the pET-15b expression vector (Novagen, San Diego, CA) using standard cloning techniques. CaM was overexpressed in BL21(DE3)-pLysS strain of *Escherichia coli* (Single Shot, Novagen, San Diego, CA). Uniform ^{13}C , ^{15}N enrichment was achieved by growing cells in Luria–Bertani medium and then inducing in minimal media containing ^{13}C -glucose and $^{15}\text{NH}_4\text{Cl}$ following established protocols.¹² Isotopically labeled and unlabeled CaM were purified using a slight modification to an existing procedure.¹³ Thus, 5 mM CaCl_2 was added to the cleared cell lysate, which was loaded onto a phenyl-sepharose CL-4B column (Sigma, St. Louis, MO), and the CaM was eluted with 1 mM ethylene glycol tetraacetic acid (EGTA). The CaM fractions were further purified using a HiTrap Q column (Amersham Biosciences, Uppsala, Sweden) and a 0–1 M NaCl gradient. CaM was greater than 95 % pure, judging by SDS-gel electrophoresis with Coomassie Brilliant Blue staining. The identity of the CaM was confirmed by N-terminal sequencing as well as by LC–MS analysis of tryptic digests of labeled and unlabeled CaM. The molecular weight

and labeling efficiency (96 %) were verified by ESI-MS by direct infusion. Smooth muscle myosin light chain kinase (smMLCK) isoform 5 was prepared as previously described.¹⁴

Human MLC cDNA was sub-cloned into pET-15b expression vector (Novagen, San Diego, CA) using standard cloning techniques. MLC was overexpressed in BL21(DE3)-pLysS strain of *E. coli* (Single Shot, Novagen, San Diego, CA). The regulatory light chain (AL050318) was amplified from dT-primed cDNA derived from human lens epithelial cells using Fusion polymerase from New England Bio Labs. The primers used for amplification were NdeI forward gccatgatgccagcaagcgggcaaa and SpeI reverse gaactagtctagctgtctttatccttgccgc. The amplified cDNA was cloned into a pET 15 B vector containing an N-terminal his tag linearized with NdeI and SpeI using standard cloning techniques. Recombinant clones were sequence verified. Protein expression was performed using Magic Media (Invitrogen). Briefly, an isolated clone was grown overnight in 50 ml Magic Media. The cells were pelleted by centrifugation at 5000g and lysed in Bug Buster media (Novagen). The inclusion bodies were collected by centrifugation and resuspended in 50 mM Tris-HCl (pH 8), 7 M urea, 250 mM NaCl, and 1 mM 2-mercaptoethanol. The solution was passed over a Ni-NTA column equilibrated in the same buffer. The protein was refolded on the column using a urea gradient (8 to 0 M) flowing at 0.2 ml min⁻¹ for 16 h. The protein was eluted using a buffer containing 50 % glycerol, 50 mM Tris-HCl (pH 8), 250 mM imidazole, and 1 mM 2-mercaptoethanol. The MLC was judged greater than 90 % pure by SDS-PAGE with Coomassie Brilliant Blue staining.

The skeletal myosin light chain kinase peptide recognition sequence (skMLCKp) (biotin-CAAARWKKNFIAVSAANRFKKIS) was synthesized by Genetech, inc. (San Antonio, TX).

Lactate dehydrogenase, pyruvate kinase, phosphoenolpyruvate (PEP), NADH, and ATP were purchased from Sigma (St. Louis, MO).

NMR spectroscopy

Samples of 2mM [¹³C,¹⁵N]CaM, or 2mM [¹⁵N]CaM, in aqueous solvent (95 % H₂O, 5 % D₂O), containing 100 mM KCl, 50 mM 3-morpholinopropane-1-sulfonic acid (MOPS, pH 7.2), 20 mM CaCl₂, 5 mM MgCl, 1 mM EDTA, were equilibrated with halothane to various mole ratios. It was possible to achieve up to about 1:70 CaM:halothane ratio, as determined by proton NMR. For structure determination the samples with 1:10 CaM:halothane ratio were used. Preparation of samples in the oriented media, for measurements of residual dipolar coupling (RDC), failed because of interference with halothane. It was found that the phage media coagulated upon halothane addition, and gel media gave a prohibitory fast relaxation in the presence of halothane. NMR experiments were performed at 25 °C on a 700 MHz spectrometer (Bruker Avance 700) equipped with a cryo-probe. Backbone and side-chain assignments were obtained using a combination of standard triple resonance experiments.¹⁵ 2D HNHA, 3D HNC(O), HNCA, HN(CO)CA, HNCACB and CBCA(CO)NH were used for the ¹H, ¹⁵N and ¹³C assignments of the protein backbone. Side-chains ¹H and ¹³C assignments of the non-aromatic side chains were obtained using 3D HAHB(CO)NH, (H)CC(CO)NH, HCCH-COSY and HCCH-TOCSY spectra. Assignments were crosschecked for consistency with 3D ¹⁵N-edited and ¹³C-edited [¹H, ¹H]-NOESY spectra. The ¹H and ¹³C spin systems of the aromatic side-chains were identified using 3D HCCH-COSY and HCCH-TOCSY spectra, while the sequential assignment was based on NOE connectivity in the ¹³C-edited [¹H, ¹H]-NOESY spectrum. Methionine methyl-group ¹H and ¹³C assignment was achieved using methionine-methyl ¹³C_ε-filtered [¹H-¹³C]-HSQC spectrum and ¹³C_{γ,ε}-filtered [¹H-¹³C]-HMBC spectrum.¹⁵ NOESY spectra for structural constraints were recorded at mixing times of 50 ms, 100 ms and 150 ms. Quantitative J-correlation HNHA experiment¹⁵ was used for

measurement of $^3J(\text{H}^{\text{N}}\text{H}^{\alpha})$ couplings. The ^1H - ^{15}N heteronuclear NOEs¹⁶ were recorded using a 500 MHz spectrometer (Bruker Avance 500). The multidimensional spectra were processed and analyzed in FELIX (Felix NMR, 2007). All analyses performed after peak picking (assignments and structural parameter calculations) were realized using custom programs in MATLAB (The MathWorks, 2007). About 1600 NOE distances (including 19 halothane–protein distances) were extracted (see Table I in Results) and applied with error limits deduced from values obtained at three mixing times. The backbone NOE contacts and $^3J(\text{H}^{\text{N}}\text{H}^{\alpha})$ couplings were in agreement with NMR solution structure of $[\text{Ca}^{2+}]_4\text{-CaM}$ (1J7O & 1J7P¹⁷). Therefore, backbone dihedral angles of the free $[\text{Ca}^{2+}]_4\text{-CaM}$ were used as constraints with an error limit of $\pm 10^\circ$, except in few regions of missing experimental couplings or a larger chemical shift difference at the backbone between free and complexed CaM. In these regions (residues: 19–21, 38–43, 54–57, 63–67, 70–76, 92–95, 104–108, 144–147) error limits were increased to $\pm 30^\circ$. All H-bonds of free $[\text{Ca}^{2+}]_4\text{-CaM}$ were also enforced by the distance constraints. Additional distance constraints were defined to maintain coordination geometry around Ca^{2+} .

Structure calculations

The initial conformation of the $[\text{Ca}^{2+}]_4\text{-CaM}$ N-terminus lobe (residues 1–76) or C-terminus lobe (82–148) was set to the most representative conformer of the reported NMR solution structure of $[\text{Ca}^{2+}]_4\text{-CaM}$, 1J7O.pdb or 1J7P.pdb, respectively.¹⁷ Halothane was positioned $\approx 5 \text{ \AA}$ above the hydrophobic pocket of each terminus. QUANTA/XPLOR¹⁸ was used for structure calculations: standard simulated annealing schedule, refinement by cooling and energy minimization with distance and dihedral restraints. The final structures were not sensitive to the initial positioning of halothane. Of the 50 structures produced (for each lobe), about 15 were within 10 % of the lowest energy structure. These low-energy structures were subjected to a short (100 steps steepest descend) energy minimization in the CHARMm22 force-field (Molecular Simulations Inc., 1994), without any restraints except that Ca^{2+} coordination geometry was kept fixed. Five structures (for each lobe) that fully complied with the constraints were selected in the final set.

Data deposition

The NMR constraints and atomic coordinates for the conformers were deposited at Protein Data Bank (PDB entries 2kug and 2kuh for N- and C- terminus lobes, respectively).

$[\text{Ca}^{2+}]_4\text{-CaM-skMLCKp}$ binding

Binding was determined from the change in emission of the tryptophan residue in the skMLCKp peptide measured in a stirred narrow channel 1 cm fluorescence cuvette (Helman) using a Fluoromax-3 instrument (Jobin-Yvon-Spex). The excitation wavelength was 280 nm, the emission wavelength was 333 nm, the excitation and emission slit widths were 5 nm, and the integrated emission intensity was averaged from thirty 1 s scans. The assay buffer was 50 mM MOPS (pH 7.3), 100 mM KCl, 1 mM MgCl_2 and 0.1 mM CaCl_2 . The solutions were filtered and centrifuged to remove light scattering interferants. A set of titration data were collected in the following order: the background emission from the buffer was measured first. Then 2.7 nM skMLCKp was added into the cuvette and the emission was remeasured. This solution was discarded and a fresh volume of buffer was added to a clean cuvette and the emission measured. Then $[\text{Ca}^{2+}]_4\text{-CaM}$ was added to a concentration of 1.3 nM and the emission recorded. Finally, skMLCKp peptide was added to a concentration of 2.7 nM and the emission was recorded. The solution was discarded and the series of measurements was repeated for 2.7, 4.0, 8.0, and 16.0 nM concentrations of $[\text{Ca}^{2+}]_4\text{-CaM}$. There was minimal

variation in the baseline emission intensities between the samples. The emission intensity from the skMLCKp at each $[Ca^{2+}]_4$ -CaM concentration was determined by subtracting the emission intensity of the sample of $[Ca^{2+}]_4$ -CaM and buffer from the corresponding sample of $[Ca^{2+}]_4$ -CaM, skMLCKp and buffer. The skMLCKp emission intensity was plotted as a function of $[Ca^{2+}]_4$ -CaM concentration with error bars that represent the standard deviation of the thirty intensity values collected at 1 s intervals. Three sets of $[Ca^{2+}]_4$ -CaM-skMLCKp titration data were collected and each was fitted with the following equation:

$$F = F_{\min} + F_{\max} \left[\frac{(CaM + skMLCK + K_d) - \sqrt{(CaM + skMLCK + K_d)^2 + 4CaM \times skMLCK}}{2skMLCK} \right]$$

where F_{\min} is the emission intensity from 2.7 nM skMLCKp in the absence of $[Ca^{2+}]_4$ -CaM, F_{\max} is the emission intensity from 2.7 nM skMLCKp bound to $[Ca^{2+}]_4$ -CaM, CaM is the concentration of $[Ca^{2+}]_4$ -CaM, $skMLCKp$ is the concentration of skMLCKp (fixed at 2.7 nM), and K_d is the dissociation constant.

The data fitting was realized using Origin 7.5 (OriginLab) and the parameters are reported as mean \pm *sd* of the fits to the three-titration data sets.

[Ca²⁺]₄-CaM-smMLCK activity

The $[Ca^{2+}]_4$ -CaM-dependence of the smMLCK activity was measured using a spectroscopic method coupled to pyruvate kinase and lactate dehydrogenase,¹⁹ which was modified to work in a 96-well format fluorescence plate reader. Briefly, when smMLCK transfers a phosphate group from ATP to MLC, it produces a molecule of ADP. Pyruvate kinase (PK) acts on ADP and phosphoenolpyruvate (PEP) to produce ATP and pyruvate. Lactate dehydrogenase (LDH) acts on pyruvate and NADH to produce NAD⁺ and lactate. Thus, for each MLC phosphorylated, one molecule of the fluorescent NADH is converted to the non-fluorescent NAD⁺. The specific activity of smMLCK was determined by recording the kinetics of NADH disappearance using a Fluostar Optima Fluorescence plate reader (BMG) with 350 and 460 nm excitation and emission filters, respectively. The kinetic assays were performed in triplicate on 200 μ l samples. A typical well contained 20 mM MOPS (pH 7.5), 100 mM KCl, 0.1 mM EGTA, 1.5 mM dithiothreitol (DTT), 1.2 mM PEP, 10 μ M NADH, 4.3 units of LDH/PK, 20 μ M regulatory light chain (RLC), 100 η g MLCK, and various amounts of $[Ca^{2+}]_4$ -CaM. The maximum fluorescence intensity of the NADH in the wells was recorded prior to initiating the assay by automatically injecting 10 μ l of a solution containing 6 mM ATP, 40 mM MgCl₂, and 10 mM CaCl₂, which dilute to a final concentration of 0.3 mM ATP, 2 mM MgCl₂, and 0.5 mM CaCl₂ in the wells. The time dependent decrease in NADH fluorescence was recorded at 30 s intervals for approximately 10 min, after which the reaction was stopped by automatically injecting 10 μ l of 400 μ M ADP (20 μ M final concentration) into each well. The baseline fluorescence intensity of the NADH-depleted samples was then recorded.

RESULTS

Solution structure of [Ca²⁺]₄-CaM-halothane complex

The aim was to determine the structure of the $[Ca^{2+}]_4$ -CaM-halothane complex at low halothane concentrations, because physiological concentrations of a VA in anesthesia are rather low. The titration with halothane was followed by

NMR (Supplementary material to this paper) and saturation of the $[\text{Ca}^{2+}]_4\text{-CaM}$ chemical shifts was established at about 1:30 CaM:halothane mole ratio. Significant changes were observed already at a 1:10 mole ratio, which was eventually selected as concentration at which the physiologically relevant CaM/halothane complex might be discernible.

Chemical shifts of the protein backbone in $[\text{Ca}^{2+}]_4\text{-CaM}$ -halothane complex (at 1:10 mole ratio) differ in several regions from those of $[\text{Ca}^{2+}]_4\text{-CaM}$, measured in the absence of halothane (Fig. 1, bottom). The most pronounced differences were in the N-terminus. There were no significant differences in the region of the central linker (residues 77–82). The regional mobility of the complex, as probed by backbone $\{^1\text{H}\text{-}^{15}\text{N}\}$ -NOE (Fig. 1, top), indicates that the central linker was mobile when halothane was bound. These findings signify that low-halothane complex of $[\text{Ca}^{2+}]_4\text{-CaM}$ probably retains a flexible and distant disposition of the two Ca^{2+} binding domains, as was found in the NMR solution structure of $[\text{Ca}^{2+}]_4\text{-CaM}$.¹⁷

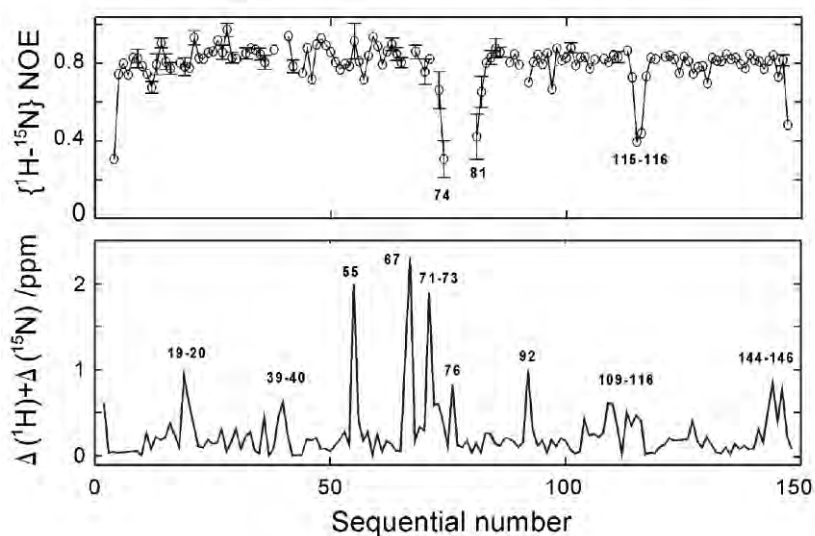


Fig. 1. Top: sequential values (open circles) of the backbone $\{^1\text{H}\text{-}^{15}\text{N}\}$ -NOE; error bars are shown only when larger than the size of the open circles. Bottom: comparison of the CaM backbone chemical shift difference ($\Delta^1H = |\delta^1H_{\text{complex}} - \delta^1H_{\text{free}}|$, $\Delta^{15}N = |\delta^{15}N_{\text{complex}} - \delta^{15}N_{\text{free}}|$) between $[\text{Ca}^{2+}]_4\text{-CaM}$ alone (free) and complexed with halothane.

A number of inter-molecular, $[\text{Ca}^{2+}]_4\text{-CaM}$ to halothane NOE contacts were observed in each Ca^{2+} binding domain. All of them were between the single halothane proton and methyl-groups of CaM residues: Leu-32, Val-35, Met-36, Leu-39, Met-51, Val-55, Met-71, Met-72 and Met-76 in the N-terminus lobe, and

Leu-105, Val-108, Met-109, Leu-112, Met-124, Ala-128, Met-144 and Met-145 in the C-terminus lobe. The best quality NOE contacts were seen for the methyl groups of methionines because of their favorable relaxation properties (Fig. 2). Numerous intra-calmodulin NOE contacts (≈ 800 per lobe) were all in support of the lobe structures as found in the NMR solution structure of $[\text{Ca}^{2+}]_4\text{-CaM}$.¹⁷

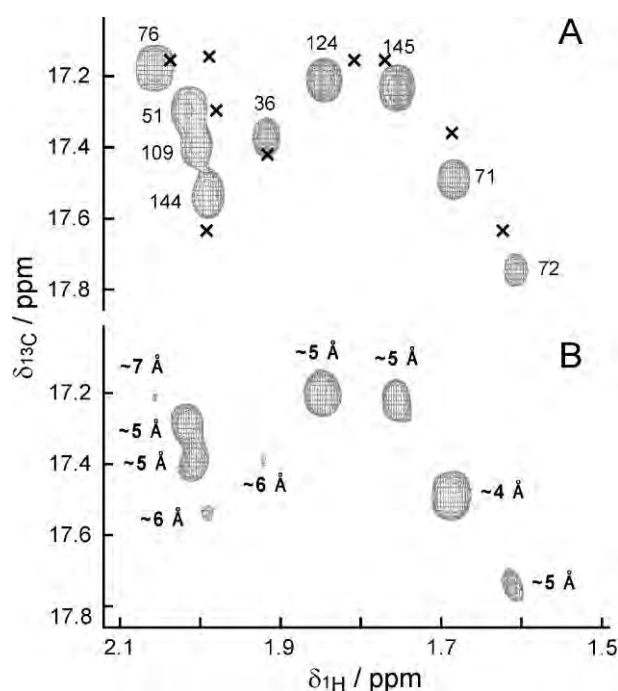


Fig. 2. Methyl-methionine ^{13}C -filtered 3D NOESY (200 ms mixing time) spectrum of $[\text{Ca}^{2+}]_4\text{-CaM}$ -halothane complex. A) Diagonal peaks region (^1H region 1.5–2.1 ppm) of the spectrum. Peaks are labeled by sequential numbers of the methionines. The corresponding positions in halothane free $[\text{Ca}^{2+}]_4\text{-CaM}$ ²⁰ are marked by crosses. B) Halothane cross-peaks region (^1H region: 6.2–6.4 ppm) of the spectrum displayed peaks having centers at 6.3 ppm. Calculated methyl-halothane distances are shown.

The structure of the complex was solved under the assumption that halothane binding has a minor effect on the protein fold, which was justified by the similarity of the chemical shifts in $[\text{Ca}^{2+}]_4\text{-CaM}$ determined with and without halothane, by the NOE contacts, and the $^3J(\text{H}^{\text{N}}\text{H}^{\alpha})$ couplings. Thus, the protein dihedral angles (ψ , ϕ and χ^1) were constrained to those of free $[\text{Ca}^{2+}]_4\text{-CaM}$ except in the regions of more pronounced (> 0.5 ppm) chemical shift differences (Fig. 1, bottom). Due to the flexible disposition of the two CaM lobes, the NMR solution structure was solved separately for the N-terminus and for the C-terminus lobes. The final structures were similar to the uncomplexed $[\text{Ca}^{2+}]_4\text{-CaM}$

structure¹⁷ having an average deviation between the backbone or side-chains of ≈ 2 Å and ≈ 3 Å, respectively. The structural statistics are given in Table I.

The obtained structures (Fig. 3) show halothane binding in the region of the hydrophobic pockets, which are binding targets for many other ligands.²¹ The N-terminus lobe structural models show a deeper imbedding of halothane than in the C-terminus, as could have been expected from the induced chemical shift changes of CaM (see above, Fig. 1, bottom). The orientation of the halothane varies considerably in the models, because there are no empirical constraints on the trifluoromethyl half of the molecule. An attempt was made to obtain additional constraints by measuring the ¹H–¹⁹F dipolar couplings in oriented media, but halothane was found to disrupt the properties of the orientation media, *i.e.*, phage and co-solvents.

TABLE I. Summary of conformational restraints and structural statistics for 5 energy-refined conformers of [Ca²⁺]₄-CaM in complex with halothane

Parameter	N-terminus	C-terminus
NOE distance restraints		
Intraresidual ($ i-j = 0$)	314	337
Sequential ($ i-j = 1$)	157	188
Medium range ($1 < i-j < 5$)	131	137
Long range ($ i-j \geq 5$)	128+9 ^a	137+10 ^a
Total NOE	735	808
Dihedral angle restraints ^b (ψ, ϕ, χ^1)	220	195
H-bond restraints ^b	37	23
RMSD over all distance constraint violations, Å	0.1	0.1
RMSD over all dihedral angle restraints violations, deg.	2.5	3.2
CHARMM energies ^c , kcal mol ⁻¹)		
Total	-2270±90	-1913±90
van der Waals	-316±9	-230±10
Electrostatic	-2285±90	-1970±100
Ramachandran plot statistics, %		
Residues in most favored region	90.3	95.7
Residues in additionally allowed regions	9.7	4.3
Residues in generously allowed regions	0	0
Residues in disallowed regions	0	0
Average RMSD from mean coordinates, Å		
All atoms	0.75	0.64

^aProtein-halothane NOE; ^btarget values are same as in [Ca²⁺]₄-CaM structure (1J70 & 1P70); ^ccharged protein without Ca²⁺ counter-ions contribution

skMLCKp [Ca²⁺]₄-CaM binding

The emission spectrum of the *skMLCKp* peptide excited at 280 nm was measured and it was found that the peak increased in intensity and was blue-shifted upon binding to [Ca²⁺]₄-CaM (Fig. 4, top panel). This result is consistent

with previous.²² The most significant difference between the spectra of the bound and unbound peptide was observed at 333 nm. The emission of the peptide at 333 nm at various $[Ca^{2+}]_4$ -CaM concentrations up to 16 nM was measured (Fig. 4, bottom panel). The binding curves yielded a mean K_d of 1.3 ± 0.4 nM, which agrees with the K_d value of 4 nM determined previously using surface plasmon resonance.²³ Moreover, 10 mM isoflurane did not significantly affect the fluorescence intensity of skMLCKp in the presence of 2.7 nM $[Ca^{2+}]_4$ -CaM.

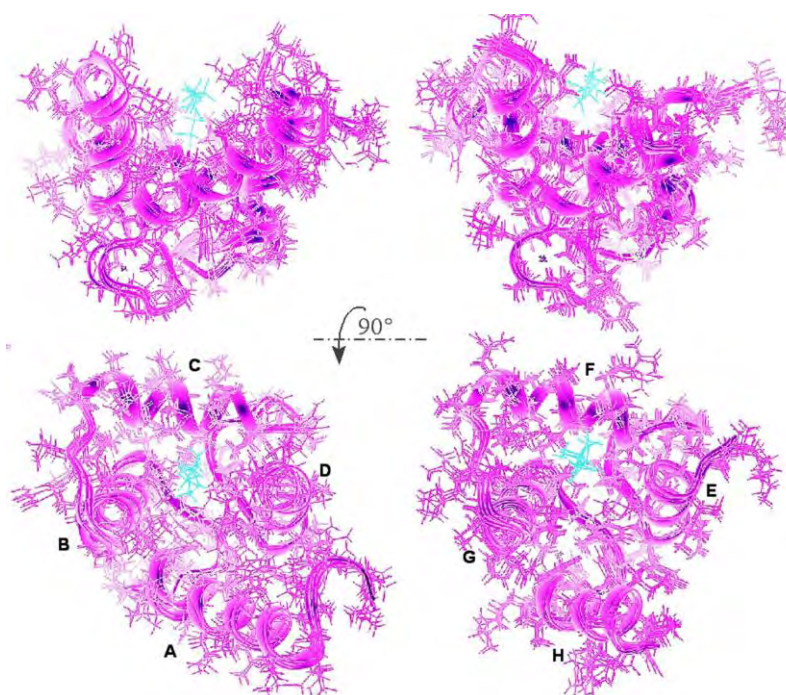


Fig. 3. Models of five conformers for N-terminus (to the left, 2KUG.pdb) and C-terminus (to the right, 2KUH.pdb) lobes of the $[Ca^{2+}]_4$ -CaM-halothane complex. Halothane is given in cyan color, protein in magenda. The atomic stick-plot is overlain with protein cartoon (helices are denoted by letters).

smMLCK activity

The specific activity of smMLCK was determined using an ADP/NADH coupled assay. Representative spectra recorded in the presence of various concentrations of $[Ca^{2+}]_4$ -CaM up to 300 nM illustrate the assay (Fig. 5, top panel). The initial plateau is the maximal emission from NADH, determined prior to initiating the assay. The drop in intensity ($\approx 10\%$) that occurred when a solution of ATP, $MgCl_2$, and $CaCl_2$ was automatically injected to start the reaction was due to minor ADP contamination. This was followed by a steady decrease in

NADH fluorescence that was dependent on the $[\text{Ca}^{2+}]_4\text{-CaM}$ concentration. The rate of fluorescence decrease was directly proportional to the phosphorylation of the myosin light chain. The final steep drop occurred when an ADP solution was automatically injected, which consumes the remaining NADH. The end plateau was the signal from the sample without NADH. The difference between the plateaus at the beginning and end of the assay was used to calibrate the instrument response to the amount of NADH present.

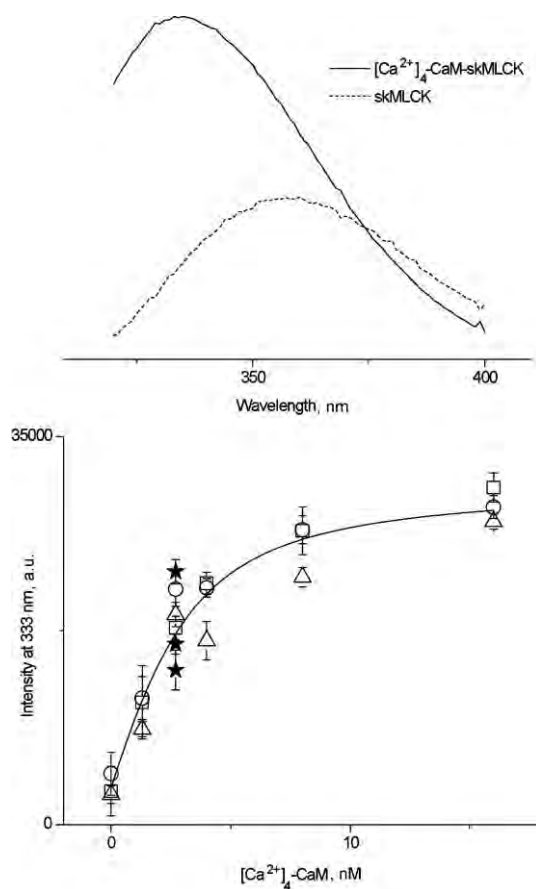


Fig. 4. Top: Change in tryptophan emission spectrum (at 280 nm) from skMLCKp upon binding to $[\text{Ca}^{2+}]_4\text{-CaM}$. Bottom $[\text{Ca}^{2+}]_4\text{-CaM}$ concentration dependence of tryptophan emission (at 333 nm) from 2.7 nM skMLCKp. The titrations were repeated in triplicate (circles, squares and triangles). The error bars represent the standard deviation in the mean of thirty, 1 s fluorescence measurements. The solid line was generated using the mean parameters from the curve fits to the three sets of titration data. It was found that 10 mM isoflurane did not significantly affect the fluorescence intensity of skMLCKp in the presence of 2.7 nM $[\text{Ca}^{2+}]_4\text{-CaM}$ (closed stars).

The specific activities of the smMLCK, calculated from the slopes are plotted as a function of $[\text{Ca}^{2+}]_4\text{-CaM}$ concentration in Fig. 5, bottom panel. The maximum activity of smMLCK in the presence of $[\text{Ca}^{2+}]_4\text{-CaM}$ was found to be approximately $12 \mu\text{mol min}^{-1} \text{mg MLCK}^{-1}$, which is consistent with previous results.¹⁹ The effect of various concentrations of halothane on the activity of MLCK alone and in the presence of $[\text{Ca}^{2+}]_4\text{-CaM}$ at concentrations that produce half-maximal

(2 nM) and maximal (100 nM) activation was measured. Halothane was found to inhibit the MLCK activity, but it was not $[Ca^{2+}]_4$ -CaM dependent (Fig. 6).

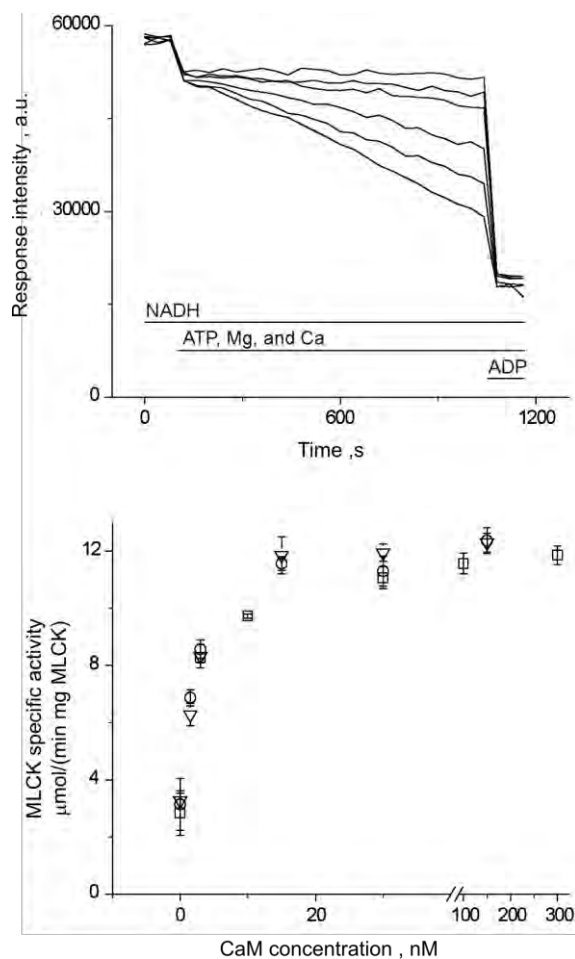


Fig. 5. Top: raw fluorescence data for assay of CaM-dependent MLCK activity. From top to bottom trace, CaM concentration was 0, 1, 3, 10, 30, and 100 nM. Bottom: $[Ca^{2+}]_4$ -CaM dependence of MLCK specific activity.

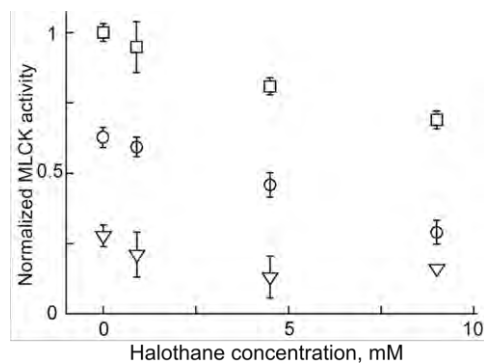


Fig. 6. Effect of halothane on MLCK activity. The activities were measured in the presence of 0, 2 and 100 nM concentrations of $[Ca^{2+}]_4$ -CaM, indicated by the triangle, circle and square symbols, respectively. The activities are normalized to the specific activity of MLCK measured in the presence of 100 nM $[Ca^{2+}]_4$ -CaM without halothane. Increasing concentrations of halothane inhibited MLCK, independent of the $[Ca^{2+}]_4$ -CaM concentration.

DISCUSSION

Halothane binding site

The NMR solution structure of the $[\text{Ca}^{2+}]_4\text{-CaM}$ –halothane complex appears to retain an open structure with a flexible central-linker, which is consistent with free $[\text{Ca}^{2+}]_4\text{-CaM}$. Therefore, halothane binding does not seem to induce a global conformational change in the $[\text{Ca}^{2+}]_4\text{-CaM}$ structure. To gain insight into the structural features of halothane binding, its binding is compared in Fig. 7 with that of a potent CaM-peptide binding antagonist *N*-(6-aminohexyl)-5-chloro-1-naphthalenesulfonamide (W-7).²⁴ Halothane does not penetrate as deep into the hydrophobic pockets in the termini of $[\text{Ca}^{2+}]_4\text{-CaM}$ as does W-7. Halothane mainly

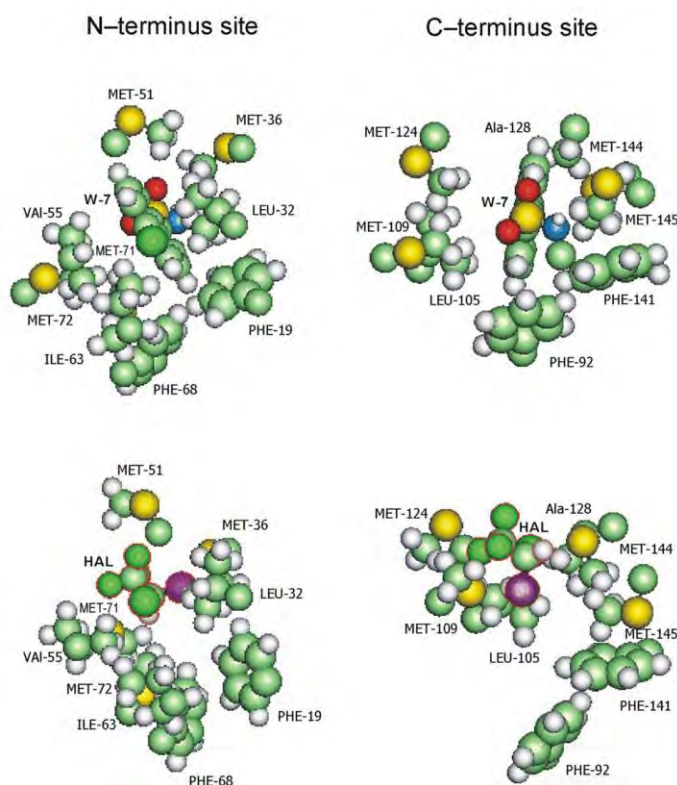
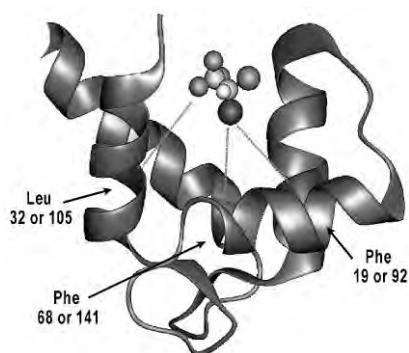


Fig. 7. Top: partial structure of the binding sites of *N*-(6-aminohexyl)-5-chloro-1-naphthalenesulfonamide (W-7) to $[\text{Ca}^{2+}]_4\text{-CaM}$ (taken from 1mux.pdb, first NMR structure). Shown are the side-chain groups of $[\text{Ca}^{2+}]_4\text{-CaM}$ binding sites in contact with the W-7 aromatic ring. Bottom: analogous view of the binding site in the $[\text{Ca}^{2+}]_4\text{-CaM}$ –halothane structure. The structure of the conformer with a deepest imbedding of halothane is shown. Atoms are represented by solid spheres at 50 % of the van der Waals radii. Colors are by atom nature: H (white-gray), C (light green), N (blue), O (red), F (deep-green), S (yellow), Cl (deep-green), Br (magenta).

interacts with methyl groups, primarily from methionine residues, whereas W-7 also interacts with complementary aromatic groups at the base of the pockets. This preferential interaction with methyl groups is likely supported by their high concentration at the pockets entry. In a more dominant aromatic environment, halothane could also engage aromatic groups.²⁵ The lack of halothane penetration into the C-terminal pocket is particularly significant because that is where the tryptophan side chains (*i.e.*, Trp-4 of the CaM-binding peptide from the MLCK,²⁴ or Trp-8 of the CaM-binding peptide^{26,27}) anchor the peptide to $[Ca^{2+}]_4$ -CaM.

To substantiate further this finding, comparison of the ligand penetration depth into the hydrophobic pockets of $[Ca^{2+}]_4$ -CaM by triangulation to three residues at the bottom of the pockets that are iso-topical in the N- and C-terminuses was made (Scheme 1 and Table II). The data in the last two columns of Table II verify that ligand penetration depth into the C-terminus hydrophobic pocket is crucial for the onset of antagonist behavior.



Scheme 1. Ligand penetration into the hydrophobic pockets of $[Ca^{2+}]_4$ -CaM.

TABLE II. Ligand penetration-depths into hydrophobic pockets of Ligand/CaM (Ligand/#pdb) structures obtained by triangulation to three residues at the bottom of the hydrophobic pockets. Distances (Å) were calculated between the backbone C^α atom of the three residues and the closest heavy atom of the ligand; TFP: 10-[3-(4-methyl-piperazin-1-yl)-propyl]-2-trifluoromethyl-10H-phenothiazine

Ligand/#pdb	Phe19	Leu32	Phe68	Mean	Phe92	Leu105	Phe141	Mean	Antagonist
EtOH	C1:	C1:	C2:	–	Any	Any	Any	–	–
/1c1l	8.1	7.5	5.9	5.6	>15	>15	>15	>15	No
Halothane	Br:	Cl2:	Br:	–	C1:	Cl2:	F2:	–	–
/2kug, 2kuh	11.5	8.2	7.6	9.1	13.1	7.3	8.3	9.6	No
W-7	C3:	C4:	C3:	–	C3:	C3:	Cl1:	–	–
/1mxu	6.4	6.6	7.2	6.7	6.1	6.4	6.4	6.3	Yes
TFP	C3:	C3:	C2:	–	C9:	C9:	C10:	–	–
/1ctr	13.6	17.3	15.2	15.4	7.6	5.8	6.5	6.6	Yes
MLCK	10CB:	14CD1:	17CD2:	–	8O1:	8O1:	4CZ2:	–	–
/1qs7	7.0	6.9	7.4	7.1	5.3	5.7	5.5	5.5	Yes

The finding that halothane interacts with methyl groups in $[Ca^{2+}]_4$ -CaM is consistent with previous observations that VAs contact primarily aliphatic residues in serum albumin²⁸ and interact solely with the choline methyl groups in dipalmitoylphosphatidylcholine vesicles.²⁹ This appears to be a general feature of VAs–protein interactions, which were used as criteria to identify amphiphilic pockets in protein structures where VAs bind.^{10,11} This finding is consistent with the possibility that protein methyl groups act as weak hydrogen bond donors to the methyl halogens, namely fluorine, found in VAs.³⁰ However, this is only speculation because data necessary for the determination of the orientation of halothane relative to the methyl groups of $[Ca^{2+}]_4$ -CaM is lacking.

Isoflurane does not affect steady-state $[Ca^{2+}]_4$ -CaM–skMLCKp binding

The steady state fluorescence assay indicated that even high concentrations of isoflurane and, by extension, probably other VAs, do not significantly alter the amount of $[Ca^{2+}]_4$ -CaM–skMLCKp formed in the presence of 2.7 nM $[Ca^{2+}]_4$ -CaM. Isoflurane was used because it does not quench fluorescence unlike halothane, which would complicate the interpretation of this assay, and skMLCKp was employed because its affinity for $[Ca^{2+}]_4$ -CaM is not too high to quantify.²³ Thus VAs do not behave like the $[Ca^{2+}]_4$ -CaM antagonist W-7, which reduces the amount of $[Ca^{2+}]_4$ -CaM–MLCK peptide formed without significantly altering the K_d value.³¹ This was unexpected since halothane was shown to reduce the amount of synaptic PDZ domain-mediated protein interactions with NMDA receptor and nNOS without significantly altering the K_d value.³² It is possible that VAs behave like the $[Ca^{2+}]_4$ -CaM antagonist TFP and alter the on-rate of the MLCK peptide, but not the steady state amount of complex formed.³¹ However, a reduction in the on-rate would increase the steady state K_d and right-shift the binding curve. This was not the case since isoflurane had no effect on the intensity observed near the half-maximal $[Ca^{2+}]_4$ -CaM. These results indicate that VAs do not significantly antagonize the interaction of $[Ca^{2+}]_4$ -CaM with skMLCKp.

Halothane inhibits smMLCK activity

The kinetic fluorescence assay indicated that the MLCK activity is inhibited in a concentration-dependent manner by halothane. Fluorescence quenching by halothane does not present a problem for this assay because the instrument response is calibrated using the NADH fluorescence from each sample condition. It was found that MLCK is inhibited by VAs in the absence of $[Ca^{2+}]_4$ -CaM and in the presence of sub-maximal and maximal concentrations of $[Ca^{2+}]_4$ -CaM. This indicates that the mechanism by which halothane inhibits MLCK is independent of $[Ca^{2+}]_4$ -CaM, which is consistent with the finding that isoflurane does not inhibit $[Ca^{2+}]_4$ -CaM binding to skMLCKp.

CONCLUSIONS

The obtained results indicate that VAs bind to antagonist sites in $[Ca^{2+}]_4$ -CaM, yet inhibit MLCK activity only *via* unspecified interactions with the enzyme. The inability of VAs to act as potent CaM-peptide binding antagonists can be traced to the ligand-penetration-depth into the C-terminus hydrophobic pockets. The result is significant because it shows, at least in the case of calmodulin-dependent smMLCK activity, that effect of VAs on enzyme function do not arise from the low affinity of VA binding to the druggable sites of the protein.

Since mechanism of general anesthesia remains unsolved,³³ structural studies at an atomic resolution level, such as those presented herein, could help understand modalities of anesthetic–biomacromolecule interactions.

SUPPLEMENTARY MATERIAL

Two figures presenting halothane/CaM NMR titration data are available electronically at <http://www.shd.org.rs/JSCS/> or at: https://www.researchgate.net/profile/Nenad_Juranic/publications/?pubType=dataset&ev=prf_pubs_dat

Acknowledgment. This study was supported in part by grants GM070585 and HL-45532 from the National Institutes of Health, Bethesda, Maryland, USA.

ИЗВОД

ХАЛОТАН СЕ ВЕЗУЈЕ ЗА АКТИВНА МЕСТА $[Ca^{2+}]_4$ -КАЛМОДУЛИН, АЛИ НЕ ИНХБИРА $[Ca^{2+}]_4$ -КАЛМОДУЛИН-ЗАВИСНУ АКТИВАЦИЈУ КИНАЗЕ

NENAD O. JURANIĆ¹, KEITH A. JONES², ALAN R. PENNEITER¹, THOMAS J. HOCK² и JOHN H. STREIFF²

¹Mayo College of Medicine at Rochester, U.S.A. и ²University of Alabama at Birmingham, U.S.A.

Механизам деловања испарљивих анестетика је слабо познат. Применом NMR спектроскопије високе резолуције ми смо решили структуру комплекса којег испарљиви анестетик халотан чини са калцијум-везујућим протеином калмодулином ($[Ca^{2+}]_4$ -CaM). Утврдили смо да се халотан везује за калмодулин на местима која су позната као примарна места везивања разних лиганата, и сматрају се примарним циљем за примену лекова у системима зависним о сигнализирању калцијума. То је указивало на могућност дејства анестетика путем модулације сигнализирања калцијум-кадмодулина. Зато смо испитали да ли везивање испарљивих анестетика (VA) утиче на калцијум-кадмодулин зависну активност ензима миозин-киназе (*myosin light chain kinase*, MLCK). Применом флуоресцентне анализе утврдили смо да VA утичу на активацију MLCK, али да не мења константу везивања калцијум-кадмодулина за моделну регију ензима (skMLCKp). Овај резултат сугерише да анестетик (VA) не утиче директно путем сигнализирања калцијум-кадмодулина.

(Примљено 23. маја 2013)

REFERENCES

1. N. P. Franks, E. R. Lieb, *Nature* **310** (1984) 599
2. M. Zhang, T. Tanaka, M. Ikura, *Nat. Struct. Biol.* **2** (1995) 758

3. L. J. Van Eldick, D. M. Watterson, *Calmodulin and Signal Transduction: An Introduction*, in *Calmodulin and Signal Transduction*, L. J. Van Eldick, D. M. Watterson, Eds., Academic Press, New York, USA, 1998, p. 1
4. W. J. Cook, L. J. Walter, M. R. Walter, *Biochemistry* **33** (1994) 15259
5. L. Massom, H. Lee, H. W. Jarett, *Biochemistry* **29** (1990) 671
6. F. Orosz, T. Y. Christova, J. Ovadi, *Mol. Pharmacol.* **33** (1988) 678
7. R. Chattopadhyaya, W. E. Meador, A. R. Means, F. A. Quioco, *J. Mol. Biol.* **228** (1992) 1177
8. L. Ohashi, R. Pohoreki, K. Morita, P. M. Stemmer, *Biochim. Biophys. Acta, Mol. Cell Res.* **1691** (2004) 161
9. A. Levin, T. J. J. Blanck, *Anesthesiology* **83** (1995) 120
10. J. H. Streiff, T. W. Allen, E. Atanasova, N. Juranic, S. Macura, A. R. Penheiter, K. A. Jones, *Biophys. J.* **91** (2006) 3405
11. J. H. Streiff, K. A. Jones, *J. Chem. Inf. Model.* **48** (2008) 2066
12. J. Marley, M. Lu, C. Bracken, *J. Biomol. NMR* **20** (2001) 71
13. J. A. Putkey, G. R. Slaughter, A. R. Means, *J. Biol. Chem.* **260** (1985) 4704
14. K. Ajtai, M. F. Halstead, M. Nyitrai, A. R. Penheiter, Y. Zheng, T. P. Burghardt, *Biochemistry* **48** (2009) 5263
15. A. Bax, *Curr. Opin. Struct. Biol.* **4** (1994) 738
16. S. Grzesiek, A. Bax, *J. Am. Chem. Soc.* **115** (1993) 12593
17. J. J. Chou, S. P. Li, C. B. Klee, A. Bax, *Nat. Struct. Biol.* **8** (2001) 990
18. A. T. Brunger, *X-PLOR Version 3.1: A System for X-ray Crystallography and NMR*, Yale University, New Haven, CT, 1992
19. K. Torok, D. J. Cowley, B. D. Brandmeier, S. Howell, A. Aitken, D. R. Trentham, *Biochemistry* **37** (1998) 6188
20. M. Ikura, L. E. Kay, A. Bax, *Biochemistry* **29** (1990) 4659
21. S. W. Vetter, E. Leclerc, *Eur. J. Biochem.* **270** (2003) 404
22. A. M. Weljie, H. J. Vogel, *Protein Eng.* **13** (2000) 59
23. S. Montigiani, G. Neri, P. Neri, D. Neri, *J. Mol. Biol.* **258** (1996) 6
24. M. Osawa, M. B. Swindells, J. Tanikawa, T. Tanaka, T. Mase, T. Furuya, M. Ikura, *J. Mol. Biol.* **276** (1998) 165
25. T. Cui, V. Bondarenko, D. Ma, C. Canlas, N. R. Brandon, J. S. Johansson, Y. Xu, P. Tang, *Biophys. J.* **94** (2008) 4464
26. B. Elshorst, M. Hennig, H. Forsterling, A. Diener, M. Maurer, P. Schulte, H. Schwalbe, C. Griesinger, J. Krebs, H. Schmid, T. Vorherr, E. Carafoli, *Biochemistry* **38** (1999) 12320
27. N. Juranic, E. Atanasova, A. G. Filoteo, S. Macura, F. G. Prendergast, J. T. Penniston, E. E. Strehler, *J. Biol. Chem.* **285** (2010) 4015
28. K. Shikii, S. Sakurai, H. Utsumi, H. Seki, M. Tashiro, *Anal. Sci.* **20** (2004) 1475
29. S. Yokono, K. Ogli, S. Miura, I. Ueda, *Biochim. Biophys. Acta* **982** (1989) 300
30. E. Kryachko, S. Scheiner, *J. Phys. Chem., A* **108** (2004) 2527
31. K. Sasaki, T. Ozawa, Y. Umezawa, *Anal. Chim. Acta* **447** (2001) 63
32. M. Fang, Y. X. Tao, F. H. He, M. J. Zhang, C. F. Levine, P. Z. Mao, F. Tao, C. L. Chou, S. Sadegh-Nasseri, R. A. Johns, *J. Biol. Chem.* **278** (2003) 36669
33. P. L. Chau, *Br. J. Pharmacol.* **161** (2010) 288.

SUPPLEMENTARY MATERIAL TO
**Halothane binds to druggable sites in the $[Ca^{2+}]_4$ -calmodulin
(CaM) complex, but does not inhibit $[Ca^{2+}]_4$ -CaM
activation of kinase**

NENAD O. JURANIĆ^{1*}, KEITH A. JONES², ALAN R. PENHEITER¹,
THOMAS J. HOCK² and JOHN H. STREIFF²

¹Mayo College of Medicine at Rochester, U.S.A. and

²University of Alabama at Birmingham, U.S.A.

J. Serb. Chem. Soc. 78 (11) (2013) 1655–1670

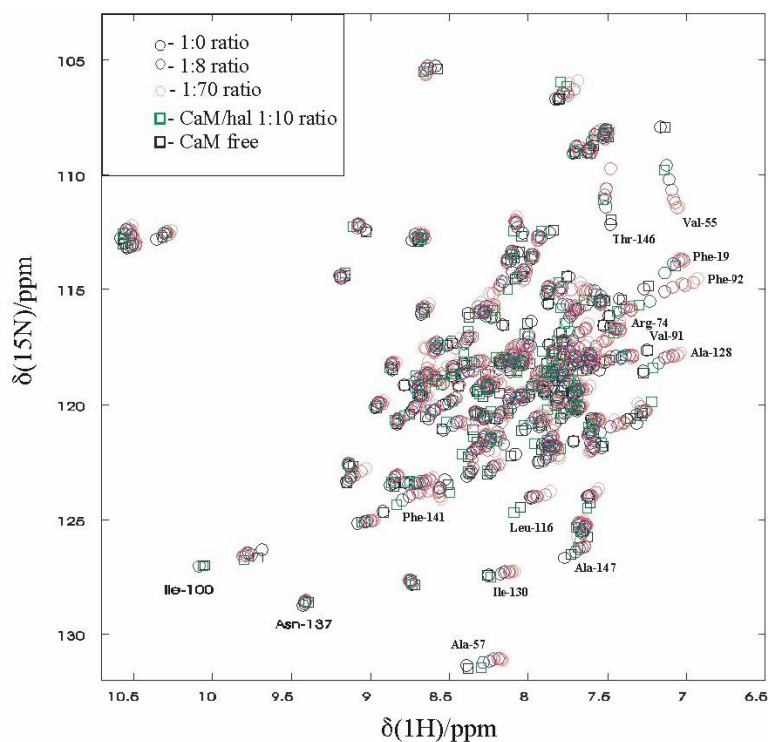


Fig. S-1. Backbone amide 1H - ^{15}N peaks positions determined from 3D HNC0 titration spectra.

* Corresponding author. E-mail: juranic.nenad@alumni.mayo.edu

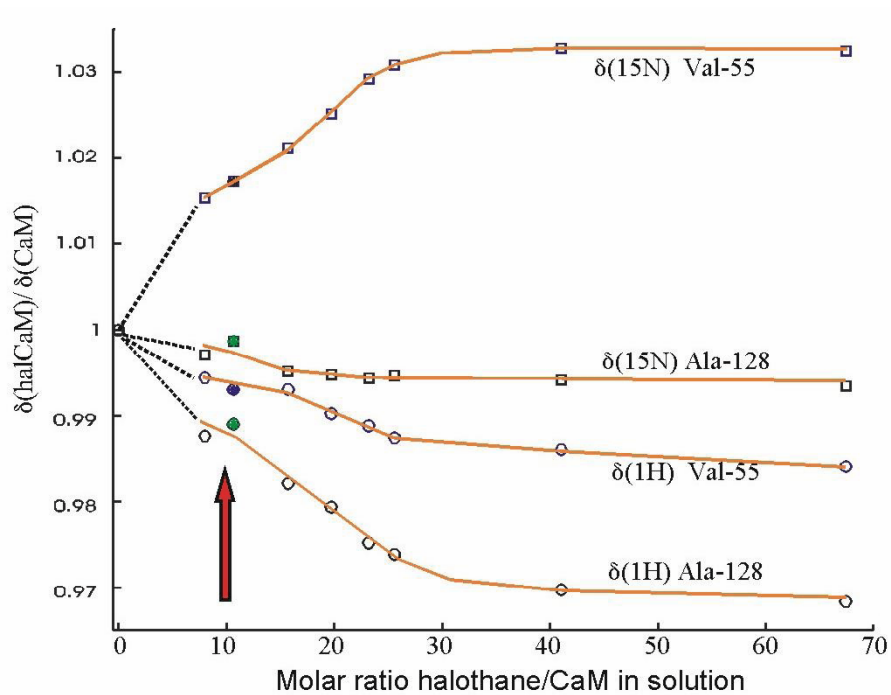


Fig. S-2. Titration curves for the prominent residues from each CaM lobe. Red arrow indicates mole ratio at which NMR structure determination of CaM/halothane complex is done.



J. Serb. Chem. Soc. 78 (11) 1671–1688 (2013)
JSCS–4526

REVIEW

Super-resolution fluorescence imaging and correlation spectroscopy: principles and examples of application

TIJANA JOVANOVIĆ-TALISMAN^{1,2} and VLADANA VUKOJEVIĆ^{3*}

¹Department of Molecular Medicine, Beckman Research Institute of the City of Hope Comprehensive Cancer Center, Duarte, CA 91010, USA, ²Department of Chemistry, University of Hawaii at Manoa, Honolulu, Hawaii 96822, USA and ³Department of Clinical Neuroscience, Karolinska Institutet, CMM L8:01, Stockholm, Sweden

(Received 15 August, revised 30 September 2013)

Abstract: Self-organization of cell-surface receptors in structurally distinct domains in the plasma membrane is of vital importance for correct cellular signaling. However, this dynamic process is difficult to study in cells with sufficiently high temporal and spatial resolution. Herein, two quantitative high-resolution methods with single-molecule sensitivity are presented, *i.e.*, fluorescence correlation spectroscopy (FCS) and pair-correlation photo-activated localization microscopy (pcPALM), which enable the non-destructive study of receptor diffusion and lateral organization at the nanoscale level. The methods are introduced and their application in studies of lateral organization of G protein-coupled receptors (GPCRs) is reviewed. Examples from studies on the lateral organization of opioid receptors are presented in order to illustrate the most recent advances in the field.

Keywords: fluorescence correlation spectroscopy, super-resolution fluorescence imaging, sub-diffraction limit, photo-activated localization microscopy, G protein-coupled receptors, lipid rafts.

CONTENTS

1. INTRODUCTION
2. FLUORESCENCE CORRELATION SPECTROSCOPY (FCS)
 - 2.1. FCS measurements and data analysis
 - 2.2. Probing the lateral organization in the plasma membrane at the nanoscale level by varying spatial scales FCS
 - 2.3. Limitations of FCS
3. PHOTO-ACTIVATED LOCALIZATION MICROSCOPY (PALM) AND PAIR-CORRELATION PALM (PCPALM)
 - 3.1. Limitations of PALM and pcPALM

* Corresponding author. E-mail: vladana.vukojevic@ki.se
doi: 10.2298/JSC130815102J

4. GPCR LATERAL ORGANIZATION INVESTIGATED BY FCS AND PALM
5. CONCLUSIONS

1. INTRODUCTION

Lateral diffusion of cell surface receptors and receptor sorting into specific compartments in the plasma membrane play an essential role in cell signal transduction.^{1–7} Plasma membrane compartmentalization arises spontaneously, due to the natural tendency of lipids to separate into distinct liquid-ordered (L_o) or liquid-disordered (L_d) phases, forming submicroscopic domains where certain lipids (such as cholesterol and sphingolipids) and proteins can be concentrated while others can be excluded. The thus formed L_o submicroscopic domains, frequently referred to as lipid rafts, are believed to participate in a number of vital cellular functions.^{1–7} In spite of intense research that followed the original proposition of these domains,¹ *in vivo* existence of lipid rafts and their biological role remained difficult to confirm for many years. The main obstacle was the limitation of experimental techniques that were available for quantitative characterization of these dynamic structures under non-destructive (living cells) or minimally invasive (fixed cells) conditions.

To date, fluorescence microscopy imaging and spectroscopy techniques have provided compelling evidence for the existence of lateral heterogeneity of protein and lipid organization in intact cell membranes.^{8–22} The aim of this paper is to present two quantitative methods with single-molecule sensitivity, fluorescence correlation spectroscopy (FCS) and pair-correlation photo-activated localization microscopy (pcPALM), and review their application for the study of lateral organization of G protein-coupled receptors (GPCRs). Examples from studies on opioid receptors are used to illustrate how concomitant application of these specialized techniques enables the quantitative characterization of the surface density, lateral diffusion in living cells and heterogeneous distribution in intact plasma membranes of opioid receptors at the nanoscale level.

2. FLUORESCENCE CORRELATION SPECTROSCOPY (FCS)

FCS is a quantitative method with single molecule-sensitivity that uses statistical analysis of fluorescence intensity fluctuations recorded over time to obtain information about molecular numbers and their transporting properties and/or molecular brightness distribution.^{23–25} The principles of FCS were formulated about thirty years ago,^{26–30} and the method was successfully applied for in solution studies of molecular diffusion and kinetics in the founding laboratories. More widespread application in biological systems became possible only after confocal optical arrangement and ultra-sensitive avalanche photodiode (APD) detectors were implemented.^{31,32} Application of these innovations significantly improved the signal-to-noise ratio, enabling single-molecule detection sensitivity, low excitation intensities and short measurement times. Building on these

innovations, second and third generations of versatile instruments that combined FCS with confocal laser scanning microscopy (CLSM) were developed,^{33,34} which paved the way for a more widespread use of FCS in biomedical research. FCS measurements on live PC12 cells stably transformed to express mu-opioid receptors fused with the enhanced Green Fluorescent Protein (MOP^{eGFP}) are shown as an example (Fig. 1 B). A schematic presentation of a typical FCS–CLSM setup is given in Fig. 1A. To induce fluorescence, the sample is illuminated by incident light delivered by a continuous wave laser. The laser beam is reflected by a dichroic mirror and sharply focused by the objective to form a mini-

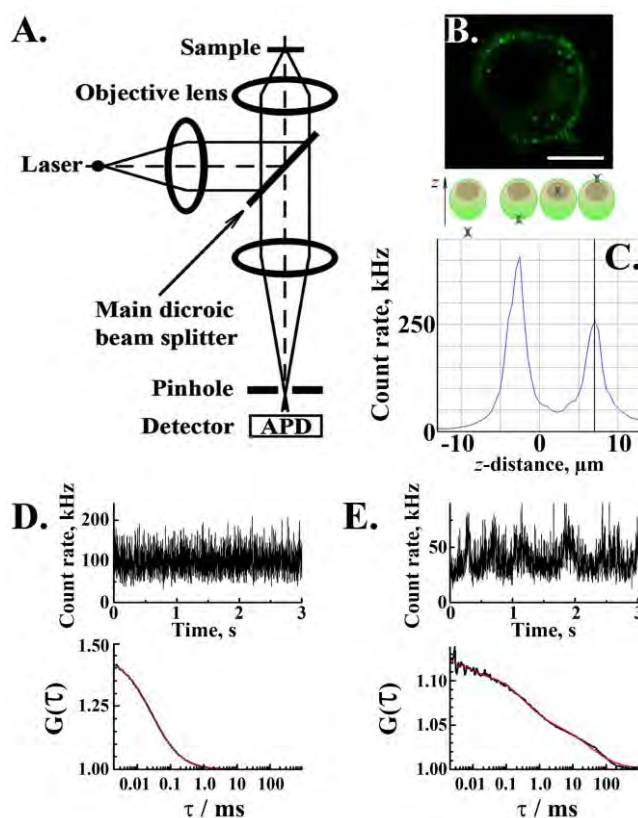


Fig. 1. FCS measurements and data analysis. A. Schematic drawing of a typical FCS/CLSM setup. B. Confocal image of a single PC12 cell stably expressing MOP^{eGFP} (green), acquired using APD. Scale bar: 5 μm . C. Fluorescence intensity distribution across a single PC12 cell expressing MOP^{eGFP} determined by a linear scan in the axial direction (z -scan). The first and second maximums indicate the position of the basal and apical plasma membrane, respectively, as schematically depicted in the panel above. D and E. Fluorescence intensity fluctuations (top) and corresponding autocorrelation curves (bottom) recorded in a standard solution of rhodamine 6G (Rho6G) in water (D) and on the apical plasma membrane of a single PC12 cell expressing MOP^{eGFP} (E).

ature volume element, the size of which is determined by the diffraction of light. The volume from which fluorescence is detected is further reduced by a pinhole (confocal aperture) in the image plane, rejecting stray and out of focus light and keeping the Raman scattered light to a minimum. In this way, fluorescence is detected from a minute observation volume element that is about $2 \times 10^{-19} \text{ m}^3$. This enables a submicrometer resolution and specific detection at defined loci, as well as quantitative and background-free analysis. The light emitted by fluorescing molecules passing through the confocal volume element is separated from the exciting radiation and the scattered light by a dichroic mirror and barrier filter, and transmitted to the single-photon avalanche photodiode (APD) detector, which responds with an electrical pulse to each detected photon. The number of pulses originating from the detected photons, recorded during a specific time interval, corresponds to the measured light intensity. Thus, in one FCS experiment, changes in fluorescence intensity in time are registered. The eGFP fluorescence was excited using the 488 nm line of an Ar/ArKr laser. The main dichroic beam splitter HFT KP 700/488 was used to separate the incident and emitted light. The emitted light was further spectrally selected using a band pass filter BP 505–530 nm in front of the APD detector (Fig. 1B). Autocorrelation analysis showed that the average number of Rho6G molecules in the observation volume element was 2.3 (meaning that one typically observes 2 ($\approx 67\%$ of the time) or 3 ($\approx 33\%$ of the time) Rh6G molecules simultaneously, Fig. 1D and E), whereas the average number of observed MOPeGFP molecules is 9.2. The number of detected photons per molecule and second in Rh6G aqueous solution was $\text{CPMRho6G} = 41.9 \text{ kHz}$, yielding a virtually noise-less autocorrelation curve (black in Fig. 1C and D) that is well fitted with the autocorrelation function for free 3D diffusion and singlet/triplet transition of a single component (red in Fig. 1D and E). In contrast, the eGFP brightness is an order of magnitude lower, $\text{CPMMOPeGFP} = 3.8 \text{ kHz}$. The experimental autocorrelation curve is complex, showing several characteristic times (black in Fig. 1D and E), and could be well fitted using an autocorrelation function for free 2D diffusion and singlet/triplet transition of two components (red curve, see Eq. (2)).

2.1. FCS measurements and data analysis

In studies of protein lateral organization in plasma membranes by FCS, live cells genetically modified to express the receptor of interest fused with a fluorescent protein marker are typically used.^{18,19,35,36} This is somewhat disadvantageous for FCS because the quantum yield of fluorescent proteins is typically smaller than those of organic fluorophores or quantum dots, which necessitates longer measurement times. However, an obvious advantage of genetic labeling is that it obviates artifacts associated with covalent protein labeling and/or protein organization disruption due to multiple crosslinking with antibodies.

Before an FCS measurement can be initiated, confocal imaging is used to identify cells suitable for FCS analysis. For example, a confocal image of PC12 cells stably transformed to express the mu-opioid receptor fused with an enhanced green fluorescent protein (MOP^{eGFP}) is shown in Fig. 1B. When a suitable cell has been identified, which does not have another cell on top of it and is not too bright (overexpression of proteins can introduce artifacts in their lateral organization), fluorescence intensity scanning is performed in the axial direction (a so-called *z*-scan) to localize the apical plasma membrane of the cell (schematically depicted above Fig. 1C). A fluorescence intensity profile generated in this way is shown in Fig. 1C. Thereafter, continuous wave laser light is delivered to a small area in the plasma membrane, and fluctuations in fluorescence intensity are recorded as a function of time (Fig. 1D and E, top).

To evaluate the gathered data, *i.e.*, to analyze time series sampled during one run, statistical methods are applied to detect non-randomness in the data. Typically, this is realized by temporal autocorrelation analysis, but other methods such as higher order autocorrelation functions,^{37,38} fluorescence intensity distribution analysis (FIDA),^{39,40} photon-counting histograms (PCH),^{41,42} fluorescence cumulant analysis (FCA),⁴³ and time-integrated fluorescence cumulant analysis (TIFCA)^{44,45} can be also applied. However, the temporal autocorrelation analysis of fluorescence intensity fluctuations is still the most frequently used method in FCS applications.

In temporal autocorrelation analysis, the normalized autocorrelation function $G(\tau)$ is first derived:

$$G(\tau) = 1 + \frac{\langle \delta I(t) \delta I(t + \tau) \rangle}{\langle I(t) \rangle^2} \quad (1)$$

that relates the fluctuation in fluorescence intensity measured at a certain time point t , $\delta I(t) = I(t) - \langle I(t) \rangle$, which is given as the difference in fluorescence intensity $I(t)$ and the mean fluorescence intensity over the recorded time-series ($\langle I(t) \rangle$), and its intensity measured at a later time, $\delta I(t + \tau) = I(t + \tau) - \langle I(t) \rangle$. For further analysis, $G(\tau)$ is plotted as a function of different lag times τ , also called autocorrelation times, to construct the corresponding autocorrelation curve (Fig. 1D and E, bottom). In molecular systems undergoing stochastic fluctuations, random variations of $G(\tau)$ around the value $G(\tau) = 1$ would be observed. For processes that are not random, an autocorrelation curve builds up with a maximal limiting value of $G(\tau)$ as $\tau \rightarrow 0$, decreasing to the value of $G(\tau) = 1$ at long times, indicating that correlation between the initial and the current property value has been lost. For simple systems, with only one chemical species and one process that underlie the fluorescence intensity fluctuations, autocorrelation curves with only one characteristic time are observed (Fig. 1D, bottom). In complex systems, where more than one process underlies the fluorescence intensity

fluctuations, or chemical species with different diffusion times exist, more than one characteristic time could be observed if the processes are sufficiently well separated in time (Fig. 1E, bottom).

To obtain information about the average number of molecules observed, the so-called non-uniform part of the normalized autocorrelation function is used, $g(\tau) = G(\tau) - 1$. In this case, one observes a maximal limiting value of $g(\tau)$ as $\tau \rightarrow 0$ is observed that decreases to the value of $g(\tau) = 0$ at long times. The limiting value of $g(\tau)$, as $\tau \rightarrow 0$ is then inversely proportional to the absolute concentration of the fluorescing molecules. Both the normalized autocorrelation function $G(\tau)$ and its non-uniform part $g(\tau)$ are independent of the properties of the experimental setup, such as the laser intensity, fluorescence quantum yield and detection efficiency.²³ A comprehensive description of autocorrelation analysis and the derivation of the autocorrelation function for the simplest case, free three-dimensional (3D) diffusion in an isotropic medium, can be found at <http://www.biotech.tu-dresden.de/cms/index.php?id=151>.⁴⁶ Here, only the most relevant results for lateral diffusion (two-dimensional (2D) diffusion in a plane) are given.

To extract the information about molecular numbers (N) and lateral diffusion times (τ_D), the experimental autocorrelation curves are fitted using autocorrelation functions derived for the appropriate model system.²³ For measurements performed at a plasma membrane, a model for free 2D diffusion with triplet contribution is typically used:

$$G(\tau) = 1 + \frac{1}{N} \left(\sum_i \frac{x_i}{(1 + \tau/\tau_{Di})} \right) \left(1 + \frac{T}{1-T} \exp\left(-\frac{\tau}{\tau_T}\right) \right) \quad (2)$$

In Eq. (2), T is the average equilibrium fraction of molecules in the triplet state, τ_T is the relaxation time of the triplet state, i is the number of components, τ_{Di} is the diffusion time of the i -th component and x_i is its relative amplitude ($\sum x_i = 1$). The diffusion times, τ_{Di} , of the investigated components are determined from the autocorrelation function (2) that best matches the actual, experimentally determined autocorrelation curve.

The diffusion time, τ_D , is related to the translation diffusion coefficient, D , through the relationship:

$$\tau_D = \frac{w_{xy}^2}{4D} \quad (3)$$

where w_{xy} is the so-called lateral radius, *i.e.*, the radial distance of the focused laser beam at which the collected fluorescence intensity has dropped by a factor of e^2 compared to its peak value in the center. This parameter is derived in calibration measurements, using standard aqueous solutions of fluorescent molecules the diffusion coefficients of which are known. For this purpose, the fluores-

cent properties of the standard dye need to match the properties of the fluorescent protein, and identical optical settings have to be applied for FCS measurements (Fig. 1D and E). Diffusion coefficients of organic fluorophores typically used as reference standards in FCS can be found at http://www.picoquant.com/tech-notes/appnote_diffusion_coefficients.pdf.⁴⁷ The lateral radius w_{xy} depends on the instrumental setting, but the theoretical limit for a diffraction-limited spot size gives a range from 200–270 nm for typically used excitation wavelengths 488–633 nm.

Thus, FCS examines a small area ($(w_{xy})^2\pi$) in the plasma membrane that is limited in size by the diffraction of light and the quality of the optics. It provides quantitative information about the local density of cell surface receptors and the lateral diffusion in the observed area in living cells. Even though the spatial resolution of FCS is limited by light diffraction, FCS can give information about the structural organization at the nanoscale level, *i.e.*, beyond the spatial resolution limit that is imposed by diffraction of light, as will be shown later.

2.2. Probing the lateral organization in the plasma membrane at the nanoscale level by varying spatial scales FCS

Lateral heterogeneity and the presence of microdomains affect the diffusion behavior of molecules composing the plasma membrane. However, long-range diffusion measurements, such as fluorescence recovery after photobleaching (FRAP), which is the most widely used technique for measuring molecular diffusion in cellular membranes, have largely failed to recognize such differences. The main reason for this is that FRAP measurements are typically conducted on an ensemble of molecules, such that individual behavior of molecules cannot be distinguished. Owing to the high temporal resolution and single molecule sensitivity of FCS, it was recently shown that FCS measurements performed at varying spatial scales can provide information about local differences in the diffusion properties of cell-surface receptors in the plasma membrane.^{48–52} Using this method, three models of diffusion could be distinguished by plotting the lateral diffusion time (τ_D) as a function of the observation area size, which is proportional to $(w_{xy})^2$, and determining the intercept for a vanishingly small observation area (Fig. 2A). A positive intercept was associated with partitioning in domains as the predominant mode of lateral organization, free diffusion yielded a zero intercept, and a negative intercept reflected receptor confinement by the cytoskeletal meshwork.^{48–52}

To corroborate this remarkable observation, single nanometric apertures of different sizes were combined with FCS to reduce the size of the observation area from which photons are collected and thus achieve the high spatial resolution that is necessary to characterize the underlying structures at the nanoscale level.⁵³ This approach verified the previous observations that FCS can give information

about structures that are smaller in size than the spatial resolution limit that is imposed by light diffraction.^{48–52} FCS at varying spatial scales was also shown to be superior to single particle tracking (SPT) because of the high temporal resolution, high sampling and the robust autocorrelation analysis that is much simpler than the tedious analysis of large numbers of individual trajectories, which is necessary for the accurate interpretation of SPT results.

The experimentally derived dependence of the autocorrelation time for MOPe^{GFP} as a function of the size of the observation area is shown in Fig. 2B. The positive intercept suggests that opioid receptors partition between microdomains and the surrounding lipid bilayer.

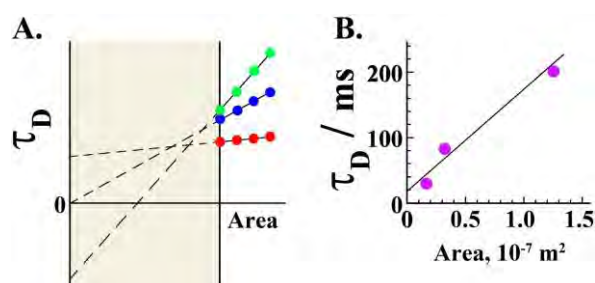


Fig. 2. Probing the lateral organization in the plasma membrane at the nanoscale level by varying spatial scales FCS. A. Lateral diffusion time as a function of the size of the observation area for different types of lateral organization in the plasma membrane: a network of barriers defining contiguous corrals (green), free diffusion (blue) and isolated domains (red), derived by numerical simulations according to the so-called FCS diffusion law.^{48–53} The shaded region indicates observation areas that are smaller in size than the area defined by diffraction of light. Direct FCS measurements in this domain cannot be performed by classical FCS, but the behavior can be inferred by extrapolation (dashed line) of the data set collected for areas that are larger in size than the diffraction limited area (solid line). B. Experimentally measured dependence of the lateral diffusion time of opioid receptors in live cells as a function of the observation area size. The size of the observation volume element was changed by changing the pinhole size (ph) in front of the detector. The observed area, expressed as $(ph)^2\pi$, is proportional to the actual observation area.

2.3. Limitations of FCS

Endogenous non-fluorescent protein molecules, protein constructs with irreversibly photobleached fluorophores or with fluorophores residing in dark states, and proteins associated with large immobile structures will all be invisible for FCS and will lead to an underestimation of the receptor surface density. Irreversible photobleaching of fluorophores may also induce errors in the measurements of the lateral diffusion time, yielding shorter values of τ_D , and hence larger diffusion coefficients. To avoid artifacts due to photobleaching, the incident laser intensity used for FCS measurements needs to be as low as possible. The appropriate laser intensity is usually selected so that the detected number of photons

per molecule and second, so-called count per molecule, is not lower than 1 kHz (to ensure that the measured signal is coming from the fluorophore, rather than from autofluorescent molecules abundant in the cell), and the lateral diffusion time does not increase when the laser intensity is reduced.

FCS gives a dynamic readout, yielding characteristic times of processes underlying fluorescence intensity fluctuations. However, its localization precision is poor – FCS can localize the receptor in the plasma membrane with an uncertainty that is limited by the diffraction of light, which is about ± 200 nm at best. To visualize a receptor and determine its localization with greater precision, super-resolution fluorescence imaging techniques are required.

3. PHOTO-ACTIVATED LOCALIZATION MICROSCOPY (PALM) AND PAIR-CORRELATION PALM (pcPALM)

Reconstruction based super-resolution fluorescence microscopy imaging techniques such as photo-activated localization microscopy (PALM),⁵⁴ stochastic optical reconstruction microscopy (STORM)⁵⁵ and fluorescence photo-activation localization microscopy (fPALM)⁵⁶ use repetitive activation and imaging of single fluorophores. This process is reiterated over several minutes (tens of thousands of frames are typically acquired) allowing single fluorophores to be generally positioned with respect to one another at distances greater than the diffraction limit in any particular frame. The centers of the peaks are mathematically calculated for each frame based on the photon distribution from single fluorophores, and all frames are added together. This approach yields pointillistic images, where individual molecules can be localized with a high precision, typically 15–40 nm.^{21,22,54–61} The principles of reconstruction based super-resolution fluorescence microscopy imaging techniques were primarily defined in the seminal works of Michalet *et al.*,⁵⁷ Thompson *et al.*,⁵⁸ Yildiz *et al.*⁵⁹ and Betzig *et al.*,⁵⁴ in which it was shown that the fluorescence intensity, *i.e.*, the number of detected photons, determines the precision by which a single molecule can be localized. By showing that the accuracy of single molecule localization depends on the width of the point spread function (PSF) and the square root of the collected number of photons (n):

$$\sigma = \frac{\omega_{xy}}{\sqrt{n}} \quad (4)$$

they showed that if $n = 10000$ photons, for a single fluorescing molecule could be detected, $\lambda = 500$ nm ($\omega_{xy} \approx 250$ nm), the molecule could be localized with a precision of ± 1.3 nm.

In order to acquire a sufficient number of photons from a single molecule, which are required for achieving the high localization precision in accordance with Eq. (4), these super-resolution techniques rely on switchable fluorescence reporters, which can cycle to/from a metastable dark state many times, in the case

of photo-activatable fluorophores, or from one color to another in the case of photoconvertible fluorophores. By stochastically activating, localizing, and then photobleaching (in PALM) the switchable fluorescence reporters, a sufficient number of photons can be collected from single molecules, enabling their localization with a high precision.

In order to detect optimally the relatively faint emission from single molecules localized in the plasma membrane, pointillistic imaging techniques use total internal reflection fluorescence (TIRF) to generate an evanescent excitation wave that penetrates 100–200 nm into the specimen, leading to extreme rejection of the background fluorescence (Fig. 3A). The sequence of events for determining the precise location of a single set of photo-activated fluorescent probes, for example the photo-activatable GFP (paGFP)⁶² is as follows. Initially all molecules in the specimen are inactive (native non-emissive state; dark circles). A violet 405 nm laser is used to photo-activate a subset of molecules in the specimen. The number of activated paGFP molecules can be maintained low by ensuring the laser intensity is sufficiently weak at the focal plane. Photo-activation of the molecules occurs stochastically, where the probability of activation is proportional to the intensity of the activation laser. After photo-activation, the 488 nm laser is used to detect and record the position of the photo-activated molecules within the illu-

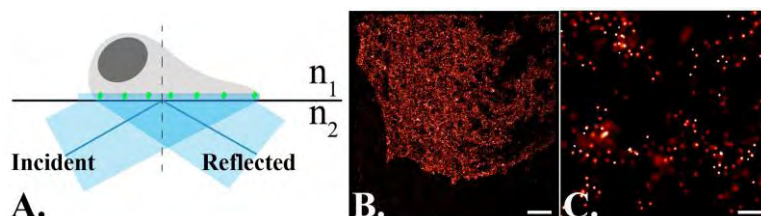


Fig. 3. PALM imaging. A. In order to optimally detect the relatively faint emission from single molecules, PALM uses total internal reflection fluorescence (TIRF) to suppress the background fluorescence. In TIRF, the sample is illuminated at an angle that causes total internal reflection of the incident light at the boundary of the two media. In this way, an evanescent excitation wave is generated that propagates across the boundary surface, penetrating approximately 150 nm into the specimen. TIRF enables the simultaneous imaging of the complete basal plasma membrane, as schematically depicted. B. PALM image of the basal plasma membrane of a Cos7 cell expressing MOP^{paGFP}, showing the localization of individual receptor molecules. Super-resolution images were generated by analyzing the datasets using standard PALM analysis.⁵⁴ The identified peaks were fitted using a cylindrically symmetric Gaussian point spread function, with the amplitude being proportional to the number of photons collected, and the standard deviation (σ) depending on the localization precision. Peaks were grouped using maximum dark time due to blinking of 10 s for paGFP and group radius of $2.5 \times \sigma$ (98.8 % confidence level). The figures are rendered and show the probability to observe a molecule, with white color representing the highest value.

Scale bar: 5 μ m. C. Magnified PALM image showing a detail from the image in B. Scale bar: 200 nm.

minated area. During readout, the photo-activated molecules spontaneously photobleach, eventually reducing the number of active molecules in the specimen. A new set of molecules is photo-activated to repeat the sequence, which is reiterated until all molecules in the specimen have been exhausted.

Typically, 10^3 – 10^5 diffraction-limited digital TIRF images are acquired to yield one super-resolution image; data analysis is performed to identify single molecules over the background noise, calculate the PSFs for the identified single molecules, and determine their centers and localization precision.

Quantitative super-resolution imaging techniques can provide information about nanoscale spatial organization and help delineate mechanisms of various biological processes.^{63–69} For this purpose, statistical methods for spatial analysis, such as the Ripley K-function, the Getis and Francklin L-function or pair correlation function (PCF) are typically used to derive various cluster parameters.^{70,71} Recently developed, pair-correlation PALM (pcPALM) utilizes autocorrelation analysis to separate contributions from a) stochastic clustering (single fluorophores often appear in multiple frames and not sequentially due to variable intervals of fluorescent blinking) and b) protein clustering to provide quantitative information about lateral protein organization. Typically, 2–5 μm wide square regions of interest (ROIs) are selected. The size of the ROI depends on the size of the continuous plasma membrane region of the cell. Generally, a larger ROI and higher number of localized molecules per μm^2 lead to better statistical analyses. The spatial dispersion of identified molecules in the selected ROI is quantified in order to determine whether the investigated molecules are randomly distributed or clustered. For regions that indicate clustering, protein autocorrelation contribution is fit to an exponential function, and pcPALM analysis yields important clustering parameters: cluster size, number of detected proteins in the cluster and increased local density in clusters.

PALM has advantages over FCS because it enables the study of cell surface protein organization with nanoscopic (15–40 nm) precision across the complete basal plasma membrane, rather than in a very small area. For example, the lateral distribution of MOPpaGFP in transiently transformed Cos7 cells is shown in Figs. 3B and C. Furthermore, pcPALM^{21,22} enables the quantitative characterization of the lateral organization of proteins in the plasma membrane in terms of extent of protein clustering, protein density per cluster, and cluster size distributions. Pair-correlation analysis of MOPpaGFP PALM datasets in transiently transformed Cos7 cells is currently under way in our lab. Preliminary results suggest that opioid receptors largely reside in clusters that are smaller than 100 nm in size, characterized by a MOPpaGFP surface density that is several times larger than in the surrounding lipid bilayer. Thus, PALM and pcPALM suggest that MOPpaGFP partitions in domains, which is in line with the FCS results (Fig. 2B).

3.1. Limitations of PALM and pcPALM

Quantitative pointillistic microscopy techniques provide precise information about molecule localization and quantitatively characterize their patterning in the plasma membrane, which yields information about cluster size and protein density per cluster distributions. However, they do not give any information about the molecular dynamics in the plasma membrane. A recently developed technique, single-particle tracking PALM (sptPALM), can be used for dynamics studies in live cells.⁷² In sptPALM, raw data are acquired under continuous activation/excitation while the cells are maintained under physiological conditions. The image of each molecule is fit with a Gaussian to yield nanometric localization precision; molecular positions in consecutive frames are then associated with trajectories based on their proximity, and diffusion parameters are extracted. Points-accumulation-for-imaging-in-nanoscale-topography (PAINT), an earlier method that unifies diffusion with tracking, also provides both high localization precision and dynamic information.⁷³

As in FCS, endogenous non-fluorescent protein molecules and protein constructs with irreversibly photobleached fluorophores will be invisible, yielding an undervalued estimation of total protein surface density by quantitative analysis of pointillistic microscopy data. In contrast, multiple observations of the same protein molecule may cause an overestimation of protein density – photophysical processes leading to a spontaneous molecular transition to/from dark states cause fluorophore blinking, which may be erroneously interpreted as the appearance of another molecule. Statistical methods^{21,22} and proper photophysical characterization of fluorescent probes^{74,75} reduce issues associated with multiple appearances of a single molecules.

4. GPCR LATERAL ORGANIZATION INVESTIGATED BY FCS AND PALM

G protein-coupled receptors (GPCRs), which consist of approximately 800 members, represent one of the largest receptor groups in the metazoa, GPCRs account for approximately 2 % of the coding genes in the human genome and regulate a myriad of physiological processes through the binding of structurally diverse ligands, such as ions, amino acids, biogenic amines, alkaloids and peptides. They are also the largest class of molecular targets with proven therapeutic value: more than 50 % of today's pharmaceuticals target GPCRs. In spite of their great relevance and intensive research, detailed mechanisms of GPCR functions are still not sufficiently understood at the molecular and cellular level. Hence, concerted efforts were embarked on several years ago to unravel crystal structures of GPCRs and identify molecules that modulate their function. This resolute effort has led to the determination of the crystal structure of 16 distinct GPCRs, which was recently reviewed by Katritch *et al.*⁷⁶ In parallel, intensive effort is continuously being dedicated to understanding cellular mechanisms that regulate

the surface density GPCRs and their lateral organization, *i.e.*, oligomerization and sorting to specialized compartments in the plasma membrane.^{77–79} The latter mechanism is of particular interest because it may diversify the GPCR repertoire without the need for creating new genetic protein variants. For many years, receptor oligomerization and sorting to lipid rafts were investigated using standard biochemical techniques. However, these methods are largely disruptive, may introduce artifacts, and do not provide sufficient information about the dynamics of these processes. This, in turn, necessitates live cell studies and the application of minimally invasive techniques, such as high-resolution fluorescence microscopy imaging and correlation spectroscopy.

The earliest FCS studies of GPCR dynamics, interactions in solution,⁸⁰ and interactions on isolated cell membranes⁸¹ date back to 1999, whereas the first application on live cells was reported in 2002.⁸² The same year, FCS was used to characterize the photo-induced oligomerization of bacteriorhodopsin in giant unilamellar vesicles (GUVs), which were identified through the change in the mobility of bacteriorhodopsin upon photo-activation.⁸³ These pioneering studies demonstrated the usefulness of FCS for quantitative characterization of ligand–receptor interactions, which paved the way for future applications. In the past 10 years, numerous studies were dedicated to the quantitative characterization of the lateral organization of different GPCRs in different cell lines. The effect of selective agonists, selective antagonists, and non-specific substances (such as lipids, ions and alcohols (ethanol in particular)) on GPCR surface density, oligomerization status, association with lipid rafts and cellular trafficking have also been studied in detail. In particular, the following representatives of GPCR were investigated: the 5-hydroxytryptamine or serotonin receptor 5-HT_{2A}, adrenergic receptors α_{1b} -AR and β_2 -AR, muscarinic receptors M₁ and M₂, and dopamine receptor D₁ in human embryonic kidney 293 (HEK293) cells;³⁶ bradykinin type 2 receptor B₂R and the mu-opioid receptor MOP in fisher rat thyroid (FRTwt) cells;⁸⁴ serotonin receptor 5-HT_{2C} in HEK293 cells;⁸⁵ neuropeptide Y receptor NPY in HEK293T and HEK293TR cells;⁸⁶ histamine receptor H₁ in chinese hamster ovary (CHO-K1) cells;⁸⁷ serotonin receptor 5-HT_{1A} in CHO-K1 cells;⁸⁸ corticotropin-releasing factor receptors CRFR₁ and CRFR₂ in HEK293 cells;⁸⁹ muscarinic receptors M₁ in HEK293 cells;⁹⁰ MOP in rat Pheochromocytoma (PC12) cells;^{18,19} chemokine receptor 4 (CXCR4) in HEK293;⁹¹ adenosine receptor A₃ in CHO cells;⁹² bradykinin type 2 receptor B₂R in HEK293;⁹³ adenosine receptor A₁ in CHO cells;⁹⁴ and adrenergic receptor β_2 -AR in alveolar epithelial type II (A549) cells and hippocampal neurons.⁹⁵

In comparison, the number of GPCR-dedicated PALM studies is still limited, with only two publications to date, in which the lateral organization of adrenergic receptor β_2 -AR was investigated in HeLa, CHO and cardiomyocyte H9C2 cells.^{64,96} These studies suggested that β_2 -AR is partially pre-associated in nano-

scale-sized clusters only in the cardiomyocyte H9C2 cells, but not in HeLa and CHO cells. Cholesterol sequestration and removal was shown not to affect β_2 -AR clustering, whereas the inhibition of actin polymerization decreased their formation, suggesting that β_2 -AR clustering is influenced by the actin cytoskeleton, and that β_2 -AR is not related to lipid rafts.

5. CONCLUSIONS

Studies of GPCRs lateral organization by FCS^{18,19,36,84–95} revealed that there are significant differences in the lateral organization, dynamics, and selectivity to ligands, modulators, and downstream signaling effectors between the investigated GPCRs. Furthermore, these studies revealed that lateral organization of GPCRs may be cell-type specific, and suggested that differences may persist even in the same subfamily of GPCRs, where different subtypes share a high degree of sequence similarity (> 60 % in the case of opioid receptor subtypes).^{18,19,84}

Hitherto published FCS and pcPALM results support the general notion that the complexity of GPCR lateral organization is vast. However, some unifying concepts seem to be slowly emerging. For example, FCS studies showed that several GPCRs dynamically partition between lipid-enriched domains and the lipid bilayer constituting the plasma membrane. Super-resolution PALM imaging reveals that GPCRs cluster in the plasma membrane, and pcPALM enabled the derivation of important lateral distribution parameters, such as the local cluster density (a unitless number that compares the density of proteins inside and outside the clusters), cluster radius, and number of detected proteins per cluster. Thorough understanding of GPCR lateral organization in the plasma membrane and the dynamical mechanisms that uphold these dissipative structures is essential for a quantitative understanding of GPCRs function, which appears to be finely tuned by the immediate local lipid environment.

The work presented herein demonstrates that FCS and pcPALM are suitable for the quantitative characterization of the spatial heterogeneity GPCRs, and that these methods provide complementary information. PALM offers visual information that is intuitively easy to understand and is of immense value for the interpretation of temporal autocorrelation curves recorded by FCS, which may be challenging at times. Thus, FCS and pcPALM seem to be the methods of choice for quantitative studies of protein organization in cellular plasma membranes, but more standardized approaches in experimental design and data analysis are required to enable future application of these techniques on a larger scale. In spite of these difficulties, which will be resolved in the course of future applications, these techniques hold the promise to bring closer the quantitative characterization of protein–lipid interactions, and their dynamic organization in the plasma membrane.

Acknowledgements. Support from the Karolinska Institute Research Funds, the Ministry of Education, Science and Technological Development of the Republic of Serbia, Grants Nos. 172015 and 45001, and the University of Hawaii at Manoa and City of Hope Startup Funds are gratefully acknowledged. We acknowledge S. Tobin and E. Cacao for the acquisition and analysis of MOPpaGFP data.

ИЗВОД

СУПЕР-РЕЗОЛУЦИОНА ФЛУОРЕСЦЕНТНА МИКРОСКОПИЈА И КОРЕЛАЦИОНА СПЕКТРОСКОПИЈА: ПРИНЦИП РАДА И ПРИМЕНА

ТИЈАНА ЈОВАНОВИЋ-ТАЛИСМАН^{1,2} и ВЛАДАНА ВУКОЈЕВИЋ³

¹*Department of Molecular Medicine, Beckman Research Institute of the City of Hope Comprehensive Cancer Center, Duarte, CA 91010, USA,* ²*Department of Chemistry, University of Hawaii at Manoa, Honolulu, Hawaii 96822, USA* и ³*Department of Clinical Neuroscience, Karolinska Institutet, CMM L8:01, Stockholm, Sweden*

Латерална дифузија и спонтана организација протеинских молекула у суб-микроскопске домене на површини ћелије, су од виталног значаја за правилан пренос сигнала из спољашње средине. У овом раду представљене су квантитативне методе високе осетљивости, флуоресцентна корелациона спектроскопија (енгл. *fluorescence correlation spectroscopy* (FCS)) и корелациона фотоактивациона микроскопија (енгл. *pair-correlation photoactivated localization microscopy* (pcPALM)), које омогућавају да ове динамичке процесе изучавамо са високом временском и просторном резолуцијом. Циљ овог прегледног рада јесте да опише наведене методе и прикаже њихову примену за проучавање латералне организације G-протеин-спрегнутих рецептора (енгл. *G-protein-coupled receptors* (GPCRs)). Резултати наших истраживања латералне организације опијатних рецептора дати су као пример.

(Примљено 15. августа, ревидирано 30. септембра 2013)

REFERENCES

1. K. Simons, E. Ikonen, *Nature* **387** (1997) 569
2. D. A. Brown, E. London, *Annu. Rev. Cell Dev. Biol.* **14** (1998) 111
3. M. Edidin, *Annu. Rev. Biophys. Biomol. Struct.* **32** (2003) 257
4. J. F. Hancock, *Nat. Rev. Mol. Cell Biol.* **7** (2006) 456
5. D. Marguet, P. F. Lenne, H. Rigneault, H. T. He, *EMBO J.* **25** (2006) 3446
6. K. Jacobson, O. G. Mouritsen, R. G. Anderson, *Nat. Cell Biol.* **9** (2007) 7
7. C. S. Flordellis, *Curr. Pharm. Des.* **18** (2012) 145
8. A. Pralle, P. Keller, E. L. Florin, K. Simons, J. K. Horber, *J. Cell Biol.* **148** (2000) 997
9. D. A. Zacharias, J. D. Violin, A. C. Newton, R. Y. Tsien, *Science* **296** (2002) 913
10. H. Niv, H. O. Gutman, Y. Kloog, Y. I. Henis, *J. Cell Biol.* **157** (2002) 865
11. I. A. Prior, C. Muncke, R. G. Parton, J. F. Hancock, *J. Cell Biol.* **160** (2003) 165
12. K. Gaus, E. Gratton, E. P. Kable, A. S. Jones, I. Gelissen, L. Kritharides, W. Jessup, *Proc. Natl. Acad. Sci. USA* **100** (2003) 15554
13. P. Sharma, R. Varma, R. C. Sarasij, Ira, K. Gousset, G. Krishnamoorthy, M. Rao, S. Mayor, *Cell* **116** (2004) 577
14. K. Bacia, D. Scherfeld, N. Kahya, P. Schwille, *Biophys. J.* **87** (2004) 1034
15. A. Ianoul, D. D. Grant, Y. Rouleau, M. Bani-Yaghoob, L. J. Johnston, J. P. Pezacki, *Nat. Chem. Biol.* **1** (2005) 196

16. M. J. Swamy, L. Ciani, M. Ge, A. K. Smith, D. Holowka, B. Baird, J. H. Freed, *Biophys. J.* **90** (2006) 4452
17. A. Fujita, J. Cheng, M. Hirakawa, K. Furukawa, S. Kusunoki, T. Fujimoto. *Mol. Biol. Cell* **18** (2007) 2112.
18. V. Vukojević, Y. Ming, C. D'Addario, M. Hansen, U. Langel, R. Schulz, B. Johansson, R. Rigler, L. Terenius. *FASEB J.* **22** (2008) 3537.
19. V. Vukojević, Y. Ming, C. D'Addario, R. Rigler, B. Johansson, L. Terenius. *PLOS ONE* **3** (2008) e4008
20. R. Kraut, N. Bag, T. Wohland. *Methods Cell Biol.* **108** (2012) 395.
21. P. Sengupta, T. Jovanovic-Talisman, D. Skoko, M. Renz, S. L. Veatch, J. Lippincott-Schwartz, *Nat. Methods* **8** (2011) 969
22. P. Sengupta, T. Jovanovic-Talisman, J. Lippincott-Schwartz, *Nat. Protoc.* **8** (2013) 345
23. V. Vukojević, A. Pramanik, T. Yakovleva, R. Rigler, L. Terenius, G. Bakalkin, *Cell. Mol. Life Sci.* **62** (2005) 535
24. E. L. Elson, *Methods Enzymol.* **518** (2013) 11
25. J. Ries J. P. Schwille, *Bioessays* **34** (2012) 361
26. D. Magde, W. W. Webb, E. Elson, *Phys. Rev. Lett.* **29** (1972) 705
27. M. Ehrenberg, R. Rigler, *Chem. Phys. Lett.* **14** (1972) 539
28. E. L. Elson, D. Magde, *Biopolymers* **13** (1974) 1
29. M. Ehrenberg, R. Rigler, *Chem. Phys.* **4** (1974) 390
30. D. E. Koppel, *Phys. Rev., A* **10** (1974) 1938
31. R. Rigler, Ü. Mets, J. Widengren, P. Kask, *Eur. Biophys. J.* **22** (1993) 169
32. M. Eigen, R. Rigler, *Proc. Natl. Acad. Sci. USA* **91** (1994) 5740
33. K. Weisshart, V. Jüngel, S. J. Briddon, *Curr. Pharm. Biotechnol.* **5** (2004) 135
34. V. Vukojević, M. Heidkamp, Y. Ming, B. Johansson, L. Terenius, R. Rigler, *Proc. Natl. Acad. Sci. USA* **105** (2008) 18176
35. R. Saxena, A. Chattopadhyay, *J. Neurochem.* **116** (2011) 726
36. K. Herrick-Davis, E. Grinde, A. Cowan, J. E. Mazurkiewicz, *Mol. Pharmacol.* **84** (2013) 630
37. N. L. Thompson, *Fluorescence Correlation Spectroscopy*, in: *Topics in Fluorescence Spectroscopy: Techniques*, Vol. 1, J. R. Lakowicz, Ed., Plenum Press, New York, USA, 1991, Ch. 6, p. 337
38. H. Qian, E. Elson, *Biophys. J.* **57** (1990) 375
39. P. Kask, K. Palo, D. Ullmann, K. Gall, *Proc. Natl. Acad. Sci. USA* **96** (1999) 13756
40. P. Kask, K. Palo, N. Fay, I. Brand, U. Mets, D. Ullmann, J. Jungmann, J. Pschorr, K. Gall, *Biophys. J.* **78** (2000) 1703
41. Y. Chen, J. D. Müller, P. T. C. So, E. Gratton, *Biophys. J.* **77** (1999) 553
42. L. N. Hillesheim, J. D. Müller, *Biophys. J.* **85** (2003) 1948
43. J. D. Müller, *Biophys. J.* **86** (2004) 3981
44. B. Wu, J. D. Müller, *Biophys. J.* **89** (2005) 2721
45. B. Wu, Y. Chen, J. D. Müller, *Biophys. J.* **91** (2006) 2687
46. E. Petrov, *Derivation of expressions for the FCS correlation function*, 2005, <http://www.onlinedegreediscussion.com/free-online-textbooks/fluorescence-correlation-spectroscopy/> (accessed in November, 2013)
47. P. Kapusta, *Absolute Diffusion Coefficients: Compilation of Reference Data for FCS Calibration*, PicoQuant Application Note 2010
48. L. Wawrezinieck, P. F. Lenne, D. Marguet, H. Rigneault, *Proc. SPIE Int. Soc. Opt. Eng.* (2004) 92

49. L. Wawrezinieck, L. H. Rigneault, D. Marguet, P. F. Lenne, *Biophys. J.* **89** (2005) 4029
50. P.-F. Lenne, L. Wawrezinieck, F. Conchonaud, O. Wurtz, A. Boned, X. J. Guo, H. Rigneault, H.-T. He, D. Marguet, *EMBO J.* **25** (2006) 3245
51. H.-T. He, D. Marguet, *Annu. Rev. Phys. Chem.* **62** (2011) 417
52. D. M. Owen, D. Williamson, C. Rentero, K. Gaus, *Traffic* **10** (2009) 962
53. J. Wenger, F. Conchonaud, J. Dintinger, J. L. Wawrezinieck, T. W. Ebbesen, H. Rigneault, D. Marguet, P.-F. Lenne, *Biophys. J.* **92** (2007) 913
54. E. Betzig, G. H. Patterson, R. Sougrat, O. W. Lindwasser, S. Olenych, J. S. Bonifacino, M. W. Davidson, J. Lippincott-Schwartz, H. F. Hess, *Science* **313** (2006) 1642
55. S. T. Hess, T. P. K. Girirajan, M. D. Mason, *Biophys. J.* **91** (2006) 4258
56. M. J. Rust, M. Bates, X. Zhuang, *Nat. Methods* **3** (2006) 793
57. X. Michalet, T. D. Lacoste, S. Weiss, *Methods* **25** (2001) 87
58. R. E. Thompson, D. R. Larson, W. W. Webb, *Biophys. J.* **82** (2002) 2775
59. A. Yildiz, J. N. Forkey, S. A. McKinney, T. Ha, Y. E. Goldman, P. R. Selvin, *Science* **300** (2003) 2061
60. J. Fölling, M. Bossi, H. Bock, R. Medda, C. A. Wurm, B. Hein, S. Jakobs, C. Eggeling, S. W. Hell, *Nat. Methods* **5** (2008) 943
61. R. Wombacher, M. Heidebreder, S. van de Linde, M. P. Sheetz, M. Heilemann, V. W. Cornish, M. Sauer, *Nat. Methods* **7** (2010) 717
62. G. H. Patterson, J. Lippincott-Schwartz, *Science* **297** (2002) 1873
63. M. R. T. Dale, P. Dixon, M.-J. Fortin, P. Legendre, D. E. Myers, M. S. Rosenberg, *Ecography* **25** (2002) 558
64. M. Scarselli, P. Annibale, A. Radenović, *J. Biol. Chem.* **287** (2012) 16768
65. D. Lando, U. Endesfelder, H. Berger, L. Subramanian, P. D. Dunne, J. McColl, D. Klenerman, A. M. Carr, M. Sauer, R. C. Allshire, M. Heilemann, E. D. Laue, *Open Biol.* **2** (2012) 120078
66. S. Malkusch, W. Muranyi, B. Muller, H. G. Krausslich, M. Heilemann, *Histochem. Cell Biol.* **139** (2013) 173
67. C. Coltharp, R. P. Kessler, J. Xiao, *PLOS ONE* **7** (2012) e51725
68. D. M. Owen, C. Rentero, J. Rossy, A. Magenau, D. Williamson, M. Rodriguez, K. Gaus, *J. Biophotonics* **3** (2010) 446
69. S. AbdAlla, H. Lothar, A. el Massiery, U. Qwitterer, *Nat. Med.* **7** (2001) 1003
70. A. Getis, J. Franklin, *Ecology* **68** (1987) 473
71. S. Manley, J. M. Gillette, J. Lippincott-Schwartz, *Nat. Methods* **5** (2008) 155
72. A. Sharonov, R. M. Hochstrasser, *Proc. Natl. Acad. Sci. USA* **103** (2006) 18911
73. G. Giannone, E. Hosy, F. Levet, A. Constals, K. Schulze, A. I. Sobolevsky, M. P. Rosconi, E. Gouaux, R. Tampe, D. Choquet, L. Cognet, *Biophys. J.* **99** (2010) 1303
74. P. Annibale, S. Vanni, M. Scarselli, U. Rothlisberger, A. Radenovic, *Nat Methods* **8** (2011) 527
75. P. Annibale, S. Vanni, M. Scarselli, U. Rothlisberger, A. Radenovic, *PLOS ONE* **6** (2011) e22678
76. V. Katritch, V. Cherezov, R. C. Stevens, *Annu. Rev. Pharmacol. Toxicol.* **53** (2013) 531
77. G. Liapakis, A. Cordomi, L. Pardo, *Curr. Pharm. Des.* **18** (2012) 175
78. X. Deupi, B. K. Kobilka, *Physiology (Bethesda)* **25** (2010) 293
79. T. Kenakin, *J. Recept. Signal. Transduct. Res.* **30** (2010) 313
80. T. Wohland, K. Friedrich, R. Hovius, H. Vogel, *Biochemistry* **38** (1999) 8671

81. R. Rigler, A. Pramanik, P. Jonasson, G. Kratz, O. T. Jansson, P. Nygren, S. Ståhl, K. Ekberg, B. Johansson, S. Uhlén, M. Uhlén, H. Jörnvall, J. Wahren, *Proc. Natl. Acad. Sci. USA* **96** (1999) 13318
82. R. C. Patel, U. Kumar, D. C. Lamb, J. S. Eid, M. Rocheville, M. Grant, A. Rani, T. Hazlett, S. C. Patel, E. Gratton, Y. C. Patel, *Proc. Natl. Acad. Sci. USA* **99** (2002) 3294
83. N. Kahya, D. A. Wiersma, B. Poolman, D. Hoekstra, *J. Biol. Chem.* **277** (2002) 39304
84. R. C. Calizo, S. Scarlata, *Anal. Biochem.* **440** (2013) 40
85. K. Herrick-Davis, E. Grinde, T. Lindsley, A. Cowan, J. E. Mazurkiewicz, *J. Biol. Chem.* **287** (2012) 23604
86. L. E. Kilpatrick, S. J. Briddon, N. D. Holliday, *Biochim. Biophys. Acta* **1823** (2012) 1068
87. R. H. Rose, S. J. Briddon, S. J. Hill, *Br. J. Pharmacol.* **165** (2012) 1789
88. S. Ganguly, A. Chattopadhyay, *Biophys. J.* **99** (2010) 1397
89. L. Milan-Lobo, I. Gsandtner, E. Gaubitzer, D. Rünzler, F. Buchmayer, G. Köhler, A. Bonci, M. Freissmuth, H. H. Sitte, *Mol. Pharmacol.* **76** (2009) 1196
90. B. Ilien, B. N. Glasser, J. P. Clamme, P. Didier, E. Piemont, R. Chinnappan, S. B. Daval, J. L. Galzi, Y. Mely, *J. Biol. Chem.* **284** (2009) 19533
91. M. Triantafilou, P. M. Lepper, C. D. Briault, M. A. Ahmed, J. M. Dmochowski, C. Schumann, K. Triantafilou, *Eur. J. Immunol.* **38** (2008) 192
92. Y. Cordeaux, S. J. Briddon, S. P. Alexander, B. Kellam, S. J. Hill, *FASEB J.* **22** (2008) 850
93. F. Philip, P. Sengupta, S. Scarlata *J. Biol. Chem.* **282** (2007) 19203
94. R. J. Middleton, S. J. Briddon, Y. Cordeaux, A. S. Yates, C. L. Dale, M. W. George, J. G. Baker, S. J. Hill, B. Kellam, *J. Med. Chem.* **50** (2007) 782
95. O. Hegener, L. Prenner, F. Runkel, S. L. Baader, J. Kappler, H. Häberlein, *Biochemistry* **43** (2004) 6190
96. M. Scarselli, P. Annibale, C. Gerace, A. Radenovic, *Biochem. Soc. Trans.* **41** (2013) 191.



Single crystalline thin films as a novel class of electrocatalysts

JOSHUA SNYDER, NENAD M. MARKOVIC and VOJISLAV R. STAMENKOVIC*

Materials Science Division, Argonne National Laboratory, Argonne, IL 60439, USA

(Received 16 September, revised 30 October 2013)

Abstract: The ubiquitous use of single crystal metal electrodes has garnered invaluable insight into the relationship between surface atomic structure and functional electrochemical properties. However, the sensitivity of their electrochemical response to surface orientation and the amount of precious metal required can limit their use. Herein, a generally applicable procedure for the production of thin metal films with a large proportion of atomically flat (111) terraces without the use of an epitaxial template is presented. Thermal annealing in a controlled atmosphere induces long-range ordering of magnetron sputtered thin metal films deposited on an amorphous substrate. The ordering transition in these thin metal films yields characteristic (111) electrochemical signatures using a minimal amount of material and provides an adequate replacement for oriented bulk single crystals. This procedure could be generalized towards a novel class of practical multimetallic thin film-based electrocatalysts with tunable near-surface compositional profiles and morphologies. Annealing of atomically corrugated sputtered thin film Pt-alloy catalysts yields an atomically smooth structure with highly crystalline, (111)-like ordered and Pt segregated surface that displays superior functional properties, bridging the gap between extended/bulk surfaces and nanoscale systems.

Keywords: thin films; magnetron sputtering; Pt-alloys; oxygen reduction reaction.

INTRODUCTION

Well-defined, single crystal metal electrodes and their stepped/vicinal derivatives have helped to elucidate the correlation between surface structure and functional properties for many electrochemical and electrocatalytic processes. Their use has also guided investigations of the mechanistic reaction pathways relevant to hydrogen economy, most notably the oxygen reduction reaction (ORR),^{1–4} providing valuable insight into the link between bulk surfaces and nanoscale catalysts,^{5–7} To this end, Pt(111)⁸ has been the most widely studied single crystal as its close-packed atomic arrangement and wide atomically flat terraces provide an ideal, well-defined surface essentially devoid of defects when

* Corresponding author. E-mail: vrstamenkovic@anl.gov

doi: 10.2298/JSC130916119S

properly prepared. The study of oriented single crystals of single-phase metal alloys has inspired an entire branch of electrocatalyst research and development focused on the optimization of surface interaction with reaction intermediates and products. Most notably, the discovery that annealing a Pt₃Ni(111) single crystal can drive the formation of a segregated compositional profile, where a Pt-skin covering a Ni-rich second atomic layer was found to be the most active surface to date for the ORR.⁹

The wide spread use of high quality single crystal metal electrodes was enabled through the introduction of a technique to reproducibly prepare single crystal bead electrodes by melting, cooling and careful orientation before cutting and polishing to expose the desired crystallographic face.^{10–12} Significant care must be taken as even small degrees of miscut can result in significantly altered electrochemical properties due to the increased step density on the surface.^{13–16} The cylindrical single crystal geometry is more amenable for use in a rotating disk electrode (RDE) setup for determining the kinetic parameters of electrochemical reactions than the bead type single crystals. These cylindrical single crystals are typically several millimeters in diameter and thickness, requiring a significant amount of material and can only be manufactured in a small number of facilities that have the proper capabilities. As such, cylindrical bulk single crystals are cost prohibitive for general use, especially when composed of precious metals and precious metal containing alloys. Metal thin films present a potential replacement for bulk single crystals as the nature of their geometry both significantly lowers the precious metal content and provides a surface that is susceptible to ordering upon annealing, driven by a tendency to expose the lowest energy surface, the (111) family. The formation of (111) textured thin films is typically achieved through epitaxial growth on single crystal substrates either by slow physical vapor deposition (PVD)^{15,17–24} or in solution through electrochemical deposition.^{25,26} Films produced in such a manner can be highly strained due to lattice mismatch between the film and substrate and, depending upon the deposition/annealing parameters, the film may contain holes and discontinuities. These PVD films often lack the long-range order required to exhibit cyclic voltammetric (CV) finger-print adsorption features characteristic of (111) single crystals^{17,18,26,27} and the few that do have a form factor that is difficult to integrate into an RDE for proper determination of kinetic parameters from electrochemical data.^{28,29}

In this report, a simple approach to reproducibly generate well-defined highly ordered (111) surfaces on polycrystalline thin metal films without the use of epitaxial templates or seeded layer growth is presented. The processing of these magnetron sputtered polycrystalline thin films by controlled atmosphere, low temperature annealing drives ordering through surface energy reduction to an equilibrium structure composed predominately of wide, atomically flat (111) ter-

ances, as evidenced through both their electrochemical signature and surface structure determined by scanning tunneling microscopy (STM). Using single component metal and alloy thin films as a template, it is possible to tune the composition, compositional profile and surface structure through thermally induced segregation and ordering, providing valuable insight into the correlation between structure/composition and functional electrocatalytic properties. This insight will help to guide the transition from extended bulk surfaces to nanoscale systems for the development of the next generation of practical electrocatalysts.

EXPERIMENTAL

Thin films were prepared by magnetron sputter deposition onto glassy carbon (GC) disks (6 mm dia., 4 mm thick) in a sputter deposition chamber (AJA International, Inc.) equipped with both radio frequency (RF) and direct current (DC) power supplies and operating with a base pressure of 10^{-10} torr and a sputtering pressure of 1.5 mtorr. Prior to deposition of the metal films, the GC substrates were cleaned with an RF Ar plasma. The Pt films were deposited onto a room temperature GC substrate with 100 W RF power, yielding a rate of 0.75 \AA s^{-1} , while the Au films were deposited with 50 W DC power, yielding a rate of 0.74 \AA s^{-1} . Both the Pt and Au films were between 10 and 25 nm thick as determined by a quartz crystal thickness monitor. The as-deposited films were annealed in a tube furnace under a controlled atmosphere, 3 % H_2/Ar at 500 °C for Pt and 300 °C for Au.

The nanostructured thin film catalysts (NSTF) were formed through magnetron sputter deposition of platinum and platinum alloys onto the surface of an oriented, crystalline organic pigment (*N,N*-di(3,5-xylyl)perylene-3,4:9,10bis(dicarboximide), Perylene Red) whiskers.³⁰ Structural ordering of the NSTF was achieved through thermal annealing at 400 °C in a H_2/Ar atmosphere.

A typical three-compartment, Pyrex electrochemical cell was used for all electrochemical measurements, in which the SCE (Hg/HgCl, Beckman) reference electrode was separated from the working electrode compartment by a salt bridge and the Pt counter electrode was separated with a porous glass frit. All potentials in this study are reported *versus* the reversible hydrogen electrode (RHE). The thin, sputtered/annealed films on GC disks were characterized electrochemically in the hanging meniscus configuration in Ar-purged 0.1 M HClO_4 and 0.1 M H_2SO_4 electrolytes, which were made from high purity acids. The thin films were immersed in the electrolyte under potential control (0.1 V *vs.* RHE).

The scanning tunneling microscopy (STM) images for the Pt-thin films were acquired with a Digital Instruments Multi-Mode Dimension STM controlled by a Nanoscope III control station. During the measurement, the microscope and sample were enclosed in a pressurized cylinder with a CO atmosphere. Prior to the introduction of the sample into the STM, a CO layer was adsorbed onto the surface in CO saturated 0.1 M HClO_4 , to both preserve the order and cleanliness of the surface and to aid in the visualization of the surface atomic structure with respect to the formation of an ordered CO adlayer. STM images of the Au and Pt-thin films were also recorded in an Omicron UHV system equipped with an STM chamber. Samples were imaged at 0.20 V and 1.0 nA.

A Hitachi H-9500 environmental transmission electron microscope operated at 300 kV was used to perform microstructural characterization and the *in situ* heating TEM study. Powder samples were attached to the heating zone of a Hitachi gas injection–heating holder. Images of the nanoparticles were first recorded at room temperature, followed by heating of

the specimen inside the microscope chamber with a vacuum level of about 10^{-4} Pa. A CCD (charged-couple device) camera was used to monitor the microstructural evolution and record images and videos. Each heating temperature was held for at least 10 min for detailed structural characterization, including morphology and atomic structure. A Hitachi SU70 high-resolution field-emission SEM was used for routine inspection of NSTF samples. For a detailed study of the surface morphology study at nanometer scale, a Hitachi S-5500 ultrahigh resolution cold field-emission SEM delivered a much higher resolution power (0.4 nm secondary electron image resolution at 30 kV) than normal SEM because of the specially designed objective lens. On both SU70 and S-5500, secondary electron images were taken at 15 or 30 kV to reveal the surface morphology of both the as-deposited and annealed samples.

RESULTS AND DISCUSSIONS

Magnetron sputter deposition is well suited for the efficient growth of thin single component, layered and well-mixed alloy films. The surface morphology of the as-sputtered thin films, however, is typically three-dimensional (3D) with grain sizes averaging 5 nm, Figs. 1a and 2a. Consequently, their electrochemical behavior is typical of bulk polycrystalline materials, Figs. 1a and 2a. The extent of this 3D morphology and surface roughness can be limited through optimization of the sputtering parameters, where lower sputter gas pressures will limit gas incorporation into the films and maintain the high kinetic energy of the impinging atoms. High kinetic energy impingement facilitates the formation of dense films with an absence of columnar grains, which may limit grain growth during annealing, and produce a film with predominately (111) orientation of the individual grains.^{31,32} For FCC metals; however, the surface orientations of these small grains are not necessarily (111).

Annealing thin films in a reductive atmosphere facilitates surface diffusion, which tends to smoothen defects and promote growth of the lowest energy (111) facets. This process is promoted by the use of an amorphous substrate as the film is not epitaxially constrained to the crystallographic structure of the underlying substrate, and hence, surface diffusion and grain boundary motion are sufficiently fast at moderate annealing temperatures to induce coalescence and growth of grains. Evolution of film discontinuities, holes, hillocks,^{33–35} grain boundary grooves³⁶ and film dewetting,³⁷ can cause films to roughen during annealing. These processes become exacerbated as both film thickness and melting point of the metal decrease. Therefore, care must be taken when annealing thin, sputtered films to balance effectively the competitive atomic processes of smoothening driven by surface energy reduction and roughening through formation of film discontinuities. Roughening can be avoided by using moderate annealing temperatures, $\approx 0.3 T_m$ (melting point), above which, film dewetting and incorporation of carbon impurities are evidenced by the loss of the characteristic (111) features in the CVs. These lower temperatures prove to be sufficient to induce surface diffusion driven structural ordering in the thin films. When comparing the CV signatures of as-sputtered and annealed Pt-thin films to that of a Pt(111) single

crystal, Fig. 1a, c and d, the dramatic transition from polycrystalline to a highly ordered surface becomes apparent. The as-sputtered Pt-thin film has an electrochemical signature resembling that of a polycrystalline Pt-electrode with hydrogen underpotential deposition (H_{UPD}) peaks associated with proton adsorption on steps and defect sites and broad oxidation/reduction features at higher potentials, consistent with the small grained, atomically rough structure of the film. The surface of the annealed Pt-thin film, on the other hand, is characterized by a well ordered morphology containing large, interconnected, atomically flat terraces, as shown by the hexagonal (2×2)- $3CO$ adstructure of the CO_{ad} layer on Pt in the STM image in Fig. 1b; an adsorbate structure that only occurs on atomically ordered (111) terraces.³⁸

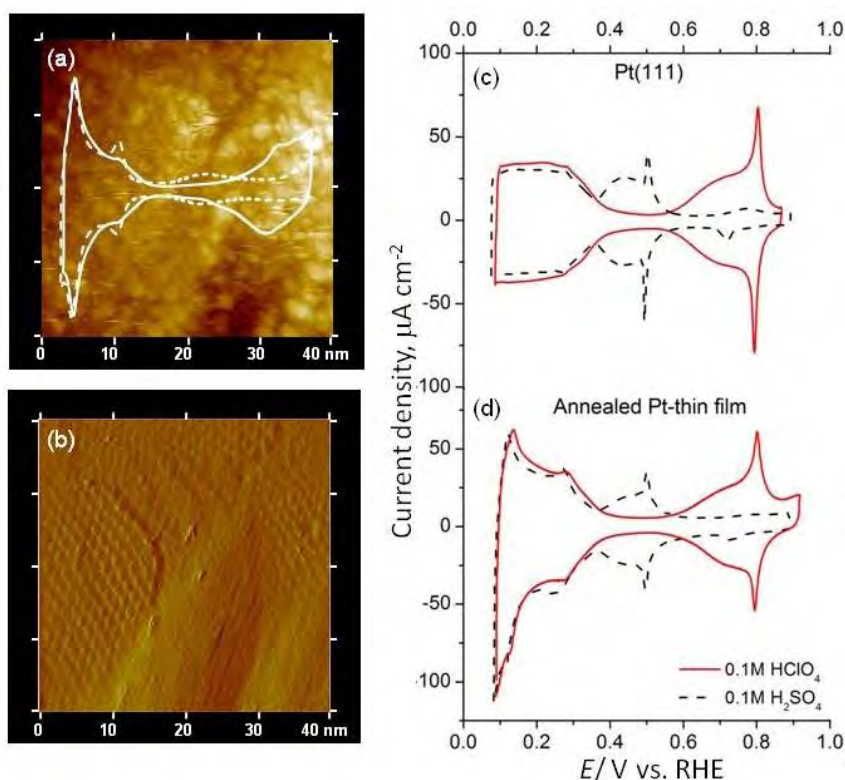


Fig. 1. Scanning tunneling microscopy (STM) images of: a) as-sputtered Pt-thin film and b) a CO_{ad} layer on an annealed Pt-thin film on a GC substrate. The hexagonal structures shown in (b) are attributed to an ordered CO_{ad} layer that is only visible on clean, atomically flat (111) terraces. The overlying CVs in (a) represent the electrochemical signature of the as-sputtered Pt films in 0.1 M $HClO_4$ (solid line) and 0.1 M H_2SO_4 (dashed line). c) CVs of Pt(111) in 0.1 M $HClO_4$ (red line) and 0.1 M H_2SO_4 (dashed black line); d) CVs of an annealed Pt-thin film in 0.1 M $HClO_4$ (red line) and 0.1 M H_2SO_4 (dashed black line). All electrolytes were purged with Ar and the CVs were recorded at a sweep rate of 50 mV s^{-1} .

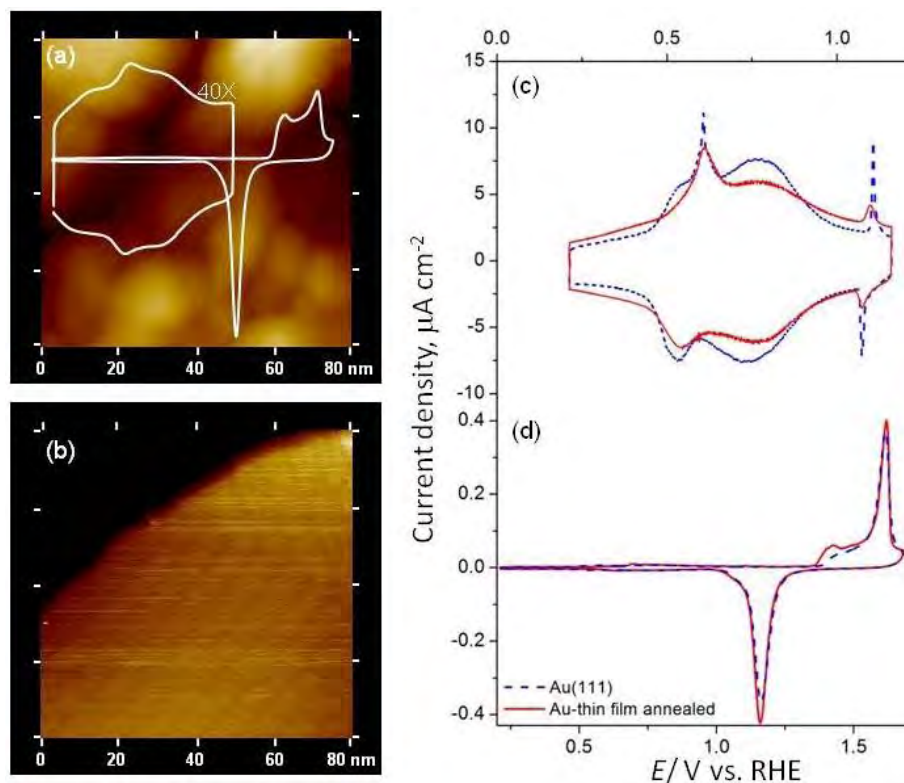


Fig. 2. Scanning tunneling microscopy (STM) images recorded in UHV ($100\text{ nm} \times 100\text{ nm}$), 0.20 V and 1.0 nA , of: a) an as-sputtered Au-thin film, overlain with the CV of the as-sputtered Au-thin film in $0.1\text{ M H}_2\text{SO}_4$, including an expanded current signal for the low potential region and b) an atomically flat Au(111) terrace on an annealed, sputtered Au-thin film on a GC disk substrate. The herringbone ($\sqrt{3} \times 23$) reconstruction is clearly visible and the terrace width of over 50 nm was routinely found over the entire surface of the annealed Au-thin films. c) CVs of the low potential region for Au(111) (blue dashed line) and annealed Au-thin film (red line); d) CVs including the Au oxidation region for Au(111) (blue dashed line) and annealed Au-thin film (red line) recorded in room temperature, Ar purged $0.1\text{ M H}_2\text{SO}_4$ at a sweep rate of 50 mV s^{-1} .

Characteristic electrochemical features of Pt(111) appeared for the annealed Pt-thin films in both HClO_4 and H_2SO_4 electrolytes, Fig. 1c and d. The most telling feature for Pt(111) in HClO_4 , Fig. 1c, is the sharp, reversible butterfly peak at $\approx 0.8\text{ V vs. RHE}$, which is attributed to adsorption/desorption of OH_{ad} species and its peak current and sharpness is a descriptive metric for both the cleanliness and crystalline order of the surface.^{39–42} It is a feature that, while absent for the as-sputtered Pt-thin film, Fig. 1a, is as sharp and similar in peak current density for the annealed Pt-thin film as for a Pt(111) electrode, which is indicative of long-range ordering associated with large, interconnected (111) terraces present

on the annealed thin film, Fig. 1d. Voltammetric observation of the adsorption of anionic species other than hydroxyl can give further insight into the state of the annealed Pt-thin film surface. In 0.1 M H₂SO₄ electrolyte, Fig. 1c, a butterfly peak appears at ≈ 0.5 V vs. RHE for Pt(111), although the exact position is dependent on the HSO₄⁻ concentration in solution.^{13,43} This reversible feature is attributed to the order/disorder transition of a long-range disordered sulfate layer, the adsorption of which is represented by the current hump preceding the butterfly peak.^{43–46} The presence and sharpness of this peak is strongly tied to the defect density of the surface, whereby this feature is not observed even for evaporated¹⁷ or electrodeposited²⁶ Pt-thin films on single crystal substrates. The potential, sharpness and peak intensity of this butterfly feature may be associated with surface structures by studying the response of different miscut angles, vicinal surfaces, of a (111) single crystal. As the terrace width decreases and the step/defect density increases, the peak intensity decreases and eventually disappears.^{13,14} The minimum average terrace width for the studied annealed Pt-thin films may be estimated by comparing the CV in 0.1 M H₂SO₄, Fig. 1d, to those of a series of miss-cut Pt(111) single crystals. It is found that the finger-print features of the annealed Pt-thin films closely match those of a (13,13,12) surface.¹³ The sulfate adsorption butterfly feature in low concentration H₂SO₄ electrolytes (≤ 0.1 M) disappears for surfaces with an average terrace width below 12 atoms, but only under extremely clean conditions.^{13,14} It is not uncommon for the butterfly peak to be poorly resolved in H₂SO₄ for surfaces with terrace widths between 20 and 40 atoms.¹³ It can be inferred from the electrochemical results, as they represent an average over the entire surface that the atomic structure of the annealed Pt-thin films is characterized by a minimum average terrace width of at least 15–20 atoms. However, locally, as determined by CO_{ad} STM, Fig. 1b, the annealed Pt-thin film surface contains many areas composed of large, atomically flat terraces with widths greater than 20 nm.

To demonstrate the general applicability of the proposed approach, the presented procedure is extended to the formation of ordered thin films of other electrochemically relevant metals. The CVs of Au(111) and annealed Au-thin films on GC in 0.1 M H₂SO₄ are compared in Fig. 2c and d. The electrochemical signature in the low potential region, ≈ 0.2 to 1.2 V vs. RHE, in H₂SO₄, Fig. 2c, exhibits features characteristic of the (111) crystallographic orientation. The sharp peak in the anodic scan at ≈ 0.6 V vs. RHE is attributed to the lifting of the reconstruction of the Au(111) surface, moving from a ($\sqrt{3} \times 23$) to a (1 \times 1) structure,^{47–51} which is reformed upon reversal of the potential, as evidenced by the hump at ≈ 0.55 V vs. RHE; the asymmetry of the current feature is due to the slow kinetics of the lifting/formation of the reconstruction.⁵² After gentle annealing, the rough, small grained morphology of the as-sputtered Au-thin film, for which there are no reconstruction peaks, Fig. 2a, exhibits a clear, well-ordered

structure, as evidenced by the presence of the reconstruction lifting/formation peaks, Fig. 2c, and the visualization of the ($\sqrt{3} \times 23$) herringbone surface feature through UHV STM, Fig. 2b. Using STM to examine the atomic structure of different areas of the annealed Au-thin film, atomically flat terraces with widths of 50 to 100 nm are found to be ubiquitous across the entire surface.

The lifting of the reconstruction is accompanied by the adsorption of a disordered adlayer of sulfate onto the (111) terrace,^{49,51} represented by the broad hump between 0.65 and 1 V vs. RHE, Fig. 2c. As the potential is swept anodically, the disordered sulfate adlayer undergoes an order/disorder transition, to which the sharp, reversible “butterfly” peaks at ≈ 1.1 V vs. RHE, Fig. 2c, are attributed.^{47–52} The butterfly feature in H₂SO₄ is associated with the long-range order of the surface and disappears for Au(111) single crystals with miscut angles greater than 4° or terrace widths below 3 nm.^{15,16,53,54} On expanding the potential range into the Au oxidation/reduction region, peaks associated with the formation of AuOH at ≈ 1.4 V vs. RHE and AuO at ≈ 1.6 V vs. RHE. Au–OH_{ad} tends to adsorb preferentially at step edges and defect sites;^{55–57} therefore, the reduction in the size of the peak at ≈ 1.3 V vs. RHE upon annealing to the point where it nearly matches the current of the corresponding feature of the Au(111) CV in conjunction with an increase in the peak current and sharpness of the AuO peak at ≈ 1.6 V vs. RHE are additional indications of the low step edge density associated with the growth in size and population of atomically flat (111) features.¹⁶

The structural evolution of the surface of sputtered Pt and Au films, two metals with differing materials properties such as melting point, degree of substrate wetting and surface energy, during annealing from a rough, nano-grained surface to one that is highly ordered and consisting of a large proportion of atomically flat (111) terraces demonstrates the general applicability of the presented approach. The insight gained from these thin films opens a unique avenue for tailoring the functional properties of materials with high surface area, *i.e.*, thin film-based electrocatalysts relevant to renewable energy-based technologies. It is serendipitous that the lowest energy surface, (111), to which these thin films revert during annealing is also the most active crystallographic orientation for the oxygen reduction reaction (ORR) on Pt-transition metal alloys. Bridging the gap between these extended, well-ordered surfaces and high surface area, nanoscale systems will facilitate the development of electrocatalysts with both superior activity and optimized precious metal utilization. To this end, a thin film-based, high surface area electrocatalyst architecture, known as nanostructured thin films (NSTF), has been created through sputter deposition of Pt and Pt alloys onto the surface of an ordered array of molecular solid whiskers, composed of an organic pigment *N,N*-di(3,5-xylyl)perylene-3,4:9,10-bis(dicarboximide), commonly known as Perylene Red.^{58–63}

The morphology of these as-sputtered whiskers is shown in Fig. 3a–c, where each whisker is approximately 800–1000 nm in length and the film thicknesses range from 10–20 nm. Close examination of the surface structure of these whiskers, Fig. 3a and c, indicate a corrugated surface structure composed of “whiskerettes” with a high nanoscale roughness and defect density. The surface of these as-sputtered whiskers is easily correlated to that of the as-sputtered Au and Pt-thin film surfaces, where a rough, nano-grained morphology dominates. Optimization of this surface structure can be achieved through application of the presented experimental approach derived for extended thin films. Figure 3d–f presents *in-situ* transmission electron microscopy images (TEM) of NSTF whiskers that have been annealed up to 400 °C under vacuum. These TEMs demonstrate the structural transition of the surface of the NSTF whiskers from a densely corrugated, highly defected, 3D surface to one that is smooth, homogeneous and two-dimensional. This transition is thermodynamically driven, as the enhanced mobility of the surface atoms, imparted by the high temperature, tends to move the surface toward the lowest energy configuration. Grain growth and surface faceting, similar to that seen with the sputtered thin films on GC substrates, are confirmed through the *in-situ* TEM images Fig 3d–f where a (111) texture

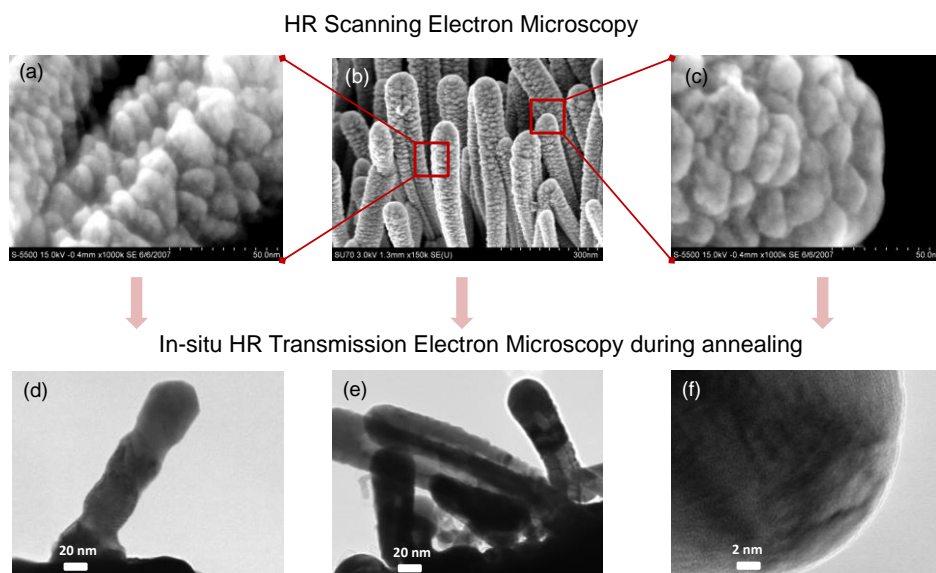


Fig. 3. *In-situ* imaging of the structural transition from nanostructured, 3D to crystalline homogeneous 2D thin films during annealing: a–c) high-resolution scanning electron microscopy (HRSEM) images of the as-sputtered NSTF catalyst; d–f) high resolution transmission electron microscopy (HRTEM) images of the annealed whiskers showing a smooth, faceted surface without corrugated, highly defected whiskerettes.

ordered, (111)-like structure, the controlled annealing atmosphere facilitates the formation of an optimized compositional profile for Pt-transition metal alloys, where the nano-segregated structure mimics that of an annealed Pt₃Ni(111) single crystal.⁹ Adsorption characteristics of the oxygenated species are optimized on these Pt segregated surfaces as the high composition of transition metal (Ni, Fe, Co, etc.), greater than the bulk composition of the alloy, in the second atomic layer, changes the electronic structure of the surface Pt atoms, affecting oxygen adsorption strength thereby resulting in improved ORR rates. This change in adsorption properties is evidenced by the CVs shown in Fig. 4a. In the hydrogen underpotential deposition region (H_{UPD}), ≈ 0 to 0.4 V vs. RHE, the signature for the annealed PtNiFe NSTF is a flat plateau that is characteristic of hydrogen adsorption on Pt(111), see Fig. 1c, and Pt alloys,^{5,9} whereas that of the as-sputtered Pt and PtNiFe NSTF contain features that may be attributed to H_{UPD} on (100) and (110) surface sites. There is also a positive shift in the onset of surface oxide formation in the order: Pt NSTF < PtNiFe NSTF < annealed PtNiFe NSTF. This shift is indicative of a significant decrease in the surface coverage of hydroxyl species, which can block the active sites for the ORR, and as shown in Fig. 4b and c, results in a significant increase in the ORR activity.

The specific activity is a fundamental property of a material that is indicative of its intrinsic catalytic activity. A higher specific activity is related to an increased turnover frequency due to improved utilization of surface Pt atoms. This improved utilization is a direct result of the ordered surface structure and optimized compositional profile obtained for the annealed PtNiFe NSTF. The ordered PtNiFe NSTF exhibits a specific activity two-times that of the as-sputtered PtNiFe NSTF and nearly 15 times that of commercial Pt/C (TKK) supported nanoparticle electrocatalysts. While film thickness and alloy composition will continue to be optimized, the current annealed PtNiFe NSTF catalyst exceeds the U.S. Department of Energy activity target for 2015 by a factor of two.

Electrocatalysts are easily categorized by their surface atomic structure and graded by their activity. The low activity class is composed of high surface area supported nanoparticle-based catalysts, followed by polycrystalline alloys and the highest activity class is reserved for single crystal metals. Ordered, annealed Pt alloy NSTF catalysts transcend these classes with activities that are characteristic of single crystal Pt alloys, while maintaining the electrochemically active surface area of nanoscale electrocatalysts. These findings indicate that the ability to tailor atomic structure, composition and morphology could lead to significant enhancements in catalyst activity and precious metal utilization. Through elucidation of the structure–function and composition–function correlations, an approach has been developed in the present study that bridges the gap between extended/bulk surfaces and nanoscale catalysts, providing a new avenue for the design of electrocatalysts with superior functional properties.

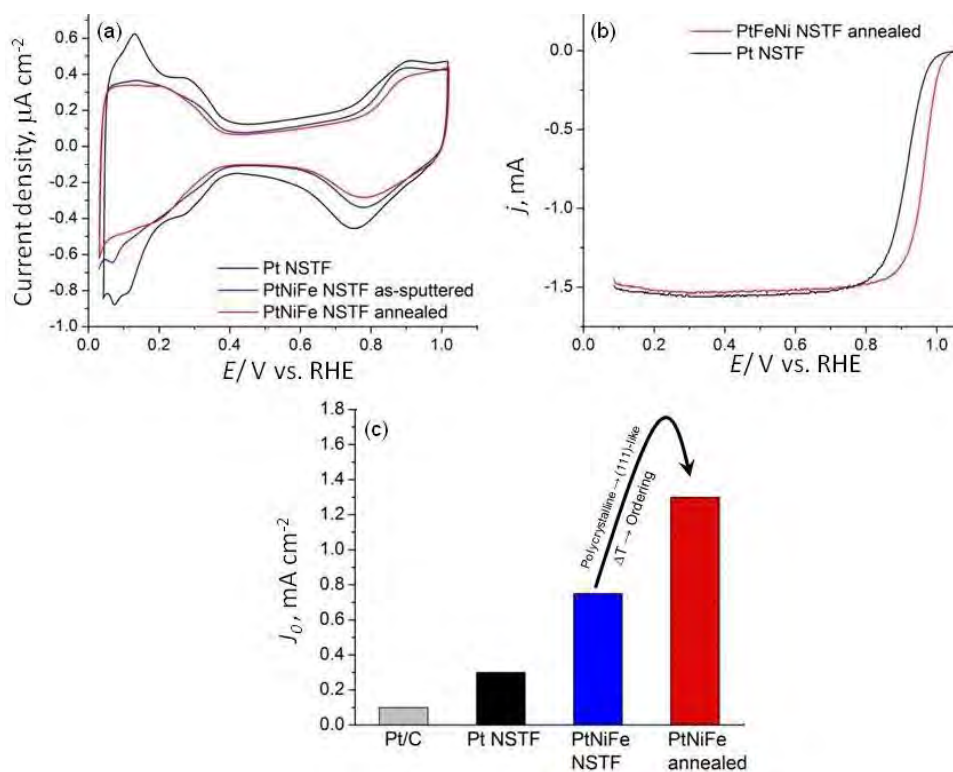


Fig. 4. a) CVs of Pt NSTF (black line), as-sputtered PtNiFe NSTF (blue line) and annealed PtNiFe NSTF (red line) in Ar purged 0.1 M HClO_4 , recorded with a sweep rate of 50 mV s^{-1} ; b) IR-corrected ORR curves for Pt NSTF (black line) and annealed PtNiFe NSTF (red line) in O_2 saturated 0.1 M HClO_4 , recorded with a sweep rate of 20 mV s^{-1} at room temperature and c) specific activities measured at 0.95 V vs. RHE.

CONCLUSIONS

Significant insight into the correlation between structure/composition and functional electrochemical properties has been gained over the years using well-defined single crystal interfaces. Herein, an overview of a generally applicable procedure to reproducibly convert sputtered, polycrystalline thin films on amorphous GC substrates into highly ordered, (111)-like thin films exhibiting the characteristic structural and electrochemical features of carefully prepared (111) single crystal electrodes has been presented. Extension of this approach to practical thin film-based materials allows for the development of a unique class of electrocatalysts that possess the specific activity of bulk/extended surfaces and the electrochemically active surface area of nanoparticle-based catalysts. The superior performance of the annealed PtNiFe thin films, which has a kinetic activity nearly 15 times that of Pt/C, is the direct result of the highly ordered, (111) crystallinity and near-surface compositional profile that develops during

annealing. This approach could facilitate the development of a wide range of practical thin film-based catalysts, bridging the gap between extended/bulk surfaces and nanoscale electrocatalysts.

Acknowledgements. This work was supported by the U.S. Department of Energy, Office of Science, Office of Basic Energy Sciences, under Contract No. DE-AC02-06CH11357. The authors are grateful to Dusan Tripkovic and Arvydas Paulikas (ANL) for support in experimental results obtained by STM, Mark Debe, Radoslav Atanasoski and Dennis van der Vliet (all from 3M) for providing the NSTF catalysts and support in the electrochemical characterizations.

ИЗВОД

ТАНКИ ФИЛМОВИ МОНОКРИСТАЛНЕ СТРУКТУРЕ КАО НОВА КЛАСА
ЕЛЕКТРОКАТАЛИЗАТОРА

JOSHUA SNYDER, NENAD M. MARKOVIC и VOJISLAV R. STAMENKOVIC

Materials Science Division, Argonne National Laboratory, Argonne, IL 60439, USA

Широко коришћење монокристалних металних електрода омогућило је значајан увид у везу између атомске структуре површине и функционалних електрохемијских својстава. Међутим, осетљивост њиховог електрохемијског одзива на оријентацију површине и захтевану количину драгоцених метала може да ограничи њихову примену. Овде је изложено опште применљив поступак за добијање танких металних филмова са великим уделом атомски равних тераса оријентације (111) без коришћења епитаксијалне матрице. Термичко одгревање у контролисаној атмосфери танког филма који је магнетронски нанет на аморфну подлогу доводи до његовог уређивања по типу дугог домета. Уређивање оваквих танких металних филмова даје карактеристично електрохемијско обележје површине оријентације (111) уз утрошак минималне количине материјала и обезбеђује адекватну замену за монокристале оријентисане у маси. Овај поступак може да се генерализује за добијање нове класе практичних електрокатализатора заснованих на мултиметалном танком филму код којих је могуће подешавање састава уз површину и морфологије. Одгревање атомски таласастог танког филма Pt-легура даје високо кристалиничну атомски глатку структуру уређену слично равни (111), чија је површина услед сегрегације обогаћена платином. Она показује супериорна функционална својства, премошћавајући јаз између макроскопских материјала развијених површина и нано-честичних система.

(Примљено 16. септембра, ревидирано 30. октобра 2013)

REFERENCES

1. N. Markovic, H. Gasteiger, P. Ross, *J. Phys. Chem.* **99** (1995) 3411
2. N. Markovic, T. Schmidt, V. Stamenkovic, P. Ross, *Fuel Cells* **1** (2001) 105
3. N. Markovic, R. Adzic, B. Cahan, E. Yeager *J. Electroanal. Chem.* **377** (1994) 249
4. M. Macia, E. Herrero, J. Feliu, *J. Electroanal. Chem.* **564** (2004) 141
5. D. van der Vliet, C. Wang, D. Tripkovic, D. Strmcnik, X. Zhang, M. Debe, R. Atanasoski, N. Markovic, V. Stamenkovic, *Nat. Mater.* **11** (2012) 1051
6. N. Markovic, H. Gasteiger, P. Ross, *J. Electrochem. Soc.* **144** (1997) 1591
7. J. Greeley, J. Rossmeisl, A. Hellman, J. Norskov, *Z. Phys. Chem.* **221** (2007) 1209
8. V. Climent, J. Feliu, *J. Solid State Electrochem.* **15** (2011) 1297

9. V. Stamenkovic, B. Fowler, B. B. Mun, G. Wang, P. Ross, P. C. Lucas, C. N. Markovic, *Science* **315** (2007) 493
10. J. Clavilier, R. Faure, G. Guinet, R. Durand, *J. Electroanal. Chem.* **107** (1979) 205
11. J. Clavilier, D. Armand, B. Wu, *J. Electroanal. Chem. Interfacial Electrochem.* **135** (1982) 159
12. J. Clavilier, *J. Electroanal. Chem.* **107** (1979) 211
13. J. Clavilier, K. El Achi, A. Rodes, *Chem. Phys.* **141** (1990) 1
14. N. Furuya, S. Koide, *Surf. Sci.* **220** (1989) 18
15. T. Wandlowski, K. Ataka, S. Pronkin, D. Diesing, *Electrochim. Acta* **49** (2004) 1233
16. M. Schneeweiss, D. Kolb, D. Liu, D. Mandler, *Can. J. Chem.* **75** (1997) 1703
17. B. Braunschweig, A. Mitin, W. Daum, *Surf. Sci.* **605** (2011) 1082
18. Y. Golan, L. Margulis, I. Rubinstein, *Surf. Sci.* **264** (1992) 312
19. N. Spiridis, M. Kisielewski, A. Maziewski, T. Slezak, P. Cyganik, J. Korecki, *Surf. Sci.* **507–510** (2002) 546
20. S. Broukhin, C. Saguy, M. Koifman, B. Pokroy, *J. Phys. Chem., C* **116** (2012) 12149
21. D. Trevor, C. Chidsey, D. Loiacono, *Phys. Rev. Lett.* **62** (1989) 929
22. G. Scavia, E. Agostinelli, S. Laureti, G. Varvaro, B. Paci, A. Benerosi, V. Albertini, S. Kaciulis, A. Mezzi, *J. Phys. Chem., B* **110** (2006) 5529
23. M. Debe, *Nature* **486** (2012) 43
24. Y. Yamada, K. Miyamoto, T. Hayashi, Y. Iijima, N. Todoroki, T. Wadayama, *Surf. Sci.* **607** (2013) 54
25. Y. Liu, D. Gokcen, U. Bertocci, T. Moffat, *Science* **338** (2012) 1327
26. K. Uosaki, S. Ye, H. Naohara, Y. Oda, T. Haba, T. Kondo, *J. Phys. Chem., B* **101** (1997) 7566
27. A. Berna, J. Delgado, J. Orts, A. Rodes, J. Feliu, *Langmuir* **22** (2006) 7192
28. A. Maljusch, J. Henry, W. Schuhmann, A. Bondarenko, *Electrochem. Comm.* **16** (2012) 88
29. J. Henry, A. Maljusch, M. Huang, W. Schuhmann, A. Bondarenko, *ACS Catalysis* **2** (2012) 1457
30. M. K. Debe, A. Hester, G. Vernstrom, A. Steinbach, S. Hendricks, A. Schmoekel, R. Atanasoski, D. McClure, P. Turner, *Nanostructured Thin Film Catalysts for PEM Fuel Cells by Vacuum Web Coating*, in *Society of Vacuum Coaters 50th Annual Technical Conference Proceedings*, 2007, p. 175
31. M. Kawamura, T. Mashima, Y. Abe, K. Sasaki, *Thin Solid Films* **377–378** (2000) 537
32. E. Slavcheva, G. Ganske, G. Topalov, W. Mokwa, U. Schnakenberg, *Appl. Surf. Sci.* **255** (2009) 6479
33. J. Tersoff, F. LeGoues, *Phys. Rev. Lett.* **72** (1994) 3570
34. H. Galinski, T. Ryll, L. Schlagenhauf, L. Gauckler, *Phys. Rev., B* **85** (2012) 125408
35. W. Pennebaker, *J. Appl. Phys.* **40** (1969) 394
36. M. Rost, D. Quist, J. Frenken, *Phys. Rev. Lett.* **91** (2003) 026101
37. S.-J. Hwang, J.-H. Jee, C.-O. Jeong, Y.-C. Joo, *Scripta Mat.* **56** (2007) 17
38. D. Strmcnik, D. Tripkovic, D. van der Vliet, K. Chang, V. Komanicky, H. You, G. Karapetrov, J. Greeley, V. Stamenkovic, N. Markovic, *J. Am. Chem. Soc.* **130** (2008) 15332
39. A. Bondarenko, I. Stephens, H. Hansen, F. Perez-Alonso, V. Tripovic, T. Johansson, J. Rossmeisl, J. Norskov, I. Chorkendorff, *Langmuir* **27** (2011) 2058
40. A. Berna, V. Climent, J. Feliu, *Electrochem. Comm.* **9** (2007) 2789
41. E. Herrero, J. Feliu, A. Wieckowski, J. Clavilier, *Surf. Sci.* **325** (1995) 131

42. N. Markovic, T. Schmidt, B. Grgur, H. Gasteiger, R. Behm, P. Ross, *J. Phys. Chem., B* **103** (1999) 8568
43. N. Garcia-Araez, V. Climent, P. Rodriguez, J. Feliu, *Electrochim. Acta* **53** (2008) 6793
44. M. Koper, J. Lukkien, *J. Electroanal. Chem.* **485** (2000) 161
45. B. Braunschweig, W. Daum, *Langmuir* **25** (2009) 11112
46. A. Funtikov, U. Stimming, R. Vogel, *J. Electroanal. Chem.* **428** (1997) 147
47. M. Schneeweiss, D. Kolb, *Solid State Ionics* **94** (1997) 171
48. K. Sato, S. Yoshimoto, J. Inukai, K. Itaya, *Electrochem. Comm.* **8** (2006) 725
49. O. Magnussen, J. Hagebock, J. Hotlos, R. Behm, *Faraday Discuss.* **94** (1992) 329
50. F. Silva, A. Martins, *Electrochim. Acta* **44** (1998) 919
51. T. Kondo, J. Morita, K. Hanaoka, S. Takakusagi, K. Tamura, M. Takahashi, J. Mizuki, K. Uosaki, *J. Phys. Chem., C* **111** (2007) 13197
52. Z. Shi, J. Lipkowski, S. Mirwald, B. Pettinger, *J. Electroanal. Chem.* **396** (1995) 115
53. A. Cuesta, M. Kleinert, D. Kolb, *Phys. Chem. Chem. Phys.* **2** (2000) 5684
54. M. Holzle, V. Zwing, D. Kolb, *Electrochim. Acta* **40** (1995) 1237
55. C. Vitus, A. Davenport, *J. Electrochem. Soc.* **141** (1994) 1291
56. H. Hondo, S. Sugawara, K. Itaya, *Anal. Chem.* **62** (1990) 2424
57. A. Hamelin, *J. Electroanal. Chem.* **407** (1996) 1
58. D. van der Vliet C. Wang, M. Debe, R. Atanasoski, N. M. Markovic, V. R. Stamenkovic, *Electrochim. Acta* **56** (2011) 8695
59. M. K. Debe, A. R. Drube, *J. Vac. Sci. Technol., B* **13** (1995) 1236
60. M. K. Debe, R. J. Poirier, *J. Vac. Sci. Technol., A* **12** (1994) 2017
61. M. K. Debe, A. K. Schmoeckel, G. D. Vernstrom, R. Atanasoski, *J. Power Sources* **161** (2006) 1002
62. L. Gancs, T. Kobayashi, M. K. Debe, R. Atanasoski, A. Wieckowski, *Chem. Mater.* **20** (2008) 2444
63. M. K. Debe, *J. Electrochem Soc.* **160** (2013) F522.



J. Serb. Chem. Soc. 78 (11) 1703–1716 (2013)
JSCS–4528

Electrochemical oxidation of methanol on Pt/(Ru_xSn_{1-x})O₂ nanocatalyst

MILA N. KRSTAJIĆ^{1#}, MAJA D. OBRADOVIĆ^{2#}, BILJANA M. BABIĆ³,
VELIMIR R. RADMILOVIĆ¹, UROŠ Č. LAČNJEVAC⁴, NEDELJKO V. KRSTAJIĆ¹
and SNEŽANA Lj. GOJKOVIĆ^{1*#}

¹Faculty of Technology and Metallurgy, University of Belgrade, Karnegijeva 4, 11000 Belgrade, Serbia, ²Institute of Chemistry, Technology and Metallurgy, University of Belgrade, Njegoševa 12, 11000 Belgrade, Serbia, ³Vinča Institute of Nuclear Sciences, University of Belgrade, P. O. Box 522, 11001 Belgrade, Serbia and ⁴Institute for Multidisciplinary Research, University of Belgrade, Kneza Višeslava 1, 11030 Belgrade, Serbia

(Received 18 July, revised 4 September 2013)

Abstract: Ru-doped SnO₂ powder, (Ru_xSn_{1-x})O₂, with a Sn:Ru atomic ratio of 9:1 was synthesized and used as a support for Pt nanoparticles (30 mass % loading). The (Ru_xSn_{1-x})O₂ support and the Pt/(Ru_xSn_{1-x})O₂ catalyst were characterized by X-ray diffraction measurements, energy dispersive X-ray spectroscopy and transmission electron microscopy (TEM). The (Ru_xSn_{1-x})O₂ was found to be a two-phase material consisting of probably a solid solution of RuO₂ in SnO₂ and pure RuO₂. The average Pt particle size determined by TEM was 5.3 nm. Cyclic voltammetry of Pt/(Ru_xSn_{1-x})O₂ indicated good conductivity of the support and displayed the usual features of Pt. The results of the electrochemical oxidation of CO_{ads} and methanol on Pt/(Ru_xSn_{1-x})O₂ were compared with those on commercial Pt/C and PtRu/C catalysts. Oxidation of CO_{ads} on Pt/(Ru_xSn_{1-x})O₂ starts at lower positive potentials than on PtRu/C and Pt/C. Potentiodynamic polarization curves and chronoamperometric curves of methanol oxidation indicated higher initial activity of the Pt/(Ru_xSn_{1-x})O₂ catalyst compared to PtRu/C, but also a greater loss in current density over time. A potentiodynamic stability test of the catalysts revealed that deactivation of Pt/(Ru_xSn_{1-x})O₂ and Pt/C was primarily caused by poisoning of the Pt surface by residues of methanol oxidation, which mostly occurred during the first potential cycle. In the case of PtRu/C, the poisoning of the surface was minor and deactivation was caused by surface area loss of the PtRu.

Keywords: methanol oxidation, CO oxidation, platinum, Ru-doped SnO₂, electrocatalysis, fuel cell.

* Corresponding author. E-mail: sgojkovic@tmf.bg.ac.rs

Serbian Chemical Society member.

doi: 10.2298/JSC130718091K

INTRODUCTION

Anode and cathode catalysts currently used for polymer electrolyte membrane fuel cells (PEMFCs) are Pt or Pt-alloy nanoparticles supported on carbon blacks.¹ The role of the support for the catalysts is to provide a physical surface for a fine dispersion of catalyst particles, necessary to achieve a high surface area. To be efficient, the support also needs to have high surface area, preferably mesoporous structure, high electrical conductivity and high stability under fuel cell operating conditions.² The main drawback of carbon blacks, as well as other carbon materials (carbon fibers, carbon nanotubes, graphene), is their insufficient corrosion resistance.^{2,3} Although the problem of instability of the supporting material is more prominent for a cathode catalyst because of its higher potential and the presence of H₂O₂ as a by-product of oxygen reduction, an anode catalyst could also be exposed to much more oxidative conditions in the case of cell reversal caused by fuel starvation.⁴ Partial oxidation of the carbon induces the formation of oxygen-containing functional groups on the surface that weaken bonding with Pt nanoparticles, thus promoting surface diffusion of Pt nanoparticles and their agglomeration. If the carbon support is oxidized to CO or CO₂, Pt nanoparticles are detached from the surface.³ In both cases, the final result is a decrease in the electrochemically active surface area of Pt. This problem has initiated a lot of research in the last few years aimed at finding an appropriate replacement for carbon supports. Ceramic materials, such as metal oxides and carbides, distinguish themselves as promising candidates not only due to their high stability in a fuel cell environment, but also because of their possible interaction with the deposited metal particles, which could result in a promotion of the activity of the catalyst.^{2,5}

Metal oxides are electric insulators at the operating temperatures of PEMFCs. However, sub-stoichiometric oxides, oxides doped with a foreign metal and nanostructured oxides, especially those of titanium, tin and tungsten, are found to have acceptable conductivity for application as a support for electrocatalysts.² When using as an anode catalyst in a direct methanol or ethanol fuel cell (DMFC, DEFC), the metal-oxide support can also serve as a co-catalyst to Pt nanoparticles, providing them with oxygen-containing species at lower electrode potentials.

The state-of-the-art anode catalyst in DMFC is a Pt–Ru nanoalloy. It is accepted that the methanol oxidation reaction (MOR) commences earlier on Pt–Ru than on Pt due to the bi-functional mechanism,⁶ according to which oxophilic Ru sites readily adsorb oxygen-containing species, which react with carbonaceous species formed by methanol adsorption on the Pt sites. Pt–Sn alloys were also investigated for the MOR, but found to be inactive.⁷ Interestingly, good activity was observed for electrosorbed Sn on Pt.⁷ It was also reported that tin oxide promotes the MOR on Pt, as shown for Pt microparticles dispersed on SnO₂ thin

films⁸ and polycrystalline Pt partially covered by SnO₂ nanoparticles.⁹ SnO₂ doped by Sb was investigated as a support for Pt nanoparticles.¹⁰ It was concluded that Sb-doped SnO₂ promotes methanol and ethanol oxidation and stabilizes the Pt nanoparticles in the fuel cell.

In the present study, Pt nanoparticles supported on SnO₂ doped with RuO₂ were prepared. RuO₂ as a dopant should increase the electrical conductivity of SnO₂ and, together with SnO₂, provide oxygen-containing species necessary for efficient methanol oxidation on Pt. The supporting material, labeled as (Ru_xSn_{1-x})O₂, and the catalyst Pt/(Ru_xSn_{1-x})O₂ were characterized by the X-ray diffraction technique (XRD), transmission electron microscopy (TEM) and energy dispersive X-ray spectroscopy (EDS). The catalyst was tested for electrochemical oxidation of CO and methanol and its performance was compared to those of commercial Pt/C and PtRu/C catalysts.

EXPERIMENTAL

Synthesis of the support and the catalyst

The Ru_xSn_{1-x}O₂ supporting particles were prepared as follows.¹¹ A solution 5.3 g of SnCl₄·5H₂O, 0.98 g of RuCl₃·xH₂O (35–45 mass % Ru), 2.5 mL of HCl and 40 mL of high purity water (Millipore, 18 MΩ cm resistivity) was prepared and mixed to homogeneity. The mixture is added dropwise in 50 mL of a 34 % aqueous solution of hydrazine at room temperature. Then, the solution was refluxed for 10 days. Subsequently, the formed precipitate was repeatedly rinsed with water and centrifuged until the supernatant was free of Cl⁻. The resulting product was dried in air for 24 h at 120 °C and heated at 400 °C for 2 h.

The Pt nanoparticles were deposited on the Ru_xSn_{1-x}O₂ support by a modified borohydride reduction method.¹² Ru_xSn_{1-x}O₂ powder was dispersed in water in an ultrasonic bath. Then H₂PtCl₆ aqueous solution was added into dispersion under continuous stirring. The metal salt was reduced with excess of sodium borohydride. The precipitate was rinsed with water and dried at 80 °C.

Physicochemical characterization

Adsorption and desorption isotherms of N₂ were measured on Ru_xSn_{1-x}O₂ support at -196°C, using the gravimetric McBain method. The BET specific surface area, *S*_{BET}, and pore size distribution were calculated from the isotherms. Pore size distribution was estimated by applying the BJH method¹³ to the desorption branch of the isotherms.

Phase composition of the (Ru_xSn_{1-x})O₂ support was investigated by XRD technique. Siemens D-500 diffractometer was employed with CuK_α radiation of wavelength 0.154056 nm in conjunction with a CuK_β nickel filter.

Elemental analysis of the (Ru_xSn_{1-x})O₂ support and the Pt/Ru_xSn_{1-x}O₂ catalyst was performed by EDS analysis using a scanning electron microscope Tescan VEGA TS 5130MM coupled with an EDS system INCAPentaFET-x3, Oxford Instruments.

The Pt/(Ru_xSn_{1-x})O₂ catalyst was characterized for morphology, particle size distribution and chemical composition by TEM. The sample was sonicated in ethanol and a drop of the suspension was placed on copper grid (300 mesh) covered with a lacey carbon film and dried in air. A combination of high angle annular dark field scanning transmission electron microscopy (HAADF, STEM) and electron energy loss spectroscopy (EELS) was applied. HAADF was chosen because of its strong correlation between atomic number and image intensity,

making it very easy to distinguish between heavy elements, such as Pt, and light supports, such as $(\text{Ru}_x\text{Sn}_{1-x})\text{O}_2$ particles. The measurements were performed on TEAM0.5 transmission electron microscope with corrected aberration operated at 80 kV. EDS analysis was performed on TEM microscope CM200-FEG operating at 400 kV using an Oxford Instruments EDS system with INCA software. Crystallographic information from individual Pt particles was obtained by numerical Fourier filtering (FFT, fast Fourier transformation) of the digital image intensity spectra. All TEM characterization was realized at the National Center for Electron Microscopy, Lawrence Berkeley National Laboratory, Berkeley, CA.

Electrochemical characterization

For the electrochemical characterization, the $\text{Pt}/(\text{Ru}_x\text{Sn}_{1-x})\text{O}_2$ catalyst was applied on a glassy carbon (GC) substrate in the form of a thin-film.¹⁴ The GC electrode (Tacussel rotating disk electrode, 5 mm in diameter) was polished with Al_2O_3 slurry and washed ultrasonically with water before use. The ink was made by mixing of 4 mg of $\text{Pt}/(\text{Ru}_x\text{Sn}_{1-x})\text{O}_2$ powder with 1 cm^3 of high purity water and 50 μL of Nafion[®] solution (5 wt. %, 1100 E.W., Aldrich). After 1 h of agitation in an ultrasonic bath, 10 μL of the suspension was placed onto the GC electrode and left to dry overnight. This procedure of film preparation gave 60 μg of Pt per cm^2 of the GC surface.

Electrochemical characteristics of the $\text{Pt}/(\text{Ru}_x\text{Sn}_{1-x})\text{O}_2$ thin film were investigated by cyclic voltammetry in 0.10 M H_2SO_4 saturated with N_2 . After immersion into the electrolyte, the electrode was subjected to 15 potential cycles between 0.04 and 1.2 V at a scan rate of 100 mV s^{-1} . The oxidation of CO_{ads} was examined in the same electrolyte after adsorbing CO at 0.1 V for 30 min and replacing CO by a N_2 atmosphere.

The MOR was investigated in an electrolyte containing 0.5 M CH_3OH . Upon oxidation of CO_{ads} , the electrode potential was held at 0.1 V, methanol was added into the electrolyte and after 2 min a linear sweep at 50 mV s^{-1} (potentiodynamic polarization curve) or potential step at 0.5 V *vs.* RHE (chronoamperometric experiment) was applied.

As reference electrocatalysts, a sample of Pt nanoparticles supported on XC-72R carbon with a loading of 20 mass % of Pt (Pt/C) and a sample of PtRu nanoparticles supported on the same carbon with a loading of 20 mass % of PtRu (PtRu/C), both of them manufactured by E-Tek, were used. The average diameters of Pt and PtRu particles were 2.5¹⁵ and 2.7 nm,¹⁶ respectively. The metal loading on the electrode was 20 $\mu\text{g cm}^{-2}$ for both Pt/C and PtRu/C.

The electrochemically active surface area of Pt and PtRu were determined from the charge of the CO_{ads} oxidation as well as from the charge of the oxidation of underpotentially deposited Cu.¹⁷ Cu was deposited from a supporting electrolyte containing 2 mM CuSO_4 at a potential of 0.33 V.

A three-compartment electrochemical glass cell was used with a Pt wire as the counter electrode and a saturated calomel electrode as the reference electrode. All the potentials reported in the paper are expressed on the scale of the reversible hydrogen electrode (RHE). A Pine RDE4 potentiostat and Philips PM 8143 X-Y recorder were used. All the measurements were performed at 25 °C.

RESULTS AND DISCUSSION

Physicochemical characterization

Analysis of N_2 adsorption and desorption isotherms revealed that the $(\text{Ru}_x\text{Sn}_{1-x})\text{O}_2$ powder had a BET surface area of 141 $\text{m}^2 \text{g}^{-1}$ and mesoporous structure with pores radii mostly between 2 and 3 nm.

Both SnO₂ and RuO₂ crystallized in the tetragonal rutile structure with similar lattice constants (SnO₂: $a = 0.47382$ nm, $c = 0.31871$ nm; RuO₂: $a = 0.44994$ nm, $c = 0.31071$ nm). The ionic radii of Sn(IV) and Ru(IV) of 0.083 and 0.076 nm are similar enough to enable the formation of a substitutional solid solution, designated as (Ru_xSn_{1-x})O₂.¹⁸ The experimental XRD pattern for the (Ru_xSn_{1-x})O₂ support and the reference spectra of RuO₂ and SnO₂, taken from the corresponding JCPD cards, are shown in Fig. 1. The pattern for (Ru_xSn_{1-x})O₂ features overlapping peaks for SnO₂ and RuO₂. The 2θ peak positions and corresponding reflections for SnO₂ could be identified as 26.6° (110); 33.8° (101); 37.9° (200) 51.7° (211) and 64.7° (112) and for RuO₂ as 28.0° (110), 35.0° (101) and 54.2° (211). Such an XRD microstructure analysis suggests that (Ru_xSn_{1-x})O₂ consisted of two separate phases. Taking into account the possibility of the formation of a solid solution and greater amount of SnO₂, it could be suggested that the two phases detected by XRD were a solid solution of RuO₂ in SnO₂ and pure RuO₂.

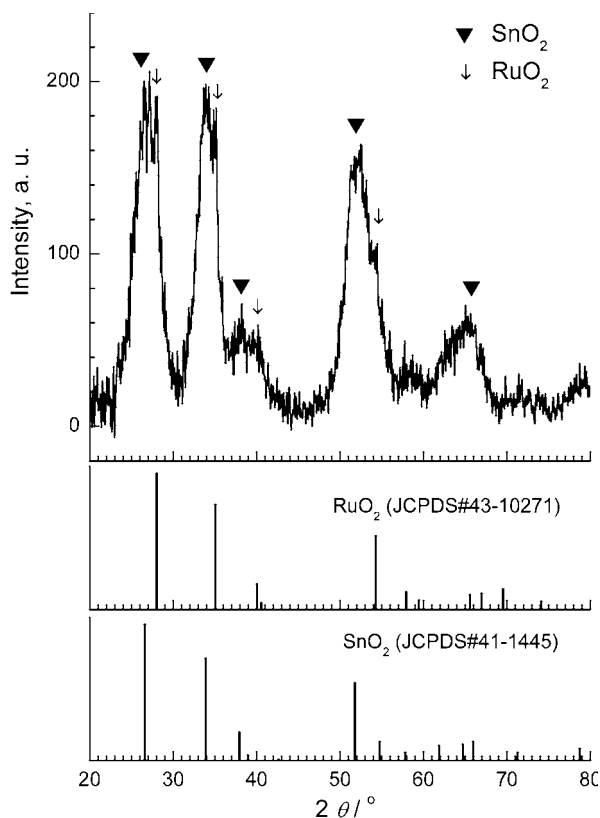


Fig. 1. XRD Pattern for the Pt/(Ru_xSn_{1-x})O₂ catalyst. The 2θ positions for bulk SnO₂ and RuO₂ are shown in the plot for reference.

EDS analysis revealed that the atomic ratio of Sn:Ru in the $(\text{Ru}_x\text{Sn}_{1-x})\text{O}_2$ powder as well as in $\text{Pt}/(\text{Ru}_x\text{Sn}_{1-x})\text{O}_2$ was 9:1. This shows that during the deposition of Pt nanoparticles on the $(\text{Ru}_x\text{Sn}_{1-x})\text{O}_2$ support, its composition remained unchanged. The Pt loading of $\text{Pt}/(\text{Ru}_x\text{Sn}_{1-x})\text{O}_2$ was found to be 30 mass %.

HAADF images of the Pt particles and the $(\text{Ru}_x\text{Sn}_{1-x})\text{O}_2$ particle clusters are presented in Fig. 2a. It can be seen that Pt was unevenly distributed in the form of separate particles and particle clusters. The histogram given in Fig. 2b indicates the log-normal distribution of Pt particle size with an average size of 5.3 nm. Pt particles were mostly located near $(\text{Ru}_x\text{Sn}_{1-x})\text{O}_2$ particle clusters, as presented in Fig. 2c and d, owing to the ability of SnO_2 to act as a nucleation agent. EELS analysis of the $(\text{Ru}_x\text{Sn}_{1-x})\text{O}_2$ clusters revealed the presence of elemental Sn besides SnO_2 . It could be assumed that Sn(IV) ions were partially reduced during Pt deposition by the borohydride reduction method.

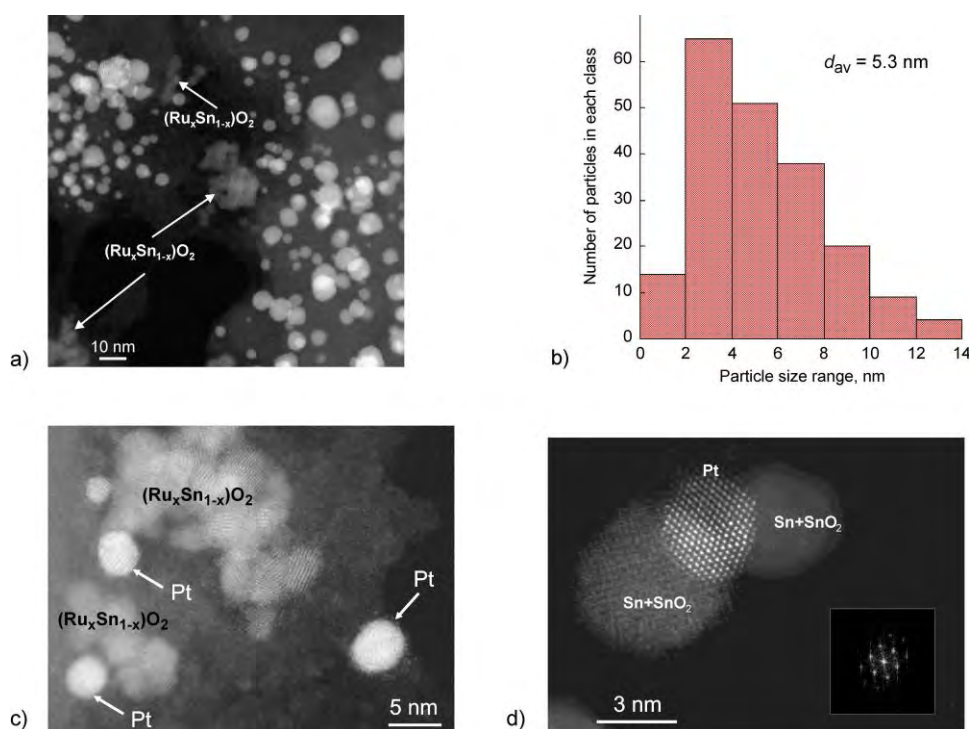


Fig. 2. TEM Images of the $\text{Pt}/(\text{Ru}_x\text{Sn}_{1-x})\text{O}_2$ catalyst: a) HAADF image of the Pt particles and $(\text{Ru}_x\text{Sn}_{1-x})\text{O}_2$ particle clusters, b) histogram of Pt particle size distribution, c) and d) close-up HAADF images of Pt particles close to $(\text{Ru}_x\text{Sn}_{1-x})\text{O}_2$ particle clusters.

Cyclic voltammetry and CO_{ads} oxidation

The voltammograms of CO_{ads} stripping recorded on $\text{Pt}/(\text{Ru}_x\text{Sn}_{1-x})\text{O}_2$, PtRu/C and Pt/C , as well as the first cyclic voltammograms after CO_{ads} stripping, are

shown in Fig. 3. The voltammograms after stripping of the CO_{ads} showed complete oxidation of the CO_{ads} and displayed the surface characteristics of the electrodes. The CO_{ads} stripping charge was used for the determination of the electrochemically active surface area (EASA) of Pt (in the case of Pt/(Ru_xSn_{1-x})O₂ and Pt/C) and PtRu (in the case of PtRu/C); hence, the current densities in Fig. 3 were normalized with respect to the EASA. It should be noted that the EASA values determined by the oxidation of underpotentially deposited monolayer of Cu (not shown) were the same, within experimental error, as those determined by oxidation of CO_{ads}.

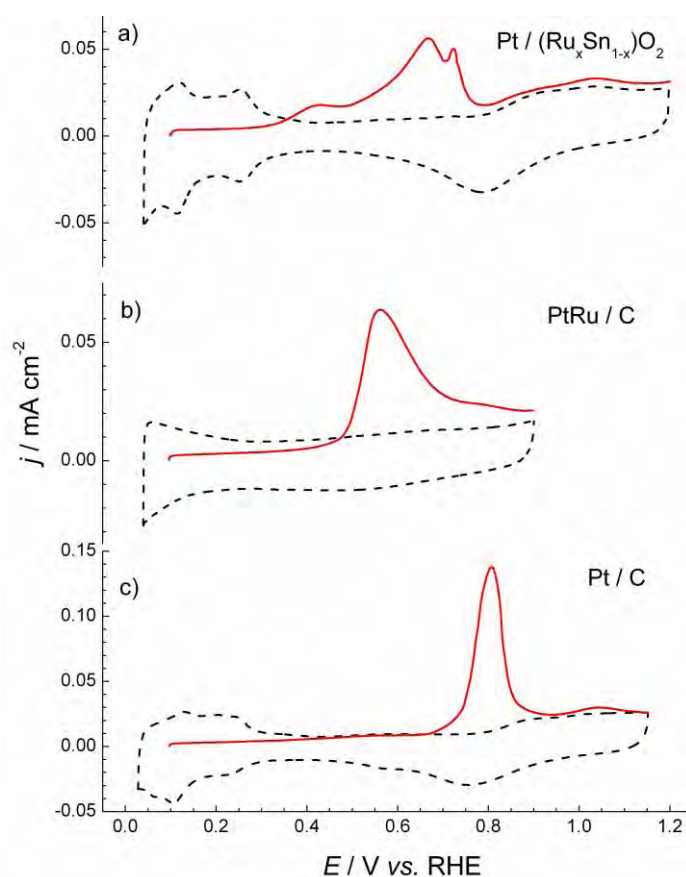


Fig. 3. Cyclic voltammograms of a) Pt/(Ru_xSn_{1-x})O₂, b) PtRu/C and c) Pt/C catalysts (dashed lines) and the corresponding stripping voltammograms of CO_{ads} (solid lines) recorded in 0.10 M H₂SO₄ at a scan rate of 20 mV s⁻¹.

The cyclic voltammogram of Pt/(Ru_xSn_{1-x})O₂ given in Fig. 3a shows well defined peaks for hydrogen adsorption/desorption and Pt-oxide formation/reduction that are characteristics of clean polycrystalline Pt. The high currents in the

so-called double-layer region of Pt can be mainly ascribed to the pseudo-capacitive behavior of the $(\text{Ru}_x\text{Sn}_{1-x})\text{O}_2$ support. The voltammogram is well centered and without inclination, demonstrating good conductivity of the $(\text{Ru}_x\text{Sn}_{1-x})\text{O}_2$ support.

Fig. 3a shows that CO_{ads} oxidation on $\text{Pt}/(\text{Ru}_x\text{Sn}_{1-x})\text{O}_2$ occurred from 0.35 to 0.8 V. At low potentials, an anodic wave with a maximum at 0.43 V was observed. The main peak is a superposition of two peaks with maxima positioned at 0.70 and 0.72 V. Contrary to $\text{Pt}/(\text{Ru}_x\text{Sn}_{1-x})\text{O}_2$, the voltammograms of the oxidation of CO_{ads} on PtRu/C (Fig. 3b) and Pt/C (Fig. 3c) showed single peaks. This suggested that the complex structure of the CO_{ads} oxidation voltammogram on $\text{Pt}/(\text{Ru}_x\text{Sn}_{1-x})\text{O}_2$ was related to the presence of SnO_2 . Indeed, a profile of CO_{ads} stripping with three peaks at almost the same potentials as those for $\text{Pt}/(\text{Ru}_x\text{Sn}_{1-x})\text{O}_2$ was reported recently for $\text{Pt}_3\text{Sn}/\text{C}$ catalyst containing Sn in the form of SnO_2 .¹⁹ On Pt_3Sn bulk alloy, it was also found that the CO_{ads} stripping begins at 0.25 V, but most of the CO_{ads} is oxidized in the second anodic wave starting at 0.68 V with the peak at about 0.75 V.²⁰ The authors assumed that a unique state of CO_{ads} existed on the Pt_3Sn surface, which is only formed at high coverage with an adsorption energy lower than that for pure Pt. Therefore, the first anodic wave in Fig. 3a could be ascribed to the oxidation of weakly bound CO_{ads} on the Pt sites directly contacting SnO_x , while the main peak corresponds to the oxidation of strongly bound CO_{ads} . The splitting of this peak might reflect CO_{ads} oxidation on Pt sites directly contacting SnO_x and the reaction on Pt sites completely surrounded by other Pt atoms. Comparing the CO_{ads} oxidation on $\text{Pt}/(\text{Ru}_x\text{Sn}_{1-x})\text{O}_2$ to that on PtRu/C and Pt/C , the lowest onset potential on $\text{Pt}/(\text{Ru}_x\text{Sn}_{1-x})\text{O}_2$ suggests that this catalyst should exhibit high CO tolerance.

Methanol oxidation

The activity of the catalysts for the MOR was first tested under potentiodynamic conditions. The polarization curves recorded in the positive going sweeps over 250 potential cycles are displayed in Fig. 4. The voltammograms recorded in the supporting electrolyte are also displayed. The $\text{Pt}/(\text{Ru}_x\text{Sn}_{1-x})\text{O}_2$ catalyst features remarkably high current densities in the first potential cycle compared to Pt/C and especially to PtRu/C . Hydrogen desorption peaks were not attenuated, indicating that the electrocatalysts were not poisoned by the product of the dissociative adsorption of methanol during a 2-min potential hold at 0.1 V. However, already in the second cycle, the onset potential of the MOR on $\text{Pt}/(\text{Ru}_x\text{Sn}_{1-x})\text{O}_2$ and Pt/C had shifted positively, probably as a consequence of poisoning of the Pt surface, which was evidenced by suppression of the hydrogen desorption peaks. Although the maximum current density on $\text{Pt}/(\text{Ru}_x\text{Sn}_{1-x})\text{O}_2$ did not change with potential cycling, the activity at low potentials relevant for the operation of the anode in PEMFC was reduced. On the other hand, the activity of PtRu/C in the

first cycle was much lower than the activity of Pt/(Ru_xSn_{1-x})O₂ and Pt/C, but without significant loss of activity over the applied 250 potential cycles.

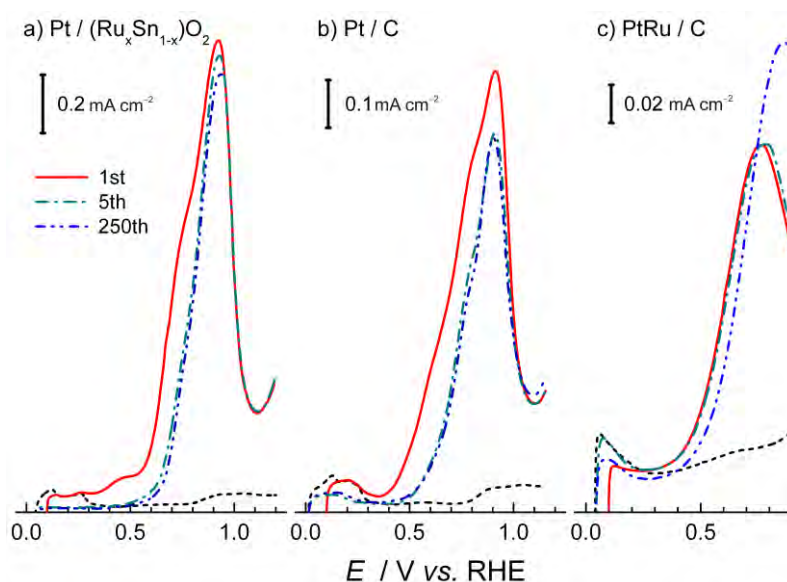


Fig. 4. Potentiodynamic polarization curves for the MOR recorded on a) Pt/(Ru_xSn_{1-x})O₂, b) Pt/C and c) PtRu/C in 0.1 M H₂SO₄ containing 0.5 M CH₃OH at a rate of 50 mV s⁻¹ over 250 potential cycles. Anodic parts of the cyclic voltammograms recorded in 0.1 M H₂SO₄ before the addition of CH₃OH are also presented (dash line).

High activity of Pt/(Ru_xSn_{1-x})O₂ in the first cycle as well as the lower onset potential of CO_{ads} oxidation on this catalyst (Fig. 3a) compared to Pt/C and PtRu/C could be ascribed to SnO_x and its donation of oxygen-containing species. A recent investigation of CO and methanol oxidation on Pt partially covered by SnO₂ nanoparticles^{9,21} showed that the lattice oxygen from Sn(II)O rather than Sn(IV)O is active in the oxidation of CO and methanol. This could suggest an explanation for the sharp drop in the activity for the MOR after the first cycle. Namely, during the 2 min potential hold at 0.1 V prior to the potential cycling experiment, the Sn(IV) ions in (Ru_xSn_{1-x})O₂ could be partially reduced to Sn(II) ions. If the partial reduction of Sn(IV) ions is a slow process, there is not enough time to form Sn(II) ions in the following continuous cycles.

The chronoamperometric test of Pt/(Ru_xSn_{1-x})O₂ and PtRu/C was performed at 0.50 V for 25 min. Similar to the findings of the potentiodynamic experiments, the chronoamperometric results (Fig. 5) confirmed the higher activity of the PtRu catalyst, but the difference in the activity between Pt/(Ru_xSn_{1-x})O₂ and PtRu/C slightly decreased during the experiment.

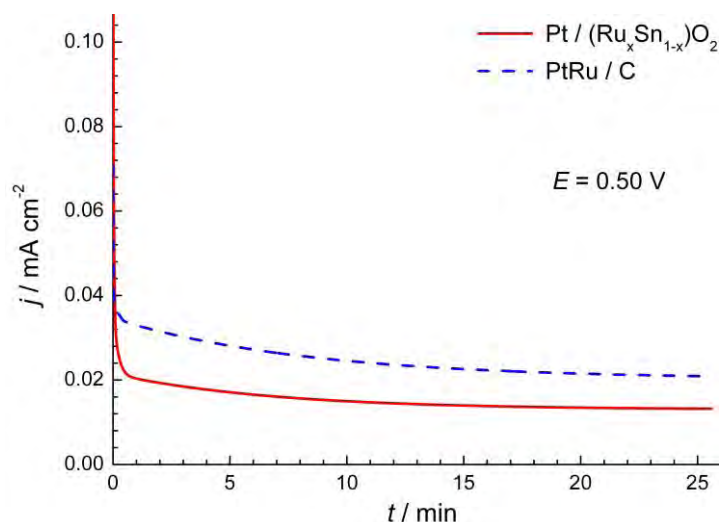


Fig. 5. Chronoamperometric curves of the MOR recorded on Pt/(Ru_xSn_{1-x})O₂ and PtRu/C catalysts in 0.1 M H₂SO₄ containing 0.5 M CH₃OH at a constant potential 0.50 V.

Stability of the catalysts

The activity of the catalysts for the MOR could deteriorate over time because of a gradual poisoning of the Pt surface by the methanol oxidation residues and/or because of a loss of the electrochemically active surface area. In order to resolve which effect was predominant, all three catalysts were subjected to potential cycling in the supporting electrolyte containing no methanol. At the beginning and at the end of the experiment, the procedure for CO adsorption was employed in order to determine the EASA. Additionally, for the Pt/(Ru_xSn_{1-x})O₂ catalyst, the EASA was continuously monitored by the changes in the hydrogen adsorption/desorption peaks. The changes in the Pt/(Ru_xSn_{1-x})O₂ cyclic voltammograms over 250 cycles are presented in Fig. 6. The currents in the hydrogen adsorption/desorption region as well as in the Pt-oxide formation/reduction region gradually decreased, revealing a loss of EASA. Degradation of Pt under the potentiodynamic conditions could be explained by two mechanisms; surface diffusion of low-coordinated Pt atoms²² and electrochemical dissolution of Pt,^{23–25} either as the direct electro-oxidation of Pt to soluble Pt²⁺ (mostly for particles smaller than 4 nm) or as dissolution from the oxide (larger particles).

It should be stressed that the voltammetric currents in the double-layer region, ascribed to pseudo-capacitive currents of the (Ru_xSn_{1-x})O₂ support (Fig. 6), do not change during potential cycling. Moreover, the characteristic shape of the voltammogram of CO_{ads} oxidation (Fig. 3a), which was related to the presence of SnO_x in the catalyst, was maintained over the potential cycling. The same shape of the CO_{ads} stripping curve before and after the stability test under the poten-

tiodynamic conditions was also reported for Pt₃Sn/C catalyst with Sn in a form SnO₂.¹⁹ These results indicate that (Ru_xSn_{1-x})O₂ is a stable material and suitable for use as a catalyst support.

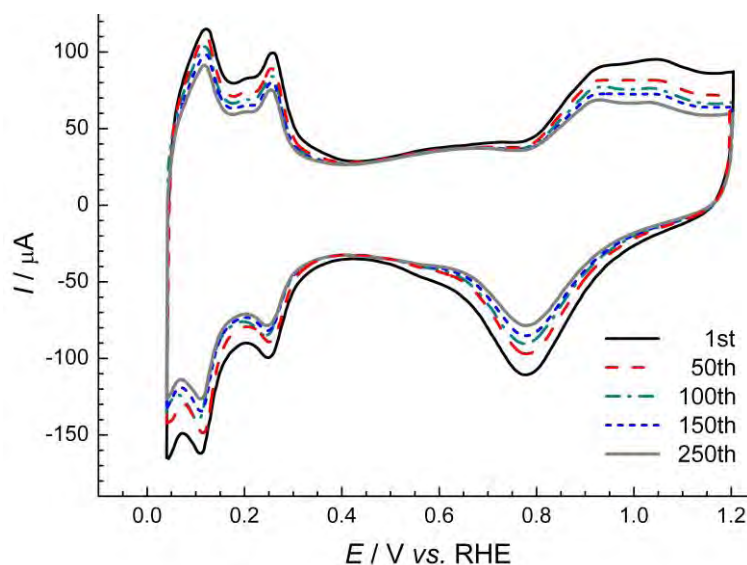


Fig. 6. Cyclic voltammograms of the Pt/(Ru_xSn_{1-x})O₂ catalyst recorded in 0.1 M H₂SO₄ at a scan rate of 50 mV s⁻¹ over 250 cycles.

The EASA and the methanol oxidation current density for the Pt/(Ru_xSn_{1-x})O₂ catalyst collected over 250 potential cycles are shown in Fig. 7. The EASA data were determined from the hydrogen adsorption/desorption charge in all the cycles and from the CO_{ads} oxidation at the beginning and the end of the experiment. The values obtained by these two methods correspond to each other within experimental error. The current densities for the MOR were taken from the potentiodynamic curves in Fig. 4 at a constant potential of 0.50 V. They were calculated using the EASA at the beginning of the experiment. Both the EASA and the methanol oxidation current densities given in Fig. 7 were normalized with respect to their initial values. The results showed that 80 % of the initial activity for the MOR was lost while the EASA decreased by 32 %.

The results of the EASA and the MOR activity loss determined on all three catalysts are summarized in Table I. It is clear that the deactivation of the Pt/(Ru_xSn_{1-x})O₂ and Pt/C catalysts was primarily caused by the poisoning of the Pt surface by the methanol oxidation residues, mostly occurring during the first potential cycle (Fig. 4). Contrary to these two catalysts, for PtRu/C the loss of EASA and MOR activity were quite similar, indicating that poisoning of the PtRu nanoparticles was minor. Therefore, it seems that mixing of Pt and Ru at

the atomic level in necessary to achieve high and long-term resistance to poisoning by CO_{ads} .

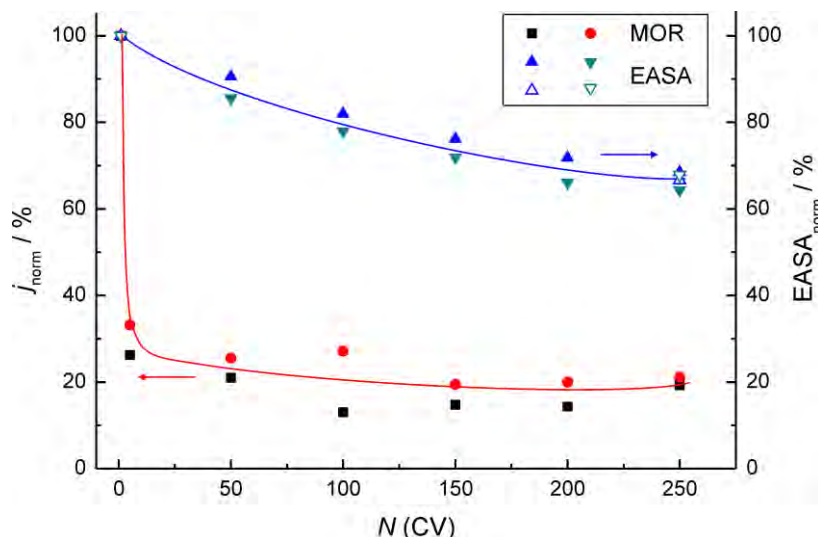


Fig. 7. The current densities for the MOR taken at 0.5 V and the EASA values during the potential cycling of $\text{Pt}/(\text{Ru}_x\text{Sn}_{1-x})\text{O}_2$ in 0.1 M H_2SO_4 with and without 0.5 M CH_3OH . Both types of data are normalized to their initial values. EASA values were calculated from hydrogen desorption charge (bold symbols) and from CO_{ads} oxidation (open symbols). The results of two independent experiments are shown.

TABLE 1. Decrease in the activity for the MOR and the EASA values of the three investigated catalysts, determined during 250 potential cycles in 0.1 M H_2SO_4 solution with and without the addition of 0.5 M CH_3OH

Catalyst	MOR Activity loss, %	EASA Loss, %
$\text{Pt}/(\text{Ru}_x\text{Sn}_{1-x})\text{O}_2$	80	32
Pt/C	70	18
PtRu/C	30	24

Prospects for the $\text{Pt}/(\text{Ru}_x\text{Sn}_{1-x})\text{O}_2$ catalyst

The study of $\text{Pt}/(\text{Ru}_x\text{Sn}_{1-x})\text{O}_2$ catalyst demonstrated that $(\text{Ru}_x\text{Sn}_{1-x})\text{O}_2$ is stable within the potential range that might be encountered during the operation of a DMFC. This characteristic, as well as good conductivity, makes this oxide material suitable for application as a catalyst support.

The action of $(\text{Ru}_x\text{Sn}_{1-x})\text{O}_2$ as co-catalyst is excellent in short time after running the MOR. However, very soon $\text{Pt}/(\text{Ru}_x\text{Sn}_{1-x})\text{O}_2$ loses its high initial activity and the current densities for the MOR drop to 60 % of those attained on the commercial PtRu/C catalyst. Since the experiments show that $(\text{Ru}_x\text{Sn}_{1-x})\text{O}_2$ cannot be an active co-catalyst to Pt over long-term operation, in further impro-

vement of the MOR catalyst without high area carbon as the support, PtRu nanoparticles could be deposited on a (Ru_xSn_{1-x})O₂ support.

Acknowledgement. This work was financially supported by the Ministry of Education, Science and Technological Development of the Republic of Serbia, Contract No. ON-172054.

ИЗВОД

ЕЛЕКТРОХЕМИЈСКА ОКСИДАЦИЈА МЕТАНОЛА НА КАТАЛИЗАТОРУ Pt/(Ru_xSn_{1-x})O₂

МИЛА Н. КРСТАЈИЋ¹, МАЈА Д. ОБРАДОВИЋ², БИЉАНА М. БАБИЋ³, ВЕЛИМИР Р. РАДМИЛОВИЋ¹,
УРОШ Ч. ЛАЧЊЕВАЦ⁴, НЕДЕЉКО В. КРСТАЈИЋ¹ и СНЕЖАНА Љ. ГОЈКОВИЋ¹

¹Технолошко–металуршки факултет, Универзитет у Београду, Карнегијева 4, 11000 Београд,

²Институт за хемију, технологију и металургију, Универзитет у Београду, Његошева 12, Београд,

³Институт за нуклеарне науке „Винча“, Универзитет у Београду, п. пр. 522, Београд и ⁴Институт за мултидисциплинарна истраживања, Универзитет у Београду, Кнеза Вишеслава 1, Београд

Синтетизован је прах SnO₂ допован рутенијумом, (Ru_xSn_{1-x})O₂, са атомским односом Sn:Ru од 9:1, и коришћен као носач наночестица платине. Удео Pt у добијеном катализатору, Pt/(Ru_xSn_{1-x})O₂, био је 30 мас. %. Носач и катализатор су карактерисани дифракцијом X-зрака, енергетски дисперзивном спектроскопијом X-зрака и трансмисионом електронском микроскопијом (ТЕМ). Показано је да је (Ru_xSn_{1-x})O₂ двофазни материјал који вероватно садржи чврст раствор RuO₂ у SnO₂ и чист RuO₂. Просечна величина зрна Pt, одређена ТЕМ анализом, износи 5,3 nm. Циклична волтаметрија Pt/(Ru_xSn_{1-x})O₂ указала је на добру проводност носача катализатора и на уобичајене карактеристике Pt. Упоредени су резултати електрохемијске оксидације CO_{ads} на Pt/(Ru_xSn_{1-x})O₂, Pt/C и PtRu/C. Оксидација CO_{ads} на Pt/(Ru_xSn_{1-x})O₂ почиње на негативнијим потенцијалима у односу на PtRu/C и Pt/C. Потенциодинамичке поларизационе криве и хроноамперометријске криве за оксидацију метанола указују на већу почетну активност катализатора Pt/(Ru_xSn_{1-x})O₂ у односу на PtRu/C, али и на веће смањење густине струје током времена. Тест потенциодинамичке стабилности катализатора је указао да је смањење активности Pt/(Ru_xSn_{1-x})O₂ и Pt/C првенствено проузроковано тровањем површине Pt производима непотпуне оксидације метанола, које се углавном одиграва током првог циклуса. Код PtRu/C тровање површине је минимално, а смањење активности је проузроковано смањењем електрохемијски активне површине PtRu.

(Примљено 18. јула, ревидирано 4 септембра 2013)

REFERENCES

1. E. Antolini, *Appl. Catal.*, **B 88** (2009) 1
2. E. Antolini, E. R. Gonzales, *Solid State Ionics* **180** (2009) 746
3. J. Wang, G. Yin, Y. Shao, S. Zhang, Z. Wang, Y. Gao, *J. Power Sources* **171** (2007) 331
4. A. Taniguchi, T. Akita, K. Yasuda, Y. Miyazaki, *J. Power Sources* **130** (2004) 42
5. G. R. Dieckmann, S. H. Langer, *Electrochim. Acta* **44** (1998) 437
6. S. Wasmus, A. Küver, *J. Electroanal. Chem.* **461** (1999) 14
7. K. Wang, H. A. Gasteiger, N. M. Markovic, P. N. Ross Jr., *Electrochim. Acta* **41** (1996) 2587
8. A. L. Santos, D. Profeti, P. Olivi, *Electrochim. Acta* **50** (2005) 2615
9. W.-P. Zhou, W. An, D. Su, R. Palomino, P. Liu, M. G. White, R. R. Adzic, *J. Phys. Chem. Lett.* **3** (2012) 3286

10. K.-S. Lee, I.-S. Park, Y.-H. Cho, D.-S. Jung, H.-Y. Park, Y.-E. Sung, *J. Catal.* **258** (2008) 143
11. A. Hagemeyer, Z. Hogan, M. Schlichter, B. Smaka, G. Streukens, H. Turner, A. Volpe Jr., H. Weinberg, K. Yaccato, *Appl. Catal., A* **317** (2007) 139
12. K. W. Park, K. S. Seul, *Electrochem. Commun.* **9** (2007) 2256
13. E. P. Barret, L. G. Joyner, P. P. Halenda, *J. Am. Chem. Soc.* **73** (1951) 373
14. T. J. Schmidt, H. A. Gasteiger, R. J. Behm, *Electrochem. Commun.* **1** (1999) 1
15. I. Esparbé, E. Brillas, F. Centellas, J. A. Garrido, R. M. Rodríguez, C. Arias, P.-L. Cabot, *J. Power Sources* **190** (2009) 201
16. S. Lj. Gojković, T. R. Vidaković, D. R. Đurović, *Electrochim. Acta* **48** (2003) 3607
17. C. L. Green, A. Kucernak, *J. Phys. Chem., B* **106** (2002) 1036
18. X. Wang, F. Deng, Z. Tang, B. Wu, D. Tang, W. Linz, *Phys. Chem. Chem. Phys.* **15** (2013) 3977
19. E. Lee, A. Murthy, A. Manthiram, *J. Electroanal. Chem.* **659** (2011) 168
20. K. Wang, H. A. Gasteiger, N. M. Markovic, P. N. Ross, *Electrochim. Acta* **41** (1996) 2587
21. S. Axnanda, W.-P. Zhou, M. G. White, *Phys. Chem. Chem. Phys.* **14** (2012) 10207
22. Q. Xu, E. Kreidler, D. O. Wipf, T. He, *J. Electrochem. Soc.* **155** (2008) B228
23. L. Tang, B. Han, K. Persson, C. Friesen, T. He, K. Sieradzki, G. Ceder, *J. Am. Chem. Soc.* **132** (2010) 596
24. L. Tang, X. Li, R. C. Cammarata, C. Friesen, K. Sieradzki, *J. Am. Chem. Soc.* **132** (2010) 11722
25. A. A. Topalov, I. Katsounaros, M. Auinger, S. Cherevko, J. C. Meier, S. O. Klemm, K. J. J. Mayerhofer, *Angew. Chem Int. Ed.* **51** (2012) 12613.



J. Serb. Chem. Soc. 78 (11) 1717–1727 (2013)
JSCS–4529

Nanostructured materials for sensing Pb(II) and Cd(II) ions: manganese oxyhydroxide *versus* carbonized polyanilines

BILJANA ŠLJUKIĆ*, DARKO MICIĆ, NIKOLA CVJETIĆANIN,
GORDANA ČIRIĆ-MARJANOVIĆ#

*Faculty of Physical Chemistry, University of Belgrade, Studentski trg 12–16,
11158 Belgrade, Serbia*

(Received 31 July, revised 29 September 2013)

Abstract: Nanostructured materials including three different carbonized polyanilines and manganese oxyhydroxide were prepared and evaluated as electrode materials for sensing of lead and cadmium ions in aqueous media. Anodic stripping voltammetry results indicated that all prepared materials could be successfully used for determination of these two heavy metal ions. Carbonized polyaniline-based electrodes have higher signal and lower limits of detection (10^{-7} M) compared to manganese oxyhydroxide-based electrode. Among the three studied carbonized polyanilines, the one that was derived from polyaniline precursor produced in the presence of 3,5-dinitrosalicylic acid showed the highest electrocatalytic activity towards the lead and cadmium oxidation.

Keywords: lead ions; cadmium ions; carbonized nanostructured polyaniline; manganese oxyhydroxide; electrochemical sensors.

INTRODUCTION

Sensing of heavy metal ions in aqueous media, with lead (Pb^{2+}) and cadmium (Cd^{2+}) ions being the major metal pollutants, is one of the priority tasks in environmental monitoring. Lead has been introduced into the environment during automotive leaded fuel burning, as well as during lead mining, smelting and refining processes. Lead–acid batteries, paints and tin can solders represent further sources of lead in the environment, while nickel–cadmium batteries, cadmium pigmented plastics, ceramics, glasses, paints and enamels are major sources of cadmium.¹ Their consequent accumulation in the environment poses a serious risk to human health and safety.² Heavy metal ions are known to be non-biodegradable; for instance, lead in bone has a half-life of more than 20 years, while cadmium has a biological life of 10 to 30 years.³ The level of heavy metals

* Corresponding author: E-mail: biljka@ffh.bg.ac.rs

Serbian Chemical Society member.

doi: 10.2298/JSC130731101S

toxicity mostly depends on their chemical forms and exposure levels.⁴ Lead poisoning was reported to be one of the most common environmental child health threats that can cause serious physical and mental problems, including brain and kidney damage, mental retardation, behavior problems and development delays.⁵

It has been estimated that nearly 20 % of human exposure to lead occurs through the consumption of contaminated drinking water.⁶ Therefore, the monitoring of these heavy metal ions in water resources is essential. Current methods for sensing of Pb^{2+} and Cd^{2+} include atomic absorption spectrometry (AAS), inductively coupled plasma-atomic emission spectrometry (ICP-AES), inductively coupled plasma-mass spectrometry (ICP-MS) and X-ray fluorescence spectrophotometry.⁷⁻⁹ Although these methods show satisfactory sensitivity, they have the drawbacks of using expensive equipment in controlled laboratory conditions and requiring sample preparation and relatively large sample volumes.

On the other hand, electroanalytical methods offer not only high sensitivity but also intrinsic miniaturization and portability along with low cost.¹⁰⁻¹³ Stripping voltammetry techniques employing a mercury (Hg) electrode were found to allow the detection of trace heavy metals.¹⁴⁻¹⁶ However, the high toxicity of Hg has initiated the search for novel electrode materials for the sensing of heavy metal ions and different materials such as bismuth (Bi),¹⁷⁻¹⁹ gold (Au),²⁰ silver (Ag),²⁰ antimony (Sb),²¹ carbon (C),^{22,23} and boron-doped diamond (BDD)^{24,25} have been investigated.

Herein, the sensing of Pb^{2+} and Cd^{2+} has been explored employing four different electrode materials. The electrodes chosen for the study were glassy carbon electrode (GCE) modified with manganese oxyhydroxide (MnOOH) and GCE modified with three different carbonized nanostructured polyanilines (c-PANIs). The interest in studying a manganese oxide-based electrode arose from studies reporting the successful employment of carbon-supported manganese oxide electrodes for electroanalysis of different analytes, such as hydrogen peroxide, nitrite ions and ascorbic acid.²⁶⁻²⁹ Manganese oxides are economic, non-toxic and abundant.³⁰⁻³² They are present in a wide range of various crystal structures and their composition rarely corresponds to the stoichiometric formula but rather contains Mn in different oxidation states. The MnOOH studied herein has found application in rechargeable batteries, but it still has not been broadly investigated for application in electroanalysis. During a recent study of the sensing of the two named ions on composites of MnO_2 with different carbon materials, it was indicated that c-PANI (produced by the carbonization of PANI doped with 5-sulfosalicylic acid) showed activity for their sensing.³³ PANI in general has attracted significant attention during the last three decades due to its simple and inexpensive synthesis, acid-doping/base-dedoping chemistry, high stability and conductivity.³⁴ Carbonization of polyaniline and other N-containing aromatic polymers appeared during recent years as an efficient and simple way to produce new

N-containing (nano)materials with mainly preserved morphology of the polymer precursor and changed/improved physico-chemical properties, such as increased conductivity, specific surface area or pore volume, desirable for a variety of applications.^{34–40} It was shown that nanostructured c-PANIs exhibit excellent electrocatalytic properties toward oxygen reduction³⁹ and also represent promising materials for electrochemical capacitors.³⁷ The properties of c-PANI materials can be tuned by the protonation level, oxidation state, type of counter ions and morphology of PANI precursors.^{35–38}

The idea behind this study was to gather analytical information about the oxidation of Pb^{2+} and Cd^{2+} at MnOOH and different c-PANI electrodes, such as limit of detection (*LOD*), linear range response and reproducibility, and to compare their performances.

EXPERIMENTAL

Carbonized nanostructured PANIs were prepared by the procedures reported in previous works.^{35–38} PANI precursor salts were made by the gram-scale template-free oxidative polymerization of aniline with ammonium peroxydisulfate as an oxidant in three different media: a) in water (PANI),^{35,37} b) in 5-sulfosalicylic acid (SSA) aqueous solution (PANI–SSA)^{36,37} and c) in 3,5-dinitrosalicylic acid (DNSA) aqueous solution (PANI–DNSA).^{37,38} Subsequently, the precursors were carbonized by gradual heating in a nitrogen atmosphere up to 800 °C at a heating rate of 10 °C min⁻¹ to obtain c-PANI,^{35,37} c-PANI–SSA^{36,37} and c-PANI–DNSA,^{36,38} respectively. Detail characterization of the prepared materials was previously carried out using several physico-chemical techniques, including X-ray diffraction (XRD) analysis, scanning (SEM) and transmission (TEM) electron microscopy, Raman and Fourier transform infra-red spectroscopy.^{37,39}

Synthesis of MnOOH nanorods was done by oxidizing the saturated manganese sulphate aqueous solution by adding drop by drop of 10% hydrogen peroxide solution until the end of precipitation.

Catalytic ink was prepared by adding 4 mg of one of the investigated materials (c-PANI, c-PANI–SSA, c-PANI–DNSA or MnOOH) into 1 mL of a 2:3 water–ethanol mixture, followed by homogenization in an ultrasonic bath for 30 min. The working electrodes were prepared by pipetting 10 μl of a catalytic ink onto polished glassy carbon tip (5 mm diameter) and leaving the solvents to evaporate at room temperature.

Platinum (Pt) foil and saturated calomel electrode (SCE) served as the counter and reference electrode, respectively. All potentials in the paper are expressed *vs.* SCE. All electrochemical measurements were performed using Gamry PCI4/750 potentiostat, employing a cell of 15 cm³ volume. The supporting electrolyte was 20 mM H_2SO_4 + 30 mM KCl and all studies were performed at room temperature, without removal of oxygen from the supporting electrolyte.

Electroanalytical sensing of Pb^{2+} and Cd^{2+} was carried out using anodic stripping voltammetry. The electrode was kept at a potential of –1.3 V during the 120 s deposition step, with the electrolyte solution being stirred. Subsequently, the potential was swept in the anodic direction up to +0.6 V with no solution stirring. The same measurement was performed for a series of aqueous solutions of Pb^{2+} and Cd^{2+} with concentrations ranging from 5 to 100 μM .

RESULTS AND DISCUSSION

Pb²⁺ and Cd²⁺ sensing using the MnOOH-based electrode

Sensing of Pb²⁺ and Cd²⁺ employing MnOOH/GCE electrode was first studied. Linear scan voltammograms (LSVs) were initially separately recorded in 100 μM Pb²⁺ solution and 100 μM Cd²⁺ solution in the range from -1.3 to 0.6 V at a scan rate of 50 mV s⁻¹ (Fig. 1A). On each of the two LSVs, a clear peak originating from the oxidation of the corresponding heavy metal could be seen, *i.e.* a peak at *ca.* -0.46 V for Pb oxidation and a peak at *ca.* -0.69 V for Cd oxidation (Fig. 1A). Furthermore, it could be noticed that the Cd oxidation peak current (*I_p*) was *ca.* 33 % higher than that arising from Pb oxidation. No peak was observed in the LSV recorded on MnOOH/GCE in the absence of the studied heavy metal ions.

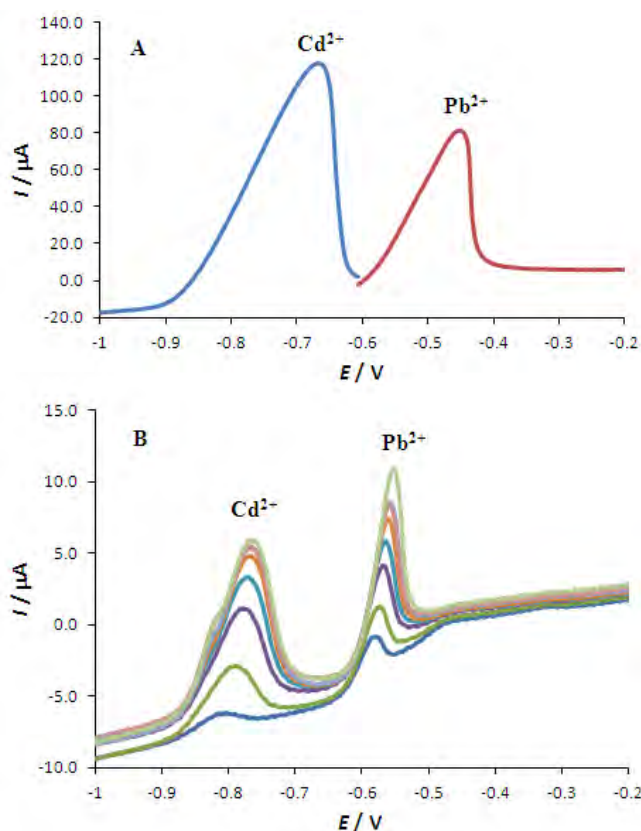


Fig. 1. A – LSVs of MnOOH/GCE recorded in 100 μM Pb²⁺ and Cd²⁺ solution in 20 mM H₂SO₄ + 30 mM KCl supporting electrolyte at a scan rate of 50 mV s⁻¹; B – increase in the peak currents of Pb and Cd oxidation with increasing concentration of heavy metal ions (between 5 and 40 μM). *E* in V vs. SCE.

Subsequently, the LSV was recorded on MnOOH/GCE in a solution containing both Pb^{2+} and Cd^{2+} in order to examine the possibility of the simultaneous detection of the two heavy metal ions and two distinct peaks could still be observed (Fig. 1B). The appearance of oxidation peaks of Pb and Cd at potentials that are *ca.* 0.25 V apart offers the possibility for the simultaneous detection of the two heavy metal ions with no mutual interference at MnOOH/GCE. Furthermore, good reproducibility of the signal was observed with the standard deviation of 6.8 % calculated for repeated measurements using a sample of constant concentration of 100 μM Pb^{2+} and Cd^{2+} ($n = 20$).

Next, the linear range and limits of detection of Pb^{2+} and Cd^{2+} sensing using the MnOOH-based electrode were determined. For these purposes, the blank solution was spiked with 5 μM additions of the two heavy metal ions and the recorded peak currents were observed to increase linearly with heavy metal ions concentration (*c*). The linear ranges were found to be limited up to 50 μM concentrations of the ions, which was reduced compared to linear ranges obtained when only one of the two studied heavy metal ions was present in the solution. The *LOD* values were calculated using 3σ method:

$$LOD = 3\sigma/b \quad (1)$$

where σ is the standard deviation of the regression line and b is the slope, *i.e.* sensitivity. The *LOD* values for Pb^{2+} and Cd^{2+} using the GCE modified with MnOOH were found to be 3.7 and 2.2 μM , respectively, and sensitivity to be 0.008 and 0.029 AM^{-1} , respectively. These *LOD* values are comparable with those obtained employing different electrodes (Table I). It should be mentioned that further improvement of MnOOH/GCE performance for sensing of the two

TABLE I. Comparison of the performance of different electrochemical sensors of various electrode materials for the sensing of Pb^{2+} and Cd^{2+} ; PolyL – poly(4-azulen-1-yl-2,6-bis(2-thiethyl)pyridine), GCD – glassy carbon disc, BDD – boron doped diamond, CPE – carbon paste electrode, SPE – screen printed electrode

Electrode	Pb^{2+}		Cd^{2+}	
	<i>LOD</i>	Deposition time, s	<i>LOD</i>	Deposition time, s
Bi-Modified Cu mini-sensor ⁴¹	8.3×10^{-7} M	120	5.3×10^{-7} M	150
PolyL film-modified GCD ⁴²	7×10^{-10} M	600	1×10^{-8} M	600
Sb-BDD ⁴³	25.4 $\mu\text{g L}^{-1}$	–	38.1 $\mu\text{g L}^{-1}$	–
Zeolite-modified CPE ⁴⁴	3.6 $\mu\text{g L}^{-1}$	–	1 $\mu\text{g L}^{-1}$	–
Benzoic acid-modified GCE ⁴⁵	0.2 $\mu\text{g L}^{-1}$	–	0.13 $\mu\text{g L}^{-1}$	–
Au-SP sensor ⁴⁶	0.5 $\mu\text{g L}^{-1}$	120	1.4 $\mu\text{g L}^{-1}$	120
BDD ^{47,48}	2 nM	900	2.5×10^{-8} M	60
			3.9×10^{-9} M	
SP microarrays ⁴⁹	3 μM	120	–	–
Nafion-modified GCE ⁵⁰	3 ppb	600	–	–
Nafion [®] -SPE ⁵¹	15 $\mu\text{g L}^{-1}$	–	–	–

heavy metal ions could be achieved by optimizing the experimental conditions, including solution pH, and deposition potential and time. For instance, relatively short deposition time of 120 s was used throughout this study as could be seen from comparison with some of those given in Table I.

A further study was performed in order to confirm the potential application of the investigated MnOOH-based electrode for heavy metal ions sensing in real samples. LSVs were recorded in a solution made with tap water. With no optimization of experimental conditions, such as optimization of solution pH value, two distinct peaks could still be observed (Fig. 2). The oxidation peak of Pb was somewhat suppressed in the studied solution as evidenced by smaller peak currents recorded, but was still clearly visible.

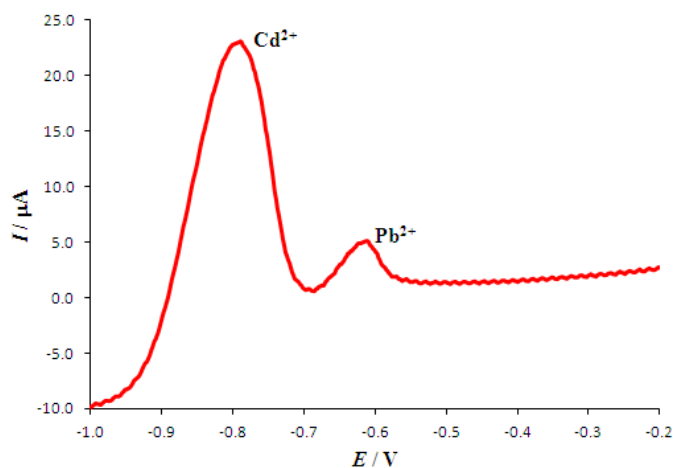


Fig. 2. LSV of MnOOH/GCE recorded in 25 μM Pb^{2+} and Cd^{2+} solutions in tap water at a scan rate of 50 mV s^{-1} ; E in V vs. SCE.

Pb²⁺ and Cd²⁺ sensing using c-PANIs-based electrodes

Control voltammograms of GCE modified with one of the three studied c-PANIs were recorded in the supporting electrolyte in the range from -1.3 to $+0.6$ V at a scan rate of 50 mV s^{-1} . The LSVs of all three electrodes showed no peaks in the absence of Pb^{2+} and Cd^{2+} . Upon the addition of 100 μM Pb^{2+} and Cd^{2+} , two clear peaks, at -0.37 and -0.64 V, could be seen at the LSVs of the GCE modified with each of c-PANI based electrodes (Fig. 3). In the case of c-PANI electrodes, the peak at -0.37 V, originating from Pb oxidation, was of significantly higher intensity compared to the peak at -0.67 V, corresponding to Cd oxidation. It should also be mentioned that only a small Pb oxidation peak could be observed on the LSV of the unmodified GCE, with no appearance of a Cd oxidation peak.

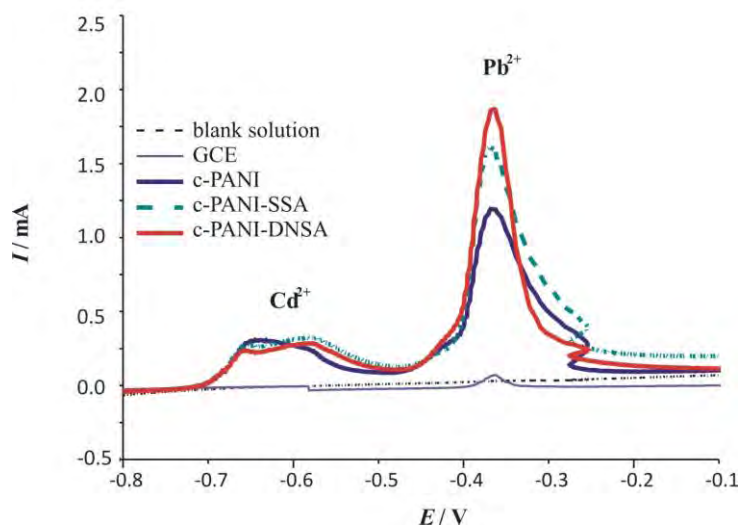


Fig. 3. LSVs of unmodified GCE and GCE modified with three different c-PANIs in 100 μM Pb^{2+} and Cd^{2+} solution in 20 mM H_2SO_4 + 30 mM KCl supporting electrolyte. A control voltammogram recorded in the absence of heavy metal ions is also presented; E in V vs. SCE.

The highest Pb oxidation peak current was obtained at the c-PANI–DNSA-based electrode, indicating its highest activity for the detection of the heavy metal ions. Peak current at the c-PANI–DNSA/GCE was *ca.* 17 % higher than that obtained at the c-PANI–SSA/GCE and 57 % higher than that recorded at c-PANI/GCE for the same Pb^{2+} concentration. This is most likely due to the high specific surface area S_{BET} of PANI–DNSA ($441 \text{ m}^2 \text{ g}^{-1}$ compared to $322 \text{ m}^2 \text{ g}^{-1}$ in case of c-PANI and $317 \text{ m}^2 \text{ g}^{-1}$ of c-PANI–SSA),³⁷ providing a high contact area for Pb^{2+} and Cd^{2+} during the deposition step. Other factors determining electroactivity of the c-PANIs include their structural and morphological properties, the presence of functional groups at their surface, and their pore structure and electronic structures. Peak currents corresponding to Cd oxidation were practically the same at all three studied carbonaceous electrodes. Using voltammetric sample of constant concentration of 100 μM Pb^{2+} and Cd^{2+} ($n = 20$), the standard deviation was found to be 7.2 %.

Compared to the MnOOH -based electrode, the first peak corresponding to Pb oxidation appeared at a somewhat less negative potential at the c-PANI-based electrodes, while the second peak corresponding to Cd oxidation was found at almost the same potential as at the MnOOH /GCE. Comparison of peak currents showed that the currents obtained at the electrodes based on the c-PANIs were one order of magnitude higher than those recorded at the MnOOH -based electrode. Significantly higher peak currents at the nitrogen containing carbon-based electrodes than at the manganese oxide-based electrode could be due to the diffe-

rence in the surface area of the materials. Manganese oxide electrocatalysts are reported to be active but they often suffer from having a small surface area and, in order to increase their electrochemical response, they have to be grafted onto carbon or other high surface supports.

Subsequently, the supporting electrolyte was spiked with 10 μM additions of the two heavy metal ions. The increase in the peak currents with increasing of Pb^{2+} and Cd^{2+} concentrations obtained at the c-PANI–DNSA/GCE are shown in Fig. 4, together with the corresponding I_p vs. C linear response plots in range up to a 100 μM solution. *LOD* values were calculated using the 3σ method (Eq. (1)) and are given in Table II. The lowest *LOD* of Pb^{2+} was obtained at the c-PANI–DNSA/GCE (0.58 μM), while lowest *LOD* of Cd^{2+} was obtained at the c-PANI/GCE (0.50 μM). The obtained results indicate that by choosing the right experimental conditions, c-PANI-based electrodes have potential application for the determination of the two heavy metal ions in aqueous media, offering a great benefit of eliminating use of mercury electrodes.

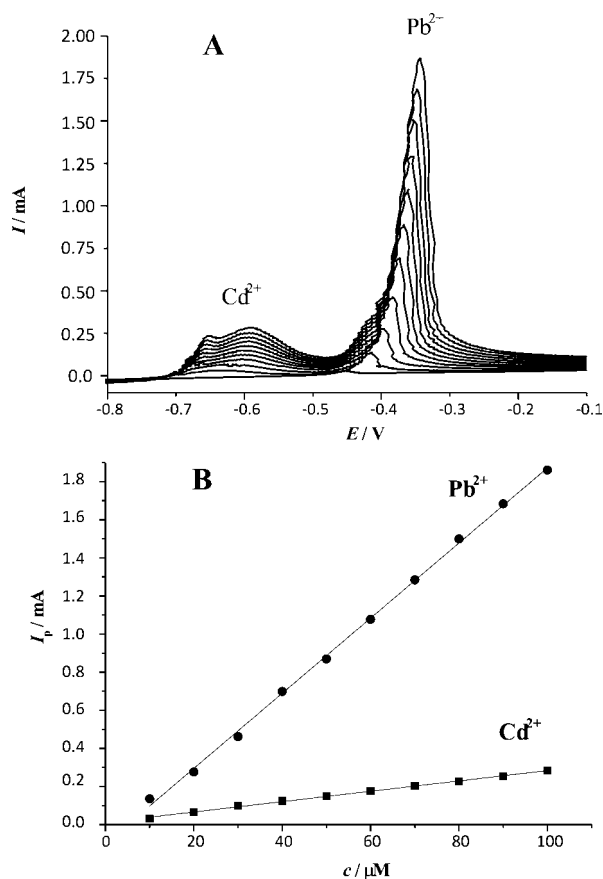


Fig. 4. A – Increase in the voltammetric response of the c-PANI–DNSA electrode with increasing Pb^{2+} and Cd^{2+} concentration from 0 to 100 μM ; B – linear dependences of peak current on the concentrations of the ions.

TABLE II. Limits of detection (μM) of Pb^{2+} and Cd^{2+} in aqueous media obtained using a GCE modified with MnOOH or different c-PANIs

Ion	MnOOH	c-PANI-SSA	c-PANI-DNSA	c-PANI
Pb^{2+}	3.70	0.69	0.58	1.70
Cd^{2+}	2.20	0.93	0.72	0.50

Other nanostructured carbon materials, including carbon nanoparticles, carbon nanotubes (CNTs), graphenes and fullerenes have been explored as electrode modifiers or electrode materials for the sensing of heavy metal ions and have shown themselves to be quite promising.^{52,53} Among them, CNTs have attracted the most attention due to their high electro-activity, originating from their high surface area and the presence of a high number of edge plane sites. Compared to CNTs, c-PANIs have the advantage of simpler and less expensive synthesis procedures, while still being characterized with high surface areas and number of edge plane sites.

CONCLUSIONS

Three different nanostructured carbonized polyanilines and nanostructured manganese oxyhydroxide were synthesized and examined with respect of their electrocatalytic activity in the sensing of lead and cadmium ions in aqueous solutions. Anodic stripping voltammetry showed that all the prepared electrodes gave a clear response corresponding to the oxidation of the two heavy metals. The method was further quantitatively evaluated and the limits of detection were found to be comparable to those reported in the literature for different electrochemical sensors. Comparison between peak currents recorded at MnOOH- and c-PANI-modified electrodes revealed significantly higher currents in the case of the c-PANIs. Among the three studied c-PANIs, c-PANI-DNSA gave the highest signal for Pb oxidation and lowest limit of detection, while response for Cd oxidation was similar at all three materials. The obtained results indicate that c-PANIs could be used for the fabrication of low-cost, rapid and sensitive electrochemical sensors for lead and cadmium ions determination.

Acknowledgments. The authors would like to thank the Ministry of Education, Science and Technological Development of the Republic of Serbia for financial support within Projects Nos. OI172043 and III45014.

ИЗВОД

НАНОСТРУКТУРНИ МАТЕРИЈАЛИ ЗА ДЕТЕКЦИЈУ Pb(II) И Cd(II) ЈОНА: МАНГАН-ОКСИХИДРОКСИД И КАРБЕНИЗОВАНИ ПОЛИАНИЛИНИ

БИЈАНА ШЉУКИЋ, ДАРКО МИЦИЋ, НИКОЛА ЦВЈЕТИЋАНИН И ГОРДАНА БИРИЋ-МАРЈАНОВИЋ
Универзитет у Београду, Факултет за физичку хемију, Студентски трг 12-16, 11158 Београд

Наноструктурни материјали, укључујући три различита карбенизована полианилина као и манган-окси хидроксида, су синтетисани и испитани као електродни матери-

јали за одређивање јона олова и кадмијума у воденим срединама. Резултати анодне „stripping“ волтаметрије су показали да сви припремљени материјали имају потенцијалну примену у одређивању јона ова два тешка метала. Електроде на бази карбонизованих полианилина дале су значајно већи сигнал и ниже границе детекције (ред величине 10^{-7} M) него електрода на бази манган-оксихидроксида. Међу три испитивана карбонизована полианилина, материјал који је добијен карбонизацијом полианилина синтетисаног у присуству 3,5-динитросалицилне киселине је показао највећу електрокаталитичку активност за оксидацију олова и кадмијума.

(Примљено 31. јула, ревидирано 29. септембра 2013)

REFERENCES

1. K. Kadirvelu, J. Goel, *Eco-Friendly Technologies for Removal of Hazardous Heavy Metal from Water and Industrial Wastewater*, in *Hazardous Materials and Wastewater. Treatment, Removal and Analysis*, A. A. Lewinsky, Ed., Nova Science Publishers, Hauppauge, New York, 2006, p.p. 27–148
2. M. A. El Mhammedi, M. Achak, M. Hbidd, M. Bakassee, T. Hbidd, A. Chtainib, *J. Hazard. Mater.* **170** (2009) 590
3. R. A. Goyer, *Toxic Effects of Metals*, in: *Casarett & Doull's Toxicology: The Basic Science of Poisons*, 5th ed., C. D. Klaassen, Ed., McGraw-Hill, New York, 1996, p. 691
4. S. Porter, K. Scheckel, C. Impellitteri, J. Ryan, *Crit. Rev. Env. Sci. Technol.* **34** (2004) 495
5. Committee on Environmental Health, *Pediatrics* **116** (2005) 1036
6. U.S. Environmental Protection Agency (EPA), *Lead in Drinking Water*, <http://www.epa.gov/safewater/lead/leadfacts>
7. M. A. Korn, J. B. de Nadrade, D. S. de Jesus, V. A. Lemos, M. L. S. F. Bandeira, W. N. L. dos Santos, M. A. Bezerra, F. A. C. Amorin, A. S. Souza, S. L. C. Ferreira, *Talanta* **69** (2006) 16
8. F. Barbosa Jr., F. J. Krug, E. C. Lima, *Spectrochim. Acta*, **B 54** (1999) 1155
9. G. W. Ewing, *Analytical Instrumentation Handbook*, 2nd ed., Marcel Dekker, New York, USA, 1997
10. M. A. El Mhammedi, M. Achak, *J. Hazard. Mater.* **161** (2009) 55
11. R. De Marco, G. Clarke, B. Pejcic, *Electroanalysis* **19–20** (2007) 1987
12. J. Wang, B. Tian, J. Wang, J. Lu, C. Olsen, C. Yarnitzky, K. Olsen, D. Hammerstrom, W. Bennett, *Anal. Chim. Acta* **385** (1999) 429
13. J. Wang, B. Tian, J. Lu, J. Wang, D. Luo, D. MacDonald, *Electroanalysis* **10** (1998) 399
14. J. A. Rodrigues, C. M. Rodrigues, P. J. Almeida, I. M. Valente, L. M. Goncalves, R. G. Compton, A. A. Barros, *Anal. Chim. Acta* **701** (2011) 152
15. S. C. C. Monterroso, H. M. Carapuc, J. E. J. Simao, A. C. Duarte, *Anal. Chim. Acta* **503** (2004) 203
16. J. Wang, *Stripping Analysis: Principles, Instrumentation, and Applications*, VCH, Weinheim, 1985
17. F. Arduini, J. Quintana Calvo, A. Amine, G. Palleschi, D. Moscone, *Trends Anal. Chem.* **29** (2010) 1295
18. Y. Bonfil, M. Brand, E. Kirowa-Eisner, *Anal. Chim. Acta* **464** (2002) 99
19. M. Khairy, R. O. Kadara, D. K. Kampouris, C. E. Banks, *Anal. Methods* **2** (2010) 645
20. R. Torabi Kachoosangi, C. E. Banks, X. Ji, R. G. Compton, *Anal. Sci.* **23** (2007) 283
21. V. Guzsvany, H. Nakajima, N. Soh, K. Nakano, T. Imato, *Anal. Chim. Acta* **658** (2010) 12
22. O. Estevez-Hernandez, I. Naranjo-Rodriguez, J. L. Hidalgo-Hidalgo de Cisneros, E. Reguera, *Sens. Actuators, B* **123** (2007) 488

23. D. A. C. Brownson, A. C. Lacombe, D. K. Kampouris, C. E. Banks, *Analyst* **137** (2012) 420
24. A. Manivannan, R. Kawasaki, D. A. Tryk, A. Fujishima, *Electrochim. Acta* **49** (2004) 3313
25. B. R. Šljukić, C. E. Banks, R. G. Compton *Hem. Ind.* **63** (2009) 529
26. B. Šljukić, R. O. Kadara, C. E. Banks, *Anal. Methods* **3** (2011) 105
27. B. Šljukić, I. Stojković, N. Cvijetićanin, G. Ćirić-Marjanović, *Russ. J. Phys. Chem., A* **85** (2011) 2406
28. B. Šljukić, R. G. Compton, *Electroanalysis* **19** (2007) 1275
29. C. E. Langley, B. Šljukić, C. E. Banks, R. G. Compton, *Anal. Sci.* **23** (2007) 165
30. R.N. Reddy, R. G. Reddy, *J. Power Sources* **132** (2004) 315
31. S.-J. Bao, B.-L. He, Y.-Y. Liang, W.-J. Zhou, H.-L. Li, *Mater. Sci. Eng., A* **397** (2005) 305
32. J. Li, N. Wang, Y. Zhao, Y. Ding, L. Guan, *Electrochem. Commun.* **13** (2011) 698
33. M. Mališić, A. Janošević, B. Šljukić Paunković, I. Stojković, G. Ćirić-Marjanović, *Electrochim. Acta* **74** (2012) 158
34. G. Ćirić-Marjanović, *Synth. Met.* **177** (2013) 1
35. S. Mentus, G. Ćirić-Marjanović, M. Trchová, J. Stejskal, *Nanotechnology* **20** (2009) 245601
36. A. Janošević, I. Pašti, N. Gavrilov, S. Mentus, G. Ćirić-Marjanović, J. Krstić, J. Stejskal, *Synth. Met.* **161** (2011) 2179
37. N. Gavrilov, I. A. Pašti, M. Vujković, J. Travas-Sejdic, G. Ćirić-Marjanović, S. V. Mentus, *Carbon* **50** (2012) 3915
38. A. Janošević, I. Pašti, N. Gavrilov, S. Mentus, J. Krstić, M. Mitrić, J. Travas-Sejdic, G. Ćirić-Marjanović, *Micropor. Mesopor. Mater.* **152** (2012) 50
39. N. Gavrilov, I. A. Pašti, M. Mitrić, J. Travas-Sejdic, G. Ćirić-Marjanović, S. V. Mentus, *J. Power Sources* **220** (2012) 306
40. G. Ćirić-Marjanović, I. Pašti, N. Gavrilov, A. Janošević, S. Mentus, *Chem. Pap.* **67** (2013) 781
41. L. C. S. Figueiredo-Filho, B. C. Janegitz, O. Fatibelilo-Filho, L. H. Marcolino-Junior, C. E. Banks, *Anal. Methods* **5** (2013) 202
42. G.-O. Buica, E.-M. Ungureanu, L. Birzan, A. C. Razus, L.-R. Mandoc (Popescu), *J. Electroanal. Chem.* **693** (2013) 67
43. K. E. Toghill, L. Xiao, G. G. Wildgoose, R. G. Compton, *Electroanalysis* **21** (2009) 1113
44. S. Senthilkumar, R. Saraswathi, *Sensors Actuators, B* **141** (2009) 65
45. L. Fan, J. Chen, S. Zhu, M. Wang, G. Xu, *Electrochem. Commun.* **11** (2009) 1823
46. S. Laschi, I. Palchetti, M. Mascini, *Sensors Actuators, B* **114** (2006) 460
47. D. Dragoe, N. Spataru, R. Kawasaki, A. Manivannan, T. Spataru, D. A. Tryk, A. Fujishima, *Electrochim. Acta* **51** (2006) 2437
48. C. E. Banks, M. E. Hyde, R. Jacobs, R. G. Compton, *Talanta* **62** (2004) 279
49. S. J. Hood, R. O. Kadara, D. K. Kampouris, C. E. Banks, *Analyst* **135** (2010) 76
50. K. Crowley, J. Cassidy, *Electroanalysis* **14** (2002) 1077
51. I. Palchetti, C. Upjohn, A. P. F. Turner, M. Mascini, *Anal. Lett.* **33** (2000) 1231
52. G. Aragay, A. Merkoçi, *Electrochim. Acta*, **84** (2012) 49
53. A. K. Wanekaya, *Analyst* **152** (2011) 4383.



J. Serb. Chem. Soc. 78 (11) 1729–1761 (2013)
JSCS–4530

AUTHORS' REVIEW

Ion selective electrodes in environmental analysis

ALEKSANDAR RADU^{1*‡}, TANJA RADU^{2‡}, CHRISTINA MCGRAW^{3‡}, PETER DILLINGHAM⁴, SALZITSA ANASTASOVA-IVANOVA^{5‡} and DERMOT DIAMOND⁶

¹*Keele University, Birchall Centre and Environment, Physical Sciences and Mathematics (EPSAM) Research Institute, Lennard-Jones Labs, Stoke-on-Trent, ST5 2BG, United Kingdom,* ²*Loughborough University, School of Civil and Building Engineering, Loughborough, LE11 3TU, United Kingdom,* ³*Institute for Marine and Antarctic Studies (IMAS), University of Tasmania, Private Bag 129, Hobart 7005, Tasmania, Australia,* ⁴*University of New England, School of Science and Technology, Armidale, Australia,* ⁵*Queen Mary University London, School of Engineering and Mathematical Sciences, London, E1 4NS, United Kingdom and* ⁶*National Centre for Sensor Research, CLARITY Centre for Sensors Web Technologies, Dublin City University, Dublin 7, Ireland*

(Received 29 August, revised 26 September 2013)

Abstract: An overview is given dealing with the application of ion-selective electrodes (ISEs) in environmental analysis. ISEs are placed into the context of the trend of development of sensors for extensive and frequent monitoring. Discussed are the issues such as sensing platforms and their mass-production, improvement of precision, diagnostic of sensor functionality, and development of reference electrodes. Several examples of real-life application of ISEs in environmental analysis are given. The main emphasis of this article is directed towards summarizing recent results of the authors during the past several years.

Keywords: potentiometric sensors; wireless sensing networks; reference electrode; sensor precision.

CONTENTS

1. A BRIEF HISTORY OF ION SELECTIVE ELECTRODES
2. THE PLACE OF ISEs IN ENVIRONMENTAL ANALYSIS
3. SENSING PLATFORM DESIGNS AND EXAMPLES OF APPLICATION OF ION SELECTIVE ELECTRODES IN ENVIRONMENTAL ANALYSIS
 - 3.1. *Liquid-contact ISEs*

* Corresponding author. E-mail: a.radu@keele.ac.uk

‡ During the execution of parts of this work, these authors were at Dublin City University, Ireland.

doi: 10.2298/JSC130829098R

- 3.2. *Solid-contact ISEs*
- 3.3. *Screen-printed ISEs*
- 3.4. *Development of simple all-solid-contact potentiometric systems*
- 3.5. *Wireless sensing networks*
- 4. IMPROVING THE PRECISION OF ISEs
 - 4.1. *Modelling the response curve*
 - 4.2. *Calibration and precision of ISEs*
- 5. REFERENCE ELECTRODE
- 6. REDUCING THE NEED FOR CALIBRATION AND DIAGNOSTIC OF SENSOR FUNCTIONALITY
 - 6.1. *Reducing the need for calibration by producing sets of identically performing sensors*
 - 6.2. *Diagnostic of sensor functionality*
- 7. FUTURE TRENDS
 - 7.1. *Technology*
 - 7.2. *Analytical methodologies*
 - 7.3. *Materials*
- 8. CONCLUSIONS

1. BRIEF HISTORY OF ION SELECTIVE ELECTRODES

Ion-selective electrodes (ISEs) are one of the oldest classes of chemical sensors. Described for the first time by Cramer in 1906,¹ they entered into routine laboratory practise with Beckman's invention of the pH-sensitive glass electrode in 1932.^{2,3} Today, there is hardly any chemistry laboratory that does not have a pH electrode. It is estimated that the market for pH electrodes is worth nearly a billion USD annually.⁴

The golden age of ISEs started in the 1960s with the discovery that some antibiotics are capable of selective binding of particular ions. The group of Simon utilised valinomycin, monensin and nonactin to make potassium, sodium and ammonium selective electrodes, respectively.⁵⁻⁷ This was quickly followed by the realization that other compounds could be utilized and/or synthesized for the purpose of binding selected ions. The word "ionophores" was specially coined for such compounds. The 1960s and 70s were the time of exponential growth in the field of ISEs, so much so that Orion (a company that almost exclusively worked on development of new ISEs) featured "electrode of the month".^{2,3} Being responsive only to the bioavailable ion fraction, having excellent ability to discriminate ions of interest *versus* other ions, and having suitable sensitivity and quick response time, ISEs based on ionophores demonstrated sensing characteristics that were excellently suited for application in clinical analysis. The most valuable application was in the analysis of blood electrolytes, such as Na⁺, K⁺,

Ca^{2+} , Mg^{2+} , and Cl^- . It is estimated that market for ion-sensor-based analysers was worth >3 billion USD in 2011.⁸

After the initial excitement, the pace of the development in the ionophore-based sensors field slowed and by the 1990s, the common opinion was that there were no significant discoveries left to be made.⁹ Fortunately, a few groups continued to pursue further research in the field in the late 1990s and early 2000s. The thorough re-examination of past practices completely revolutionized the field when it was realized that the existence of inner membrane ion fluxes introduce significant bias in the determination of selectivity coefficients and underestimated of limits of detection (LODs).^{9–11} Previous definitions of the mechanisms of response were re-evaluated and re-defined. Consequently, selectivity and sensitivity were improved by up to 6 orders of magnitude.¹² It is noteworthy that such an unprecedented feat was achieved simply by slight alteration of the experimental protocol – no additional instrumentation was introduced. Descriptions of important factors that influenced such great advantages and the corresponding experimental protocols exceed the scope of this review and the curious reader is advised to read some of the many reviews written on these topics.^{10,11,13–16}

The achievements that led to *LODs* in part-per-billion (ppb) and part-per-trillion (ppt) levels and excellent selectivity greatly expanded the application fields of ISEs. This paper reviews the efforts that the authors invested in optimization of ISEs for environmental analysis and give few thoughts on possible future directions of development.

2. THE PLACE OF ISEs IN ENVIRONMENTAL ANALYSIS

In his *Analytical Chemistry* editorial, Prof Royce Murray analysed challenges that environmental analytical chemistry is facing. He said that “A ‘Grand Challenge’ posed for analytical chemistry is to develop a capability for sampling and monitoring air, water, and soil much more extensively and frequently than is now possible. Such goals will require improvements in sampling methodology and in techniques for remote measurements, as well as approaches that greatly lower per-sample and per-measurement costs”.¹⁷ In order to address this challenge, chemical sensors need to be simple, sensitive, and very cheap. The latter is arguably the most difficult, since there are many factors that dictate the cost of sensors. For example, from a technological perspective, ISEs need to: a) be produced on a mass-scale, b) require very simple electronic circuitry and c) require minimal power for operation. From a chemistry perspective, sensors have to: a) show great long-term stability (minimal drift over time), b) be resistant to biofouling, c) have sufficient selectivity to distinguish analyte of interest from all of the interferences in the sample and d) have sufficient accuracy and precision. These are all very significant challenges and many research groups are spending

significant amounts of time, energy and resources addressing them. As an illustration, there have been more than 1100 reviews published since 2010 on the topic of Environmental Analysis, 21 of these involving potentiometric sensors; however the avid reader is invited to read reviews by Diamond and De Marco that discuss the issues arising from the application of ISEs in environmental analysis.^{15,18}

Phenomenal improvements of detection limits re-ignited the excitement in the field of ISEs and brought tremendous amount of optimism for the expansion of the utility of ISEs. From a technique that was largely constrained to blood electrolyte analysis, improved LODs opened opportunities that were considered previously unreachable, such as environmental analysis. Table I compares Detection limits of ISEs are compared Table I with those of the most widely used instrumental techniques in elemental environmental analysis. As a reference, the last column contains EPA action levels for drinking water. Clearly, the detection limits of ISEs are very competitive with the most sensitive techniques and sufficient for the determination of drinking water quality.

TABLE I. Detection limits in ppb for selected ions obtainable using flame atomic absorption spectrometry (FAAS), graphite furnace atomic absorption spectrometry (GFAAS), inductively coupled plasma mass spectroscopy (ICPMS) and ion selective electrodes (ISE) as well as action levels for selected ions in drinking water

Method/element	FAAS	GFAAS	ICPMS	ISE	EPA
Ag	1.5	0.02	0.005	0.1 ¹⁹	50
Ca	150	0.01	0.5	0.1 ²⁰	
Cd	1.5	0.003	0.005	0.01 ²¹	10
ClO ₄ ⁻	–	–	–	3 ²²	1 ^a
Cu	1.5	0.1	0.005	0.01 ²³	1300
Cs	5	–	0.01	1 ²⁴	–
K	3	0.008	0.5	0.2 ²⁵	–
I	–	–	1	0.25 ²²	–
Na	0.3	0.02	0.05	0.7 ²⁶	–
Pb	15	0.1	0.001	0.001 ¹²	50
NH ₄ ⁺	–	–	–	0.2 ²⁵	100 ^b

^asuggested; ^bdependent on pH and *T*

In addition to competitive detection limits, ISEs carry some other great advantages regarding the analysis of trace metals in the environment. Perhaps the most significant one is their ability to sense “free” ion activity. Uptake of ions by biota and the ion toxicity is dependent on the free ion content²⁷ and ISEs are an excellent tool for monitoring the impact of trace metal inputs into the environment. Moreover, acidification of natural samples is expected to mobilize ions from their complexes thereby allowing the determination of the “total” ion concentration. Consequently, ISEs can be an extremely powerful research tool that

can allow the simultaneous monitoring of metal inputs (reflected by their total concentration) and the bioavailability of these inputs (reflected in the level of “free” metal), thereby providing environmental scientists with a monitoring dataset that is rich in chemical information.

Attractiveness of ISEs for environmental analysis also lies in the simple and inexpensive instrumentation. ISEs are used in potentiometric setup where the potential of the indicator electrode (ion selective electrode) is measured against a reference electrode under zero-current conditions. Simple and inexpensive instrumentation as well as simple measurement principles and portability make ISEs suitable for on-site, ship-board, *in situ* field analysis. Notwithstanding highly attractive examples of application of ISEs in environmental analysis (some of which will be mentioned later in this review), here a curious example of the application of ISEs in space research is mentioned. The Phoenix spacecraft landed on Mars on 25th May 2008 carrying a Wet Chemistry Laboratory (WCL) among other instrumentation. The WCL contained ISEs for Ca^{2+} , Mg^{2+} , K^+ , Na^+ , NH_4^+ , H^+ and halides, Cl^- , Br^- and I^- . While the elemental composition of the Martian surface had been measured on previous expeditions using X-ray fluorescence, soil analysis using ISEs enabled of the solution chemistry of Martian soil to be studied, which led to insight into possible biological activity, pre-biotic organic synthesis and the thermo-physical properties of any liquid solution.²⁸

Another very attractive feature of ISEs is that they are unaffected by colour and turbidity. The ISEs have been successfully utilized in direct analysis of milk and processed cheese,^{29–31} while Fig. 1 depicts an experiment utilizing ISEs for the determination of nutrients in a sample containing 10 mass % organic solid matter (unpublished data).

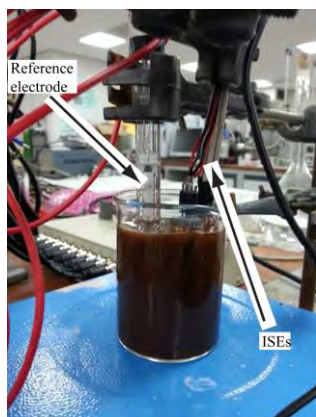


Fig. 1. ISEs in the determination of nutrients in a sample containing 10 % solid matter.

ISEs are extremely versatile chemical sensors. Today, there are more than 60 ions for which ISEs have been described.³² They are one of the very few instrumental techniques capable of the determination of both positive and negative

ions. Moreover, ISEs have the ability to detect both monatomic (Na^+ , Cl^- , Pb^{2+} , *etc.*) and polyatomic ions (SO_4^{2-} , CO_3^{2-} , ClO_4^- , *etc.*). Since both cations and anions have significant importance in the environment, the ability to utilize the same instrumental setup for both groups of analytes can significantly reduce the cost of the total analyses.

By analysing the aforementioned properties, it is clear that ISEs have many very attractive properties suitable for application in environmental analysis. Herein, the work that this group of authors undertook will be presented in order to demonstrate such applications and to address some of the issues mentioned in the opening paragraph of this section.

3. SENSING PLATFORM DESIGNS AND EXAMPLES OF APPLICATION OF ION SELECTIVE ELECTRODES IN ENVIRONMENTAL ANALYSIS

ISEs utilize extremely simple experimental setup where the potential of indicator electrode is measured against reference electrode under zero-current conditions. The potential is measured by a simple voltmeter with high input impedance. Simple electrodes and their accompanying electronic circuitry for data acquisition present an excellent basis for the development of an extremely cheap (ideally disposable) sensing system that can be deployed for *in situ* analysis. However, the current costs of commercially available ISEs (EUR 600–800 at www.sigmaaldrich.com) prohibit their integration into autonomous field-deployable sensing systems. It is therefore critical to develop methods for mass-scale production hence significantly lowering the cost per electrode.

Based on the utilized material, ISEs can be grouped into three categories:

Glass electrodes – glass was the material used to describe and develop first ISEs; however glass-based electrodes are limited to very few ions (*e.g.*, H^+ , Na^+ and K^+).²

Solid-state ISEs – based on low soluble salts of the ion of interest and while they have been actively and very successfully utilized in environmental analysis,^{15,33–35} their mechanism of response limits the number of ions for which electrodes can be developed.

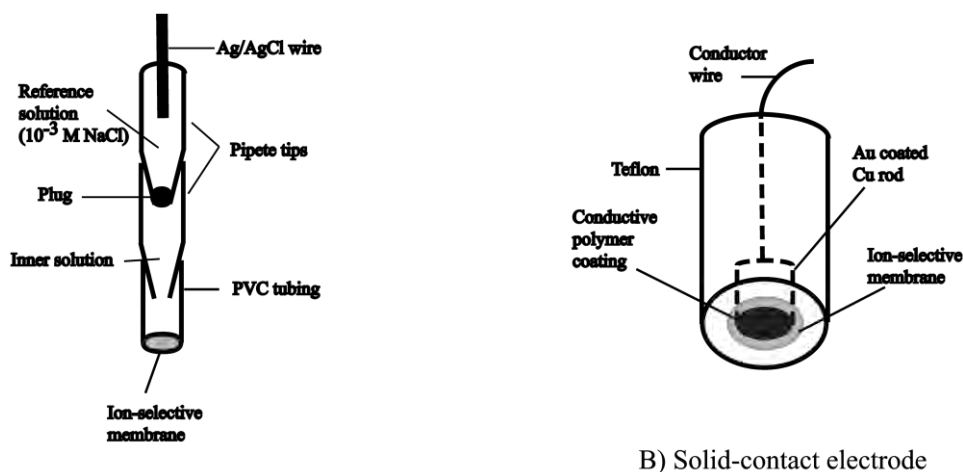
Ionophore-based polymer membrane ISEs, the most versatile and the focus of many research groups, hold the most promise for expansion into environmental analysis. They can be constructed as:

- liquid-contact electrodes and
- solid-contact electrodes.

The following text discusses liquid- and solid-contact electrodes from the standpoint of the construction of the sensing platform and related issues in regards to their application in environmental analysis. The utilization of screen-printing technology for the mass-production and integration of sensors into large wireless sensing networks (WSNs) is also discussed.

3.1. Liquid-contact ISEs

In traditional ISEs, the polymeric membrane establishes the contact with the solid electrode *via* an aqueous layer (typically referred to as the inner filling solution) that contains a solution of the ion of interest. In the works of Bakker, Buhlmann and Pretsch in the late 1990s, it was realized that ion fluxes in the membrane have deterministic effect on its response.^{9,10,13} Reducing the activity of primary ion in the inner filling solution was suggested as a suitable solution for reducing the membrane fluxes. This required slight modification of the experimental setup; the single-compartment housing inner filling solution had to be split in two. The compartment at the inner solution–membrane phase boundary contained a solution of primary ions buffered to a very low activity (nano-molar or lower). This compartment was in contact with the one containing milli-molar amounts of a Cl⁻-containing solution in contact with the Ag/AgCl inner reference. A very simple solution was suggested; two pipette tips were used to hold the two compartments of the inner solution and the membrane was glued on PVC tubing attached to distal end of the bottom compartment, as shown in Fig. 2A.



A) Liquid-contact electrode

Fig. 2. A) Construction of liquid-contact electrode. B) Construction of solid-contact electrode.

Such a construction had a two-fold impact on ISEs. By reducing the activity of the primary ions in the inner filling solution, the membrane fluxes were indeed reduced, which resulted in a drastic reduction of the *LOD*. Moreover, it demonstrated the possibility for drastic cost reduction of ISE as a sensing platform. In the seminal paper by Ceresa *et al.*, a pipette tip-based ISE was used to measure Pb²⁺ in Zurich's drinking water. The obtained results were evaluated with ICPMS and excellent correspondence between the two techniques was evidenced.³⁶ A

period of vigorous research into factors affecting the optimisation of membrane fluxes ensued. Some of the authors of this paper contributed to the general discussion by publishing a set of guidelines for the improvement of *LODs*.²⁰ In addition, the first ISE for measurement of fission products in natural water²⁴ was demonstrated. A range of Cs⁺-selective ionophores and cation exchangers were investigated in order to develop a Cs-selective electrode with a trace level *LOD*. An ion-exchange resin was utilized to buffer Cs⁺ in the inner filling solution to nano-molar levels and an *LOD* of 1 ppb was achieved. This electrode was used to demonstrate the feasibility of determination of Cs⁺ in the presence of Sr²⁺ in natural waters since these two ions are expected to pose the most significant threat to public safety in the case of detonation of a radiological dispersal device or a so-called “dirty bomb”.

3.2. Solid-contact ISEs

Very quickly after the invention of the ionophore-based ISEs, Cattrall suggested the complete removal of the inner filling solution and reported the so called “coated wire” ISE.³⁷ However, such electrodes showed significant signal instabilities and found very limited application. In the seminal paper by Fibbioli *et al.*, these instabilities were assigned to the formation of a thin water layer between the membrane and the metal electrode.³⁸ This aqueous layer behaves as a reservoir the composition of which can change upon sample changes, leading to drifting potentials. The addition of a lipophilic intermediate layer that could define redox couple and prevent the formation of water layer between the membrane and electrode was suggested and redox-active self-assembled monolayers and conductive polymers (CPs) emerged as a suitable solution.^{39,40} A period of very intensive research followed these discoveries. Consequently the selectivity, sensitivity, robustness and response time of solid-contact electrodes approached those of liquid-contact electrodes and opened the possibility for their utilization in environmental analysis.^{41–48} A schematic representation of a typical solid-contact ISE utilizing CP as an intermediate layer is depicted in Fig. 2B.

Liquid- and solid-contact electrodes were evaluated and compared for application in soil analysis.⁴⁹ This research was part of the work on development of chemical sensors for long-term *in situ* deployment for frequent monitoring of airborne dust polluted with heavy metals. Major dust blows of heavy metal-contaminated soil from the Gortmore Tailings site of an abandoned mine near Silvermines, Co., Tipperary, Ireland, were connected with cattle death in the 1980s. Later, several governmental reports showed that about 20 % of the agricultural soil samples collected near the Silvermines had levels of heavy metals up to 30 times higher than the average values for Irish soils.⁴ Therefore, there was an urgent need for high-frequency, real-time and *in situ* monitoring of heavy metals in airborne dust. Due to their properties, ISEs were suggested as detectors in the

monitoring device. However this type of application highlighted several issues, including bias at low analyte concentrations and unsuitable soil digestion techniques. The issue of utilization of the entire response curve to reduce bias will be discussed in the Section 4.2. Development of a suitable soil digestion technique was important since typical soil digestion techniques utilize very harsh and dangerous acids (*e.g.*, *aqua regia* or hydrofluoric acid). Finally, the potential of using solid-contact ISEs as simpler and cheaper solution relative to liquid-contact electrodes was evaluated. In the evaluation of digestion technique and suitability of solid-contact ISEs, atomic absorption spectroscopy (AAS) was used as the reference technique. It was established that short sonication of soil samples in 10^{-3} M HNO_3 mobilized a suitable amount of heavy metal ions for detection by ISEs. Solid-contact ISEs indeed showed satisfactory *LODs* and excellent correlation with AAS measurements was obtained.

3.3. Screen-printed ISEs

Technologies for mass-production, such as screen- and inkjet printing, have occupied an important place in sensor production.^{50–53} Development of robust solid-contact ISEs with selectivity and *LODs* almost identical to liquid-contact ones allowed progress to truly low-cost sensors *via* the utilization of such technologies. In the production of ISEs, screen-printing is typically used to produce the platform followed by the deposition of a CP and an ion selective membrane. Details of the preparation of ISEs by the screen-printed platform are given in Fig. 3.

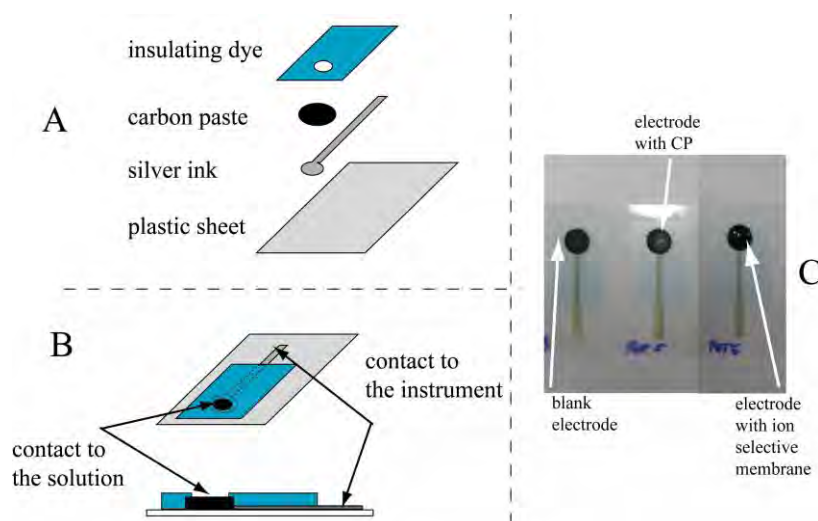


Fig. 3. A) Preparation process of a screen-printed electrode. Silver ink is printed on a plastic substrate followed by printing of carbon ink and finished by printing of an insulating layer. B) Top view and side view of the finished electrode. C) Picture of electrode (left) covered with CP (middle) and finally with an ion selective membrane (right).

Detailed characterization of such electrodes showed that their behaviour was no different to those of traditionally prepared solid-contact ISEs. They were evaluated for the analysis of Pb^{2+} in various water bodies within the city limits of Dublin, Ireland.⁵⁴ Twelve water samples were collected from the River Liffey, the Royal Canal and the Grand Canal that pass through Dublin. The sampling and sample storage was realised according to EPA recommendations.⁵⁴ The samples were acidified to pH 4 to ensure that all Pb^{2+} were present in the free, uncomplexed form. The unknown concentration of lead was determined using standard addition method and the results were evaluated using ICPMS. The obtained results are summarized in Table II.

TABLE II. Total Pb^{2+} concentration (ppb) of environmental water samples (with 95 % confidence interval) determined by ISEs using the standard addition method and ICPMS. The relative error (RE) was calculated as $RE = 100(X^{ISE} - X^{ICPMS}) / X^{ICPMS}$, where X^{ICPMS} was assumed to be the “true” value

Sample ID	Pb^{2+} (ICPMS)	Pb^{2+} (ISE)	% RE
1	0.32±0.02	0.52±0.06	-62.5
2	0.51±0.04	0.66±0.08	-29.4
3	1.67±0.08	1.65±0.09	-15.6
4	1.98±0.07	2.07±0.09	1.2
5	4.87±0.11	5.20±0.14	-4.5
6	1.23±0.08	1.65±0.09	-6.8
7	0.90±0.03	1.04±0.05	-34.1
8	2.14±0.07	2.61±0.09	22.0
9	9.68±0.25	10.1±0.1	-3.3
10	2.90±0.11	2.61±0.30	10.0
11	5.52±0.18	6.55±0.05	-18.7
12	172±12	207.20±0.14	-20.2

It is striking that the two sets of data closely correspond over the full range of samples even though for 11 out of the 12 results, the lead concentration was below 10 ppb (50 nM). While the relative error (RE) may appear high in some cases (samples 1, 2, 7 and 8 have $RE > \pm 20\%$), it should be appreciated that in every case, the lead concentration was ≤ 2 ppb, which is just at the LOD as defined by the IUPAC. As discussed in the Section 4, large RE are expected due to the bias introduced by estimating unknown concentrations using linear regression. These results have important implications in further application of ISEs in quality control of surface waters. Considering that the European Water Framework Directive recommends a concentration of 7.2 ppb for Pb^{2+} as the upper limit for surface waters, and that 10 out of 12 samples had concentrations below this limit, the ISEs can be suitable for use as detectors in very low-cost early warning systems.

3.4. Development of simple all-solid-contact potentiometric system

Development of polymer membrane-based liquid junction-free reference electrodes (please see Section 5) allowed the construction a simple all-solid-contact potentiometric system and its use in the determination of Pb^{2+} speciation in natural water.⁵⁵ Mobilization and ion speciation is dependent on pH and therefore requires pH monitoring in parallel to determination of the concentration of the ion of interest. A multi-sensor probe developed in order to house the reference electrode, polymer membrane-based pH electrode and Pb^{2+} -selective ISE is shown in Fig. 4 (top).

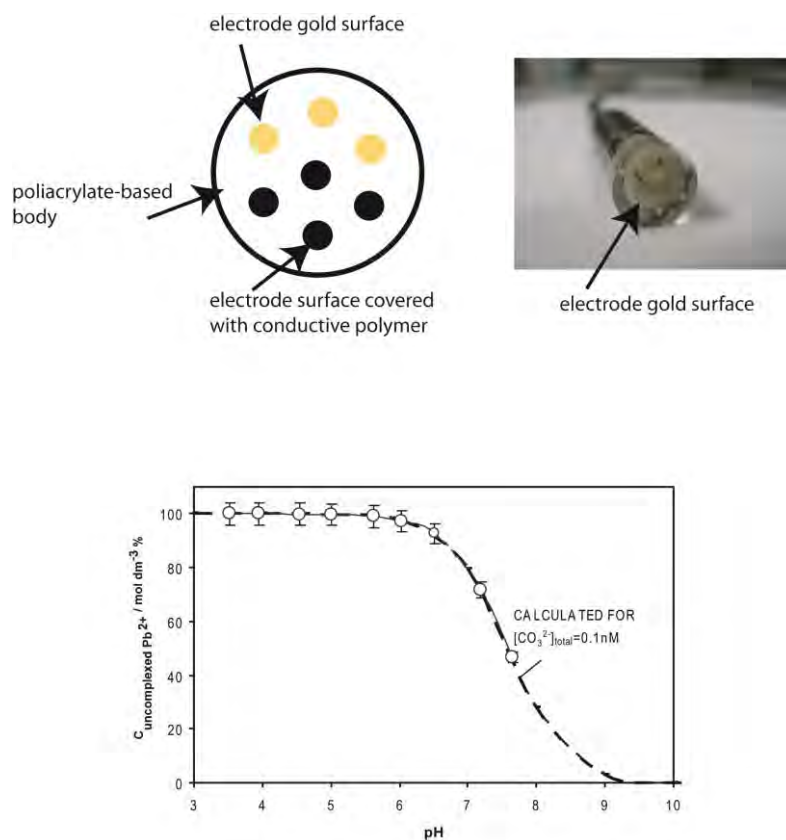


Fig. 4. Top) multi-sensor probe. Schematic representation of electrodes (left) and photo of a multi-sensor probe (right). Bottom) direct potentiometric determination of the speciation of lead in deionized water spiked with 9.1 ppb Pb^{2+} as a function of pH. Circles: experimental data. Dashed line: fraction of uncomplexed Pb^{2+} calculated based on complexation of Pb^{2+} and CO_3^{2-} as dominant complexing anion present in the sample.

All three types of electrodes (pH- and Pb^{2+} -selective and solid-contact reference electrodes) were carefully characterized according to published proce-

dures⁵⁵ and used for the measurement of pH in deionised water, rain water, tap water and samples from natural water bodies in and around the city of Dublin, Ireland. Lead-speciation analysis was performed on the simplest sample, deionised water spiked with 9.1 ppb Pb²⁺ at various pH levels. The results where full circles are experimental results obtained by calculating the fraction of uncomplexed lead based on sample pH are illustrated in Fig. 4. The dotted line represents the theoretically calculated values taking into account lead complexation with sample ions. Excellent agreement between the experimental measurements and theoretical calculations demonstrates that the sensing array consisting of solid-contact pH- and Pb²⁺-selective ISEs coupled with solid-contact RE could be used to accurately determine lead speciation using direct potentiometric measurements.

3.5. Wireless sensing networks

Analytical instruments are becoming smaller and more automated. In parallel, wireless communication devices are getting smaller and capable of long-term operation. Some believe that the next step in the information revolution will be driven by linking cheap sensors to microprocessors.⁵⁶ Personalized medicine and point-of-care devices are an excellent example of the integration of sensors with communication devices. Another very attractive example is the integration of sensors within clothing and the concept of “wearable sensors”.^{57,58} The concept of integration of chemical sensors with communication devices into wireless sensing networks (WSNs) is highly attractive in environmental analysis. Deployment of a very large number of extremely cheap, autonomous and mutually connected devices provides the ability to harvest much more complex data, such as origin (time and location) of pollution, speed and direction of spreading.^{59–61} However, integration of chemical sensors in WSNs is proving to be extremely challenging. This is partly due to inherent difficulties associated with field deployment of autonomous chemical sensors and partly due to usability issues of current wireless hardware platforms. In fact, of the very few literature examples of wireless chemical sensor networks (WCSNs) most are focused on the design and development of a single wireless sensing node. In a very interesting example of real deployment of multi-nodal WCSN, Shepherd *et al.* deployed LED-based pH sensors for monitoring chemical plumes.⁶²

The simplicity of ISEs and their data acquisition instrumentation motivated us to develop a wireless ISE-based autonomous sensing system.⁶³ In collaboration with the engineering team from the Diamond Group, integration of these sensing systems into WSNs was explored. A block diagram for four key system elements (wireless sensing platform, base station and data harvester (PC/laptop)) and data flow interactions is depicted in Fig. 5A. pH-sensitive ISEs were selected for the simplicity of their operation. Ion selective membranes and RE were deposited on the platform that was designed with a view of integration with a

microfluidic system where Au-based contacts were prepared by sputter-coating and encased into a plastic film. The wireless sensing platform was designed to acquire three individual ISEs against a single RE. The base station worked much in the same way as the wireless sensing platform but without the conditioning circuitry. The gathering, storage and visualisation of the data on the data harvester were achieved using a purpose built control program written in the Java programming language. Figure 5B–D show a screen capture of the WISE system's front-end graphical user interface, the wireless sensing platform, and the base station.

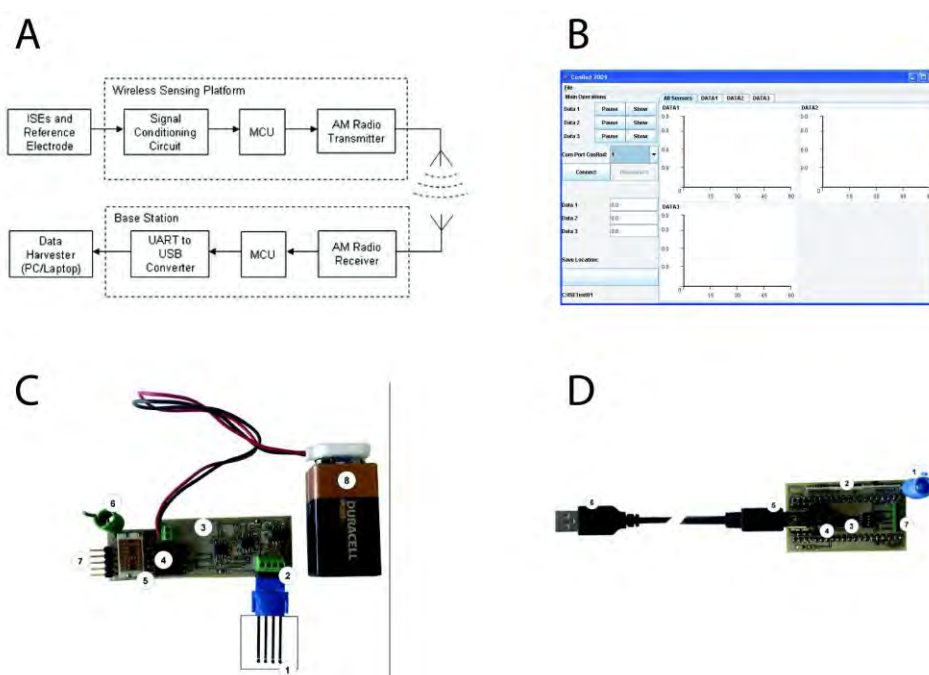


Fig. 5. A wireless ion selective electrode autonomous sensing system. A) Block diagram showing the architecture of the system and the flow of signal/data from the sensors to the data harvesting system element. B) Screen capture of the system GUI. C) PCB Implementation of the wireless sensing node. 1) screen-printed electrode, 2) terminal block interfacing the electrodes and signal conditioning board, 3) signal conditioning board, 4) interface from the signal conditioning board to the wireless transmitter, 5) wireless AM transmitter module, 6) antenna, 7) programming interface and 8) power source (PP3 9V battery). D) PCB Implementation of the base station. 1) antenna, 2) AM radio receiver, 3) PIC microcontroller, 4) USB to UART transceiver, 5) mini-B USB connection, 6) USB-A connection to PC/laptop and 7) terminal block for programming the wireless module.

Validation of the sensing system was realised by *in situ* determination of the pH of various natural water samples, including water from the Tolka River and Royal Canal flowing through the city of Dublin, Ireland. Excellent correlation of

data between WISE system and portable pH meter was achieved ($R^2 = 0.991$, $n = 8$) and the errors were low ($RE \leq 2.6\%$). These results encouraged us to develop a testing system for ISE-based WSNs. An environmental sensing chamber was developed capable of housing a model of a river with ISEs integrated on the wireless data transmission platform, as depicted in Fig. 6. The model contains a stagnant section to allow for modelling of the variation of the flow rates along the River. Sampling positions are located on strategic locations to allow for introduction of the pollutant, as well as to position sensors to enable pollution spread to be monitored. This allows monitoring of the water quality by observing the pattern of the response of the sensors (unpublished data).

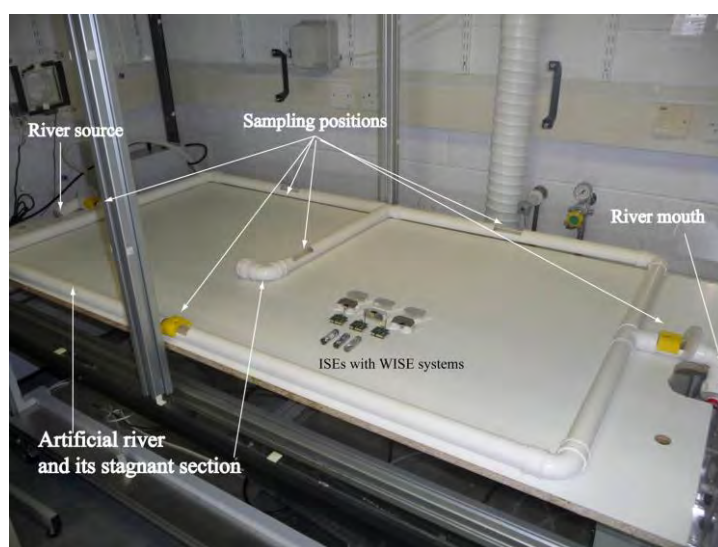


Fig. 6. Model of an artificial river developed for deployment and testing of WSNs.

4. IMPROVING THE PRECISION OF ISEs

Since the invention of ionophore-based ISEs, the characteristics of ionophores and the analytical behaviour of concomitant sensors were studied in great depth. Sets of recommendations regarding the determination of selectivity, sensitivity, calibration and nomenclature of ISEs, as critical parameters for real-life applications, were published by the IUPAC.^{64–67} However, the significant breakthroughs achieved in late 1990s and early 2000s led to an almost complete re-definition of recommendations for experimental protocols necessary for obtaining optimal selectivity and *LODs*.⁶⁸

As it is often the case, the opening of new research horizons highlights issues that were previously overlooked or were considered not worthy of investigation. Here, the case of the definition of *LOD* and its impact on the potential for application of ISEs in environmental analysis are considered.

The potentiometric response of ISEs, the EMF, in a solution containing mixture of ions of interest (a_I) and interfering ions (a_J) is given according to the Nikolskii–Eisenman Equation:

$$E = E^0 + \frac{RT}{z_1 F} \ln \left(a_I + \sum a_J K_{I,J}^{\text{pott}} \right) \quad (1)$$

Responses below the LOD ($a_I = 0$) have a constant value, which is ideally defined by the response of the sensor to interfering ions (a_J). $K_{I,J}^{\text{pot}}$ symbolizes the potentiometric selectivity coefficient. When the activity of the primary ions becomes sufficiently high, the term $\sum a_J K_{I,J}^{\text{pot}}$ becomes negligible and the equation is transformed into the Nernst Equation with a slope of $59.2/z_1$ mV decade⁻¹ (at 25 °C). The expected responses of ISEs are demonstrated in Fig. 7, using dotted lines to depict two extreme cases ($a_I = 0$ and $a_J = 0$).

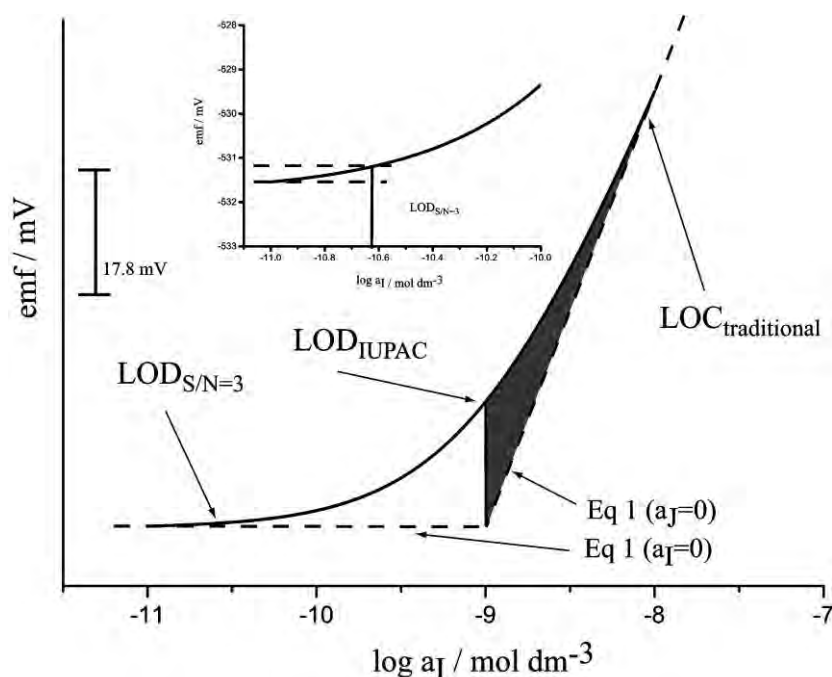


Fig. 7. Response curve of ISEs (full line) and extrapolation of the responses in the cases of $a_I = 0$ and $a_J = 0$ in Eq. (1) (dashed lines; traditional detection limit is defined as the cross-section of these two lines (LOD_{IUPAC}). Shaded area indicates the bias obtained in a determination of unknown activity if it falls in the region between LOD_{IUPAC} and $LOC_{traditional}$. Inset – illustration of the detection limit defined as signal-to-noise ratio $S/N = 3$.

The crossing-point of the two lines (10^{-9} in the figure above) is defined as the limit of detection according to IUPAC (LOD_{IUPAC}). The concentration is then estimated by the Nernst Equation above LOD_{IUPAC} . Due to the substantial

bias between the ISE response (Eq. (1)) and the Nernst Equation near LOD_{IUPAC} (shaded area of Fig. 6), ISEs have been considered useful only if the lowest expected level of target analyte is about an order of magnitude higher than the LOD . Such a value can be defined as the limit of quantification (LOC). This was quite acceptable in clinical analysis where levels of blood electrolytes are typically 2–3 orders of magnitude higher than traditionally achievable $LODs$. However, the prospect of application of ISEs in environmental analysis increased the importance of utilization of the entire response curve and required improvement of the precision of the determination at levels near the LOD . The luxury of neglecting a usable signal above the noise levels is not acceptable for *in situ* deployed devices. Therefore it is critical to work on methodologies that would utilize the entire response curve, eliminate the bias introduced by the curvilinear response range and improve the precision of analysis. If an ISE with noise ≈ 0.1 mV is considered and the general analytical chemistry definition of LOD (three times the standard deviation of noise, $LOD_{S/N=3}$) is used, then the LOD is orders of magnitude lower than LOD_{IUPAC} . Furthermore, if the bias is eliminated, then quantification can extend all the way to $LOD_{S/N=3}$.

4.1. Modelling the response curve

One solution to the problem of biased results near the LOD is utilizing theoretical models of the ISE response.^{19,69} These allow modelling of the entire response curve using experimentally available parameters, hence eliminating the bias due to the deviation from the straight line. Unfortunately, such models are limited only to liquid-contact electrodes since currently there is no suitable experimental methodology to obtain certain parameters in solid-contact electrodes. Current trends of miniaturization of ISEs and transition to solid-contact electrodes (for more details on solid- and liquid-contact electrodes please read the section Sensing Platform Designs) dictate that until such methods are developed, non-linear empirical formulas are more suitable for modelling the full response of ISEs. In our work we have used the following formula:

$$E = E^0 + \beta_1 * \log(a_1 + \beta_2) + \varepsilon \quad (2)$$

Equation (2) represents Eq. (1) where β_1 is equal to the slope parameter related to the temperature and charge of the primary ion, a_1 is the activity of the primary ion, β_2 relates to the selectivity and activity of interfering ions and the error ε is assumed to follow a normal distribution with variance σ^2 .

An added benefit of non-linear modelling of the entire response curve is the ability to obtain a revised LOD defined by the signal-to-noise ratio (*i.e.*, $LOD_{S/N=3}$). This ultimately expands the useful range of ISEs by more than two orders of magnitude (see the span from $LOD_{S/N=3}$ to $LOC_{traditional}$ in Fig. 7), while simultaneously removing the bias near the LOD . The benefits of using the entire response curve and $LOD_{S/N=3}$ vs. a traditional analysis were explored by

comparing the analysis results using data from ISEs in a soil analysis.⁴⁹ The empirical model (Eq. (2)) and $LOD_{S/N=3}$ were used to determine the level of Pb in digested soil samples. The results were then compared to results obtained using the traditional treatment (*i.e.*, using linear regression in the Nernstian range above LOD_{IUPAC}), and to reference results obtained using AAS. As expected, the results did not differ in the case of samples containing values of Pb falling in the Nernstian response range. However, in two cases, the values of the sample were in the curvilinear part of the response curve. With the linear regression treatment, results were rendered biased and/or below LOD . However, by utilizing non-linear regression the bias was removed and the results approached the reference results obtained using AAS. That is, it was possible to extend the useful range of the ISEs simply by using Eq. (2) and $LOD_{S/N=3}$ in place of the Nernstian approximation and LOD_{IUPAC} .

4.2. Calibration and precision of ISES

Unlike other analytical techniques, ISEs have an extremely large measurement range. Hitherto, the largest reported spans twelve orders of magnitude,¹² although measurement ranges spanning eight to nine are more common. Unfortunately, this benefit is offset by lower precision. The slope of $59.2/z$ mV decade⁻¹ and the noise in the region of 0.1 mV indicate that reporting results with more than two decimal places may be quite problematic. Therefore, ISEs are typically considered as a tool for routine measurements and as early warning systems.

On the other hand, typical ISE calibration protocols used in estimation of unknown activities of analytes provide only a single value for measured activities (for both calibration point and unknown sample) not estimates of measurement uncertainty. Since no estimate of uncertainty is given, these so called “point estimates” imply a level of precision that is not achieved with ISEs. With increased importance of ISEs in environmental analysis, estimates of precision become critical, especially in the analysis of samples in which the values approach regulatory limits. In this respect, methods of statistical calibration are becoming increasingly popular in the analysis of chemical data,^{70,71} including ISEs.⁷²

A very interesting approach to statistical calibration is the use of a Bayesian model for the non-linear response of ISEs.⁷³ The power of this approach is that realistic estimates of measurement uncertainty are returned and information from redundant ISEs can be used to easily improve measurement precision and to identify and discard data from failing electrodes.

Bayesian statistical analysis is based on the concept of prior knowledge or beliefs about random variables ($\Pr(A)$) being combined with a model relating data to those variables ($\Pr(B|A)$) to form updated beliefs about the variables, given the collected data ($\Pr(A|B)$). The updated beliefs are called the posterior probability distribution of event A given event B. This can be present as:

$$\Pr(A|B) \propto \Pr(B|A)\Pr(A) \quad (3)$$

In the context of ISE calibration, A represents the unknown variables (analyte concentrations and calibration parameters), while B represents the data (all calibration data and sample emf values).

A model for single or multiple ISEs being used to measure the same sample was developed and extended to include standard addition data.⁷³ Inclusion of multiple ISEs increases the overall precision of the analysis even though each ISE will have different calibration parameters and levels of precision. This is done by down-weighting poor-performing ISEs and incorporating asymmetry in calibration intervals into the final calibration interval. Inclusion of standard addition data minimizes bias due to electrode drift. The method was developed using the OpenBUGS variant (version 3.0.3) of BUGS, linked to R using the R2WinBUGS library and the code is available in Dillingham *et al.*⁷³ Moreover, additional software was developed in R (www.r-project.org) to create a user-friendly implementation of these models, and is available, along with a tutorial, at: <http://turing.une.edu.au/~pdilling/calibration.html>. The Bayesian calibration method was used to analyse levels of lead in 17 soil samples collected from the abandoned mining site near Silvermines, Co., Tipperary, Ireland. The standard technique was used to collect and store samples that were digested by sonication of 1 g of sample in 1.0×10^{-3} M nitric acid. This method of digestion was shown to be a good compromise between satisfactory detection limit, sufficient extraction of metal ions from the soil and limited effect on the ISE lifetime.⁷⁴

Results using ISEs were obtained using the standard addition method. Briefly, the calibrated electrodes were immersed in a predetermined volume of the sample. After a baseline had been recorded, an aliquot of standard Pb^{2+} solution was added and a second reading was obtained and the unknown activity of Pb^{2+} was calculated.

Figure 8 depicts estimates of Pb^{2+} in the soil samples using three individual ISEs (Fig. 8a–c) compared with the ones obtained when all three ISEs were incorporated into the multiple-ISE model (Fig. 8d).

By observing the error bars, it could be seen that long tails, asymmetry, and extreme variability in the width of calibration intervals considerably decreases in the multiple-ISEs model. Although the ISEs varied substantially in response and $LOD_{S/N=3}$, the final estimate was much more precise than the estimate from any single ISE. This shows that the final precision of the multiple ISE model was not driven by one ISE of high quality, but took advantage of information from each electrode. Fig. 8 also shows that the ISE with the lowest $LOD_{S/N=3}$ is not necessarily the best ISE to use when making single ISE measurements. Although ISE#3 has nearly an order of magnitude better estimated LOD than the other two electrodes, it was much noisier and therefore gave less precise estimates. By

combining the response of all three electrodes, the model takes advantage of the low $LOD_{S/N=3}$ of ISE#3 and the high precision of ISEs#1 and #2. It should be noted that the appropriate LOD for the multiple ISE model is unclear and the lowest $LOD_{S/N=3}$ is displayed for reference only.

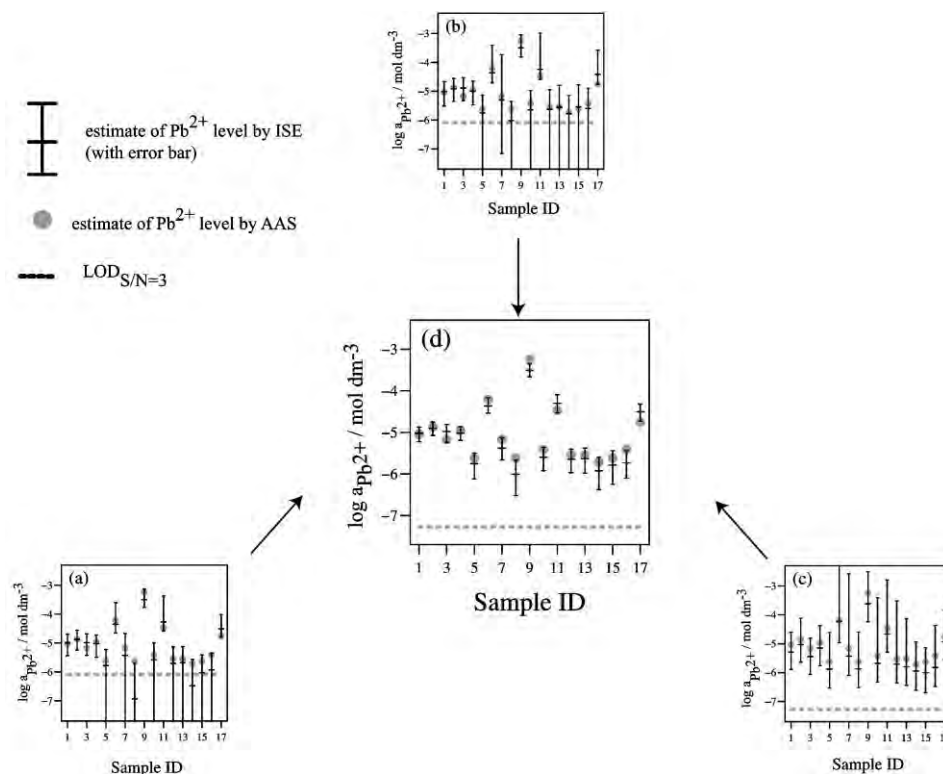


Fig. 8. Estimations of Pb^{2+} in each soil sample from individual ISEs (a–c) and the combined response (d) using standard addition. The error bars indicate 95 % confidence intervals; mid-line dashes indicate the point estimate obtained by the ISEs. The closed circles are estimates obtained using AAS. $LOD_{S/N=3}$ (dashed line) are presented for comparison.

5. REFERENCE ELECTRODE

Interestingly, while the research in the field of ISEs and their application in environmental analysis are vigorous, the pace of the transition from controlled laboratory conditions to the real-life application does not follow the amount of breakthroughs in ISEs' performance. This is partly related with the need for collaborative effort between chemists and mechanical and electronic engineers in order to develop deployable devices capable of autonomous sensing.^{61–63,75}

Another factor inhibiting progress is often the unsatisfactory robustness of reference electrodes (REs). While there are many examples of design and application of reference electrodes in deployable and/or miniaturized sensing devices,

they are often limited to a particular design and/or application. The limitations may be grouped around the mechanism of action of REs and their fabrication. In a review of REs, Bakker nicely outlines several concepts of their action mechanisms. One of the most promising is the one based on the phase boundary potential equation:

$$E_{\text{PB}} = \frac{RT}{z_1 F} \ln \left(\frac{k_1 a_1}{\gamma [I^{z_1}]} \right) \quad (4)$$

where a_1 is the activity of an ion of charge z_1 in the sample phase boundary, γ_1 , and $[I^{z_1}]$ are the activity coefficient and the concentration of the free ion I^{z_1} in the organic membrane phase boundary, and R , T , and F are the gas constant, the absolute temperature and the Faraday constant, respectively. The E_{PB} in this system is defined by the degree of partition of the lipophilic electrolyte from the membrane into the sample. In essence, the membrane is doped with a lipophilic electrolyte capable of partitioning into the sample. Since the ions of the used electrolyte are not present in the sample, the concentration of ions in the membrane and in the sample is constantly rendering the E_{PB} of the RE constant, thus enabling its use as the RE. This basic idea was used by several authors to demonstrate simple REs, for example by doping a membrane with lipophilic salts.^{76–80}

In order to achieve truly low-cost potentiometric sensor fabrication of REs, they must be simple, cost-effective, and compatible with mass-production techniques. Ideally, the fabrication of both ISEs and REs should be compatible with the existing production lines with minimal adjustments.

Our approach to development of new REs consisted of tackling both issues simultaneously.⁸¹ Encouraged by the success in the development of miniaturized platforms suitable for mass-production based on the screen-printing technology (as described in the Section 3), we were driving the development of REs that could utilize the same platform as ISEs. The aim was to fabricate both electrodes using identical platform and prepared using the same protocol. In the preparation of REs, the aim was to use a material that acts as a matrix and serves as the source of ions that could partition into the sample, thus defining E_{PB} , instead of doping the membrane with a lipophilic electrolyte. Ionic liquids (ILs) are excellent candidates for such materials. It was shown that they can behave as plasticizers,⁸² simple salt bridges and liquid-junction-free REs.^{83–85} In continuation of these ideas, we experimented on the use of a variety of ILs containing imidazolium ([Rmim] where R stands for C₂, C₄, C₆, C₈ or C₁₂ substituents at position 1), phosphonium ([P_{4 4 4 14}]⁺ or [P_{6 6 6 14}]⁺) and ammonium ([N_{1 8 8 8}]⁺) cations and the bis(trifluoromethanesulphonyl) amide [NTf₂][−] anion. The membranes were prepared by mixing an appropriate IL with PVC in the traditional mass ratio 66:33 of plasticizer. It was found that [C₂mim][NTf₂] showed the best performance as a RE. The responses of [C₂mim][NTf₂]-based RE compared to com-

mercially available Methrom Ag/AgCl double junction and solid-state (REFEX Sensors, Ltd.) reference electrodes are depicted in Fig. 8A–C. The stability of the signal was tested using three different protocols. Electrodes were tested for long-term response upon changing the concentration of the same electrolyte, the influence of larger concentration differences and mobilities of ions, and dynamic response (response occurring within seconds after the electrolyte change). The [C₂mim][NTf₂]-based RE shows remarkable stability, comparable to those of commercially available REs.

In order to demonstrate the utility of the [C₂mim][NTf₂]-based RE, it was employed in various electrochemical techniques and its performance was evaluated against the traditional Ag/AgCl double junction RE. Figure 9 depicts the application of [C₂mim][NTf₂]-based RE in potentiometry (Fig. 9D), voltammetry (Fig. 9E) and electrochemical impedance spectroscopy (Fig. 9F). Excellent stability and correspondence of the signal is obvious in all three cases.

It is noteworthy that the [C₂mim][NTf₂]-based RE was prepared on a screen-printed platform by simple drop-casting of the membrane components, as explained in the Section 3. This allows preparation of a disposable potentiometric sensing system where both electrodes (ISE and RE) are prepared using the same protocols (drop-casting membrane cocktail on the identical platform). Advances in ink-jet printing of polymers could further simplify the process and result in fully automated, mass-production of extremely low-cost, yet ultra-sensitive potentiometric sensing systems.

6. REDUCING THE NEED FOR CALIBRATION AND DIAGNOSTIC OF SENSOR FUNCTIONALITY

The need for regular calibration and the cost associated with it is the major limitation in development of fully autonomous sensing devices. There are issues from the point of view of electronic platforms (matching of hierarchies, data safety, *etc.*) as well as from a chemistry perspective (*e.g.*, cost issues mainly associated with calibration involving calibration solutions, pumps, waste, *etc.*).⁷⁵ Many different groups are exploring a wide variety of approaches to develop sensors with reduced need for calibration or completely calibration-free sensors.⁸⁶ The subject of a completely calibration-free sensor is somewhat esoteric since all sensors need calibration at least at some point. Some interesting concepts have emerged that suggest using materials the properties of which can be switched using external stimulus in the description of calibration-free sensors.^{59,87–90} However, with regards to the employment of ISEs in environmental analysis, some technological solutions for significantly reducing the need for calibration have been explored.

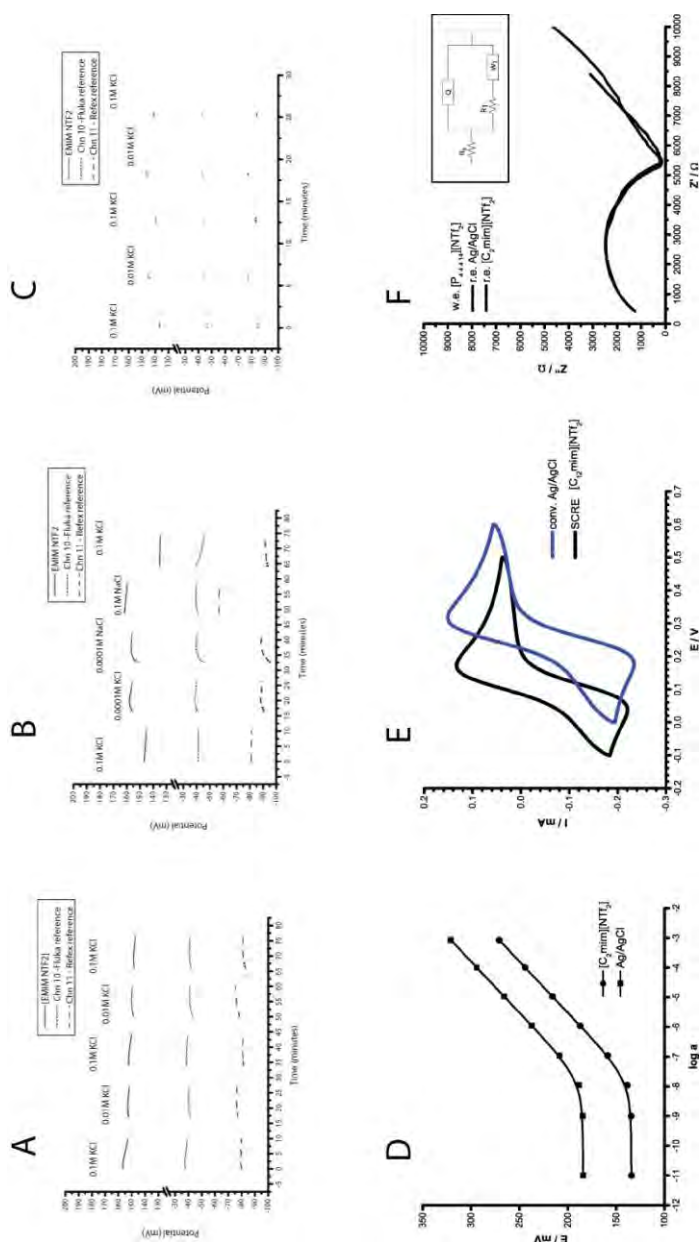


Fig. 9. Top: potentiometric responses of a [C2mim][NTf2]-based SCRE (full line) compared with responses of Methrom Ag/Ag/Cl (dashed line) and REFEX (dotted line) reference electrodes. A) Potential responses on the test for long-term response upon changing the concentration of the same electrolyte. B) Potential responses based on the influence of larger concentration differences and mobilities of ions. C) Dynamic response (response occurring within seconds after an electrolyte change). Bottom: Application of IL-based reference electrode in various electrochemical techniques and its comparison with traditional Ag/AgCl RE. D) IL-Based RE in potentiometry for the determination of Pb²⁺. E) Cyclic voltammograms of the Fe^{III}(CN)₆³⁻/Fe^{II}(CN)₆⁴⁻ redox couple. F) Nyquist plot of PVC-[P₄4.4.14][NTf₂] membrane recorded vs. IL-based RE (dashed line) and Ag/AgCl electrode (full line).
 Inset: equivalent circuitry used to fit the experimental data.

6.1. Reducing the need for calibration by producing sets of identically performing sensors

The introduction of technologies for the mass-production of sensors triggered the expectation of nearly identical response profile of all electrodes produced in the same batch. Reinforced by the fact that sensors produced on mass scale would be disposable, only one electrode from each batch would need to be calibrated, while all the others would be used only once with their response pattern corresponding to the single calibrated electrode. This approach is employed very successfully in the clinical area, in which single use disposable sensors are commonplace. However, the translation of this approach to the environmental arena remains difficult, due to the lower concentrations of the primary target ions and matrix effects, which require a more complex calibration protocol to enable the low-limit-of-detection capability of ISEs to be exploited. Unfortunately, it appears that obtaining solid-contact ISEs with reproducible standard potentials is still quite a challenge.¹⁴ The non-optimised protocol for the deposition of the intermediate layer and the ion selective membrane is one of the issues. The evolution of the reproducibility of the signal across a set of electrode with optimization of the polymer deposition process is shown in Fig. 10.

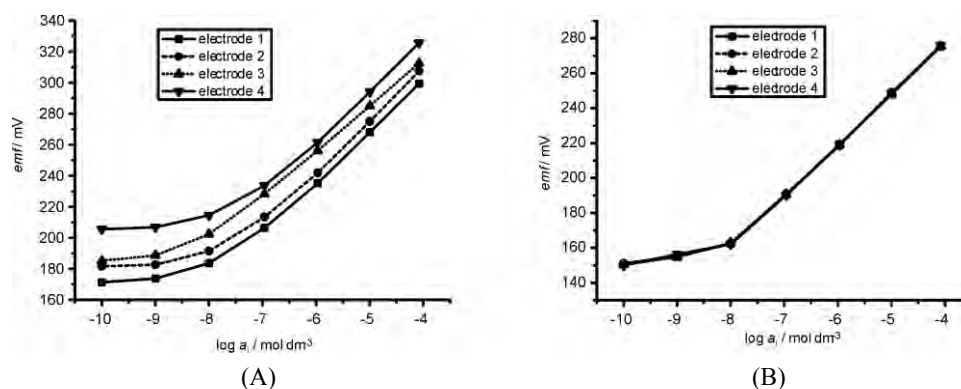


Fig. 10. Calibration curves of solid-contact ISEs. A) Without careful control of the drop-casting of conducting polymer step. B) Electrodeposited conducting polymer.

When the ISEs were produced without careful control of step of drop-casting polymers onto screen-printed electrodes, the baseline, slope and LODs are misaligned (Fig. 10A). On the other hand, careful manual deposition of intermediate layer can produce response curves that differ only in the baseline (data not shown). Finally, electrodeposition of the intermediate layer on the electrodes produced in the same batch of screen-printing results in response curves that are superimposed and with virtually no offset (Fig. 10B). These electrodes were suc-

cessfully utilized for the determination of Pb^{2+} in environmental samples, as described in the Section 3.3.

6.2. Diagnostic of sensor functionality

In another approach, the electronic signal was used to probe the performance of sensors.⁹¹ Since the response of ISEs depends on processes at sample/membrane interface, changes on the membrane surface are likely to influence the response characteristics of a device. For example, deployed sensors could be easily physically damaged due to contact with debris present in the water. Membrane components may leach and affect the bulk composition of sensing membrane. Perhaps one of the most significant factors influencing the performance of *in situ* deployed sensors is biofouling. Every year, millions of Euros are spent in active sensor maintenance and in research on combating biofouling. A common denominator of these factors is the influence they can exert on the resistance and capacitance of a membrane. Therefore, we suggested that electrochemical impedance spectroscopy (EIS) could provide important information on membrane composition and sensor functionality. We attempted to find the optimal parameters of a simple circuitry capable for the generation of an AC signal and utilize it for simple diagnostics of the functionality of a sensor and argued that the ability to very quickly and simply diagnose the functionality of ISEs without classical calibration could simplify fabrication and operation of the sensing device. Multiple sets of miniaturized, solid-contact ISEs were prepared using the screen printing technology as described elsewhere.⁵⁵ In order to mimic potential physical damage, the electrodes were punctured and cut to inflict damage to the membrane surface. For mimicking leaching of the membrane components, major membrane constituents known to be of fundamental importance for electrode response (ionophore and/or ionic sites) were intentionally excluded. Biofouling was studied by exposing electrodes to microbe-rich natural water for predestined periods. For each of the mentioned conditions, the potentiometric response was recorded together with impedance spectra analysis. The loss of potentiometric functionality was evident through the diminishing of the slope and *LOD* (Fig. 11 A–C) and could be easily related with concomitant changes in the resistance and capacitance of the membrane. By careful analysis of the impedance spectra, critical parameters could be identified for which changes in impedance could be easily related with the loss of potentiometric functionality. Specifically, it was identified that the change of impedance could be monitored at a single frequency and excitation signal. For example, Fig. 11D–F depict changes in impedance at 1 Hz with an excitation signal of 100 mV of electrodes that were subjected to severe mechanical damage, biofouling and leaching of membrane components.

The difference in time that measurable change may occur could also be an important indication of the nature of process that affects the potentiometric res-

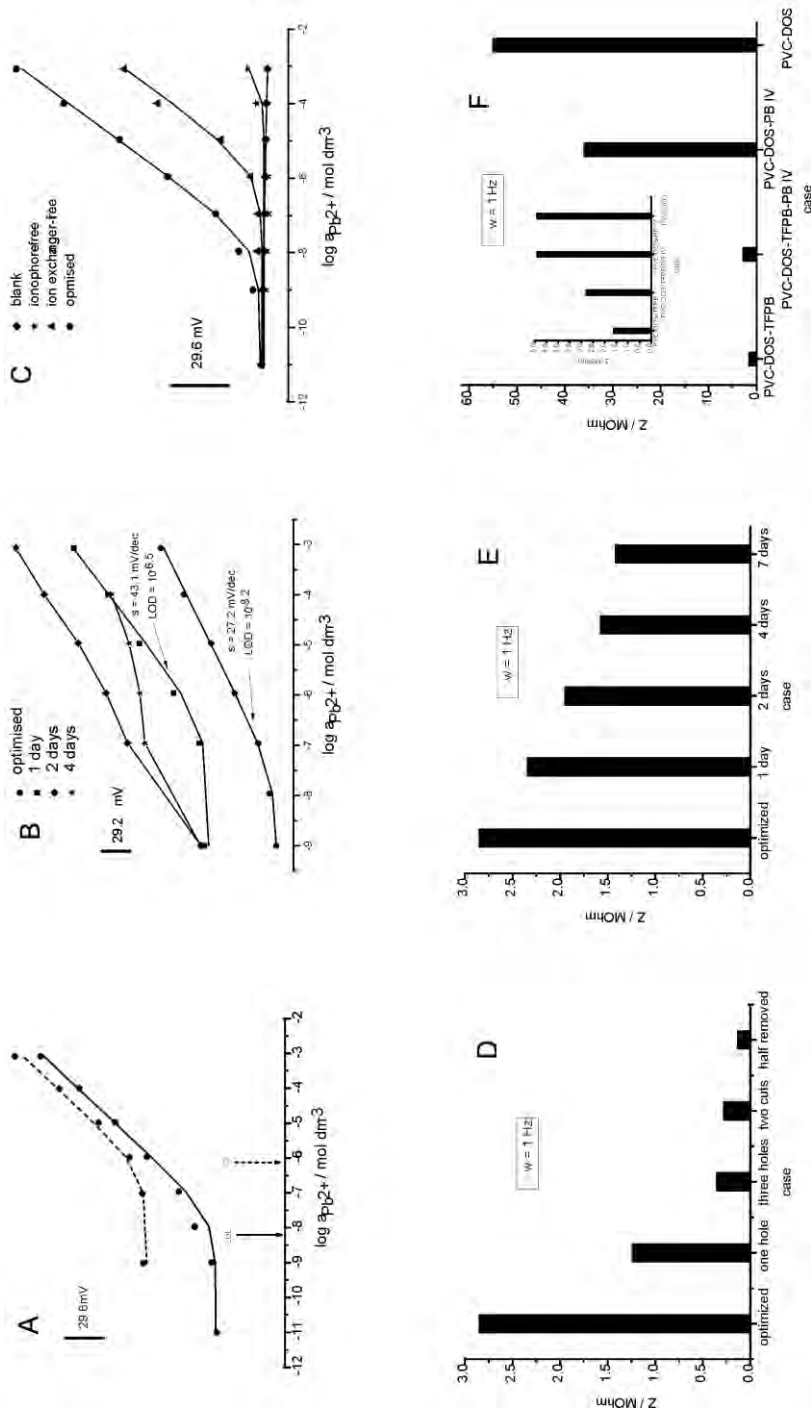


Fig. 11. Top: potentiometric response of: A) mechanically damaged ISEs, B) deterioration of the potentiometric response of ISEs due to biofouling over the course of several days and C) potentiometric responses of ISEs missing membrane components, thereby mimicking the process of their leaching. Bottom: D) impedance of mechanically damaged ISEs, E) reduction of impedance of ISEs corresponding to the loss of potentiometric response due to biofouling and F) impedance of ISEs that are missing membrane components.

ponse. A continuous and gradual change over a relatively short period (a few days) is a good indication that biofouling hampers the functionality. On the other hand, a continuous and gradual change occurring over a long time (a few months^{92,93}) indicates leaching of the membrane components. Finally, a sudden change indicates physical damage. Therefore, we argued that a microfluidic chip that integrates ISEs with a simple AC-generating circuitry using a single frequency and excitation signal could be used as a very simple diagnostic tool for the functionality of sensors. By periodically checking the impedance, the user can generate information about the functionality of the sensor system. Based on the obtained information, a built-in local intelligence could make a decision whether the systems requires calibration under the current state of the sensor. Consequently, a slight increase in sophistication could significantly reduce the size and cost of the operation and maintenance of devices.

7. FUTURE TRENDS

Since the breakthrough in lowering the *LOD* of ISEs, many serious strides were made towards real-life application of ISEs in environmental analysis. In the opinion of the authors, there will be three important avenues for further development of ISEs as environmental analytical tools. These avenues will be increasing the importance of technology, development of novel methodologies and utilization of new materials in order to achieve, low-cost and robust analytical devices.

7.1. Technology

Modern polymer membrane-based ISEs possess excellent analytical attributes in terms of selectivity and *LOD*. Interestingly, while conditioning and storage protocols are very important in achieving optimal *LODs*, guidelines for standardizing such protocols are not widely agreed.⁶⁸ Some interesting steps were taken by the group of Michalska, who realized that potential stability of ISEs prepared using two different conductive polymers (CPs) strongly depended on the storage conditions.^{94,95} On the other hand, long-term deployment and remote, real-time monitoring (*e.g.*, as part of WSNs) could be quite problematic due to fouling of the sensors with biological films, as well as the need for their calibration. It is expected that future research will involve integration of ISEs within microfluidic devices⁹⁶ capable of directing the flow of sample and calibration solutions according to the analytical needs. The effects of hydrodynamic flow showed very desirable effects in rotational disc electrode (RDE), flow injection analysis (FIA) and continuous flow analysis (CFA) in both detection limit and adsorption phenomena.^{35,97–99} Utilization of microfluidic platforms with built-in intelligence would therefore be capable of utilizing both hydrodynamic flow and automated methodologies for storage and calibration.

7.2. Analytical methodologies

Complex matrixes, extremely low activity of target analyte and the need for calibration render the application of direct potentiometry in environmental analysis quite limited. We are already witnessing the development of very interesting and exciting methodologies that could overcome these issues. Backside calibration as reported by Malon *et al.*¹⁰⁰ is a very interesting approach capable of evaluating the response of liquid-contact ISEs through a variation of in the composition of inner filling solution. Another very interesting concept for achieving chemical amplification is named switchtrodes.¹⁰¹ With this method, two polymer membrane ISEs are programmed to give kinetically controlled detection limits so as to produce a peak-shaped differential signal between the electrode pair when the activity of the sample is resonant with the intermediate activity required for switchtrode response. Since ISEs are in the super-Nernstian response mode, a switchtrode expresses chemical amplification. Like all electrochemical sensors, ISEs are excellently suited for use in “electronic tongues” where an array of carefully selected ISEs with appropriate cross-sensitivities may be used to establish response patterns that could be analysed using principal component analysis, artificial neural networks, partial least squares regression, *etc.*¹⁰²

In the authors’ opinion, a very important trend of the utilization of ISEs as detectors in a combination of techniques (analogous to hyphenated techniques) is currently being witnessed. Extremely sensitive ISEs are demonstrated as highly sensitive detectors in combination to nano-labels for immuno-analysis^{103–106} and DNA analysis.^{107,108} A very interesting approach for the elimination of the matrix effect was reported in the groups of Wang and Bakker. Highly sensitive Cd-selective electrodes were coupled with stripping voltammetry in the analysis of sea water. Accumulation of Cd from sea water using stripping voltammetry was performed prior to the release of Cd into a buffer solution where its concentration was determined using ISEs. This effectively eliminated the matrix and resulting analysis was by far more sensitive than either of the two employed techniques alone.¹⁰⁹ On the other hand, coupling ISEs with thin layer coulometry promises achievement of robust, calibration-free sensors that are highly attractive where recalibration *in situ* is difficult or undesirable.^{110–112}

7.3. Materials

Various materials had a deterministic influence on ISEs, starting from pH-sensitive glass to polymer membranes. Over the course of the development of the field of potentiometric sensors, many different materials played a very important role. For example, conducting polymers are currently a staple in the preparation of solid-contact electrodes. They serve as a lipophilic intermediate layer that enables transition from electronic-to-ionic conductivity and block the formation of water layer between ion selective membrane and metallic electrode; hence

enabling the realization of solid-contact electrodes with trace level sensitivity.¹¹³ Carbon nanotubes are increasingly finding their way into ISEs as intermediate layers due to their lipophilic and conducting properties.^{114,115}

A methyl methacrylate–decyl methacrylate (MMA–DMA) copolymer was used to produce toughened much more robust polymer membrane-based ISEs with excellent time responses and reproducibility.¹¹⁶ Moreover, new di- and tri-block copolymers introduce new dimension in improving the physico-chemical properties of ISEs.¹¹⁷ Thus, it is reasonable to expect that such copolymers will gain strong ground in future research.

Perfluorinated materials present a very interesting alternative to traditional materials used in ISEs. They are extremely hydrophobic, for example on the π^* scale of solvent polarity, water has a π^* value of 1, cyclohexane defines 0, and perfluoro-octane has a value of -0.41 .¹¹⁸ Such tremendous hydrophobicity is evidenced through exceptionally strong ion pair formation and more importantly great improvement in selectivity.^{119–123}

Another very interesting and promising class of materials are ionic liquids. They can be used as plasticizers, ion exchangers and ionophores.^{124,125} ILs demonstrate large variations in polarity and viscosity hence demonstrate significant influence on selectivity and sensitivity.¹²⁶ Moreover, the relative ease of the preparation of new ILs and their intrinsic conductivity present excellent fundamentals for modulating physico-chemical properties of the membrane, thereby opening new avenues for development and application of ISEs.

8. CONCLUSIONS

In summary, ISEs are making significant strides towards becoming a very important tool in environmental analysis. While many issues indeed exist, the energy and the pace of research addressing these issues are very promising. This conclusion indicates the importance of fundamental research in nanotechnology as a key strategy to the design, development, and engineering of sensing layers capable of addressing these critical needs.

Acknowledgments. The corresponding author gratefully acknowledges support from Keele University and Royal Society (RG120118).

ИЗВОД

ЈОН-СЕЛЕКТИВНЕ ЕЛЕКТРОДЕ У АНАЛИЗИ ЖИВОТНЕ СРЕДИНЕ

ALEKSANDAR RADU¹, TANJA RADU², CHRISTINA MCGRAW³, PETER DILLINGHAM⁴,
SALZITSA ANASTASOVA-IVANOVA⁵ и DERMOT DIAMOND⁶

¹Keele University, Birchall Centre and Environment, Physical Sciences and Mathematics (EPSAM) Research Institute, Lennard-Jones Labs, Stoke-on-Trent, ST5 2BG, United Kingdom, ²Loughborough University, School of Civil and Building Engineering, Loughborough, LE11 3TU, United Kingdom, ³Institute for Marine and Antarctic Studies (IMAS), University of Tasmania, Private Bag 129, Hobart 7005, Tasmania, Australia, ⁴University of New England, School of Science and Technology, Armidale, Australia, ⁵Queen Mary University London, School of Engineering and Mathematical Sciences, London, E1 4NS, United Kingdom и ⁶National Centre for Sensor Research, CLARITY Centre for Sensors Web Technologies, Dublin City University, Dublin 7, Ireland

Овај чланак даје преглед радова који се баве применом јон-селективних електрода (ISA) у анализи животне средине. ISA су стављене у контекст тренда за развој сензора за обимна и честа мерења. Разматране су теме као што су носачи сензора и њихове масовне производње, побољшање прецизности сензора, дијагноза њихове функционалности као и развој референтних електрода. Анализа ових тема је дата кроз примере примене ISA у анализи животне средине. Главни акценат овог чланка је стављен на сумирање резултата рада потписника овог текста у последњих неколико година.

(Примљено 29. августа, ревидирано 26 септембра 2013)

REFERENCES

1. M. Cremer, *Z. Biol.* **47** (1906) 562
2. M. S. Frant, *Analyst* **119** (1994) 2293
3. S. F. Martin, *J. Chem. Educ.* **74** (1997)
4. Final Report of the Expert Group for Silvermines County Tipperary, *Lead and Other Relevant Metals*, Office of Environmental Enforcement, EPA, 2004
5. W. K. Lutz, H. K. Wipf, W. Simon, *Helv. Chim. Acta* **53** (1970) 1741
6. L. A. R. Pioda, A. H. Wachter, R. E. Dohner, W. Simon, *Helv. Chim. Acta* **50** (1967) 1373
7. Z. Stefanac, W. Simon, *Chimia* **20** (1966) 436
8. *In-Vitro Diagnostic (IVD) Market (Applications, End-users & Types) Trends & Global Forecasts (Major & Emerging Markets – G7, Japan & BRIC) (2011–2016)*, 2012, www.marketsandmarkets.com
9. E. Bakker, E. Pretsch, *Angew. Chem. Int. Ed.* **46** (2007) 5660
10. E. Bakker, P. Buhlmann, E. Pretsch, *Electroanalysis* **11** (1999) 915
11. E. Bakker, E. Pretsch, *Advances in Potentiometry*, In *Electroanalytical Chemistry: A Series of Advances*, Vol 24, A. J. Bard, C. G. Zoski, Eds., CRC Press, Boca Raton, FL, 2011, p.p. 1–74
12. T. Sokalski, A. Ceresa, T. Zwickl, E. Pretsch, *J. Am. Chem. Soc.* **119** (1997) 11347
13. E. Bakker, P. Buhlmann, E. Pretsch, *Talanta* **63** (2004) 3
14. J. Bobacka, A. Ivaska, A. Lewenstam, *Chem. Rev.* **108** (2008) 329
15. R. De Marco, G. Clarke, B. Pejcic, *Electroanalysis* **19** (2007) 1987
16. A. Radu, D. Diamond, *Ion-selective electrodes in trace level analysis of heavy metals: potentiometry for the XXI century*, In *Comprehensive Analytical Chemistry*, D. Barcelo, Ed., Vol. 49, *Electrochemical sensor analysis*, S. Alegret, A. Merkoci, Eds., Elsevier, Oxford, 2007, p. 25

17. R. Murray, *Anal. Chem.* **82** (2010) 1569
18. C. Zuliani, D. Diamond, *Electrochim. Acta* **84** (2012) 29
19. A. Ceresa, A. Radu, S. Peper, E. Bakker, E. Pretsch, *Anal. Chem.* **74** (2002) 4027
20. A. Radu, S. Peper, E. Bakker, D. Diamond *Electroanalysis* **19** (2007) 144
21. A. C. Ion, E. Bakker, E. Pretsch, *Anal. Chim. Acta* **440** (2001) 71
22. A. Malon, A. Radu, W. Qin, Y. Qin, A. Ceresa, M. Maj-Zurawska, E. Bakker, E. Pretsch *Anal. Chem.* **75** (2003) 3865
23. Z. Szigeti, I. Bitter, K. Tóth, C. Latkoczy, D. J. Fliegel, D. Günther, E. Pretsch, *Anal. Chim. Acta* **532** (2005) 129
24. A. Radu, S. Peper, C. Gonczy, W. Runde, D. Diamond, *Electroanalysis* **18** (2006) 1379
25. W. Qin, T. Zwickl, E. Pretsch, *Anal. Chem.* **72** (2000) 3236
26. T. Vigassy, C. Huber, R. Wintringer, E. Pretsch, *Anal. Chem.* **77** (2005) 3966
27. J. Buffle, R. S. Altman, M. Filella, A. Tessier, *Geochim. Cosmochim. Acta* **54** (1990) 1535
28. M. H. Hecht, S. P. Kounaves, R. C. Quinn, S. J. West, S. M. M. Young, D. W. Ming, D. C. Catling, B. C. Clark, W. V. Boynton, J. Hoffman, L. P. DeFlores, K. Gospodinova, J. Kapit, P. H. Smith, *Science* **325** (2009) 64
29. M.-J. Lin, A. Grandison, *Int. J. Dairy Technol.* **59** (2006) 192
30. N. On-Nom, A. Grandison, M. Lewis, *J. Dairy Sci.* **93** (2010) 515
31. P. Upreti, L. Metzger, P. Bühlmann, *Talanta* **63** (2004) 139
32. P. Buehlmann, E. Pretsch, E. Bakker, *Chem. Rev.* **98** (1998) 1593
33. R. De Marco, B. Pejčić, X. D. Wang, *Lab. Rob. Autom.* **11** (1999)
34. B. Pejčić, R. D. Marco, *Electrochim. Acta* **49** (2004)
35. A. Zirino, R. De Marco, I. Rivera, B. Pejčić, *Electroanalysis* **14** (2002) 493
36. A. Ceresa, E. Bakker, B. Hattendorf, D. Guenther, E. Pretsch, *Anal. Chem.* **73** (2001) 343
37. R. W. Cattrall, H. Freiser, *Anal. Chem.* **43** (1971) 1905
38. M. Fibbioli, W. E. Morf, M. Badertscher, N. F. de Rooij, E. Pretsch, *Electroanalysis* **12** (2000) 1286
39. M. Fibbioli, K. Bandyopadhyay, S. G. Liu, L. Echegoyen, O. Enger, F. Diederich, D. Gingery, P. Buehlmann, H. Persson, U. W. Suter, E. Pretsch, *Chem. Mater.* **14** (2002) 1721
40. J. Sutter, A. Radu, S. Peper, E. Bakker, E. Pretsch, *Anal. Chim. Acta* **523** (2004) 53
41. K. Y. Chumbimuni-Torres, N. Rubinova, A. Radu, L. T. Kubota, E. Bakker, *Anal. Chem.* **78** (2006) 1318
42. C.-Z. Lai, M. Joyer, M. Fierke, N. Petkovich, A. Stein, P. Bühlmann, *J. Solid State Electrochem.* **13** (2009) 123
43. T. Lindfors, H. Aarnio, A. Ivaska, *Anal. Chem.* **79** (2007) 8571
44. A. Michalska, C. Appaih-Kusi, L. Heng, S. Walkiewicz, E. Hall, *Anal. Chem.* **76** (2004) 2031
45. A. Michalska, J. Dumańska, K. Maksymiuk, *Anal. Chem.* **75** (2003)
46. N. Rubinova, K. Chumbimuni-Torres, E. Bakker, *Sensors Actuators, B* **121** (2006) 135
47. M. Vázquez, J. Bobacka, A. Ivaska, *J. Solid State Electrochem.* **9** (2005) 865
48. M. Vázquez, J. Bobacka, M. Luostarinen, K. Rissanen, A. Lewenstam, A. Ivaska, *J. Solid State Electrochem.* **9** (2005) 312
49. C. M. McGraw, T. Radu, A. Radu, D. Diamond, *Electroanalysis* **20** (2008) 340
50. O. Dominguez Renedo, M. A. Alonso-Lomillo, M. J. Arcos, Martinez *Talanta* **73** (2007) 202
51. J. P. Hart, A. Crew, E. Crouch, K. C. Honeychurch, R. M. Pemberton, *Anal. Lett.* **37** (2004) 789

52. M. Heule, S. Vuillemin, L. J. Gauckler, *Adv. Mater.* **15** (2003) 1237
53. F. Loffredo, A. D. G. Del Mauro, G. Burrasca, V. La Ferrara, L. Quercia, E. Massera, G. Di Francia, D. D. Sala, *Sensors Actuators, B* **143** (2009) 421
54. S. Anastasova, A. Radu, G. Matzeu, C. Zuliani, U. Mattinen, J. Bobacka, D. Diamond, *Electrochim. Acta* **73** (2012).
55. S. Anastasova-Ivanova, U. Mattinen, A. Radu, J. Bobacka, A. Lewenstam, J. Migdalski, M. Danielewski, D. Diamond, *Sensors Actuators, B* **146** (2010) 199
56. M. Kaku *Visions: How Science will Revolutionize the 21st Century*, Anchor Books, New York, 1997
57. B. Schazmann, D. Morris, C. Slater, S. Beirne, C. Fay, R. Reuveny, N. Moyna, D. Diamond, *Anal. Methods* **2** (2010) 342
58. J. R. Windmiller, J. Wang, *Electroanalysis* **25** (2013) 29
59. R. Byrne, D. Diamond, *Nature Mat.* **5** (2006) 421
60. D. Diamond, *Anal. Chem.* **76** (2004) 278A
61. J. F. van Staden, R. I. Stefan-van Staden, S. C. Balasoiu, *Crit. Rev. Anal. Chem.* **40** (2010) 226
62. R. Shepherd, S. Beirne, K. T. Lau, B. Corcoran, D. Diamond, *Sensors Actuators, B* **121** (2007) 142
63. C. Fay, S. Anastasova, C. Slater, S. T. Buda, R. Shepherd, B. Corcoran, N. E. O'Connor, G. G. Wallace, A. Radu, D. Diamond, *IEEE Sens. J.* **11** (2011) 2374
64. Commission on Analytical Nomenclature, *Pure Appl. Chem.* **48** (1975) 127
65. R. P. Buck, V. V. Cosofret, *Pure Appl. Chem.* **65** (1993) 1849
66. R. P. Buck, E. Lindner, *Pure Appl. Chem.* **66** (1994) 2527
67. Y. Umezawa, K. Umezawa, H. Sato, *Pure Appl. Chem.* **67** (1995) 507
68. E. Lindner, Y. Umezawa, *Pure Appl. Chem.* **80** (2008) 85
69. A. Radu, A. J. Meir, E. Bakker *Anal. Chem.* **76** (2004) 6402
70. D. B. Hibbert, N. Armstrong, *Chemom. Intell. Lab. Syst.* **97** (2009) 194
71. K. T. Lau, W. Guo, B. Kiernan, C. Slater, D. Diamond, *Sensors Actuators, B* **136** (2009) 242
72. L. T. Duarte, C. Jutten, S. Moussaoui, in *Lect. Notes Comput. Sc.*, T. Adali, C. Jutten, J. M. T. Romano, A. K. Barros, Eds., Springer, Berlin, 2009, pp. 662–669
73. P. W. Dillingham, T. Radu, D. Diamond, A. Radu, C. M. McGraw, *Electroanalysis* **24** (2012) 316
74. C. M. McGraw, T. Radu, A. Radu, D. Diamond, *Electroanalysis* **20** (2008) 340
75. D. Diamond, K. Lau, S. Brady, J. Cleary, *Talanta* **75** (2008) 606
76. T. Blaz, J. Migdalski, A. Lewenstam, *Analyst* **130** (2005) 637
77. D. Diamond, E. McEnroe, M. McCarrick, A. Lewenstam, *Electroanalysis* **6** (1994) 962
78. A. Kisiel, H. Marcisz, A. Michalska, K. Maksymiuk, *Analyst* **130** (2005) 1655
79. A. Kisiel, A. Michalska, K. Maksymiuk, E. A. H. Hall, *Electroanalysis* **20** (2008) 318
80. U. Mattinen, J. Bobacka, A. Lewenstam, *Electroanalysis* **21** (2009) 1955
81. D. Cicmil, S. Anastasova, A. Kavanagh, D. Diamond, U. Mattinen, J. Bobacka, A. Lewenstam, A. Radu, *Electroanalysis* **23** (2011) 1881
82. B. Peng, J. W. Zhu, X. J. Liu, Y. Qin, *Sensors Actuators, B* **133** (2008) 308
83. T. Kakiuchi, *Anal. Sci.* **24** (2008) 1221
84. T. Kakiuchi, T. Yoshimatsu, N. Nishi, *Anal. Chem.* **79** (2007) 7187
85. T. Yoshimatsu, T. Kakiuchi, *Anal. Sci.* **23** (2007) 1049
86. D. Diamond, S. Coyle, S. Scarmagnani, J. Hayes, *Chem. Rev.* **108** (2008) 652

87. A. Radu, A. Kavanagh, S. Scarmagnani, R. Byrne, N. Alhashimy, C. Slater, D. Diamond, in *Proceedings of PITTCON 2009 – 60th Pittsburg Conference on Analytical Chemistry and Applied Spectroscopy*, Chicago, IL, 2009
88. R. Byrne, S. Scarmagnani, A. Radu, F. Benito-Lopez, D. Diamond, (2009). *Schizophrenic Molecules and Materials with Multiple Personalities – How Materials Science could Revolutionise How we do Chemical Sensing*, MRS Proceedings, 1190, 1190-NN08-01 doi:10.1557/PROC-1190-NN08-01
89. A. Radu, R. Byrne, N. Alhashimy, M. Fusaro, S. Scarmagnani, D. Diamond, *J. Photochem. Photobiol., A* **206** (2009) 109
90. A. Radu, S. Scarmagnani, R. Byrne, C. Slater, K. T. Lau, D. Diamond, *J. Phys., D* **40** (2007) 7238
91. A. Radu, S. Anastasova-Ivanova, B. Paczosa-Bator, M. Danielewski, J. Bobacka, A. Lewenstam, D. Diamond, *Anal. Methods* **2** (2010) 1490
92. P. Buehlmann, Y. Umezawa, S. Rondinini, A. Vertova, A. Pigliucci, L. Bertesago, *Anal. Chem.* **72** (2000) 1843
93. S. Peper, Y. Qin, P. Almond, M. McKee, M. Telting-Diaz, T. Albrecht-Schmitt, E. Bakker, *Anal. Chem.* **75** (2003) 2131
94. A. Michalska, K. Pyrzyńska, K. Maksymiuk, *Anal. Chem.* **80** (2008) 3921
95. A. Michalska, M. Wojciechowski, E. Bulska, K. Maksymiuk, *Talanta* (2010)
96. B. Tossanaitada, T. Masadome, T. Imato, *Anal. Methods* **4** (2012) 4384
97. R. De Marco, R. Eriksen, A. Zirino, *Anal. Chem.* **70** (1998) 4683
98. R. DeMarco, D. J. Mackey, A. Zirino, *Electroanalysis* **9** (1997) 330
99. A. Radu, M. Telting-Diaz, E. Bakker, *Anal. Chem.* **75** (2003) 6922
100. A. Malon, E. Bakker, E. Pretsch, *Anal. Chem.* **79** (2007) 632
101. T. Vigassy, W. E. Morf, M. Badertscher, A. Ceresa, N. F. de Rooij, E. Pretsch, *Sensors Actuators, B* **76** (2001) 477
102. P. Ivarsson, Y. Kikkawa, F. Winqvist, C. Krantz-Rulcker, N. E. Hojer, K. Hayashi, K. Toko, I. Lundstrom, *Anal. Chim. Acta* **449** (2001) 59
103. K. Y. Chumbimuni-Torres, Z. Dai, N. Rubinova, Y. Xiang, E. Pretsch, J. Wang, E. Bakker, *J. Am. Chem. Soc.* **128** (2006) 13676
104. A. Numnuam, K. Y. Chumbimuni-Torres, Y. Xiang, R. Bash, P. Thavarungkul, P. Kanatharana, E. Pretsch, J. Wang, E. Bakker, *Anal. Chem.* **80** (2008) 707
105. J. Szucs, E. Pretsch, R. E. Gyurcsanyi, *Analyst* **134** (2009) 1601
106. R. Thuerer, T. Vigassy, M. Hirayama, J. Wang, E. Bakker, E. Pretsch, *Anal. Chem.* **79** (2007) 5107
107. K. Y. Chumbimuni-Torres, J. Wu, C. Clawson, M. Galik, A. Walter, G.-U. Flechsig, E. Bakker, L. Zhang, J. Wang, *Analyst* **135** (2010) 1618
108. J. Wu, K. Y. Chumbimuni-Torres, M. Galik, C. Thammakhet, D. A. Haake, J. Wang, *Anal. Chem.* **81** (2009) 10007
109. K. Y. Chumbimuni-Torres, P. Calvo-Marzal, J. Wang, E. Bakker, *Anal. Chem.* **80** (2008) 6114
110. E. Grygolowicz-Pawlak, E. Bakker, *Electrochim. Acta* **56** (2011) 10359
111. A. Shvarev, B. Neel, E. Bakker, *Anal. Chem.* **84** (2012) 8038
112. M. Sohail, R. De Marco, K. Lamb, E. Bakker, *Anal. Chim. Acta* **744** (2012) 39
113. J. Bobacka, *Electroanalysis* **18** (2006) 7
114. G. A. Crespo, S. Macho, J. Bobacka, F. X. Rius, *Anal. Chem.* **81** (2009) 676
115. Z. Mousavi, A. Teter, A. Lewenstam, M. Maj-Zurawska, A. Ivaska, J. Bobacka, *Electroanalysis* **23** (2011) 1352

116. S. Peper, A. Ceresa, Y. Qin, E. Bakker, *Anal. Chim. Acta* **500** (2003) 127
117. Y. He, P. G. Boswell, P. Buhlmann, T. P. Lodge, *J. Phys. Chem., B* **111** (2007) 4645
118. M. J. Kamlet, J. L. Abboud, R. W. Taft, *J. Am. Chem. Soc.* **99** (1977) 6027
119. P. G. Boswell, A. C. Anfang, P. Buehlmann, *J. Fluorine Chem.* **129** (2008) 961
120. P. G. Boswell, P. Buhlmann, *J. Am. Chem. Soc.* **127** (2005) 8958
121. P. G. Boswell, E. C. Lugert, J. Rabai, E. A. Amin, P. Buhlmann, *J. Am. Chem. Soc.* **127** (2005) 16976
122. C.-Z. Lai, S. S. Koseoglu, E. C. Lugert, P. G. Boswell, J. Rabai, T. P. Lodge, P. Buhlmann, *J. Am. Chem. Soc.* **131** (2009) 1598
123. C.-Z. Lai, M. E. Reardon, P. G. Boswell, P. Buehlmann, *J. Fluorine Chem.* **131** (2010) 42
124. B. Peng, J. Zhu, X. Liu, Y. Qin, *Sensors Actuators, B* **133** (2008) 308
125. J. Zhu, J. Zhai, X. Li, Y. Qin, *Sensors Actuators, B* **159** (2011) 256
126. A. Radu (unpublished data).



Fluorine adsorption on transition metal surfaces – A DFT study

IGOR A. PAŠTI^{1*}, NEMANJA M. GAVRILOV¹ and SLAVKO V. MENTUS^{1,2#}

¹University of Belgrade, Faculty of Physical Chemistry, Studentski trg 12–16,
11158 Belgrade, Serbia and ²Serbian Academy of Sciences and Arts,
Knez Mihajlova 35, 11000 Belgrade, Serbia

(Received 29 July, revised 21 September 2013)

Abstract: Based on density functional theory calculations, the adsorption of fluorine was investigated on a) Cu(111), Au(111), Pd(111) and Pt(111) surfaces, b) on Pd monolayer surfaces over Cu(111), Au(111) and Pt(111) surfaces and c) on the surfaces of Pd(111) monocrystals with an inserted metal monolayer (M = Cu, Au or Pt) underneath the first Pd surface layer. The results evidenced that the adsorption did not cause significant changes of the structural parameters of metallic substrate. The strongest adsorption, amounting to –4.49 eV, was calculated in the case of the Cu(111) surface. The Cu(111) and Au(111) surface atoms interact with F adatoms exclusively by the mediation of the *sp*-band, while the surface atoms of Pt and Pd-based surfaces interact with F adatoms additionally by the mediation of the *d*-band. In the case of Pt(111) and Pd_{ML}/M(111) surfaces, the binding energies correlated with the *d*-band center positions, which indicated a significant contribution of covalent interaction. These results confirmed that the nature of surface interaction of highly electronegative F atom with metallic surfaces depends significantly on the nature of the metal substrate.

Keywords: Fluorine, adsorption, electronic structure, adsorption trends

INTRODUCTION

Adsorption of halogen atoms and halide ions on metallic surfaces presents important questions in different fields, which have particular importance in electrochemistry. Namely, it is well known that adsorption of ions can significantly affect the properties of metal/solution interfaces and determine electrochemical behavior of a given electrode material.^{1,2} The active debate in the scientific community on the nature of adsorbed halogens has lasted since the very beginning of investigations of halogen–metal interactions. Some experiments indicated that the nature of the bond depended on the nature of the halogen atom. For example,

* Corresponding author. E-mail: igor@ffh.bg.ac.rs

doi: 10.2298/JSC130729095P

Serbian Chemical Society member.



Huemann *et al.*³ concluded that Cl–Cu(100) and I–Cu(100) interaction are prevalently ionic and covalent, respectively.

According to a review by Koper,⁴ the first topic of electrochemical importance investigated by *ab initio* calculations was the adsorption of halides on metallic surfaces. Special care in this sense was paid to the strength of the interaction, the preferred geometry and the effects of solvent and electric field, being important parameters of all metal–solution interfaces. Some of the first Hartree–Fock calculations for Ag,⁵ Hg^{6,7} and Cu⁸ substrates indicated a large ionicity of the adsorbed halogen. The theoretically established trends in halide adsorption on metallic substrates were found to oppose the experimental results, which was explained by the absence of a solvent,⁹ but its inclusion did not resolve the problem.¹⁰ The theoretical approach can enable the investigation of charge-neutral systems (corresponding to the adsorption of halogen atom) or negatively charged systems (corresponding to the adsorption of halide ions), however, Sellers *et al.*¹¹ proposed that a simple thermodynamic cycle could be used to convert the binding energy of adsorbed halogen to the binding energy of halide ion and *vice versa*. Moreover, trends in binding energies of halide ions and halogen atoms were often found to be identical.⁴ Migani and Illas¹² performed a systematic study based on the density functional theory (DFT) and provided data regarding the structure and bonding of halogen atoms on low-index transition metal surfaces. According to the aforementioned work, surfaces with higher work function are associated with more covalent bonding of halogen atoms.

In a previous work,¹³ the adsorption of Cl, Br and I on transition metal surfaces and Pd-monolayer surfaces, having particular importance in electrocatalysis, were investigated.^{1,14} The adsorption on the three-fold adsorption sites was found to be the strongest for all the surfaces, and adsorption energies decreased with increasing size of the halogen atom. For the case of the Pd-monolayer surface, it was demonstrated that the energy of adsorption of halogen atoms could be correlated to the position of the *d*-band of the surface atoms. The provided data enabled the rationalization of the experimentally observed effects of chloride ion adsorption on the catalytic activity of a Pd-monolayer over Pt(111) towards the oxygen reduction reaction. The present work is a continuation of the previously reported studies.¹³ The herein derived calculations evidenced that the metallic substrates investigated in this work provide a possibility to separate the effects of the electronic structure and the work function on the strength of the adsorption of halogen atoms. As there is a debate on the nature of halogen–metal bonds, the extreme case of fluorine, being the most electronegative element in the Periodic Table of Elements, was investigated. Moreover, it was investigated how the electronic structure of a metallic substrate affects the adsorption strength.

CALCULATION DETAILS

DFT calculations were performed using the PWscf code of the Quantum ESPRESSO distribution.¹⁵ The Perdew–Burke–Ernzerhof (PBE) functional within the generalized gradient approximation (GGA) was used.¹⁶ Marzari–Vanderbilt cold smearing¹⁷ with a broadening of 0.02 Ry was used to augment convergence. The kinetic energy cutoff was 32 Ry. The equilibrium lattice parameter (a_0) of Cu, Au, Pd and Pt were obtained by optimization of the respective bulk unit cell and were found to be 3.63, 4.17, 4.00 and 4.01 Å, respectively. The calculated lattice parameters agree well with the experimentally determined ones.¹³ Damped dynamics¹⁸ was used for structural relaxation. The geometrical optimization was allowed to run until the forces on the atoms became less than 0.02 eV Å⁻¹. The work function (Φ) was calculated using the equation:

$$\Phi = V(+\infty) - E_F \quad (1)$$

where $V(+\infty)$ is the electrostatic potential in the middle of the vacuum region, and E_F denotes the Fermi energy of the slab. The d -band density of states was determined by projection of the plane waves onto spherical harmonic orbitals. Löwdin population analysis¹⁹ was used to determine the population of the d -states of the investigated transition metal surfaces.

Halogen adsorption was modeled using hexagonal (2×2) cell for the (111) oriented surfaces, with three metal layers in the slab. The given model corresponds to a surface coverage of 0.25 ML. The metal atoms were placed in their fully relaxed positions, obtained by structural relaxation of the clean surfaces. The first irreducible Brillouin zone was sampled using Monkhorst–Pack²⁰ scheme set to $4 \times 4 \times 1$. The applicability of this slab model to describe correctly the electronic structure of surfaces was confirmed by a number of tests involving thicker metal slabs. In addition, a number of previously published studies demonstrated that this simple model is applicable for the description of atomic and molecular adsorbates.^{13,21} Fluorine atoms were placed on one side of the slab, and the structural relaxation was allowed for adatoms as well as for the first surface layer only. Binding energies (E_{F-M}) were calculated using the following equation:

$$E_{F-M} = E_{\text{slab+fluorine}} - (E_{\text{slab}} + E_{\text{fluorine}}) \quad (2)$$

where $E_{\text{slab+Fluorine}}$, E_{slab} and E_F are the total energy of the slab with an adsorbed fluorine atom, the total energy of the metal slab and the total energy of an isolated fluorine atom, respectively. Although having a minor effect on the adsorption energetics, relaxation was taken into account in order to unveil the details regarding the local adsorption equilibrium geometry.

RESULTS AND DISCUSSION

The metallic surfaces investigated in this work as the substrates for fluorine adsorption were densely packed (111) surfaces of Cu, Au, Pd and Pt. In addition, Pd monolayers over Cu(111), Pt(111) and Au(111), denoted as Pd_{ML}/M(111), were investigated. Surface models consisted of two M layers (M = Cu, Pt or Au) over which a Pd monolayer was placed in a homoepitaxial manner with a lattice parameter matching the one of a host metal M. Furthermore, “sandwich” structures, where a single Cu, Au or Pt layer was inserted under the first surface layer of the Pd(111) surface, were also investigated. These were denoted hereafter as M_{UND}Pd(111) surfaces. In this case, the surface models consisted of three metal

layers in total, with M layer inserted within two Pd layers. Lattice constant in these three cases matched the one of Pd. The combination of these metallic surfaces presents a suitable set of model systems to investigate the effects of the work function and electronic structure on fluorine adsorption on metallic surfaces. Namely, clean M(111) surfaces (M = Pd, Pt, Cu or Au) distinguish themselves by different population of *d*-states as well as electronic structure, described through *d*-band center position ($E_{d\text{-band}}$), and work function (Table I).

TABLE I. The electronic properties of the studied surfaces: *d*-band center ($E_{d\text{-band}}$), population of *d*-states (*d*) and calculated work function (Φ). Reprinted¹³ with permission by Elsevier

Surface	$E_{d\text{-band}} / \text{eV}$	<i>d</i> / electrons	Φ / eV
Pd(111)	-1.71	9.29	5.26
Pt(111)	-2.13	8.97	5.97
Cu(111)	-2.53	9.69	4.72
Au(111)	-3.17	9.67	5.34
Pd _{ML} /Pt(111)	-1.80	9.28	5.28
Pd _{ML} /Cu(111)	-2.42	9.21	5.28
Pd _{ML} /Au(111)	-1.37	9.27	5.29
Pt _{UND} Pd(111)	-1.81	9.19	5.28
Cu _{UND} Pd(111)	-1.76	9.29	5.25
Au _{UND} Pd(111)	-1.63	9.28	5.40

Among the investigated surfaces, the Cu and Au ones have low-lying filled *d*-states while the Pd and Pt ones have partially filled *d*-states, which enable direct interaction with adsorbed F atoms (Fig. 1). Moreover, the differences of

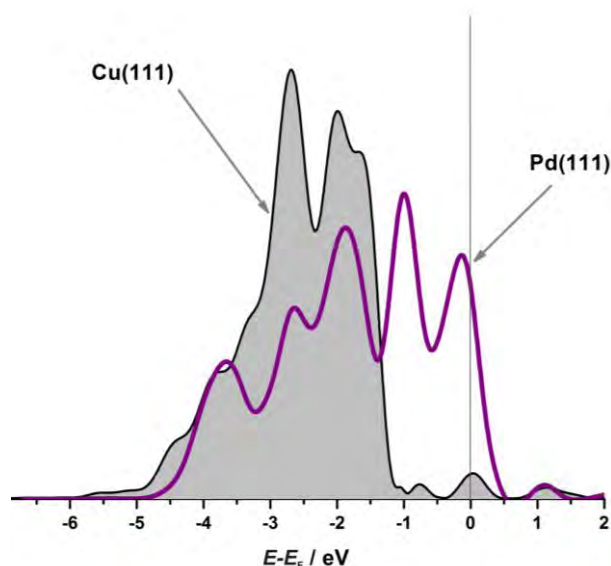


Fig. 1. Projected density of *d*-states (PDOS) for Cu(111) and Pd(111) surface. Thin vertical line indicates the position of the Fermi level.

the work function are up to 1.25 eV, enabling investigation of the role of this quantity on fluorine adsorption. By comparing these quantities for the Pd_{ML}/M(111) and M_{UND}Pd(111) surfaces, it could be seen that the population of *d*-states is almost independent of the nature of metal M (M = Cu, Au or Pt). Moreover, the calculated work functions for all these surfaces are mutually similar.¹³ However, these surfaces can be discriminated based on the position of the *d*-band center, which is tuned by the ligand effect²² (for M_{UND}Pd(111) surface) or simultaneously by the ligand and strain effect²² (for Pd_{ML}/M(111) surfaces). Hence, these surfaces could be used to analyze the effects of electronic structure on the adsorption of fluorine, while the effects of *d*-band population and work function are eliminated.

In continuation, an analysis of adsorption of F on the investigated surfaces was performed. As the adsorption could induce structural changes of the metallic substrate, first the adsorption geometry was characterized in terms of the vertical distance of the F adatom from the surface ($z(\text{F-M})$) and by the vertical displacement of surface metal atoms from their neighbors (ΔM) caused by the adsorption of F (Fig. 2).

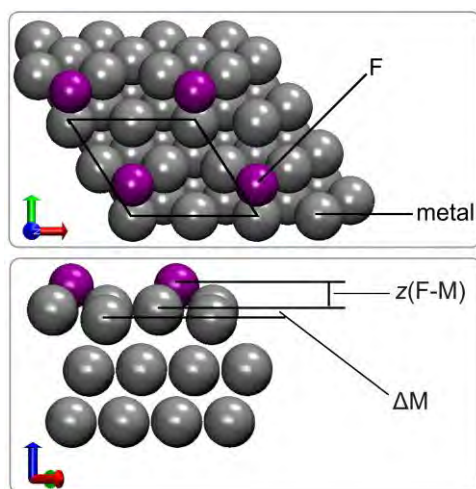


Fig. 2. Top view of a slab model used to investigate fluorine adsorption with designated surface unit cell used in calculations (top) and a side view of a three-layer slab with adsorbed fluorine accompanied by a designation of the quantities used to characterize the adsorption geometry (bottom).

Among the investigated M(111) surfaces, the Cu(111) surface displayed the strongest F adsorption, then followed Pd(111), Pt(111) and Au(111) surfaces (Table II). This trend is in fair agreement with the one reported by Migani and Illas,¹² although in the present study, somewhat more exothermic adsorption was found. With the exception of Pt(111), where top adsorption site was identified as the preferential one, three-coordinated fcc sites were found to be preferential for F adsorption. The vertical distances of adsorbed F atoms ($z(\text{F-M})$) on the investigated surfaces were found to be correlated with the lattice parameters, and

all adsorption sites follow this trend. On the other hand, the displacements of surface atoms were rather small, without an obvious trend and do not exceed 4 % of a_0 . This stimulates the conclusion that the adsorption geometry is predominantly determined by the relative differences in the atomic radii of the substrate and adsorbate, while the interaction of F adatom does not disturb significantly the substrate structure. The obtained adsorption geometries fit well to those reported previously.¹²

TABLE II. Description of F adsorption geometry and calculated binding energies on M(111) surfaces (M = Pd, Pt, Cu or Au)

Surface	Adsorption site	$\Delta(M) / \text{Å}$	$z(\text{F-M}) / \text{Å}$	$E_{\text{F-M}} / \text{eV}$
Pd(111)	fcc	0.03	1.60	-3.84
	hcp	0.04	1.63	-3.76
	top	0.04	1.99	-3.62
	bridge	0.04	1.68	-3.78
Pt(111)	fcc	0.02	1.69	-3.32
	hcp	0.02	1.75	-3.20
	top	0.15	1.98	-3.62
	bridge	0.11	1.72	-3.37
Cu(111)	fcc	0.07	1.50	-4.49
	hcp	0.07	1.52	-4.47
	top	0.04	1.85	-4.05
	bridge	0.07	1.56	-4.41
Au(111)	fcc	0.03	1.74	-3.29
	hcp	0.01	1.75	-3.29
	top	0.01	2.09	-3.13
	bridge	0.03	1.80	-3.27

When calculated binding energies of F are compared with binding energies of Cl, Br and I reported previously,¹³ it can be seen that F adsorbs more strongly than the other halogens, confirming that the strength of halogen adsorption decreases along the group of Periodic Table of Elements from top to bottom. This corresponds with the work of Migani and Illas¹¹ for the (111) and (100) surfaces of fcc metals, but it does not hold for the least densely packed (110) surface.

A much more interesting situation was found in the case of Pd_{ML}/M(111) and M_{UND}Pd(111) surfaces, where only the d -band center positions differ mutually, while the populations of d -states and the work functions do not. The previously mentioned observations regarding the adsorption geometries also hold here: the changes of the substrate structure are rather subtle, and vertical distance of F adatom from the surface can be linked to the 2D lattice constant of the substrate (Table III). However, the binding energy, ranging between -3.43 eV (Pd_{ML}/Cu(111) surface) to -3.91 eV (Pd_{ML}/Au(111)), indicated clearly that the d -band structure of the surface atoms played a significant role. Moreover, the effect of surface strain, introduced by changes in the lattice constant of the under-

lying metal in the case of Pd_{ML}/M(111) surfaces, was much more pronounced than the ligand effect, being operative for M_{UND}Pd(111) surfaces (Table III). This clearly indicates that even for highly electronegative adatom such as Fluorine, covalent interaction plays an important role and that the nature of the metal–fluorine bond is not purely ionic.

TABLE III. Description of F adsorption geometry and calculated binding energies on Pd_{ML}/M(111) and M_{UND}Pd(111) surfaces (M = Pt, Cu or Au)

Surface	Adsorption site	$\Delta(M) / \text{\AA}$	$z(\text{F-M}) / \text{\AA}$	$E_{\text{F-M}} / \text{eV}$
Pd _{ML} /Pt(111)	fcc	0.03	1.57	-3.86
	hcp	0.05	1.63	-3.74
	top	0.04	1.99	-3.62
	bridge	0.04	1.66	-3.77
Pd _{ML} /Cu(111)	fcc	0.02	1.80	-3.43
	hcp	-0.04	1.82	-3.39
	top	-0.15	2.07	-3.25
	bridge	-0.04	1.85	-3.39
Pd _{ML} /Au(111)	fcc	0.02	1.49	-3.91
	hcp	0.02	1.53	-3.78
	top	0.03	2.00	-3.48
	bridge	0.03	1.61	-3.77
Pt _{UND} Pd(111)	fcc	0.03	1.61	-3.87
	hcp	0.04	1.65	-3.78
	top	0.06	1.99	-3.67
	bridge	0.05	1.69	-3.81
Cu _{UND} Pd(111)	fcc	0.02	1.60	-3.70
	hcp	0.04	1.63	-3.61
	top	0.03	2.00	-3.43
	bridge	0.04	1.68	-3.62
Au _{UND} Pd(111)	fcc	0.02	1.58	-3.68
	hcp	0.03	1.61	-3.61
	top	0.02	1.99	-3.48
	bridge	0.03	1.67	-3.62

To backup these conclusions further, attention was turned to the work of Hammer and Nørskov,²³ who established a linear correlation between the position of the *d*-band center and the energy of adsorption, which actually assumed a covalent substrate–adsorbate interaction. Such a relationship was demonstrated previously for Cl, Br and I adsorption, when the slope of the $E_{\text{F-M}}$ vs. $E_{d\text{-band}}$ line was approximately the same for all three halogen adatoms, which was ascribed to the valence orbitals of the adatom having the same electronic structure. The continuation of previous work¹³ is clearly depicted in Fig. 3, which demonstrates the same linearity between $E_{\text{F-M}}$ and the $E_{d\text{-band}}$. However, it appears that the binding energy of fluorine is somewhat less sensitive to the

modification of electronic structure, possibly due to higher electronegativity compared to other halogen atoms and increased contribution of an ionic interaction.

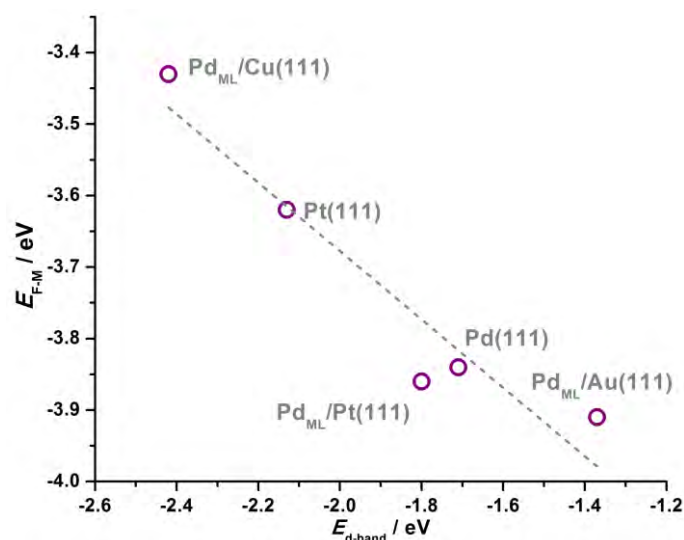


Fig. 3. Correlation between the fluorine binding energy (E_{F-M}) and the d -band center position ($E_{d\text{-band}}$). The linear fit is presented by the dashed line.

The states responsible for the interaction between the F adatom and the substrate can be identified by comparison of substrate projected densities of states prior to and after the adsorption, as introduced by Liu *et al.*²⁴. The analysis was performed in such a way that the projected density of states, in this particular case the projected d -band density of states, for a clean metallic surface and the corresponding counterpart with adsorbed F are subtracted. In this way, one may perceive a redistribution of electronic states due to interaction between the adsorbate and substrate and identify the states responsible for the interaction. In the case of Cu(111), the d -states become redistributed, positive parts of Δ PDOS are located below the Fermi energy, indicating that all the bonding and anti-bonding states arising from d - p interactions are filled (Fig. 4). Similarly, the formation of bonding and anti-bonding states upon adsorption of Cl on Cu(111) was previously observed in the same energy window by Peljhan and Kokalj.²⁵ Complete filling of bonding and anti-bonding states suppressed strong covalent bonding, but the interaction was considered to be not purely an ionic one.²⁵ This holds also for the case of an Au(111) surface, the d -band of which is located at lower values compared that of a Cu(111) surface (see the value of $E_{d\text{-band}}$, Table I). These conclusions fit to the completely filled low-lying d -band of Cu and Au and to the finding of Koper and van Saten,²⁶ who highlighted that the strength of the interaction of halogen p -states decreased when the d -band of the substrate atoms

shifted towards lower energies. However, it could also be fitted to the results of Hammer and Nørskov,²³ which explains the weaker F–Au interaction, compared to F–Cu interaction, by a more prominent Pauli repulsion. The performed population analysis confirmed the transfer of charge to the F adatom for all the studied metallic surfaces, but in the case of Cu and Au surfaces, the charge originated from the conduction *sp*-band, with the *d*-population remaining almost the same as for clean surfaces. In the cases of Pt(111) and Pd-monolayer surfaces, the *d*-states were significantly redistributed both above and below the Fermi level (Fig. 4), which indicated a higher contribution of covalent bonding in the interaction in comparison to the Cu and Au surfaces. In the case of Pt(111) and Pd-based surfaces, the charge transfer to F adatom was mainly from *d*-states although *sp*-states also contributed to some extent. It is also important to note that the charge redistribution was limited to the adsorption site only, *i.e.*, it did not extend to the surface atoms not in contact with an F adatom.

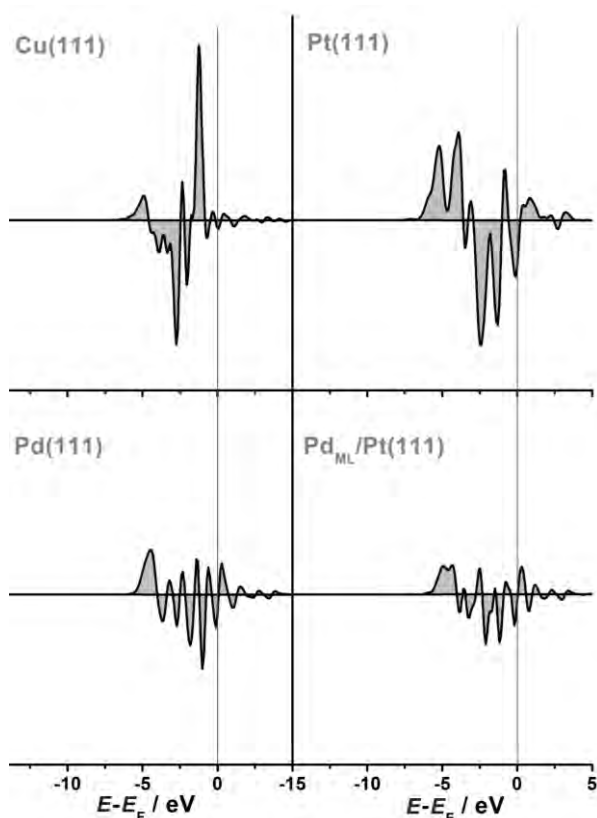


Fig. 4. Δ PDOS analysis of the modification of the *d*-band electronic structure of Cu(111) (top left), Pt(111) (top right), Pd(111) (bottom left) and Pd_{ML}/Pt(111) (bottom right) surface upon adsorption of fluorine. Pale vertical lines indicate the position of the Fermi levels.

CONCLUSIONS

In this contribution, fluorine adsorption was investigated on Cu(111), Au(111), Pd(111) and Pt(111) surfaces, as well as Pd monolayer surfaces involving Pd monolayers on Cu(111), Au(111) and Pt(111) surfaces and “sandwich” structures, denoted as $M_{\text{UND}}\text{Pd}(111)$. The selection of the analyzed substrates was made in such a way that the effects of electronic structure and work function on fluorine adsorption could be mutually discriminated. It was observed that fluorine adsorption did not result in significant structural changes of the metallic substrate. Among the investigated surfaces, F adsorbs most strongly on the Cu(111) surface with $E_{\text{F-M}}$ amounting to -4.49 eV. In the case of Pt and $\text{Pd}_{\text{ML}}/\text{M}(111)$ surfaces, it was found that binding energies scale with the d -band center position, which is characteristic for a significant contribution of covalent interaction. Cu(111) and Au(111) interact with F adatom through the sp -band, while Pt and Pd-based surfaces interact through the d -band too. The obtained results indicate that the nature of interaction of the highly electronegative F atom with metallic surfaces depended significantly on the nature of the metal, making possible to tailor the adsorption characteristics of metallic surface solely through modification of the d -band structure, while the population of the d -states and work function can be kept approximately constant. In spite of its large electronegativity, it can be concluded that the F–metal interaction is not purely ionic.

Acknowledgement. The Ministry of Education, Science and Technological Development of the Republic Serbia supported this work through Project No. III 45014. S.V.M. acknowledges the financial support provided by the Serbian Academy of Sciences and Arts, through the project F-190, “Electrocatalysis in the contemporary processes of energy conversion”.

ИЗВОД

АДСОРПЦИЈА ФЛУОРА НА ПОВРШИНАМА ПРЕЛАЗНИХ МЕТАЛА – DFT СТУДИЈА

ИГОР А. ПАШТИ¹, НЕМАЊА М. ГАВРИЛОВ¹ И СЛАВКО В. МЕНТУС^{1,2}

¹Универзитет у Београду, Факултет за физичку хемију, Студентски трг 12–16, 11158 Београд и

²Српска академија наука и уметности, Кнез Михајлова 35, 11000 Београд

На бази теорије функционала густине испитивана је адсорпција флуора на површинама а) Cu(111), Au(111), Pd(111) и Pt(111), б) на монослојевима Pd преко површина монокристала Cu(111), Au(111) и Pt(111) и с) на површинама монокристала Pd(111) са убаченим монослојевима метала М (М = Cu, Au или Pt) одмах испод првог Pd слоја. Нису нађене значајне промене структурних параметара метала подлоге после адсорпције. Највећа енергија везе од $-4,91$ eV нађена је у случају површине Cu(111). Површински атоми Cu(111) и Au(111) интерагују са адатомом флуора посредством sp -траке, док површински атоми Pt и Pd интерагују и посредством d -траке. У случају Pt и површина типа $\text{Pd}_{\text{ML}}/\text{M}(111)$, уочено је да се енергије везе корелишу са положајем центра d -траке, што је индикација значајног доприноса ковалентне интеракције приликом адсорпције. Добијени резултати указују да природа интеракције изразито електронегативног флуора са металним површинама зависи значајно од природе метала.

(Примљено 29. јула, ревидирано 21. септембра 2013)

REFERENCES

1. N. M. Markovic, P. N. Ross Jr., *Surf. Sci. Rep.* **45** (2002) 117
2. O. M. Magnussen, *Chem. Rev.* **102** (2002) 679
3. S. Huemann, N. T. M. Hai, P. Broekmann, K. Wandelt, H. Zajonz, H. Dosch, F. Renner, *J. Phys. Chem., B* **110** (2006) 24955
4. M. T. M. Koper, in *Modern Aspects of Electrochemistry*, Vol. 36, C. G. Vayenas, B. E. Conway, R. E. White, Eds., Kluwer Academic/Plenum Publishers, New York, 2003
5. P. S. Bagus, G. Pacchioni, M. R. Philpott, *J. Chem. Phys.* **90** (1989) 4287
6. M. Blanco, J. Rubio, F. Illas, *J. Electroanal. Chem.* **261** (1989) 39
7. M. Blanco, J. M. Ricart, J. Rubio, F. Illas, *J. Electroanal. Chem.* **267** (1989) 243
8. L. G. M. Pettersson, P. S. Bagus, *Phys. Rev. Lett.* **56** (1986) 500
9. A. Ignaczak, J. A. N. F. Gomes, *J. Electroanal. Chem.* **420** (1997) 71
10. V. Kairys, J. D. Head, *Surf. Sci.* **440** (1999) 169
11. H. Sellers, E. M. Patrito, P. Paredes Olivera, *Surf. Sci.* **356** (1996) 222
12. A. Migani, F. Illas, *J. Phys. Chem., B* **110** (2006) 11894
13. I. A. Pašti, S. V. Mentus, *Electrochim. Acta* **55** (2010) 1995
14. M. Arenz, V. Stamenkovic, T. J. Schmidt, K. Wandelt, P. N. Ros, N. M. Markovic, *Surf. Sci.* **523** (2003) 199
15. P. Giannozzi, S. Baroni, N. Bonini, M. Calandra, R. Car, C. Cavazzoni, D. Ceresoli, G. L. Chiarotti, M. Cococcioni, I. Dabo, A. Dal Corso, S. Fabris, G. Fratesi, S. de Gironcoli, R. Gebauer, U. Gerstmann, C. Gougoussis, A. Kokalj, M. Lazzeri, L. Martin-Samos, N. Marzari, F. Mauri, R. Mazzarello, S. Paolini, A. Pasquarello, L. Paulatto, C. Sbraccia, S. Scandolo, G. Sclauzero, A. P. Seitsonen, A. Smogunov, P. Umari, R. M. Wentzcovitch, *J. Phys.* **21** (2009) 395502
16. J. P. Perdew, K. Burke, M. Ernzerhof, *Phys. Rev. Lett.* **77** (1996) 3865
17. N. Marzari, D. Vanderbilt, A. de Vita, M. C. Payne, *Phys. Rev. Lett.* **82** (1999) 3296
18. M. C. Payne, M. P. Teter, D. C. Allan, T. A. Arias, J. D. Joannopoulos, *Rev. Mod. Phys.* **64** (1992) 1045
19. P.-O. Löwdin, *J. Chem. Phys.* **18** (1950) 365
20. H. J. Monkhorst, J. D. Pack, *Phys. Rev. B* **13** (1976) 5188
21. H. Tang, B. L. Trout, *J. Phys. Chem., B* **109** (2005) 17630
22. J. Kitchin, J. Nørskov, M. Barteau, J. Chen, *J. Chem. Phys.* **120** (2004) 10240
23. B. Hammer, J. K. Nørskov, *Surf. Sci.* **343** (1995) 211
24. Z. P. Liu, S. J. Jenkins, D. A. King, *J. Am. Chem. Soc.* **126** (2004) 10746
25. S. Peljhan, A. Kokalj, *J. Phys. Chem., C* **113** (2009) 14363
26. M. T. M. Koper, R. A. van Saten, *Surf. Sci.* **422** (1999) 118.



J. Serb. Chem. Soc. 78 (11) 1775–1787 (2013)
JSCS–4532

A study of the low-lying singlet and triplet electronic states of chlorophyll *a* and *b*

MIHAJLO ETINSKI*[#], MILENA PETKOVIĆ[#] and MIROSLAV M. RISTIĆ[#]

*Faculty of Physical Chemistry, University of Belgrade, Studentski trg 12–16,
P. O. Box 47, 11158 Belgrade, Serbia*

(Received 6 August, revised 23 September 2013)

Abstract: Chlorophylls have been extensively investigated both experimentally and theoretically owing to the fact that they are essential for photosynthesis. In the reported study, two forms of chlorophyll, chlorophyll *a* and chlorophyll *b*, were investigated by means of the density functional theory. Optimization of the S_0 , S_1 and T_1 states was performed with the B3-LYP functional. The computed fluorescence lifetimes show good agreement with available experimental data. The electronic adiabatic energies of S_1 and T_1 states are 2.09/2.12 and 1.19/1.29 eV for chlorophyll *a* and chlorophyll *b*, respectively. The implications of these results on triplet formation are discussed. In addition, the calculated vertical ionization potentials showed good agreement with the experimental results.

Keywords: electronic states, density functional theory, photosynthesis.

INTRODUCTION

Chlorophylls are green photosynthetic pigments found in plants, algae and cyanobacteria. They play a vital role in photosynthesis, a process in which plants transform light into chemical energy.¹ They are arranged in and around pigment–protein complexes called photosystems, which are embedded in the thylakoid membranes of chloroplasts. Their function is twofold: to serve as collectors of photo-energy and as electron donors in reaction centers. The vast number of chlorophylls absorbs light and transfer that light energy by resonance energy transfer to a specific chlorophyll pair in the reaction center of photosystems. The excited state of the special pair of chlorophyll molecules is lower in energy than that for single chlorophyll molecules, allowing reaction centers to trap the energy transferred from other chlorophylls. The special pair undergoes a charge sepa-

* Corresponding author. E-mail: etinski@ffh.bg.ac.rs

[#] Serbian Chemical Society member.

doi: 10.2298/JSC130806096E

ration, a specific redox reaction in which the chlorophyll donates an electron into a series of molecular intermediates, called an electron transport chain.

The multipurpose role of chlorophylls is a consequence of their chemical structure, which is that of a macrocyclic π -electron system. They contain chlorin, a dihydrogen-reduced ring skeleton of porphyrin, with a magnesium atom in its center, Fig. 1. The ring carbon atoms are labeled from 1 to 20 according to IUPAC nomenclature. Attached to the chlorin are side chains. There are several types of chlorophyll depending on the side chains. In this work, the two most common chlorophylls, chlorophyll *a* (Chl *a*) and chlorophyll *b* (Chl *b*), will be considered. Both Chl *a* and *b* have a long insoluble carbon–hydrogen (phytyl) chain. In addition, Chl *a* contains only methyl groups as short side chains while in Chl *b*, a methyl group at the C3 position on the chlorin ring is replaced with an aldehyde group.

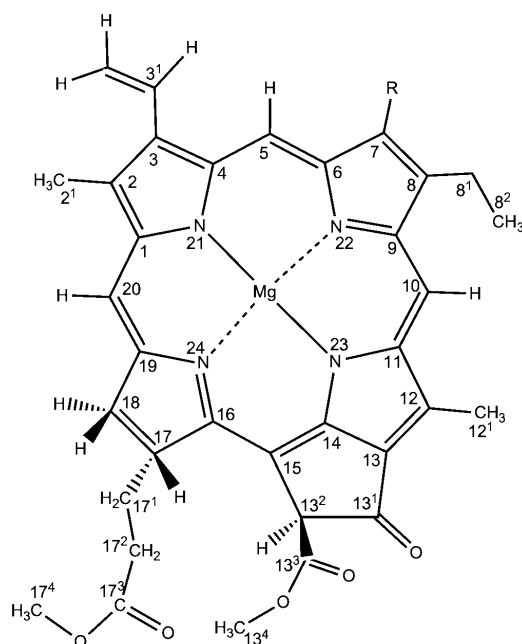


Fig. 1. The molecular structure and atom labels of Chl *a* ($R=CH_3$) and Chl *b* ($R=COH$).

Because of their fundamental significance to photosynthesis, the spectral and kinetic properties of Chl *a* and *b* have been studied extensively by both experimental^{2–20} and theoretical^{21–31} methods. The crystal structure of ethyl chlorophyllide *a* and *b*, chlorophylls that contain ethyl group instead of phytyl chain, was determined a long time ago.^{4,18}

The electronic spectrum of chlorophylls is similar to that of a free-base porphyrin (FBP). The low-energy spectrum of FBP consists of two major absorption

bands: a weak Q band in visible region (500–650 nm) and intense (Soret) B band in the near-UV region (350–400 nm). FBP belongs to the D_{2h} point group and, therefore, each of these bands consists of two components polarized in the x and y directions. The Q and B bands are qualitatively understood by the Goutermann four-orbital model.³⁰ They stem from electron promotions involving the two highest occupied molecular orbitals (HOMOs) and two lowest unoccupied molecular orbitals (LUMOs). In the case of chlorophylls, due to the presence of side groups, the electronic transitions are not degenerated and are therefore split into distinct x and y polarized bands (Q_y , Q_x , B_y and B_x). In addition, the Q_y transition gains considerable intensity relative to those observed in porphyrins. Thomas *et al.*³ measured the spectrum of Chl *a* in ACN–MeOH solution and found that the splitting was much greater between the Q_x and the Q_y transitions than between the B_x and B_y bands. In addition, they observed four peaks in the region of Q_x and the Q_y transitions belonging to 0–0 transitions and combinations of the 1–0 and 2–0 transitions. The lowest frequency band was conclusively assigned to the $Q_y(0-0)$ transition but the precise location of the $Q_x(0-0)$ transition remains unclear. The band positions in the spectrum of Chl *a* depend on the solvent and temperature.^{5,11,19}

Shafizadeh *et al.*⁵ used a supersonic cooled molecular beams to observe light absorption and ionization of isolated Chl *a*. They found that the Q_y band of Chl *a* was centered at 647 nm and the ionization potential was estimated to be 6.10 ± 0.05 eV.

Kinetic studies showed that the lowest singlet excited state (S_1) of Chl *a* and its derivatives decay on several timescales. These decays include fluorescence, intersystem crossing (ISC) and internal conversion (IC). In all, the quantum yield of fluorescence was 0.32 and its lifetime was 6.0 ns¹⁷. The IC and ISC rates were determined to be 1.7×10^7 and 1.0×10^8 s⁻¹, respectively.¹⁷ In a room temperature pyrimidine solution, the fluorescence and triplet lifetimes were 6.3 ns and 413 ± 5 μ s for Chl *a* and 3.2 ns and 556 ± 62 μ s for Chl *b*¹⁴. Interestingly, Renger and coworkers^{6,8} found a thermally activated ISC in the Chl *b* homodimer but not in the Chl *a* homodimer.

The decay of the S_1 state of photochlorophyllide *a*, a precursor in the biosynthesis of chlorophyll *a*, occurred on the time scales of 4.27 and 200 ps.⁹ Dietzek *et al.*⁹ attributed these decay constants to solvent-induced vibrational cooling, formation of an intermediate state and its subsequent decay to the ground state, respectively.

Density functional theory^{22,23,26–28,32,33} (DFT) has been the most frequently employed theoretical method to examine electronic states of chlorophylls, although the symmetry adapted cluster configuration interaction method,³¹ semi-empirical²⁹ and multireference configuration interaction methods based on density functional theory²¹ were used as well. This is due to the advantages of the

density functional over the other methods, which include features like calculation speed and reliability.

The main goal of this contribution was to gain some insight into the characters and geometries of the low-lying excited states of Chl *a* and *b*. In this respect, the geometries of the ground, the first excited singlet and the lowest triplet state were optimized. The similarities and differences between the electronic states of Chl *a* and *b* were also investigated.

In order to limit calculation to a manageable size, the phytyl ester in position 17 was replaced in all calculations with the methyl ester (Fig. 1). The obtained molecule is called methyl chlorophyllide. It was found that the replacement did not yield substantial change in any of the properties of chlorophyll. Therefore, the use of the abbreviations Chl *a* and *b* for methyl chlorophyllide *a* and *b* was retained.

COMPUTATIONAL DETAILS

All calculations were performed with the TURBOMOLE³⁴ program packages. We utilized DFT, unrestricted DFT (UDFT), and time-dependent DFT (TDDFT)³⁵ with the B3-LYP³⁶ functional implementation of TURBOMOLE for the ground-state and excited-state optimizations. It is known that the B3-LYP functional does not correctly describe charge transfer states that exist in chlorophylls.²² This is due to the self-interaction error in the orbital energies obtained in the ground-state DFT calculation.³⁷ In this study, the transitions were limited to those that include only localized transitions.

All calculations were performed in C_1 point-group symmetry. SVP (Mg, 10s6p/4s2p; C, N, O, 7s4p1d/3s2p1d; H, 4s1p/2s1p) and TZVP (Mg, 14s7p/5s3p; C, N, O, 10s6p1d/4s3p1d; H, 5s1p/3s1p) basis sets from the TURBOMOLE was used. The structures of the ground and the lowest excited singlet, as well as the lowest triplet state were optimized using the SVP basis set. The vertical electronic excitation spectrum was calculated at B3-LYP/TZVP levels. This approach based on using a smaller basis set for geometry optimization and a larger for energy calculations previously gave good results.^{38,39}

RESULTS AND DISCUSSION

The ground state geometry and vertical excitation spectrum

The bond lengths of the optimized ground state geometries of Chl *a* and *b* are presented in Table I together with data from crystallographic analysis.^{4,18} For both molecules, the chlorin rings are planar with dihedral angles smaller than 2°. Nevertheless, the dihedral angle C18–C17–C16–N24 is approximately 14°. Moreover, in both molecules, the Mg atom is not centered in the middle of the chlorin ring but the N–Mg distances vary up to 0.160 Å. The N24–Mg bond is significantly longer than other N–Mg bonds. The average bond length difference between the optimized geometry and the crystallographic data for Chl *a* was 0.005 Å. The largest deviations were encountered for C2–C3 (0.037 Å), C12–C11 (0.036 Å), C13–C13¹ (0.034 Å), C18–C18¹ (0.035 Å) and O–C17⁴ (0.042 Å). Similarly, the average bond length difference for Chl *b* was 0.004 Å. The largest

deviations were found for C20–C1 (0.036 Å), C18–C18¹ (0.033 Å) and O–C17⁴ (0.035 Å). In both molecules, the longest C–C bond is C13¹–C13². The bond length differences between Chl *a* and *b* are smaller than 0.010 Å, except for the C7–C8, C8–C9 and C7–C7¹ bonds that are located near the aldehyde group of Chl *b*. It was concluded that the ground state geometries of Chl *a* and *b* are very similar. In addition, although the structures were optimized with a relatively small basis set, the bond lengths were similar to the experimental results.

TABLE I. Optimized S₀, S₁ and T₁ state bond lengths of Chl *a* and *b* in Å. Experimental bond lengths are crystallographic data from the literature^{4,18}

Bond	Chl <i>a</i>				Chl <i>b</i>			
	S ₀	S ₀ (Exp.)	S ₁	T ₁	S ₀	S ₀ (Exp.)	S ₁	T ₁
C1–C2	1.454	1.451	1.443	1.442	1.457	1.456	1.442	1.441
C2–C3	1.384	1.347	1.394	1.397	1.383	1.353	1.395	1.399
C3–C4	1.467	1.476	1.468	1.454	1.471	1.453	1.470	1.454
C4–N21	1.379	1.384	1.370	1.360	1.382	1.402	1.372	1.359
C4–C5	1.394	1.370	1.413	1.443	1.389	1.384	1.408	1.444
C5–C6	1.415	1.419	1.403	1.376	1.421	1.415	1.406	1.378
C6–N22	1.362	1.361	1.372	1.390	1.356	1.359	1.368	1.389
C6–C7	1.454	1.464	1.464	1.472	1.454	1.439	1.462	1.468
C7–C8	1.381	1.362	1.376	1.367	1.397	1.370	1.391	1.381
C8–C9	1.456	1.463	1.465	1.478	1.443	1.438	1.454	1.469
C9–N22	1.376	1.388	1.372	1.357	1.382	1.399	1.376	1.359
C9–C10	1.408	1.378	1.413	1.415	1.412	1.392	1.416	1.418
C10–C11	1.401	1.415	1.405	1.404	1.396	1.397	1.402	1.401
C11–N23	1.391	1.402	1.390	1.393	1.394	1.406	1.390	1.396
N23–C14	1.334	1.347	1.338	1.335	1.332	1.335	1.339	1.334
C14–C13	1.424	1.416	1.427	1.417	1.425	1.420	1.426	1.417
C13–C12	1.393	1.405	1.394	1.403	1.390	1.372	1.392	1.409
C12–C11	1.456	1.420	1.461	1.457	1.458	1.439	1.463	1.456
C13–C13 ¹	1.465	1.431	1.462	1.459	1.466	1.447	1.463	1.460
C13 ¹ –C13 ²	1.581	1.569	1.581	1.583	1.580	1.570	1.581	1.581
C13 ² –C15	1.536	1.535	1.533	1.534	1.536	1.531	1.532	1.534
C15–C14	1.418	1.398	1.418	1.437	1.418	1.418	1.417	1.439
C15–C16	1.385	1.365	1.389	1.367	1.384	1.393	1.382	1.366
C17–C18	1.550	1.556	1.549	1.548	1.549	1.566	1.549	1.548
C18–C19	1.525	–	1.522	1.523	1.525	1.532	1.522	1.523
C19–C20	1.393	1.384	1.396	1.406	1.393	1.411	1.394	1.407
C20–C1	1.413	1.389	1.416	1.409	1.413	1.377	1.418	1.409
C19–N24	1.356	1.348	1.364	1.347	1.356	1.328	1.366	1.346
N21–Mg	2.036	2.063	2.039	2.047	2.033	2.055	2.037	2.045
N22–Mg	2.077	2.094	2.073	2.073	2.085	2.102	2.081	2.086
N23–Mg	2.020	2.021	2.023	2.026	2.022	2.005	2.026	2.027
N24–Mg	2.159	2.167	2.150	2.140	2.156	2.165	2.154	2.140
C3–C3 ¹	1.464	1.476	1.457	1.461	1.463	1.440	1.456	1.461
C3 ¹ –C3 ²	1.344	1.275	1.348	1.346	1.344	1.317	1.349	1.346

TABLE I. Continued

Bond	Chl <i>a</i>				Chl <i>b</i>			
	S ₀	S ₀ (Exp.)	S ₁	T ₁	S ₀	S ₀ (Exp.)	S ₁	T ₁
C2–C2 ¹	1.498	1.496	1.498	1.497	1.498	1.508	1.498	1.498
C18–C18 ¹	1.538	1.503	1.540	1.539	1.538	1.505	1.540	1.539
C1–N21	1.360	1.377	1.374	1.380	1.358	1.363	1.373	1.382
C16–N24	1.377	1.387	1.380	1.405	1.377	1.364	1.376	1.406
C7–C7 ¹	1.499	1.501	1.497	1.497	1.462	1.460	1.461	1.466
C7 ¹ =O	–	–	–	–	1.218	1.233	1.219	1.216
C8–C8 ¹	1.504	1.479	1.503	1.503	1.504	1.498	1.502	1.502
C8 ¹ –C8 ²	1.539	1.494	1.539	1.539	1.540	1.541	1.540	1.540
C12–C12 ¹	1.496	1.490	1.494	1.494	1.496	1.477	1.493	1.494
C13 ¹ –O	1.211	1.233	1.214	1.214	1.211	1.235	1.213	1.213
C13 ² –C13 ³	1.523	1.501	1.523	1.522	1.524	1.538	1.524	1.523
C13 ³ =O	1.208	1.184	1.208	1.208	1.208	1.189	1.208	1.208
C13 ³ –O	1.343	1.337	1.343	1.343	1.342	1.339	1.342	1.342
O–C13 ⁴	1.428	1.443	1.428	1.427	1.428	1.410	1.429	1.428
C16–C17	1.525	1.524	1.520	1.521	1.523	1.531	1.520	1.521
C17–C17 ¹	1.546	1.534	1.549	1.547	1.547	1.520	1.549	1.548
C17 ¹ –C17 ²	1.529	1.536	1.528	1.528	1.528	1.539	1.528	1.528
C17 ² –C17 ³	1.515	1.495	1.516	1.516	1.516	1.478	1.516	1.516
C17 ³ =O	1.207	1.213	1.207	1.207	1.207	1.216	1.206	1.206
C17 ³ –O	1.348	1.339	1.347	1.348	1.348	1.336	1.347	1.347
O–C17 ⁴	1.428	1.470	1.428	1.428	1.428	1.463	1.428	1.428

The frontier Kohn–Sham orbitals are presented in Fig. 2. The depicted orbitals have the same structure for both molecules. Generally, the occupied Chl *b* orbitals have lower energies than the Chl *a* orbitals, and the opposite is true for the unoccupied orbitals. All presented orbitals are π orbitals. The oxygen *n* orbitals are lower in energy. The HOMO-1, HOMO, LUMO and LUMO+1 electron densities are located on the chlorin ring.

In Tables II and III, the calculated first two singlet and four triplet excitation energies and oscillator strengths of Chl *a* are compared with those of other methods and experimental data. By comparing SVP and TZVP results, generally, it was found that triple zeta basis lowers the excitation energies by at most 0.05 eV. In addition, no effect on the excitation energies was found upon adding a phytol tail to methyl chlorophyllide.

The singlet excited states are Q_y and Q_x in accordance with other methods and experimental results. The oscillator strength of the Q_y state is larger by an order of magnitude than that of the Q_x state. Their energies are similar to experimental results, with respect that Q_x is better described with the B3-LYP/CAM-B3LYP functional.

The triplet states have different electronic structures compared with those of the singlet states. The lowest triplet state comes predominantly from HOMO to

LUMO transition. Its energy is 0.8 eV lower than that of the S_1 state, according to the B3-LYP results. There are three triplet states below the S_1 state. The $T_2/T_3/T_4$ states come primarily from HOMO-1 to LUMO/HOMO to LUMO+1/HOMO-1 to LUMO+1 excitation.

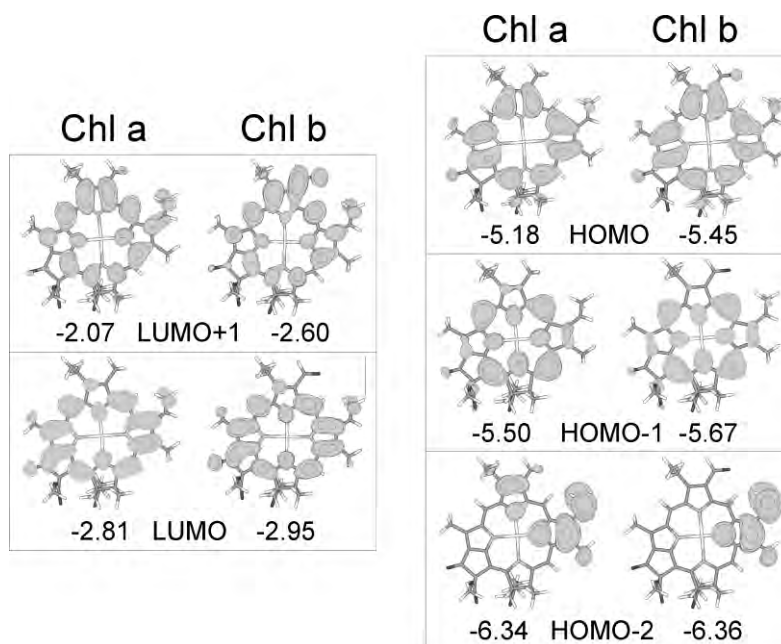


Fig. 2. Selected B3-LYP/TZVP frontier molecular orbitals and their energies.

TABLE II. Vertical excitation spectrum of the ground state of Chl *a*. All energies are in eV. Oscillator strengths are given in parentheses

State	Excitation	TDDFT/ B3-LYP/ /TZVP, this work	TDDFT/ B-P/ /SV(P) ²³	TDDFT/ /CAM- -B3LYP/ 6-31G* ²²	SAC-CI/ 6-31G* ²²	DFT/MRCI /BH-LYP/ VDZP ²¹	Exp.
S_1	HOMO→LUMO (85.0 %),	2.11	2.00	2.10	1.75	2.01	1.87, ³
	HOMO-1→	(0.2207)	(0.1820)	(0.2400)	(0.2900)	(0.4573)	1.88, ¹⁵
	→LUMO+1 (14.5 %)						1.86, ²
S_2	HOMO-1→LUMO (70.0 %),	2.28	2.04	2.47	2.26	2.27	2.14, ³
	HOMO→LUMO+1 (28.3 %)	(0.0247)	(0.0260)	(0.0260)	(0.0180)	(0.0444)	2.16 ¹⁵
T_1	HOMO→LUMO (93.5 %)	1.32	—	—	—	—	—
T_2	HOMO-1→LUMO (88.9 %)	1.54	—	—	—	—	—
T_3	HOMO→LUMO+1 (90.8 %)	2.04	—	—	—	—	—
T_4	HOMO-1→	2.35	—	—	—	—	—
	→LUMO+1 (85.2 %)						

TABLE III. Vertical excitation spectrum of the ground state of Chl *b*. All energies are in eV. Oscillator strengths are given in parentheses

State	TDDFT/B3-LYP/ TPZV	Exp.
S ₁	2.14 (0.1303) HOMO→LUMO (74.9 %), HOMO-1→LUMO+1 (22.1 %)	1.92 (in toluene ²)
S ₂	2.25 (0.0006) HOMO-1→LUMO (56.7 %), HOMO→LUMO+1 (40.5 %)	–
T ₁	1.44 HOMO→LUMO (86.9 %)	–
T ₂	1.58 HOMO-1→LUMO (86.4 %)	–
T ₃	1.84 HOMO→LUMO+1 (91.4 %)	–
T ₄	2.10 HOMO-1→LUMO+1 (86.9 %)	–

Chl *b* has similar electronic states to those of Chl *a*, but there are some minor differences. Its excited state energies and oscillator strengths are given in Table IV. The first two singlet excited states are Q_y and Q_x. They have energies that are very similar to those of Chl *a*.

TABLE IV. Vertical excitation spectrum of the S₁ state of Chl *a* and *b*. All energies are in eV. Oscillator strengths are given in parentheses

State	Chl a	Chl b
S ₀	0.05	0.06
S ₁	2.09 (0.2377) HOMO→LUMO (86.7 %)	2.12 (0.1555) HOMO→LUMO (78.9 %)
S ₂	2.30 (0.0290) HOMO-1→LUMO (69.7 %), HOMO→LUMO+1 (28.2 %)	2.25 (0.0002) HOMO-1→LUMO (55.2 %), HOMO→LUMO+1 (42.3 %)
T ₁	1.28 HOMO→LUMO (94.7 %)	1.39 HOMO→LUMO (90.6 %)
T ₂	1.53 HOMO-1→LUMO (89.2 %)	1.56 HOMO-1→LUMO (86.0 %)
T ₃	2.05 HOMO→LUMO+1 (88.7 %)	1.84 HOMO→LUMO+1 (88.4 %)
T ₄	2.34 HOMO-2→LUMO (70.0 %)	2.13 HOMO-1→LUMO+1 (70.2 %)

The triplet states of Chl *b* have the same ordering and basically the same structure as those of Chl *a*. The T₁ state is 0.7 eV lower than the S₁ state. Moreover, B3-LYP predicts four triplet states below the S₁ state, one more than in Chl *a*. This finding is in line with the work of Renger and coworkers⁶ on thermally activated ISC in chlorophylls. They proposed that the additional triplet state that is below the S₁ state in Chl *b* is responsible for the thermally activated

ISC. The present calculation showed that it is 0.04 eV lower than the S_1 state. In Chl *a*, the T_4 state is 0.24 eV higher than the S_1 state and it is not thermally accessible ($kT \approx 0.03$ eV). Hence, a small difference in the structure of chlorophyll can significantly change the photophysical properties.

The S_1 state geometry and vertical excitation spectrum

The optimized S_1 state is the Q_y state for Chl *a* and *b*. The optimized bond lengths are presented in Table I. The S_1 state comes from HOMO to LUMO excitation so the change of electronic density is located on the chlorin ring. The largest changes are in the C–C bonds. For Chl *a*, C4–N21 (0.009 Å), C4–C5 (0.019 Å), C8–C9 (0.009 Å) bonds elongate while C1–C2 (0.011 Å) and C5–C6 (0.012 Å) bonds shrink. Similarly, for Chl *b*, the largest changes are for C1–C2 (–0.015 Å), C4–C5 (+0.019 Å) and C5–C6 (–0.015 Å) bonds. The bond length changes are rather small indicating a small geometry displacement upon excitation. This can be seen as well from the adiabatic energy that is 2.09 and 2.12 eV for Chl *a* and *b*, respectively, as predicted by B3-LYP. Hence, the optimization stabilizes the S_1 state by 0.02 eV, confirming that its geometry is close to the ground state geometry. The general spectroscopic consequence of this small geometry change is that the 0–0 transition should be pronounced in absorption spectrum if the Franck–Condon approximation were valid. However, in chlorophylls, the Franck–Condon approximation is not sufficient due to the small transition dipole moment at the equilibrium geometry of the ground state and hence the 0–0 transition is not dominant.

The vertical singlet and triplet excitation energies for Chl *a* and *b* are given in Table V. The order and character of the excited singlet states of Chl *a* remain the same as at the ground state geometry. A similar situation was found for the triplet states, with the exception of the fourth state. This state comes predominantly from HOMO-2 to LUMO excitation starting from the S_1 optimized geometry and from HOMO-1 to LUMO+1 transition from the true ground state.

The fluorescence lifetimes were calculated using the oscillator strength and excitation energies. Chl *a* has a larger oscillator strength than Chl *b* and therefore, its fluorescence lifetime is larger as well. The calculated values are 7.3 and 10.8 ns. The value for Chl *a* is close to experimentally determined values of 6.0 and 6.2 ns in ether¹⁷ and toluene,² respectively. The ISC decay rate is of the order of 10 ns for Chl *a*, making the radiative and non-radiative processes competitive.

The T_1 state and vertical excitation spectrum

The lowest triplet state comes from HOMO to LUMO excitation. Its optimized bond lengths are presented in Table I. The largest differences with respect to the ground state geometry are for the C4–C5, C5–C6, C6–N22 and C16–N24

bonds. The adiabatic energies of T_1 state are 1.19 and 1.29 eV for Chl *a* and *b*, respectively. The T_1 state energies are lower by 0.13 and 0.15 eV than at the ground state geometry.

TABLE V. Vertical excitation spectrum of the T_1 state of Chl *a* and *b*. All energies are in eV. Oscillator strengths are given in parentheses

State	Chl a	Chl b
S_0	0.15	0.18
S_1	2.14 (0.2641) HOMO→LUMO (89.5 %)	2.19 (0.2050) HOMO→LUMO (85.1 %)
S_2	2.41 (0.0357) HOMO-1→LUMO (68.9 %), HOMO→LUMO+1 (28.9 %)	2.36 (0.0001) HOMO-1→LUMO (50.6 %), HOMO→LUMO+1 (45.9 %)
T_1	1.19 HOMO→LUMO (95.4 %)	1.29 HOMO→LUMO (94.1 %)
T_2	1.68 HOMO-1→LUMO (90.4 %)	1.72 HOMO-1→LUMO (84.2 %)
T_3	2.19 HOMO→LUMO+1 (90.1 %)	1.96 HOMO→LUMO+1 (86.7 %)
T_4	2.41 HOMO-2→LUMO (80.1 %)	2.28 HOMO-2→LUMO (70.9 %)

The vertical singlet and triplet excitation energies at T_1 geometry are given in Table V. At this geometry, the singlet states have slightly smaller energies than at the S_1 geometry.

The S_1 - T_1 adiabatic energy gap is 0.90 and 0.83 eV for Chl *a* and Chl *b*, respectively. The lower value for Chl *b* has an implication on the ISC transition from S_1 to T_1 state. The energy gap law^{40,41} states that for electronic states with similar geometries, the smaller the energy gap, the larger is the ISC rate. Hence, in the case of Chl *a* and *b*, assuming the same spin-orbit matrix elements and geometries of the S_1 and T_1 electronic states, Chl *b* will have a faster ISC rate for triplet formation.

The ionization potential

Chlorophylls play an important role in the initial electron transfer step in photosynthesis. Thus, an estimation of their ionization potential is necessary in order to understand the electron transfer process. Recently, Shafizadeh *et al.*⁵ measured the ionization potential (IP) of Chl *a* in a supersonic beam using a one color two photon experiment. They reported a value 6.10 ± 0.05 eV.

In order to obtain the vertical IP for Chl *a* and *b*, an unrestricted DFT calculation was performed on the cationic state at the respective ground state geometries. The IPs were determined to be 6.19 and 6.45 eV with the SVP basis set and 6.28 and 6.54 eV with the TZVP basis set for Chl *a* and Chl *b*, respectively. The increase of the IP with the basis set is a consequence of the greater

stabilization of the cationic state with respect to the ground state. It was expected that Chl *b* would have a higher IP than Chl *a* because, according to a simple rule,⁴² the IP value is proportional to the negative energy of the HOMO orbital. The implication of this result is that it is easier to ionize Chl *a* than Chl *b*.

A preliminary calculation with the SVP basis set showed that the IP of the full form of Chl *a* is 6.16 eV. This means that the phytol tail had almost no influence on the IP. Hasegawa and Noguchi⁴³ using a much bigger basis set 6-311+G(d) obtained an IP of 6.23 eV.

CONCLUSIONS

Density functional theory and its time dependent variant were employed for an investigation of the structure and electron excitation to the four lowest singlet and triplet states of chlorophyll *a* and *b*. It was determined that the phytol group did not significantly influence the electron spectra of the two investigated systems. Thus, the methyl ester was used instead of the phatyl ester in order to decrease the computational effort. The two structures optimized at the B3-LYP/SVP level show good agreement with the available experimental data, even though a modest basis set was employed. Optimization of the lowest excited singlet and triplet states did not change the structures significantly. The electronic adiabatic energies of the S₁ and T₁ states are 2.09/2.12 and 1.19/1.29 eV for Chl *a* and Chl *b*, respectively.

Vertical excitation energies and estimated fluorescence lifetimes were comparable with experimental literature values. Difference in positions of the energy levels in Chl *a* and Chl *b* explained the experimental finding that thermally activated intersystem crossing occurs in Chl *b*, and that Chl *b* has a larger intersystem crossing rate. On the other hand, the larger oscillator strength in Chl *a* explains its longer fluorescence lifetime. The computed ionization potentials were in good agreement with the previously reported measured values, and they imply easier ionization of Chl *a* compared to Chl *b*.

The obtained results confirmed that DFT and TD-DFT calculations could provide useful information about structure and electron transitions (electron spectra, excited state dynamics and ionization) in large systems, such as chlorophyll, and were able to explain the different behavior of different types of chlorophylls.

Acknowledgement. The authors acknowledge the Ministry of Education, Science and Technological Development of the Republic of Serbia for the financial support (Contract No. 172040).

ИЗВОД

ПРОУЧАВАЊЕ СИНГЛЕТНИХ И ТРИПЛЕТНИХ ЕЛЕКТРОНСКИХ СТАЊА
ХЛОРОФИЛА *a* И *b*

МИХАЈЛО ЕТИНСКИ, МИЛЕНА ПЕТКОВИЋ И МИРОСЛАВ М. РИСТИЋ

Факултет за физичку хемију, Универзитет у Београду, Студентски Трг 12–16, 11158 Београд

Због огромног значаја за фотосинтезу хлорофили су доста проучавани експериментално и теоријски. Ми смо помоћу теорије функционала густине проучавали два облика хлорофила, хлорофил *a* и хлорофил *b*. Оптимизација S_0 , S_1 и T_1 стања је извршена помоћу V3-LYP функционала. Израчуната времена флуоросценције се добро слажу са доступним експерименталним подацима. Електронске адијабатске енергије S_1 и T_1 стања су 2,09/2,12 и 1,19/1,29 eV за хлорофил *a* и хлорофил *b*. Продискутоване су последице ових резултата на стварање триплетног стања. Такође, израчунати вертикални јонизациони потенцијали се добро слажу са експерименталним резултатима.

(Примљено 6. августа, ревидирано 23. септембра 2013)

REFERENCES

1. J. M. Berg, L. J. Tymoczko, L. Stryer, *Biochemistry*, 5th ed., W. H. Freeman, New York, USA, 2002
2. J. W. Springer, K. M. Faries, J. R. Diers, C. Muthiah, O. Mass, H. L. Kee, C. Kirmaier, J. S. Lindsey, D. F. Bocian, D. Holten, *Photochem. Photobiol.* **88** (2012) 651
3. L. L. Thomas, J. H. Kim, T. M. Cotton, *J. Am. Chem. Soc.* **112** (1990) 9378
4. H. Chow, R. Serlin, C. E. Strouse, *J. Am. Chem. Soc.* **97** (1975) 1230
5. N. Shafizadeh, M. H. Ha-Thi, B. Soep, M. Gaveau, F. Piuzzi, C. Pothier, *J. Chem. Phys.* **135** (2011) 114303
6. T. Renger, M. E. Madjet, F. Müh, I. Trostmann, F.-J. Schmitt, C. Theiss, H. Paulsen, H. J. Eichler, A. Knorr, G. Renger, *J. Phys. Chem., B* **113** (2009) 9948
7. R. S. Knox, J. S. Brown, P. D. Laible, M. F. J. Talbot *Photosynth. Res.* **60** (1999) 165
8. F.-J. Schmitt, I. Trostmann, C. Theiss, J. Pieper, T. Renger, J. Fuesers, E. H. Hubrich, H. Paulsen, H. J. Eichler, G. Renger, *J. Phys. Chem., B* **112** (2008) 13951
9. B. Dietzek, R. Maksimenka, T. Siebert, E. Birckner, W. Kiefer, J. Popp, G. Hermann, M. Schmitt, *Chem. Phys. Lett.* **397** (2004) 110
10. Y. Shiu, *Chem. Phys. Lett.* **378** (2003) 202.
11. B. Mysliwa-Kurdziel, J. Kruk, K. Strzalka, *Photochem. Photobiol.* **79** (2004) 62
12. T. Noguchi, T. Tomo, C. Kato, *Biochemistry* **40** (2001) 2176
13. R. Hanf, S. Tschierlei, B. Dietzek, S. Seidel, G. Hermann, M. Schmitt, J. Popp, *J. Raman Spectrosc.* **41** (2010) 414
14. D. M. Niedzwiedzki, R. E. Blankenship, *Photosynth. Res.* **106** (2010) 227
15. C. Houssier, K. Sauer, *J. Am. Chem. Soc.* **92** (1970) 779
16. Y. Shi, J.-Y. Liu, K.-L. Han, *Chem. Phys. Lett.* **410** (2005) 260
17. D. Leupold, A. Struck, H. Stiel, K. Teuchner, S. Oberlaender, H. Scheer, *Chem. Phys. Lett.* **170** (1990) 478.
18. R. Serlin, H.-C. Chow, C. E. Strouse, *J. Am. Chem. Soc.* **97** (1975) 7237
19. L. Fiedor, M. M. Stasiak, B. Mysliwa-Kurdziel, K. Strzalka, *Photosynth. Res.* **78** (2003) 47
20. M. Rätsep, J. Linnanto, A. Freiberg, *J. Chem. Phys.* **130** (2009) 194501
21. A. B. J. Parusel, S. Grimme, *J. Phys. Chem., B* **104** (2000) 5395

22. Z.-L. Cai, M. J. Crossley, J. R. Reimers, R. Kobayashi, R. D. Amos, *J. Phys. Chem., B* **110** (2006) 15624
23. D. Sundholm, *Chem. Phys. Lett.* **302** (1999) 480
24. K. Karki, D. Roccatano, *J. Chem. Theory. Comput.* **7** (2011) 1131
25. A. Pandey, S. N. Datta, *J. Phys. Chem., B* **109** (2005) 9066
26. S. Parameswaran, R. Wang, G. Hastings, *J. Phys. Chem., B* **112** (2008) 14056
27. S. Sinnecker, W. Koch, W. Lubitz, *J. Phys. Chem., B* **106** (2002) 5281
28. R. Wang, S. Parameswaran, G. Hastings, *Vib. Spectrosc.* **44** (2007) 357
29. J. Linnanto, J. Korppi-Tommola, *Phys. Chem. Chem. Phys.* **2** (2000) 4962
30. M. Gouterman, *J. Mol. Spectrosc.* **6** (1961) 1139
31. J. Hasegawa, Y. Ozeki, K. Ohkawa, M. Hada, H. Nakatsuji, *J. Phys. Chem., B* **102** (1998) 1320
32. A. Marchanka, W. Lubitz, M. Van Gastel, *J. Phys. Chem., B* **113** (2009) 6917
33. D. Kröner, J. P. Götz, *J. Photochem. Photobiol., B* **109** (2012) 12.
34. Turbomole V6.4 2012, University of Karlsruhe and Forschungszentrum Karlsruhe GmbH, 1989–2007, TURBOMOLE GmbH, since 2007 available from www.turbomole.com
35. R. Bauernschmitt, R. Ahlrichs, *Chem. Phys. Lett.* **256** (1996) 454.
36. A. D. Becke, *J. Chem. Phys.* **98** (1993) 5648.
37. A. Dreuw, M. Head-Gordon, *J. Am. Chem. Soc.* **126** (2004) 4007
38. M. Etinski, T. Fleig, C. M. Marian, *J. Phys. Chem., A* **113** (2009) 11809
39. L. Pohler, M. Kleinschmidt, M. Etinski, C. M. Marian, *Mol. Phys.* **110** (2012) 2429
40. R. Englman, J. Jortner, *Mol. Phys.* **18** (1970) 145
41. M. Etinski, C. M. Marian, *Phys. Chem. Chem. Phys.* **12** (2010) 15665
42. C.-G. Zhan, J. A. Nichols, D. A. Dixon, *J. Phys. Chem., A* **107** (2003) 4184
43. K. Hasegawa, T. Noguchi, *Biochemistry* **44** (2005) 8865.



J. Serb. Chem. Soc. 78 (11) 1789–1795 (2013)
JSCS–4533

SHORT COMMUNICATION

An *ab-initio* study of pyrrole and imidazole arylamides

ARA M. ABRAMYAN, ZHIWEI LIU and VOJISLAVA POPHRISTIC*

*Department of Chemistry & Biochemistry, University of the Sciences, Philadelphia,
PA 19104, USA*

(Received 29 September, revised 9 October 2013)

Abstract: Arylamide foldamers have been shown to have a number of biological and medicinal applications. For example, a class of pyrrole–imidazole polyamide foldamers is capable of binding specific DNA sequences and preventing development of various gene disorders, most importantly cancer. Molecular dynamics (MD) simulations can provide crucial details in understanding the atomic level events related to foldamer/DNA binding. An important first step in the accurate simulation of these foldamer/DNA systems is the reparametrization of force field parameters for torsion around the aryl–amide bonds. Herein, the density functional theory (DFT) potential energy profiles and the derived force field parameters for four types of aryl–amide bonds for pyrrole and imidazole building blocks, which have been extensively employed in foldamer design for DNA-binding polyamides, will be highlighted. These results contribute to the development of computational tools for an appropriate molecular modeling of pyrrole–imidazole polyamide/DNA binding, and provide an insight into the chemical factors that influence the flexibility of pyrrole–imidazole polyamides and their binding to DNA.

Keywords: foldamer, torsional energy profiles, force field reparametrization, DNA-binding polyamide.

INTRODUCTION

Foldamers are synthetic oligomers that adopt stable secondary structures in solution.¹ Their functionality strongly depends on their conformation in solution. A number of important medicinal applications for foldamers have been demonstrated.^{2,3} A particular class of aromatic polyamide foldamers, consisting of pyrrole and imidazole monomers, has been shown to bind DNA sequences.^{4,5} Due to their ability to compete with DNA binding proteins, these polyamides have been used to block development of various diseases, including cancer.⁶ These DNA binders are composed of double-stranded pyrrole and imidazole carboxamides

* Corresponding author. E-mail: v.pophri@uscience.edu
doi: 10.2298/JSC130929104A

(Fig. 1). Dervan and co-workers⁴ revealed that *N*-methylimidazole (Im) paired with *N*-methylpyrrole (Py) binds G–C base pairs, and that the Py–Im pair binds C–G base pairs, whereas the Py–Py pair binds both A–T and T–A pairs. Thus, pyrrole–imidazole oligomers can be designed for DNA sequence-specific targeting.

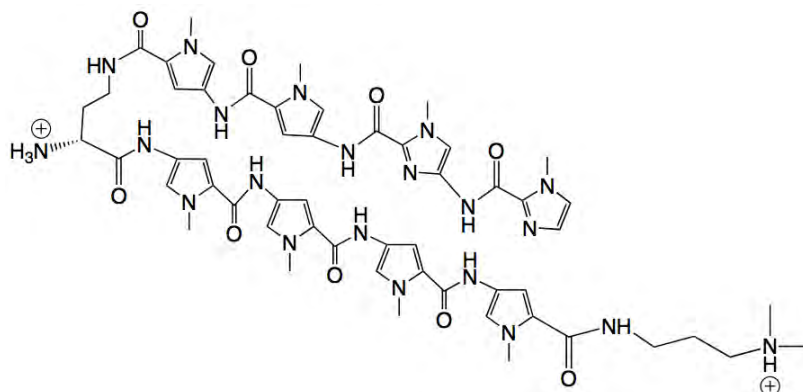


Fig. 1. Structure of a hairpin pyrrole–imidazole polyamide synthesized by Dervan *et al.*⁶ as an antitumor candidate.

Despite the importance of these polyamides, little is known about their dynamics in solution, in either free or in DNA-bound states. Molecular dynamics (MD) simulations can be used to shed light on the structural and dynamical characteristics of these DNA binding foldamers provided that accurate force fields are used.⁷ As the aromatic rings and peptide bonds are planar and rigid, the conformations of these polyamides are determined by only two types of bond rotations: those around the $C_{\text{aromatic}}-C_{\text{peptide}}$ (C_a-C_p) and $C_{\text{aromatic}}-N_{\text{peptide}}$ (C_a-N_p) bonds (see Fig. 2). In a previous work,⁷ it was shown that the general AMBER force field (GAFF)⁸ overestimates the torsional potentials for rotations around the aryl–amide bond (the GAFF torsional barrier for the C_a-C_p rotation corresponds to 29 kcal mol⁻¹,⁸ whereas quantum mechanically (QM) derived barriers are ≈ 8 kcal mol⁻¹).⁷ In addition, further studies^{9–12} showed that specific structural features significantly influence the rotational degree of freedom of an aryl–amide bond. Examples include an intramolecular hydrogen bond (H-bond) between the amide NH and an *ortho* aromatic substituent or an *ortho* endocyclic oxygen or nitrogen atoms. Therefore, to represent accurately the structure and dynamics of these polyamides by MD simulations, first the effects of various structural characteristics and energetics of aryl–amide torsions were studied using high-level QM methods. Reparametrization of the building block specific torsional parameters for GAFF was then realized using these QM potential energy profiles. In this paper, the determined QM potential energy profiles of four different aryl–amide bond types and the derived force field parameters are reported.

COMPUTATIONAL METHODS

The torsional profiles of four small molecules: *N*-(1-methyl-1*H*-imidazol-4-yl)acetamide (Im-N); *N*,1-dimethyl-1*H*-imidazole-2-carboxamide (Im-C); *N*-(1-methyl-1*H*-pyrrol-3-yl)acetamide (Py-N) and *N*,1-dimethyl-1*H*-pyrrol-2-carboxamide (Py-C) are shown in Fig. 2. These molecules were used for the reparameterization of the four different types of dihedral angles in the polyamides shown in Fig. 1. First, the molecules were optimized at several different levels of theory (HF, MP2 and B3LYP), and with basis sets ranging from B3LYP/6-31G(d,p) to B3LYP/6-311G(3df,2p). A convergence study revealed that B3LYP/6-311G(d,p) agrees well with the higher levels of calculation, as was also shown in previous studies.^{7,10} Therefore, the potential energy profiles were obtained by scanning the C_a-C_p and C_a-N_p torsional surface in 20° increments at the B3LYP/6-311G(d,p) level of theory. At each scan point, all internal coordinates except the dihedral angle in question were optimized. The calculations were realized using Gaussian 03.¹³ Then these torsional profiles were employed to reparametrize the GAFF parameters for the torsions around the C_a-C_p and C_a-N_p bonds. The new torsional parameters were obtained by the procedure described in a previous study,¹⁰ *i.e.*, by subtracting the non-bonded energies (calculated with restrained electrostatic potential, RESP,¹⁴ charges) from the *ab initio* torsional potential profile and then least square fitting of the GAFF torsional function to the “subtracted” *ab initio* torsional potential profile. Charges reported in this study were obtained by the RESP¹⁴ procedure.

RESULTS AND DISCUSSION

Torsional energy profiles with respect to the four types of dihedral angles are shown in Fig. 2. For compound Im-C, the global minimum is found with a dihedral angle N_{a1}-C_a-C_p-N_p at 180°. This is clearly due to the favorable H-bonding between the amide proton and the endocyclic unsaturated nitrogen (with a N_{a2}-H distance of 2.28 Å). Upon rotation of the C_a-C_p bond, an energy maximum is reached at around ±90°. The related increase in energy (12.97 kcal mol⁻¹) can be attributed to the loss of both the H-bond and the π-electron delocalization between the aromatic ring and the peptide group, which are co-planar in the global minimum. The highest energy point corresponds to a N_{a1}-C_a-C_p-N_p dihedral angle value of 0°, which is at 15.42 kcal mol⁻¹ with respect to its global minimum. This high energy barrier arises from several sources: a) destabilization due to the loss of the intramolecular H-bond discussed above; b) electrostatic repulsion between the carbonyl oxygen (O_{peptide}) and the endocyclic nitrogen (N_{a2}) in the highest energy conformer (the O_{peptide} to N_{a2} distance is 2.80 Å) and c) the steric repulsion between the amide proton and the N_{a1}-methyl group (the distance between amide proton and the carbon atom in the N_{a1}-methyl group (C_{methyl}) is 2.49 Å) in the highest energy conformer. The distance between the O_{peptide} and the carbon atom of the N_{a1}-methyl group in the equilibrium conformer is 2.87 Å, which is longer than the distance between the amide proton and the carbon atom in the N-methyl group in the highest energy conformer. A relatively flat energy region is observed at dihedral angles between 90° and 30° (or between -90 and -30°) which is due to a counter balancing effect of the

stabilizing (π -electron delocalization) and destabilizing factors (electrostatic and steric repulsions described above).

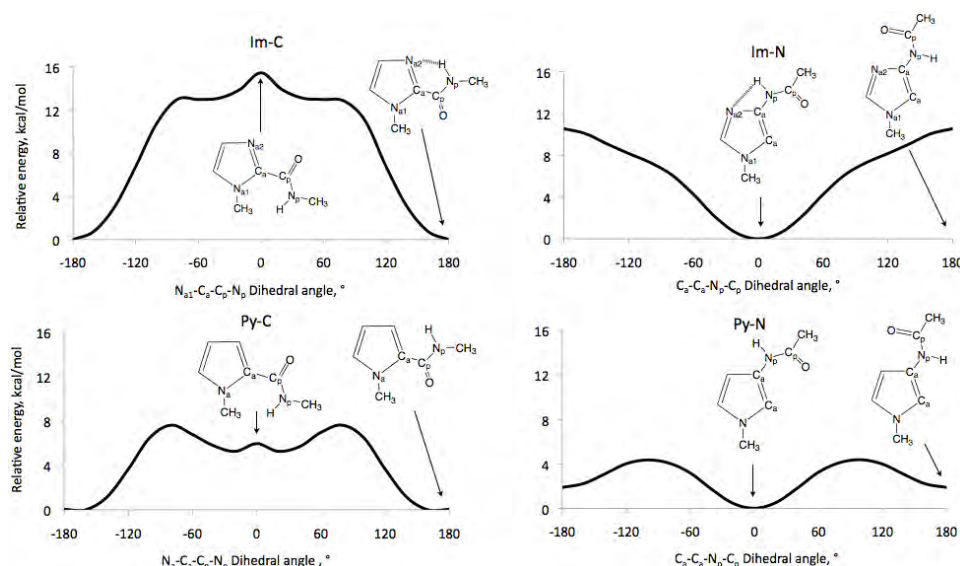


Fig. 2. Torsional energy profiles of the pyrrole and imidazole connected to the peptide bond through C and N atoms (Py-C, Py-N, Im-C, Im-N, respectively). Structures shown correspond to 0 and 180° torsional angle conformations. Dashed lines represent H-bonds.
1 kcal mol⁻¹ = 4.184 kJ mol⁻¹.

The global minimum of compound Im-N has the dihedral angle $C_a-C_a-N_p-C_p$ at 0°. Similarly to Im-C, this is due to stabilization by an H-bond between the amide proton and the endocyclic unsaturated nitrogen (with an $N_{a2}-H$ distance of 2.48 Å). Rotation around C_a-N_p leads to the energy maximum at 180°. The barrier of 10.55 kcal mol⁻¹ with respect to the minimum arises from: a) the loss of the H-bond and b) the electrostatic repulsion between the peptide oxygen and the endocyclic nitrogen (the distance between them is 2.93 Å) in the 180° conformer.

Compound Py-C has its minimum when the dihedral angle $N_a-C_a-C_p-N_p$ is at 180°. At this conformation, the arrangement of its functional groups is the most favorable due to: a) stabilization by electron delocalization between the aromatic ring and the peptide bond and b) the fact that the peptide oxygen and the N_a -methyl group (the distance between them is 2.85 Å) are not close enough for steric repulsion to have significant impact on the energy. Similarly to Im-C, rotation of the C_a-C_p bond leads to energy maximum at $\pm 90^\circ$ due to the loss of π -electron delocalization. The energy barrier of 7.63 kcal mol⁻¹ for this maximum is lower than that of the Im-C compound. This is because there is no H-bond in the global minimum of Py-C. The potential energy decreases slightly

due to the increase of π -electron delocalization when the dihedral angle $N_a-C_a-C_p-N_p$ changes from 90 to 20° (or from -90 to -20°) to reach a second minimum at $5.27 \text{ kcal mol}^{-1}$. Another energy maximum with the $N_a-C_a-C_p-N_p$ dihedral angle at 0° is observed, which is attributed to the steric repulsion between the amide proton and the N_a -methyl group ($H-C_{\text{methyl}}$ distance of 2.38 \AA).

Finally, compound Py-N has the lowest energy barrier ($4.38 \text{ kcal mol}^{-1}$) of the four considered compounds because it has no H-bond acceptors on the aromatic ring or other substituents that influence rotation around the $C_a-C_a-N_p-C_p$ dihedral angle. The maximum is at $\pm 90^\circ$ because this conformer does not have π -electron delocalization between the aromatic ring and the peptide group.

To improve the molecular mechanics description of the compounds, the *ab initio* torsional energy profiles were used to reparametrize the torsional parameters around the C_a-C_p and C_a-N_p bonds in GAFF, as described in the computational methods section. The atomic partial charges and the torsional parameters for the dihedral angles around the C_a-C_p and C_a-N_p bonds are summarized in Table I. These parameters can be used for accurate simulations of the pyrrole-imidazole polyamides and other structures containing the four torsional angles reparameterized herein.

TABLE I. Selected atomic charges and the fitted torsional parameters (bottom row) for the dihedral angles around the C_a-C_p and C_a-N_p bonds

Im-C		Im-N		Py-C		Py-N	
N_{a2}	-0.5843	N_{a2}	-0.4984	C_a	-0.1346	C_a	0.0574
C_a	0.1267	C_a	0.0529	C_p	0.5968	N_p	-0.3493
C_p	0.5496	N_p	-0.4625	O_p	-0.5458	H_p	0.2879
O_p	-0.5646	H_p	0.2780	N_p	-0.4267	C_p	0.5791
N_p	-0.3734	C_p	0.5848	H_p	0.2994	O_p	-0.5676
H_p	0.2855	O_p	-0.5627	V_n	7.63	V_n	3.0
V_n^a	10.0	V_n	3.0				

^aIn kcal mol^{-1} ($1 \text{ kcal mol}^{-1} = 4.184 \text{ kJ mol}^{-1}$). $E_{\text{torsion}} = \frac{V_n}{2} [1 + \cos(n\phi - f)]$, $n = 2$ and $f = 180^\circ$

CONCLUSIONS

Generally, higher torsional barriers were observed for aryl-amide torsions in imidazoles than in pyrroles. For example, the barrier of Im-C is 2 times higher than that of Py-C ($\approx 16 \text{ kcal mol}^{-1}$ vs. $\approx 8 \text{ kcal mol}^{-1}$), while the barrier of Im-N is ≈ 3 times that of Py-N (≈ 11 vs. $\approx 4 \text{ kcal mol}^{-1}$). This is due to the presence of the unsaturated endocyclic nitrogen (N_{a2}) in the imidazoles, which results in: 1) an H-bond between the amide proton and N_{a2} in the global minimum and 2) the electrostatic repulsion between the O_{peptide} and N_{a2} in the energy maximum. The stabilization of the minimum by the H-bond and destabilization of the maximum by the repulsion together result in a much higher barrier for the imidazole compounds.

Higher energy barriers were also observed in compounds Im-C and Py-C relative to those in Im-N and Py-N. There are two structural differences between the Im-C (or Py-C) and Im-N (or Py-N) molecules that need to be considered to account for the difference in the energy barriers. First, they differ in the type of connection (C_a-C_p vs. C_a-N_p). The C_a-C_p connection type in Im-C results in a more favorable H-bond between the amide H and the endocyclic N (the $H\cdots N_{a2}$ distance is 2.28 Å and the $N_p-H\cdots N_{a2}$ angle is 107.5°) than that in the minimum of Im-N (the $H\cdots N_{a2}$ distance is 2.48 Å and the $N_p-H\cdots N_{a2}$ angle is 72.2°). Therefore, it requires more energy to break the more favorable H-bond in Im-C than in Im-N. Secondly, the N_{a1} -methyl is *ortho* to the aryl-amide bond in the Im-C and Py-C molecules, but *meta* in the Im-N and Py-N molecules. The latter difference results in a lower (or no) steric repulsion between the amide proton and the N-methyl group in the high-energy conformers of Im-N and Py-N than in the high-energy conformers of Im-C and Py-C.

The force field parameters provided here are of immediate importance for proper modeling and binding studies of systems developed by Dervan and others.^{5,6} As has been shown in the past (with arylamides⁷), binding modes that result from MD simulations can be strikingly different, depending on the suitability of the torsional parameters. Consequently, a realistic description of the flexibility of an oligoamide backbone requires carefully derived torsional parameters.

This series of monomers allows for fine-tuning of the flexibility of oligomer backbones, as Im-C (15.42 kcal mol⁻¹), Im-N (10.55 kcal mol⁻¹), Py-C (7.63 kcal mol⁻¹) and Py-N (4.38 kcal mol⁻¹) have distinct torsional barriers for the bonds involved in a polyamide scaffold. Thus, the choice of the monomer sequence could result in various levels of backbone flexibility. This design strategy, however, is of limited benefit when sequence specific binding is sought. In such cases, quantitative information about the relative torsional barriers provides an opportunity to use alternative design features (such as “closed” double stranded structures⁵) in a better-informed manner, to affect backbone flexibility.

From a broader perspective, this and previous studies suggest caution against simply relying on chemical intuition in molecular design, since often the exact outcome of the interplay of several forces driving conformational stability cannot be predicted. Therefore, highly accurate QM calculations of the energetics of molecular building blocks and their analysis can be an important tool in molecular design.

Acknowledgments. This work was supported by the NSF MSN-1049771 and MRI CHE-1229564 grants. One of the authors (V. P.) would like to thank her former professors, members of the Faculty of Physical Chemistry, University of Belgrade, for the excellent education in physical chemistry and strong preparation for a research career. In particular, she is

grateful to her undergraduate mentor, Prof. Dr. Miljenko Perić, for introducing her to the field of computational chemistry and for his support in her development as a scientist.

ИЗВОД

AB INITIO СТУДИЈА ПИРОЛ- И ИМИДАЗОЛ-АРИЛАМИДА

ARA M. ABRAMYAN, ZHIWEI LIU и ВОЈИСЛАВА ПОПХРИСТИЋ

Department of Chemistry & Biochemistry, University of the Sciences, Philadelphia, PA 19104, USA

Фолдамери базирани на ариламидима се користе у биолошке и медицинске сврхе. На пример, једна класа пирол–имидазол полиамид–фолдамера се везује за одређене секвенције ДНК, и на тај начин спречава развијање разних генетских проблема и болести, укључујући и рак. Симулације молекулске динамике (МД) пружају могућност за увид у атомске детаље процеса који се одвијају при везивању фолдамера за ДНК. Од нарочите важности за поуздане МД симулације фолдамер/ДНК система је употреба исправних торзионих параметара за арил–амид везе. У овом раду, ми описујемо DFT (од енг. *density functional theory*; теорија функционала густине) торзионе потенцијалне површине и на основу њих изведене торзионе параметре, за четири типа арил–амид веза, које се појављују у пирол–имидазол мономерима коришћеним у дизајнирању фолдамер/ДНК комплекса. Овај рад описује једно додатно средство које омогућава поуздане МД симулације пирол/имидазол фолдамер система. Такође, резултати представљени у овом раду дефинишу на који начин одређени структурни фактори утичу на флексибилност полиамида и њихово везивање за ДНК.

(Примљено 29. септембра, ревидирано 9. октобра 2013)

REFERENCES

1. S. H. Gellman, *Acc. Chem. Res.* **31** (1998) 173
2. C. M. Goodman, S. Choi, S. Shandler, W. F. DeGrado, *Nat. Chem. Biol.* **3** (2007) 252
3. G. N. Tew, R. W. Scott, M. L. Klein, W. F. DeGrado, *Acc. Chem. Res.* **43** (2010) 30
4. S. White, J. W. Szewczyk, J. M. Turner, E. E. Baird, P. B. Dervan, *Nature* **391** (1998) 468
5. D. M. Chenoweth, P. B. Dervan, *J. Am. Chem. Soc.* **132** (2010) 14521
6. J. A. Raskatov, J. L. Meier, J. W. Puckett, F. Yang, P. Ramakrishnan, P. B. Dervan, *Proc. Natl. Acad. Sci. USA.* **109** (2012) 1023
7. V. Pophristic; S. Vemparala, I. Ivanov, Z. Liu, M. L. Klein, W. F. DeGrado, *J. Phys. Chem., B* **110** (2006) 3517
8. J. Wang, R. M. Wolf, J. W. Caldwell, P. A. Kollman, D. A. Case, *J. Comput. Chem.* **25** (2004) 1157
9. G. F. Galan, C. N. Tang, S. Chakrabarty, Z. Liu, G. Moyna, V. Pophristic, *Phys. Chem. Chem. Phys.* **15** (2013) 11883
10. Z. Liu, A. Teslja, V. Pophristic, *J. Comput. Chem.* **32** (2011) 1846
11. G. F. Galan, J. Brown, J. L. Wildin, Z. Liu, D. Liu, G. Moyna, V. Pophristic, *J. Phys. Chem., B* **113** (2009) 12809
12. Z. Liu, R. C. Remsing, D. Liu, G. Moyna, V. Pophristic, *J. Phys. Chem., B* **113** (2009) 7041
13. Gaussian 03, Revision C.02, Gaussian, Inc., Wallingford, CT, 2004
14. W. D. Cornell, P. Cieplak, C. I. Bayly, P. A. Kollmann, *J. Am. Chem. Soc.* **115** (1993) 9620.



J. Serb. Chem. Soc. 78 (11) 1797–1807 (2013)
JSCS–4534

Investigation of the charge-transfer in photo-excited nanoparticles for CO₂ reduction in non-aqueous media[•]

NADA M. DIMITRIJEVIĆ*

*Chemical Sciences and Engineering Division, and Nanoscience and Technology Division,
Argonne National Laboratory, 9700 S. Cass Ave., Argonne, IL 60439, USA*

(Received 26 July, revised 19 September 2013)

Abstract: Photo-induced charge separation in TiO₂ and Cu₂O semiconductor nanoparticles was examined using electron paramagnetic resonance spectroscopy in order to obtain insight into the photocatalytic reduction of CO₂ in non-aqueous media. For dissolution/grafting of CO₂, carboxy-PEG₄-amine was used with poly(ethylene glycol) 200 as the solvent. It was found that the reduction of CO₂ in this system starts at a potential of –0.5 V vs. Ag/AgCl, which is significantly more positive than the potential for electrochemical reduction of CO₂ in most organic solvents and water (–2.0 V vs. Ag/AgCl). The electron transfer from excited nanoparticles to CO₂ is governed by both thermodynamic and kinetic parameters, namely by the redox potential of conduction band electrons and adsorption/binding of CO₂ on the surface of the nanoparticles.

Keywords: carbon dioxide reduction, photocatalysis, titanium dioxide, cuprous oxide.

INTRODUCTION

Carbon dioxide produced by consuming fossil fuels is regarded as the most significant source of greenhouse gases.¹ Reducing the accumulation of CO₂ in the atmosphere is one of the current major scientific and social challenges. Although the chemical industry currently uses CO₂ as an inexpensive, non-flammable and non-toxic C₁ resource, the processes are conducted at relatively high pressures, at elevated temperatures and in the presence of catalysts.^{2–6} Thus, there is a need for the development of facile and inexpensive methods to convert CO₂ to usable materials under mild conditions (temperature and pressure). Using solar light as an energy source and inexpensive semiconductor nanoparticles as photocatalysts is a promising approach for the photochemical transformation of

* Correspondence to E-mail: Dimitrijevic@anl.gov

[•] Dedicated to late Dr. Olga Mičić, the greatest teacher of Physical Chemistry.

doi: 10.2298/JSC130726093D

CO₂ into fuels: CO, CH₄, and CH₃OH. Each of these fuels could be burned to produce CO₂ and then regenerated by photochemical reduction. Alternatively, CO could be used as a starting material in the water gas shift reaction to generate hydrogen from water. In all these cases, energy would be produced in a CO₂ neutral fashion avoiding a net production of CO₂. While most semiconductor-assisted photocatalytic reductions of CO₂ were realized in aqueous solution,^{7–10} the yields were relatively low not only because of the low solubility of carbon dioxide in water, but also because adsorbed/dissociated water on the surface of nanoparticles competes with adsorbed CO₂ for the photogenerated electrons.¹¹ Different strategies in improving CO₂ sequestration are currently being pursued. Several groups^{12–14} have developed reversible CO₂ capture utilizing a strong nitrogen-containing base in conjunction with a proton donor. Meanwhile, amidophosphoranes were also proved to be capable of capturing one equivalent of CO₂ through the insertion of CO₂ into a P–N bond, resulting in the generation of carbamato-phosphoranes.¹⁵ Very recently, Brennecke and co-workers¹⁶ designed an ionic liquid (IL) comprising an amino-functionalized anion and a long-chain alkyl phosphonium cation to capture CO₂, while Liu¹⁷ *et al.* employed poly(ethylene glycol) (PEG) solution with amino acid salts. In both cases almost equimolar absorption of CO₂ (1 mol CO₂ per mol of IL, or per mol of amino acid in PEG) was obtained.

In this work, the non-aqueous solvent PEG 200 was combined with short-chain amine group salts to increase CO₂ dissolution, and semiconductor nanoparticles were employed to initiate light-induced CO₂ reduction. For these studies, electron paramagnetic resonance (EPR) spectroscopy was used as a tool for examining the initial photo-induced charge separation and transfer in the presence of dissolved/grafted CO₂.

EXPERIMENTAL

Materials

All chemicals were of analytical grade and used as received, without further purification. Poly(ethylene glycol) 200 was purchased from J. T. Baker, carboxy-PEG₄-amine, C₁₁H₂₃O₆N, abbreviated in the text as CA(PEG)₄, from Thermo Scientific, tetra(*n*-butyl)ammonium hexafluorophosphate, Bu₄NPF₆, from Aldrich, anatase nanoparticles (*d* = 20 nm) from SkySpring, and Cu₂O colloidal nanoparticle (*d* = 30 nm) solution in ethanol from Aldrich. Research-grade carbon dioxide, 99.999 % (Airgas), was passed consecutively through two hydrocarbon traps (Supelco) to remove even trace amounts of impurities.

Instrumentation

X-Band continuous wave EPR experiments were conducted on a Bruker Eleksys E580 spectrometer equipped with an Oxford CF935 helium flow cryostat with an ITC-5025 temperature controller. The EPR spectra of the photogenerated charges were recorded at cryogenic temperatures from 4.5 to 77 K. The *g* factors were calibrated for homogeneity and accuracy by comparison with a coal standard, *g* = 2.00285 ± 0.00005. Simulations were performed using Bruker SimFonia, version 1.25. Samples in the EPR cavity were illuminated

using a 300-W Xe lamp (ILC) with water as the cut-off IR filter. Cyclic voltammetry measurements were performed with a three-component system containing a glassy carbon working electrode, Pt as the counter electrode, and Ag/AgCl as the reference electrode, using a BAS-100B/W (Bioanalytical Systems, USA) workstation with a single compartment closed quartz cell. Absorption spectra were recorded on a Shimadzu UV-1601 spectrophotometer.

RESULTS AND DISCUSSION

Electrocatalytic reduction of CO₂ in non-aqueous media has recently gathered increased interest,¹⁸ while semiconductor-assisted photocatalytic reduction is mainly focused on metal oxides in aqueous media. In photocatalytic processes, semiconductor metal oxide nanoparticles are used as light-harvesting materials. Nanocrystalline semiconductors are capable of coupling single photon events to the accumulation of multiple redox equivalents (photogenerated electrons) that participate in catalytic reduction of CO₂. The semiconductors Cu₂O (p-type), because of its favorable electronic properties for CO₂ reduction, Fig. 1, and TiO₂, because of its proven ability to convert carbon dioxide to methane in the presence of proton donors,⁷⁻¹¹ were chosen as photocatalysts of interest. The low yield of methane production in aqueous solutions is due to the competition of water and

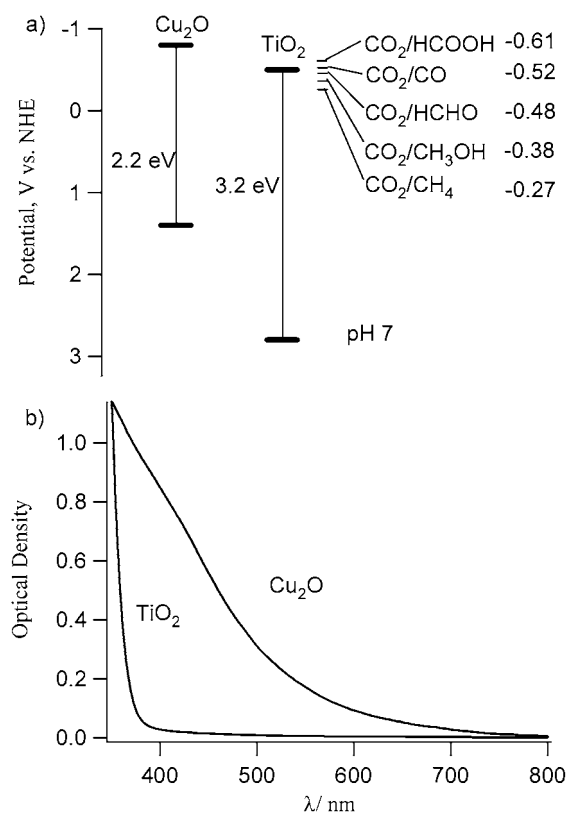


Fig. 1. a) Schematic presentation of the band positions and band gap energies and b) absorption spectra of Cu₂O and TiO₂ semiconductor nanoparticles. Optical pathlength: 0.5 cm.

carbon dioxide for the photogenerated electrons combined with the low solubility of carbon dioxide in water. Thus, the highest yields were achieved using a CO₂/water vapor (2:1) combination.¹¹ The redox potentials of CO₂ reduction products in aqueous solution are also indicated in Fig. 1a. In the absence of proton donors (as in non-aqueous solvents), the major product is carbon monoxide.

In order to increase the solubility of CO₂, 10 mM carboxy-PEG₄-amine, CA(PEG)₄ in PEG 200 solvent was used. The choice of CA(PEG)₄ was based on its high solubility in PEG 200 and because the amine group can effectively graft CO₂. It was shown previously that amino and amine groups capture CO₂ *via* the sequestration formation of the carbamic acid or carbamate pathways in a high yield.¹⁷ In order to gain insight into the photocatalytic reduction of CO₂ in non-aqueous media, photo-induced charge formation, separation and transfer in semiconductor nanoparticles were examined in CA(PEG)₄/PEG 200 solution saturated with N₂ or CO₂.

CO₂ in non-aqueous amine solution

The ability of CA(PEG)₄ dissolved in PEG 200 to sequester CO₂ efficiently was demonstrated using cyclic voltammetry. The voltammograms of the solutions saturated with N₂ and CO₂ are presented in Fig. 2a, from which it can be seen that the reversible one-electron redox process of CA(PEG)₄ with $E_{1/2} = -0.84$ V vs. Ag/AgCl occurred in the absence of CO₂. At the same time, when solution was bubbled with CO₂, a quasi-reversible electron transfer occurred. Moreover, the reduction of amine-grafted CO₂ starts at a potential of -0.5 V, while the electrochemical reduction of CO₂ occurs at rather negative potentials (more negative than -2 V) at low temperatures in most organic solvents. In the absence of CA(PEG)₄, no significant changes in the voltammograms of PEG 200 with and without CO₂ could be observed, Fig. 2b, showing that CO₂ does not dissolve in PEG 200 very efficiently, and confirming that the $-NH_2$ group is essential for the dissolving/grafting of CO₂.

Not only the increased solubility, but also the measured relatively positive potential for CO₂ reduction in this system made it the medium of choice for further studies and possible applications.

Light-induced charge transfer

The photo-excitation of TiO₂ (anatase) with energies greater than its band gap (3.2 eV) results in the formation of conduction band electrons and valence band holes (charge carriers):



EPR spectroscopy has been widely used to examine paramagnetic species in illuminated titania, starting with the seminal work of Howe and Gratzel.¹⁹ At cryo-

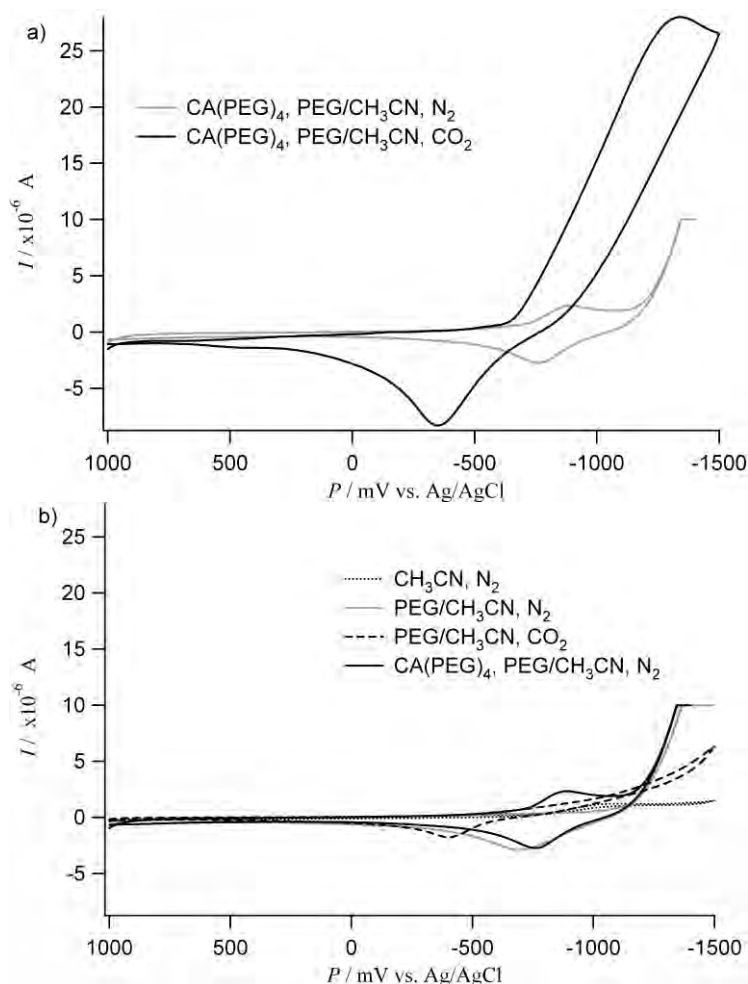


Fig. 2. Cyclic voltammograms of a) PEG 200 solutions containing 10 mM carboxy-PEG₄-amine, CA(PEG)₄, and 20 vol. % acetonitrile, saturated with N₂ and CO₂; b) solutions without CA(PEG)₄ measured as a control under the same conditions. All solutions contain 5 mM Bu₄NPF₆ as a redox relay. Glassy carbon as working, Pt as auxiliary and Ag/AgCl as reference electrodes were used. Scan rate 20 mV s⁻¹.

genic temperatures, photogenerated charge carriers localize in the interior of TiO₂ nanoparticles or migrate to the surface where they localize at surface trap sites. The signals associated with the trapped electrons are those due to lattice (Ti³⁺)_{latt}, sharp signal at $g_{\perp} = 1.990$ and $g_{\parallel} = 1.961$, and surface (Ti³⁺)_{surf} centers, broad signal with $g = 1.924$, Fig. 3a. The observed signals are characteristic of the electron in the Ti 3d orbital of the anatase lattice and surface.²⁰ Simultaneously, no signal due to the oxygen-centered radical, (Ti⁴⁺O[•])_{surf}, *i.e.* holes, was observed. The observed signal with $g = 2.001$ is due to the reaction of

photogenerated holes with carboxy-PEG₄-amine. The 6-line spectrum with the intensity ratios of 1:2:3:3:2:1 presented in Fig. 3b corresponds to CH₃CH₂[•] radicals,²¹ and is the result of C–O bond scission.²² The efficient scavenging of holes by carboxy-PEG₄-amine is facilitated by the strong binding of carboxyl groups on TiO₂.²³

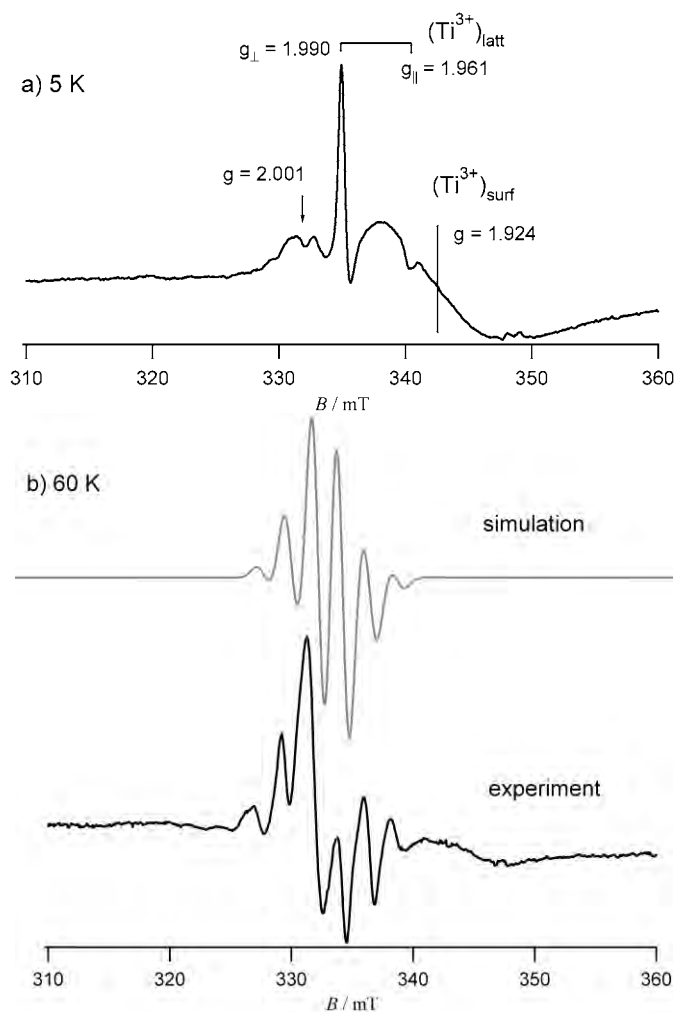


Fig. 3. EPR Spectra of TiO₂ in a solution of 10 mM carboxy-PEG₄-amine in PEG 200 measured under UV illumination at a) 5 K, power, 2 mW, modulation amplitude, 0.5 mT and b) 60 K, power, 0.2 mW, modulation amplitude, 0.3 mT. The gray line presents the simulated spectrum. The conditions of EPR measurements were adjusted to better resolve the signal from the CH₃CH₂[•] radical.

By increasing the temperature from 5 to 77 K, the electrons from the interior of the TiO₂ nanoparticle had enough energy to detrap and move to the surface where they localize at mid-gap states. The decrease of the signal for lattice-trapped and the increase of the signal that corresponds to the surface-trapped electrons, can be seen for a solution saturated with N₂, Fig. 4a.

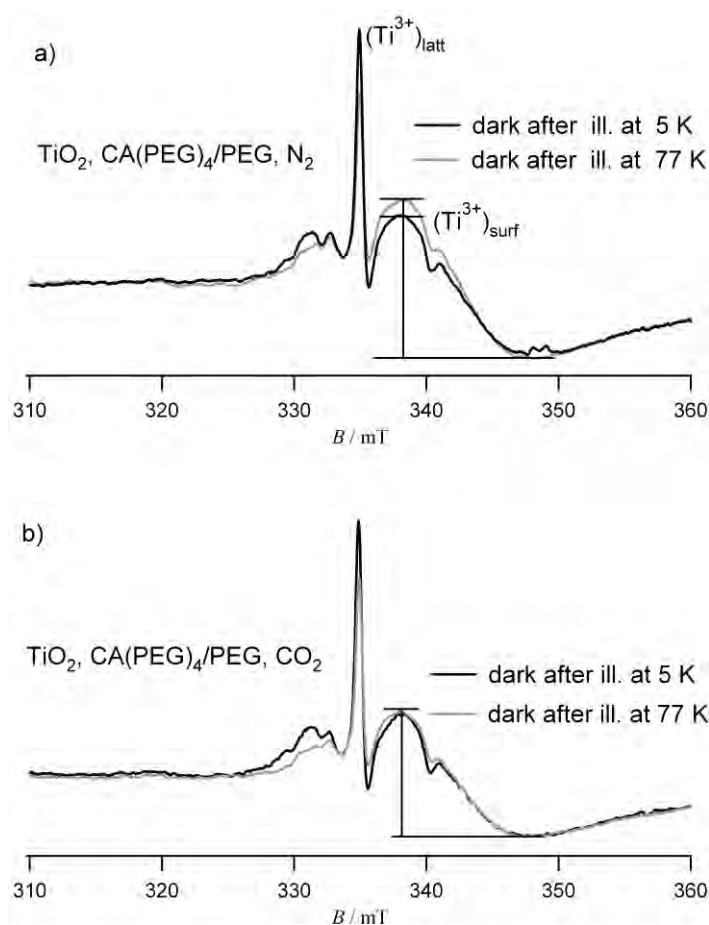
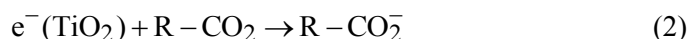


Fig. 4. EPR Spectra measured in the dark (at 5 K) after illumination at 5 and 77 K of a PEG 200 solution containing 10 mM carboxy-PEG₄-amine, CA(PEG)₄, and TiO₂ saturated with a) N₂ and b) CO₂. Power, 2 mW, modulation amplitude, 0.5 mT.

On the other hand, dissolved CO₂ acts as an electron acceptor, Eq. (2). The R-CO₂ in equations represents grafted CO₂, most probably carbamate:¹⁷



It was found that at the elevated temperature of 77 K, detrapped lattice electrons do not localize on the surface, rather they react with CO₂, Fig. 4b. Con-

sequently, no increase in the signal due to the surface-trapped electrons that were present at 5 K accompanies the decrease in the signal of the lattice-trapped electron. This means that *i*) the energy of mid-gap surface trapped electrons is below the redox potential for CO₂ reduction and *ii*) only conduction band electrons can react with CO₂. Although the driving force for CO₂ reduction with TiO₂ conduction band electrons is not high (Fig. 1), the efficient scavenging of photo-generated holes by CA(PEG)₄ enables a relatively high yield of the reduction reaction.

The conduction band electrons of cuprous oxide (Cu₂O) have a more negative potential than those of TiO₂; thus, the thermodynamic parameters favor reduction of CO₂. However, Cu⁺ is a non-paramagnetic ion and light-induced charge separation and transfer cannot be detected by EPR directly. As the Cu₂O nanoparticles used in this study did not have a protective ligand on their surface, a slow oxidation of bare nanoparticles occurred in air, resulting in the formation of thin layer of copper oxide (CuO) on the surface. This was confirmed by EPR spectra measured in the dark before illumination, Fig. 5. The spectra show hyperfine structure that is characteristic of Cu²⁺ ($I = 3/2$). In both cases (N₂ vs. CO₂ saturated solutions), the values of g_{\parallel} and g_{\perp} satisfy the relation $g_{\parallel} > g_{\perp} > g_e = 2.0023$ (g_e represents the g -tensor of free electron), indicating that the Cu²⁺ were coordinated by six ligand atoms in an axially distorted octahedron, that is characteristic of copper ions in CuO. However, the values for parallel and normal component differ, $g_{\parallel} = 2.256$ and $g_{\perp} = 2.036$ for N₂, and $g_{\parallel} = 2.276$ and $g_{\perp} = 2.038$ for CO₂, which suggests that CO₂ adsorbs/binds strongly to the surface of CuO,

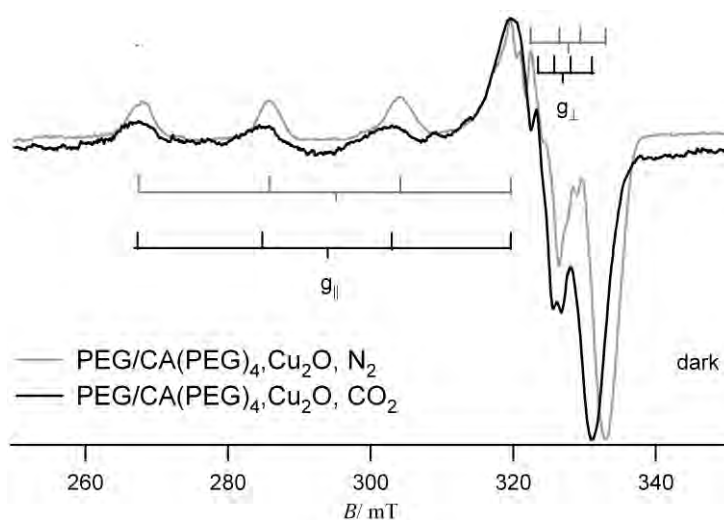
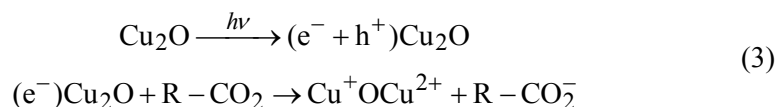


Fig. 5. EPR Spectra measured at 5 K in the dark of Cu₂O/CuO in PEG solution containing 10 mM carboxy-PEG₄-amine, CA(PEG)₄, saturated with N₂ or CO₂. Power, 2 m; modulation amplitude, 1 mT.

not only to carboxy-PEG₄-amine, affecting the hyperfine structure of surface Cu²⁺. The binding of CO₂ onto Cu₂O/CuO was previously observed in aqueous solutions.²⁴

Under illumination with visible light ($\lambda > 400$ nm), an increase in the concentration of Cu²⁺ was observed in the presence of CO₂, Fig. 6, due to electron transfer:



In the absence of CO₂, no change in the signal associated with Cu²⁺ was observed (Fig. 6a) because of the fast recombination of the photogenerated electrons and holes. The redox potential of valence band holes of Cu₂O is not

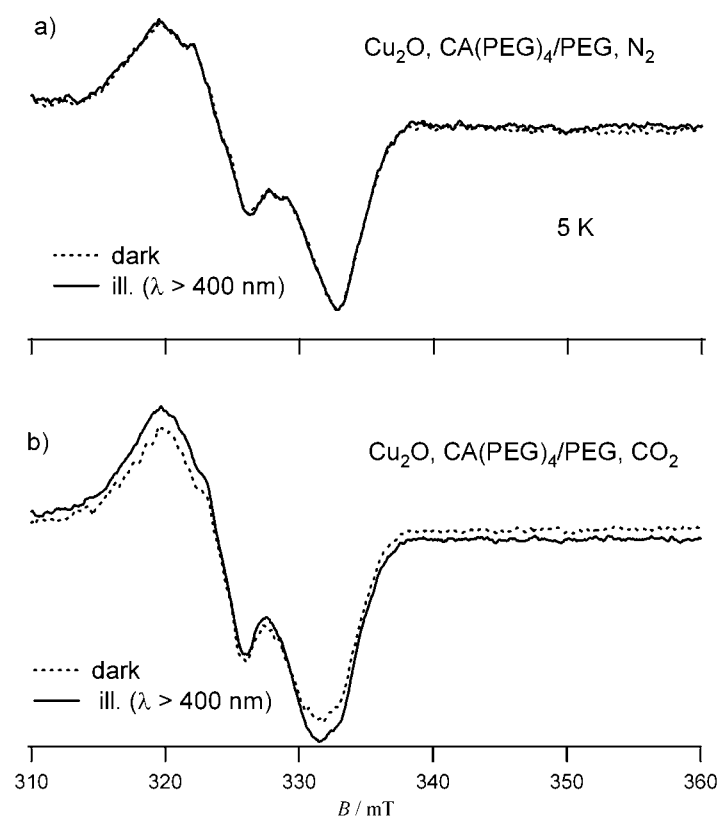


Fig. 6. EPR Spectra measured at 5 K in the dark and under illumination of Cu₂O/CuO in PEG solution containing 10 mM carboxy-PEG₄-amine, CA(PEG)₄, saturated with a) N₂ and b) CO₂. The magnetic field was centered on the normal component of the Cu²⁺ signal. Power, 2 mW; modulation amplitude, 1 mT.

positive enough to allow oxidation of carboxy-PEG₄-amine as no signals of organic radicals were observed in this system; thus, recombination of the charges was the favorable process. Therefore, the electron transfer from excited Cu₂O to CO₂ at the extremely low temperature of 5 K was due to the combined effects of the favorable redox potential of Cu₂O conduction band electrons and strong adsorption/binding of CO₂ on the nanoparticles.

CONCLUSION

Carboxy-PEG₄-amine, C₁₁H₂₃O₆N, when dissolved in poly(ethylene glycol) 200 efficiently sequesters CO₂. The grafting of CO₂ not only increases its solubility but enables reduction of CO₂ at a significantly more positive potential than the electrochemical reduction of CO₂ in most organic solvents or aqueous solutions. The efficiency of the one-electron transfer from photo-excited TiO₂ and Cu₂O nanoparticles to CO₂ was in the order Cu₂O > TiO₂, because of the preferential electronic and surface properties of the cuprous/cupric oxide nanoparticles.

Acknowledgment. This work was supported by the Department of Energy, Office of Science, Office of Basic Energy Sciences, under Contract No. DE-AC02-06CH11357.

ИЗВОД

ИСПИТИВАЊЕ ПРЕНОСА НАЕЛЕКТРИСАЊА У ЕКСЦИТОВАНИМ НАНОЧЕСТИЦАМА ЗА ФОТОКАТАЛИТИЧКУ РЕДУКЦИЈУ CO₂ У НЕВОДЕНОЈ СРЕДИНИ

НАДА М. ДИМИТРИЈЕВИЋ

Chemical Sciences and Engineering Division, and Nanoscience and Technology Division, Argonne National Laboratory 9700 S. Cass Ave., Argonne, IL 60439, USA

Раздвајање наелектрисања у побудјеним CO₂ и Cu₂O полупроводничким наночестицама је испитивано електронском парамагнетном резонантном спектроскопијом да би се добиле информације о фотокаталитичкој редукцији CO₂ у неводеној средини. Да би повећали растворљивост и везивање CO₂ користили смо карбоксил-PEG₄-амин у полиетилен гликолу 200 као растварачу. Нађено је да у том раствору редукција CO₂ почиње на потенцијалу од -0,5 V према Ag/AgCl, што је значајно позитивније него електрохемијска редукција у већини органских растварача и води (-2,0 V према Ag/AgCl). Ефикасност преноса електрона са побуђених наночестица на CO₂ зависи од термодинамичких и кинетичких параметара, наиме зависи и од потенцијала електрона у проводној траци и од адсорпције/везивања CO₂ на површину наночестица.

(Примљено 27. јула, ревидирано 19. септембра 2013)

REFERENCES

1. J. T. Kiehl, K. E. Trenberth, *Bull. Am. Meteorol. Soc.* **78** (1997) 197
2. D. H. Gibson, *Chem. Rev.* **96** (1996) 2063
3. X. Yin, J. R. Moss, *Coord. Chem. Rev.* **181** (1999) 27
4. M. Shi, Y. M. Shen, *Curr. Org. Chem.* **7** (2003) 737
5. S. Zhang, Y. Chen, F. Li, X. Lu, W. Dai, R. Mori, *Catal. Today* **115** (2006) 61
6. J. Huang, T. Ruther, *Aust. J. Chem.* **62** (2009) 298

7. T. Inoue, S. Fujishima, S. Konishi, K. Honda, *Nature* **277** (1979) 637
8. G. Li, S. Ciston, Z. V. Saponjic, L. Chen, N. M. Dimitrijevic, T. Rajh, K. A. Gray, *J. Catal.* **253** (2008) 105
9. B. Vijayan, N. M. Dimitrijevic, T. Rajh, K. A. Gray, *J. Phys. Chem., C* **114** (2010) 12994
10. K. Mori, H. Yamashita, M. Anpo, *RSC Adv.* **2** (2012) 3165
11. N. M. Dimitrijevic, B. Vijayan, O. G. Poluektov, T. Rajh, K. A. Gray, H. He, P. Zapol, *J. Am. Chem. Soc.* **133** (2011) 3964
12. a) P. G. Jessop, D. J. Heldebrant, X. W. Li, C. A. Eckert, C. L. Liotta, *Nature* **436** (2005) 1102; b) P. G. Jessop, S. M. Mercera, D. J. Heldebrant, *Energy Environ. Sci.* **5** (2012) 7240
13. a) C. M. Wang, H. M. Luo, D. Jiang, H. R. Li, S. Dai, *Angew. Chem. Int. Ed.* **122** (2010) 6114; b) C. M. Wang, X. Y. Luo, H. M. Luo, D. Jiang, H. R. Li, S. Dai, *Angew. Chem. Int. Ed.* **123** (2011) 5020
14. J. Im, S. Y. Hong, Y. Cheon, J. Lee, J. S. Lee, H. S. Kim, M. Cheong, H. Park, *Energy Environ. Sci.* **4** (2011) 4284
15. L. J. Hounjet, C. B. Caputo, D. W. Stephan, *Angew. Chem. Int. Ed.* **51** (2012) 4714
16. B. F. Goodrich, E. A. Price, W. F. Schneider, J. F. Brennecke, *J. Am. Chem. Soc.* **132** (2010) 2116
17. A.-H. Liu, R. Ma, C. Song, Z.-Z. Yang, A. Yu, Y. Cai, L.-N. He, Y.-N. Zhao, B. Yu, Q.-W. Song, *Angew. Chem. Int. Ed.* **51** (2012) 11306
18. L. L. Snuffin, L. W. Whaley, L. Yu, *J. Electrochem. Soc.* **158** (2011) F115
19. a) R. F. Howe, M. Gratzel, *J. Phys. Chem.* **89** (1985) 4495; b) R. F. Howe, M. Gratzel, *J. Phys. Chem.* **91** (1987) 3906
20. N. M. Dimitrijevic, Z. V. Saponjic, B. M. Rabatic, O. G. Poluektov, T. Rajh, *J. Phys. Chem., C* **111** (2007) 14597
21. R. W. Fessenden, R. H. Schuler, *J. Chem. Phys.* **39** (1963) 2147
22. Y. S. Won, D. Cho, Y. Kim, J. Lee, S. S. Park, *J. Appl. Polym. Sci.* **117** (2010) 2083
23. B. O'Regan, M. Gratzel, *Nature* **353** (1991) 737
24. G. Li, N. M. Dimitrijevic, L. Chen, T. Rajh, K. A. Gray, *J. Phys. Chem., C* **112** (2008) 19040.



J. Serb. Chem. Soc. 78 (11) 1809–1836 (2013)
JSCS–4535

REVIEW

**Progress in conducting/semiconducting and redox-active
oligomers and polymers of arylamines**

ALEKSANDRA JANOŠEVIĆ¹, BUDIMIR MARJANOVIĆ², ALEKSANDRA RAKIĆ³
and GORDANA ĆIRIĆ-MARJANOVIĆ^{3*}

¹Faculty of Pharmacy, University of Belgrade, Vojvode Stepe 450, 11221 Belgrade, Serbia,

²Centrohem, Vuka Karadžića bb, 22300 Stara Pazova, Serbia and ³Faculty of Physical
Chemistry, University of Belgrade, Studentski Trg 12–16, 11158 Belgrade, Serbia

(Received 9 August 2013)

Abstract: Recent advances in synthesis, characterization and application of the selected conducting/semiconducting and redox-active oligomers and polymers of arylamines are reviewed. A brief historical background of the selected topics is given. The overview of the preparation, structure and properties of polyaniline, substituted polyanilines, especially those obtained by the oxidative polymerization of *p*-substituted anilines, poly(1-aminonaphthalene) and its derivatives, carbocyclic and heterocyclic polyaryldiamines such as poly(*p*-phenylenediamine) and polydiaminoacridines, is presented. The mechanism of formation of polyaniline nanostructures is discussed. Recent approaches to the preparation of one-dimensional polyaniline nanostructures are concisely reviewed, with special attention paid to the template-free falling-pH method. Current and potential future applications of oligo/polyarylamines are briefly discussed.

Keywords: polymer, oligomer, oxidative polymerization, arylamine, polyaniline, nanostructure.

CONTENTS

1. OXIDATION *VERSUS* OXIDATIVE POLYMERIZATION OF ARYLAMINES
2. OXIDATIVE POLYMERIZATION OF ANILINE
 - 2.1. Polyaniline nanostructures
3. OXIDATIVE POLYMERIZATION OF SUBSTITUTED ANILINES
 - 3.1. Oxidative polymerization of *para*-substituted anilines
4. OXIDATIVE POLYMERIZATION OF 1-AMINONAPHTHALENE AND ITS DERIVATIVES
5. OXIDATIVE POLYMERIZATION OF ARYLDIAMINES
 - 5.1. Oxidative polymerization of phenylenediamines

* Corresponding author. E-mail: gordana@ffh.bg.ac.rs
doi: 10.2298/JSC130809097J

5.1.1. Oxidative polymerization of *p*-phenylenediamine

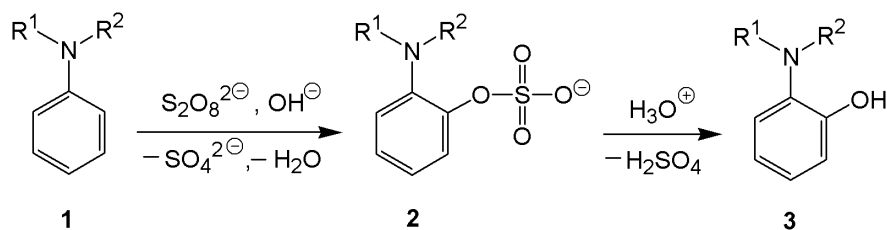
5.2. Oxidative polymerization of diaminoacridines

6. CONCLUSIONS AND OUTLOOK

1. OXIDATION *VERSUS* OXIDATIVE POLYMERIZATION OF ARYLAMINES

Chemical oxidations of arylamines can proceed in two different ways.¹ Oxidants with a relatively high oxidation potential, which do not contain a reactive oxygen atom, can remove electron(s)/hydrogen from the arylamine molecule. The *in situ* formed reactive species, *e.g.*, arylamine cation radicals, arylnitrenium cations, *etc.*, undergo further reaction with the parent arylamine molecules leading to the formation of arylamine dimers (N–N, N–C, or C–C coupled dimers in the reduced and/or oxidized form), oxidatively cyclized diarylamine products, such as substituted phenazines, and higher linear/branched oligo/polyarylamines.¹ Oxidants that contain a reactive oxygen atom can either donate an oxygen to the arylamine molecule, thus leading to oxygen-containing products of arylamine oxidation (arylhdroxylamine, nitrozoarene, nitroarene, substituted amino-phenols and aminonaphthols, substituted benzoquinones and naphthoquinones, *o*-aminoaryl sulfate, *etc.*), and/or remove electron(s)/hydrogen from the arylamine molecule.¹ Perphosphoric acid, peroxomonosulfuric acid, and percarboxylic acids are well-known efficient oxygen donors, while Fe(III), Ce(IV), Cu(II), Au(III), Pt(IV), Pd(II) and Ag(I) compounds are frequently used electron acceptors. Oxidants such as H₂O₂ and peroxydisulfate salts behave as both oxygen donors as well as electron acceptors. High temperatures and alkaline conditions are favorable for the oxygen donor mechanism, whereas low temperatures and acidic conditions are favorable for the electron acceptor mode of action of oxidants such as H₂O₂ and peroxydisulfate. The electrochemical oxidation of arylamines can also lead, depending on the reaction conditions (electrode type, anodic potential, current density, electrolyte, solvent, pH, temperature, arylamine concentration, *etc.*) to oxygen-containing monomeric/dimeric products and/or oligo/polyarylamines.¹ Depending on the arylamine concentration, the oxidation of the arylamine can lead to its degradation or polymerization.¹

Boyland and Sims reported in the 1950s the extension of Elbs peroxydisulfate (S₂O₈²⁻) oxidation of phenols in alkaline solution, leading to the prevalent formation of *p*-hydroxyaryl sulfates, to the oxidation of arylamines in alkaline solution with S₂O₈²⁻.²⁻⁶ Arylamines (Scheme 1, **1**) were found to be prevalently converted to the corresponding soluble *o*-aminoaryl sulfate (Scheme 1, **2**) under conditions similar to those used for the Elbs oxidation: room temperature or below, aqueous alkali media, and equimolar quantities of arylamine and S₂O₈²⁻.²⁻¹² Subsequent hydrolysis in highly acidic aqueous solutions leads to corresponding *o*-aminophenols (Scheme 1, **3**).



Scheme 1. Boyland-Sims oxidation of aniline ($\text{R}^1=\text{R}^2=\text{H}$) and its *N*-alkyl/aryl-substituted derivatives with $\text{S}_2\text{O}_8^{2-}$.

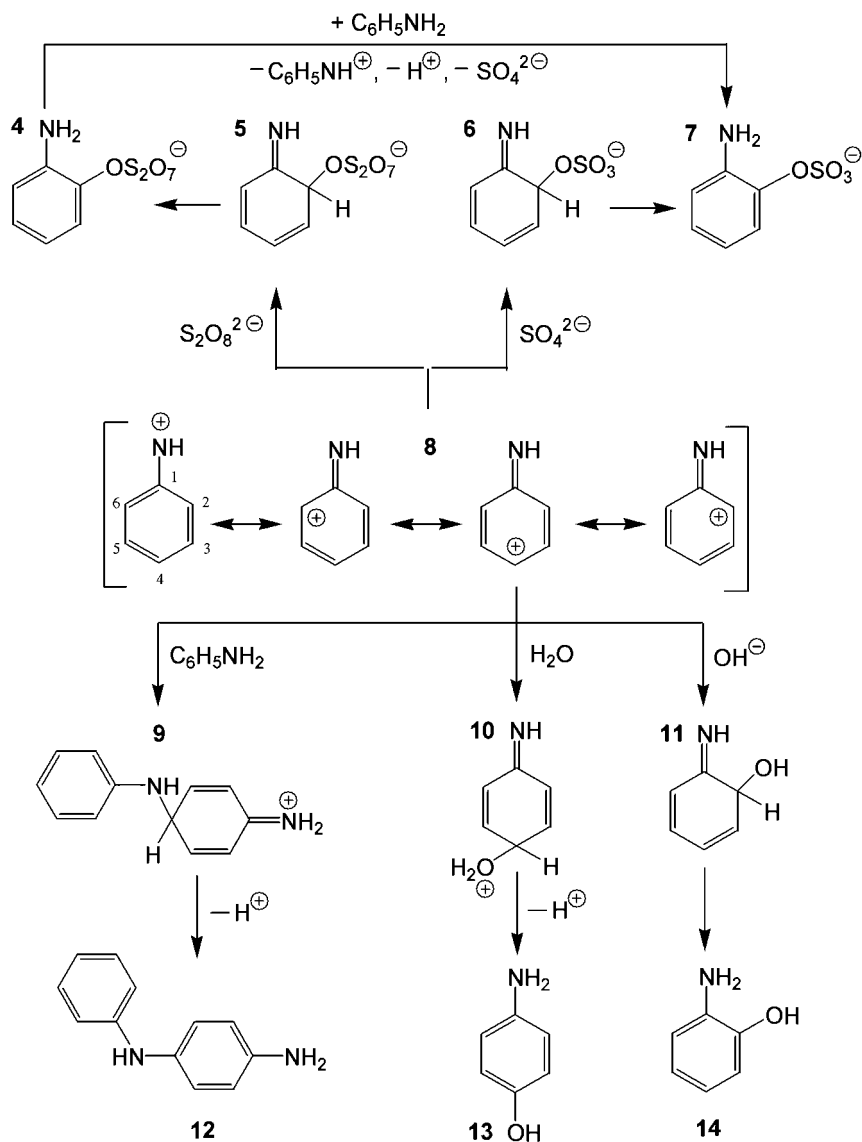
The involvement of free radical arylamine species (cation radicals and neutral radicals), as highly reactive products of single-electron oxidation of arylamines, in the formation of the *o*-aminoaryl sulfates was excluded because radical traps had no effect on the formation of the *o*-aminoaryl sulfates.⁷ Arylnitrenium cations, as initial reactive products of two-electron oxidation of primary/secondary arylamines in acidic as well as alkaline solutions, have not been considered as reactive species involved in the formation of *o*-aminoaryl sulfates because the knowledge about arylnitrenium cation chemistry became well established more than four decades after the discovery of the Boyland-Sims oxidation.¹³ Behrman noted that “a nitrene mechanism is not consistent with the fact that tertiary anilines behave in a similar manner to primary anilines”.¹¹ Based on the fact that electron-releasing substituents at the aromatic ring accelerate the oxidation of arylamines with $\text{S}_2\text{O}_8^{2-}$,⁷ and taking into account some other experimental findings,¹¹ Behrman proposed that the nucleophilic $\text{S}_{\text{N}}2$ displacement by the arylamine nitrogen on the peroxide oxygen of $\text{S}_2\text{O}_8^{2-}$ represents the rate-determining step of the Boyland-Sims oxidation which leads to the formation of arylhydroxylamine-*O*-sulfonate intermediates.¹¹ This classic mechanism did not explain the regioselectivity of the Boyland-Sims oxidation and the fact that some arylamines, such as benzidine, cannot be transformed to the corresponding aminoaryl sulfates by Boyland-Sims oxidation,² but rather give iminoquinonoid compounds upon two-electron oxidation with $\text{S}_2\text{O}_8^{2-}$.

The yields of aminoaryl sulfates in Boyland Sims oxidation are significantly lower than those of hydroxyaryl sulfates in the Elbs oxidation, especially in the case of primary and secondary arylamines, due to the competitive oxidative polymerizations of arylamines leading to the formation of insoluble materials,²⁻¹² which were described in many papers as humic acid-like polymers. Synthetic organic chemists paid no attention to their structural characterization since these precipitates were considered as undesirable by-products in the Boyland-Sims oxidation,²⁻¹² whereas scientists working in the field of conducting polymers became interested in the elucidation of the molecular structure and the mechanism of formation of these oligoaryl amines, *e.g.*, oligoanilines,¹⁴⁻¹⁸ because recent studies had revealed the crucial template function of *in situ* formed oligo-

anilines in the synthesis of polyaniline nanostructures by the oxidative polymerization of aniline with ammonium peroxydisulfate (APS) under falling pH conditions.^{14,19–21}

Marjanović *et al.*²² recently proposed a revised mechanism of the Boyland–Sims oxidation of arylamines based on the unique role of arylnitrenium cations in the case of primary and secondary arylamines, and arylamine dications and/or immonium cations in the case of tertiary arylamines. The revised mechanism comprehensively explained the formation of soluble aminoaryl sulfates and insoluble oligoarylamines in a manner more consistent with the experimental evidence than previous mechanistic schemes. It was revealed that the two-electron transfer between arylamine and peroxydisulfate, accompanied by the deprotonation, leading to the formation of arylnitrenium cations/arylamine dications/immonium cations and sulfate anions, represents the rate-determining step, while the subsequent reaction between arylnitrenium cations/arylamine dications/immonium cations and sulfate anions represents a regioselectivity-determining step (Scheme 2).²² In accordance with the experimental findings of Boyland and Sims, it was computationally confirmed by both the AM1 and RM1 semi-empirical quantum chemical methods that the reactions of arylnitrenium cations or arylamine dications/immonium cations with sulfate anions lead to the prevalent formation of *o*-aminoaryl sulfates.²² The C6–O–SO₃ rather than C2–O–SO₃ coupled aminoaryl sulfates were also computationally confirmed to be the major products of Boyland–Sims oxidation in the case of *meta*-substituted anilines that have unsymmetrical *ortho* positions. Moreover, the computations confirmed the known experimental findings that *para* substitution occurs if both *ortho* positions are blocked by substituents. The reactions between arylnitrenium cations and peroxydisulfate in an aqueous solution were found to have regioselectivities quite similar to those of the reactions between arylnitrenium cations and sulfate; *i.e.*, they lead to the prevalent formation of *o*-aminoaryl peroxydisulfates, which undergo rapid reduction to the corresponding *o*-aminoaryl sulfates (Scheme 2).²²

The formation of insoluble precipitates during the Boyland–Sims oxidation of arylamines was explained by the oxidative oligomerization of arylamines, in which the dimerization phase is the reaction of arylamines with arylnitrenium cations (Scheme 2),²² and by the oxidative co-oligomerizations of arylamines with aminoaryl sulfates and aminophenols, formed in the reaction of arylnitrenium cations/arylamine dications/immonium cations with both hydroxide anions in highly alkaline solution and water molecules in highly dilute aqueous solutions.²² Fully oxidized branched oligoarylamines, containing mainly substituted phenazine and iminoquinonoid units with the presence of iminoquinone/phenoxazine segments, were proposed to constitute the insoluble precipitates in Boyland–Sims oxidations.²²



Scheme 2. Formation of prevalent products (4, 7, 12–14), through the most stable intermediates (5, 6, 9–11), in reactions of the aniline nitrenium cation (8) with SO_4^{2-} , $\text{S}_2\text{O}_8^{2-}$, aniline, OH^- and H_2O . Reprinted²² with permission. Copyright (2011) American Chemical Society.

2. OXIDATIVE POLYMERIZATION OF ANILINE

Polyaniline (PANI) has been the most extensively studied polyarylamine during the past three decades because of its high electrical conductivity, pronounced redox-activity, good environmental stability, simple acid–base doping–

–dedoping, ease of preparation by chemical and electrochemical oxidative polymerization of aniline and its salts, and versatile applicability in various areas of modern technologies, such as rechargeable batteries, sensors and indicators, catalysts, shielding of electromagnetic interference, microwave and radar absorbing materials, non-linear optical and light-emitting devices, electron field emitters, field-effect transistors, Schottky diodes, erasable optical information storage, digital memory devices, asymmetric films, membranes, electrochemical capacitors (supercapacitors), electrochromic devices, electromechanical actuators, electrorheological (ER) fluids, antistatic and anticorrosion coatings, and fuel and solar cells.^{1,23} PANI has a variety of redox and acid–base forms²⁴ with quite different optical, magnetic, electrical and other properties. The most important form of PANI is the green emeraldine salt, which attains a conductivity of about $1\text{--}10\text{ S cm}^{-1}$ for granular PANI powders,²⁵ $\approx 10^2\text{ S cm}^{-1}$ for PANI powders with nanospherical morphology²⁶ and $\approx 10^3\text{ S cm}^{-1}$ for PANI films.²⁷ Emeraldine salt contains, depending on the preparation method and isolation procedure, various proportions of diamagnetic $[(-\text{B}-\text{NH}^+=\text{Q}=\text{NH}^+-\text{B}-\text{NH}-\text{B}-\text{NH}-)_n](\text{A}^-)_{2n}$ and paramagnetic $[(-\text{B}-\text{NH}^{\bullet}-\text{B}-\text{NH}-)_n](\text{A}^-)_n$ units; in the preceding formulae B, Q, and A denote a benzenoid ring, a quinonoid ring, and a dopant anion, respectively. Chemical/electrochemical oxidative polymerization of aniline in aqueous solutions of strong acids ($\text{pH} < 2.0$) at room temperature is a typical method for the preparation of conducting PANI emeraldine salt.^{1,25} Besides APS and Fe(III) compounds as the most frequently used oxidants in PANI syntheses, various other oxidants were recently used, *e.g.*, transition metal compounds such as Mn(III), Mn(IV), Mn(VII), Cr(VI), Ce(IV), V(V) and Cu(II) compounds, KIO_3 , H_2O_2 , and benzoyl peroxide,¹ as well as noble metal compounds such as Au(III), Pt(IV), Pd(II) and Ag(I) compounds.²⁸ Mixtures of oxidants were also used, *e.g.*, $\text{FeCl}_3/\text{H}_2\text{O}_2$ and $\text{KIO}_3/\text{NaClO}$.¹

In numerous performed oxidative polymerization experiments with “equimolar” quantities of commercially available aniline and the corresponding acid (which serves as a dopant, enabling the high conductivity of the final PANI emeraldine salt), there was up to a few percent surplus of aniline or acid because researchers assumed incorrectly that used aniline and acid were 100 % pure despite the fact that commercially available aniline is most frequently $\geq 99.0\text{--}99.5\%$ pure while the majority of employed acids (especially organics, *e.g.*, camphorsulfonic acid) are $\geq 98\%$ pure. These subtle differences in the initial aniline/acid molar ratio led to significant differences in the initial pH of the oxidative polymerization process, known to have a crucial impact on the polymerization mechanism and molecular/supramolecular structure of PANI.^{14,15,19–21,29–35} Since the initial pH of the reaction mixture was usually not recorded, this variation in the initial pH could be the major reason for the pronounced irreproducibility of most of the previously published results in the

field of PANI research noticed by MacDiarmid *et al.*³⁶ who made the well known statement – “there are as many different types of polyaniline as there are people who make it!” Therefore, it could reasonably be expected that the polymerization of purified aniline salts would provide much more reproducible results. Furthermore, it should be noted that the handling of solid aniline salts is much less hazardous than the handling of liquid aniline. Finally, because the anilinium cation is much less oxidizable than the non-protonated aniline molecule,²⁹ crystalline aniline salts are much more resistant in comparison with liquid aniline against oxidative degradation by atmospheric oxygen during storage. However, the performed oxidative chemical polymerizations of commercially available aniline salts, such as hydrochloride and sulfate, gave PANI salts that were almost insoluble in common solvents. This lack of solubility limits the processability of ordinary PANI emeraldine salts (chlorides/sulfates), which must be transformed by a dedoping–redoping procedure to a more processable PANI doped with functionalized acids. Many attempts to synthesize processable PANI salts by the oxidation of aniline with $S_2O_8^{2-}$ in the presence of various functionalized acids failed because hydrogen sulfate, formed as a by-product during the polymerization ($nC_6H_5NH_2 + nS_2O_8^{2-} \rightarrow (-C_6H_4NH-)_n + 2nH_2SO_4$), was incorporated into the PANI structure instead of a functionalized dopant anion, especially in the cases of salts of aniline and weak acids.³⁷ Therefore the quest for an aniline salt with functionalized acid which could be directly oxidized with APS or other oxidants to the processable conducting PANI emeraldine salt presents a challenge up to the present time.

It was reported that PANI solubility, crystallinity, thermal and electrochemical stability, and anticorrosive properties were improved using 5-sulfosalicylic acid (SSA) as the dopant.^{38–41} Conducting PANI–5-sulfosalicylate (PANI–SSA) was successfully prepared by chemical and electrochemical oxidation of aniline in the presence of SSA using a mole ratio [SSA]/[aniline] in the broad range from 0.25 to 10.0.^{19,30,38,39,41} It was observed that PANI–SSA nanotubes and nanorods were formed using the ratio [SSA]/[aniline] = 0.25, while granular PANI–SSA was obtained at [SSA]/[aniline] \geq 0.5.¹⁹ Anilinium 5-sulfosalicylate was recently prepared, recrystallized, and polymerized to processable conducting PANI–SSA,⁴² which had mass-average molar mass and polydispersity index of 22,900 g mol⁻¹ and 2.7, respectively, and exhibited high thermal stability. An elemental analysis and FTIR spectroscopic study of PANI–SSA revealed the doping level and the oxidation state between the emeraldine and protoemeraldine salt, while corresponding studies of the PANI base indicated a small extent of covalent bonding of SSA anions to the PANI chains.⁴²

2.1. Polyaniline nanostructures

Interest in the study of PANI nanostructures has dramatically increased during the last decade due to the significantly enhanced dispersibility and processibility as well as substantially improved performance of nanostructured PANI materials in many applications, *e.g.*, sensors, catalysts, electron field emitters, field-effect transistors, corrosion protection, data storage, actuators, membranes, solar cell devices, rechargeable batteries, fuel cells, ER fluids, Schottky diodes, supercapacitors, electromagnetic interference shielding, microwave absorption and antistatic coatings, in comparison with ordinary granular PANI materials.^{1,43} PANI nanostructures have also been successfully used as precursors in the process of carbonization leading to the formation of nitrogen-containing carbon nanomaterials that have versatile applicability.^{44–57} The formation, molecular structure, properties and applications of PANI nanostructures were reviewed during the last several years.^{1,43,58–67} PANI nanostructures were also reviewed within the frame of review articles devoted to nanostructured conducting polymers.^{68–75}

Colloidal PANI nanoparticles (NPs) can be simply prepared by dispersion polymerization of aniline in the presence of various colloidal stabilizers.⁷⁶ Several physical methods for the fabrication of PANI nanofibers (NFs) and/or nanorods (NRs) from granular PANI are known, *e.g.*, electrospinning, ultrasonication, spin coating, and irradiation of the freestanding PANI film with a pulsed electron beam.^{1,43} Various template methods for the preparation of 1-D PANI nanostructures (NFs, nanowires (NWs), NRs or nanotubes (NTs)) *via* the oxidative polymerization of aniline, *e.g.*, hard template methods (nanoporous template, nanostructured seed template and the reactive template method) and soft template methods (oligomer-, polymer-, surfactant- and amphiphilic acid-assisted syntheses) were developed during the last two decades.^{1,43} Template-free methods, *e.g.*, not-shaken/not-stirred, aqueous/organic interfacial, rapid-mixing and dilute polymerizations; photo-assisted, radiolytic, sonochemical, solid-state mechanochemical and electrochemical syntheses (voltammetric, potentiostatic, galvanostatic, *etc.*), as well dopant-free, falling-pH, “pH-stat” and hydrophobic surface methods for the synthesis of 1-D PANI nanostructures were also reported in the last decade.^{1,43} The falling-pH method was the most frequently used template-free method for the preparation of PANI–NTs accompanied with PANI–NRs,^{19,77} while in some cases, PANI–NRs were prevalently obtained (Fig. 1).^{78,79} Special attention was paid to the oxidative polymerization of aniline in water without any added acid as the simplest falling-pH method for the preparation of 1-D nanostructured PANI (Fig. 2).^{14,15,20,21,33,80–89}

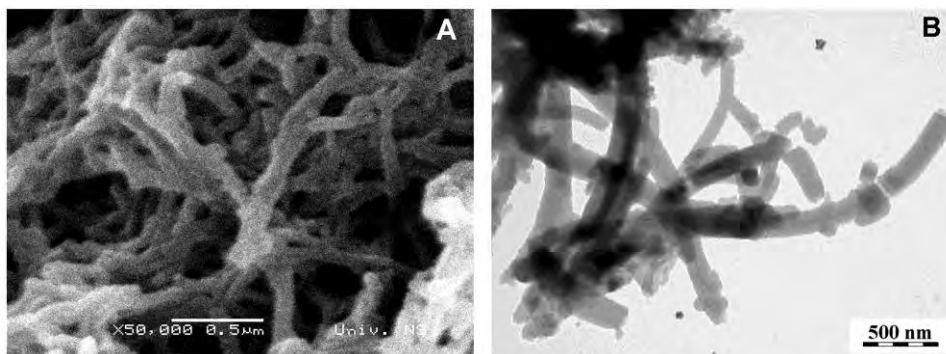


Fig. 1. SEM (A) and TEM (B) images of PANI 3,5-dinitrosalicylate NRs prepared by the chemical oxidative polymerization of aniline with APS at mole ratios [3,5-dinitrosalicylic acid]/[aniline] = 0.5 and [APS]/[aniline] = 1.25. Adapted⁵¹ with permission. Copyright (2012) Elsevier.

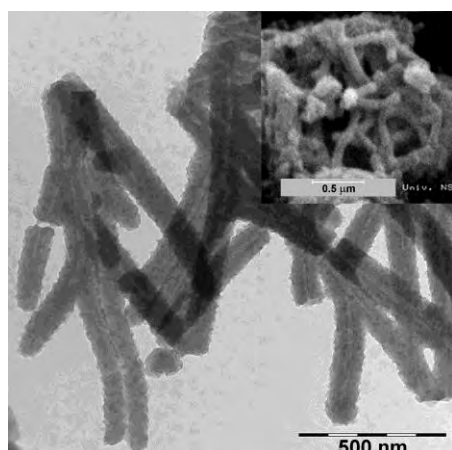


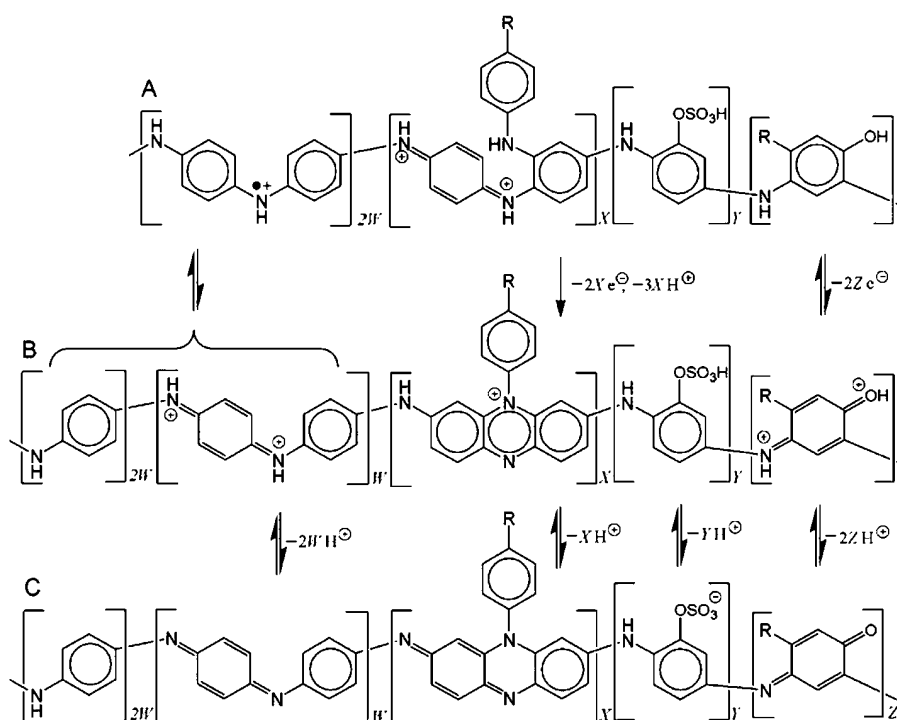
Fig. 2. TEM image of PANI hydrogensulfate/sulfate NTs prepared by the chemical oxidative polymerization of aniline with APS in water without any added acid. The corresponding SEM image is shown in the inset. Adapted⁸⁵ with permission. Copyright (2011) Elsevier.

The molecular structure of nanostructured PANIs obtained by the falling-pH method (starting from slightly acidic or neutral media) is much more complex than that of ordinary PANIs prepared in strongly acidic media (Scheme 3),⁸⁵ as was predicted by semi-empirical quantum chemical computations^{29,31,32} and confirmed by spectroscopic data (Fig. 3).^{14,15,19,78,85}

The redox-activity and paramagnetic behavior of nanostructured PANI was frequently confirmed, *e.g.*, in the case of PANI-NRs prepared in the presence of tannic acid (Fig. 4).⁷⁹

Substantial efforts have been made in order to understand the mechanisms of formation of PANI nanostructures during aniline oxidative polymerization.^{1,43,64,65} It was found that PANI-NFs/NWs/NRs are naturally formed during the chemical oxidative polymerization of aniline in acidic aqueous solutions,^{1,43} whereas PANI-NTs/NFs/NWs/NRs and/or PANI nanosheets are formed by self-

assembly under falling-pH conditions.^{1,43} The theoretical approach of Stejskal *et al.* to the genesis of PANI nanostructures under falling-pH conditions was based on the oligoaniline-guided self-assembly process,⁶⁵ while an expanded PANI nanostructure self-assembly model, based on a multi-layered approach incorporating intrinsic PANI morphologies (NFs, nanosheets and NPs) was proposed by Travas-Sejdic *et al.*⁶⁴



Scheme 3. Acid–base and redox equilibria between protonated (A and B) and deprotonated (C) oligoaniline/PANI backbones that contain *N*-phenylphenazine (R=H), substituted *N*-phenylphenazine (R = oligoaniline), *ortho*-aminophenyl sulfate, and iminoquinone/4-aminophenol units (R = H and/or R = oligoaniline), besides the classic aminophenyl and *N*-phenyl-1,4-benzoquinonediimine units. Reprinted⁸⁵ with permission.

Copyright (2011) Elsevier.

3. OXIDATIVE POLYMERIZATION OF SUBSTITUTED ANILINES

Oxidative polymerization of ring/*N*-substituted anilines was extensively studied during the past three decades. Investigations were focused on the oxidation of *ortho/meta*- and *N*-substituted anilines^{90–98} because it was expected that these monomers could give prevalently N–C4 coupled oligomers/polymers upon oxidation, similarly to aniline. Considerable attention was also paid to the oxidative polymerization of *para*-substituted anilines.^{99–178}

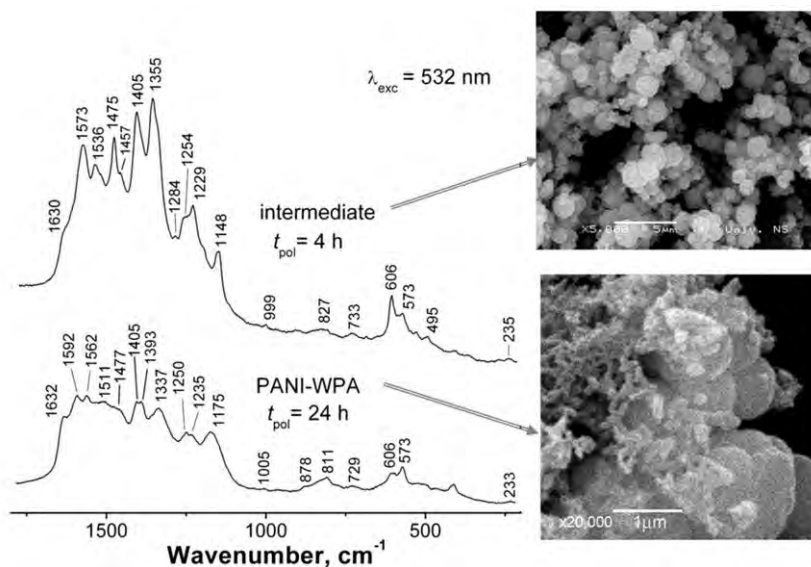


Fig. 3. Raman spectra of oligoaniline intermediate (submicro- and microspheres) and PANI-WPA (submicro- and microspheres / nanorods) produced in the presence of 12-tungstophosphoric acid (WPA) at an initial pH 5.7 (weight ratio WPA/aniline = 0.5) with the corresponding SEM images. Bands attributed to phenazine-like segments are seen at 1405 and ≈ 1630 cm^{-1} . Adapted⁷⁷ with permission. Copyright (2010) Elsevier.

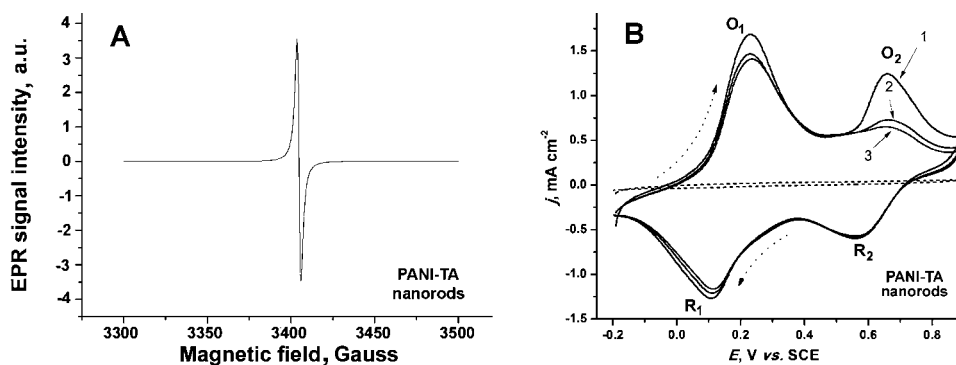


Fig. 4. A) EPR spectrum of PANI-NRs and B) first three consecutive cyclic voltammograms of PANI-NRs deposited on a glassy carbon electrode, recorded in 0.1 M aqueous H_2SO_4 solution at a sweep rate of 50 mV s^{-1} . PANI-NRs were prepared by the oxidative polymerization of aniline with APS in the presence of tannic acid, at mole ratios $[\text{tannic acid}]/[\text{aniline}] = 0.01$, $[\text{APS}]/[\text{aniline}] = 1$. Adapted⁷⁹ with permission. Copyright (2012) Elsevier.

3.1. Oxidative polymerization of para-substituted anilines

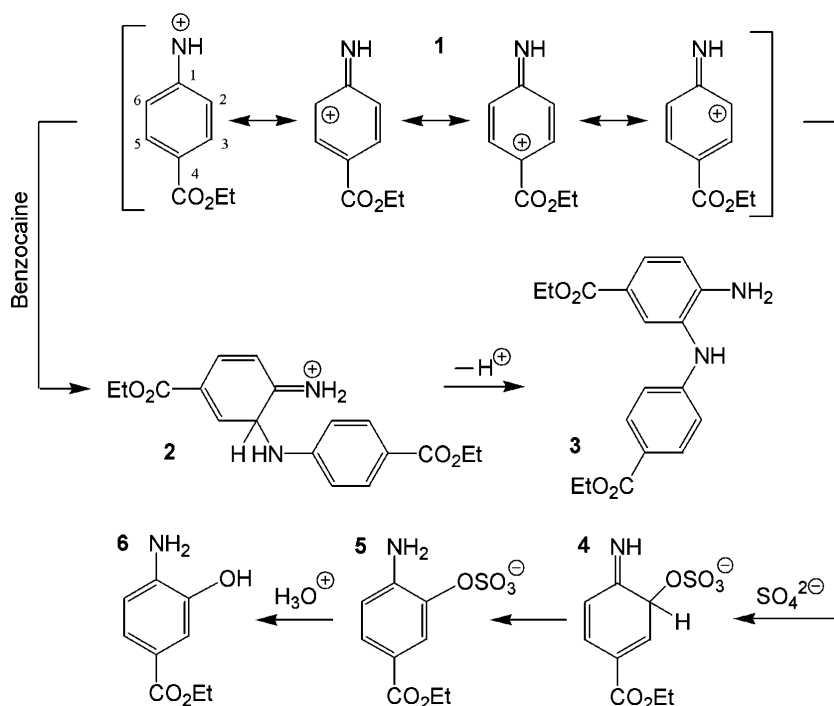
The oxidative polymerization of *para*-substituted anilines,^{99–178} e.g., CH_3- (*p*-toluidine),^{99–102} CH_3CH_2- ,¹⁰³ $(\text{CH}_3)_3\text{C}-$,¹⁰⁴ C_6H_5- ,¹⁰⁵ $\text{H}_2\text{N}-\text{C}_6\text{H}_4-$

–(benzidine),^{106–114} $\text{N}\equiv\text{C}$ –,^{104,115} HOOC – (4-aminobenzoic acid),^{115–119} F –,^{104,120–122} Cl –,^{102–104,115,121,123,124} Br –,^{104,115,121,124} I –,¹²⁴ H_2N – (*p*-phenylenediamine),^{107,112,125–151} $\text{C}_6\text{H}_5\text{–NH}$ – (4-aminodiphenylamine),^{152–163} $\text{H}_2\text{N–C}_6\text{H}_4(\text{CH}_3)$ – (*o*-tolidine),¹⁶⁴ O_2N –,^{104,115,165} HO – (4-aminophenol),^{166–173} CH_3O – (*p*-anisidine),¹¹⁵ $\text{CH}_3\text{CH}_2\text{O}$ – (*p*-phenetidine),¹¹⁵ HO_3S – (sulfanilic acid)^{116,174–176} and $\text{H}_2\text{NO}_2\text{S}$ –substituted aniline (sulfanilamide),¹⁷⁷ was reported. Peroxydisulfates were most frequently used as oxidants.^{102,103,112–114,122,124,129,140–145,153–156,164,165,173} Bromine,¹²⁶ iodine,¹⁴⁰ Fe(III) compounds,^{103,139,152} metal chelate/ O_2 ,¹³⁸ tetrachloroauric acid,¹⁵⁰ H_2O_2 without catalyst¹⁴⁶ and with horseradish peroxidase,^{147,166} *cis*-bisglycinato-Cu(II)-monohydrate/Co(II)-dionemoxime,¹⁴⁹ silver nitrate¹⁵¹ and sodium dichromate¹⁷⁷ were occasionally employed. The enzyme-catalyzed oxidative polymerization of *p*-substituted anilines was also studied.^{123,147,148,166} Electrochemical oxidative polymerizations were also widely used for the synthesis of poly(*p*-substituted anilines).^{99–101,104–111,115–121,127–137,157–163,167–172,174–176} Molar mass distribution measurements revealed that the products of oxidative polymerization of *p*-substituted anilines were low- to high-molar-mass oligomers rather than polymers.

Spectroscopic methods for structural characterization combined with semi-empirical quantum chemical studies of the polymerization mechanisms were proved to be powerful tools in the elucidation of the molecular structures of oligo/poly(substituted anilines).^{155,178} The course of the oxidation of 4-aminodiphenylamine (4-ADPA) with APS in acidic aqueous ethanol solution as well as the properties of the oxidation products were compared with those of 2-aminodiphenylamine (2-ADPA) oxidation.¹⁵⁵ Semiconducting oligomers of 4-ADPA and non-conducting oligomers of 2-ADPA of mass-average molar masses of 3,700 and 1,900 g mol^{-1} , respectively, were prepared using an oxidant to monomer mole ratio of 1.25. Molecular orbital calculations revealed the prevalence of $\text{N}_{\text{prim}}\text{–C10}$ coupling reaction of 4-ADPA, while $\text{N}_{\text{prim}}\text{–C5}$ was found to be the main coupling mode between 2-ADPA units. FTIR and Raman spectroscopic studies confirmed the prevalent formation of linear $\text{N}_{\text{prim}}\text{–C10}$ coupled oligomers of 4-ADPA and suggested chain branching and formation of phenazine structural units in the oligomers of 2-ADPA.

Electroactive paramagnetic *ortho*-coupled aniline oligomers functionalized with ethyl ester groups were recently synthesized by the oxidation of 4-(ethoxycarbonyl)aniline, the well known anesthetic benzocaine, with APS in an acidic aqueous medium at room temperature.¹⁷⁸ Molecular orbital AM1 and RM1 computations, combined with the MM2 molecular mechanics force-field method and the conductor-like screening model (COSMO) of solvation, indicated that oligo-benzocaines contain N–C2 coupled dibenzocaine units as the major structural segments, which can exist in both the reduced (aminobenzenoid) and the ox-

dized (iminoquinonoid) form (Scheme 4). Quantum chemical prediction of benzocaine oligomerization pathway was consistent with the results from FTIR spectroscopic analysis, which confirmed the transformation of the 1,4-disubstituted benzene ring of the monomer to 1,2,4-trisubstituted and 1,2,3,5-tetrasubstituted rings in oligobenzocaines containing unchanged ethoxycarbonyl ester groups (Fig. 5). The FTIR and Raman spectra also proved the presence of phenazine-like units in the benzocaine oligomers, while paramagnetism, caused by the existence of cation radical dibenzocaine structural segments, and electroactivity of the oligobenzocaines were proved by EPR and cyclic voltammetry, respectively.



Scheme 4. Formation of prevalent products (**3** and **5**) in reactions of benzocaine nitrenium cation (**1**) with benzocaine and the sulfate anion. Reprinted¹⁷⁸ with permission. Copyright (2011) Elsevier.

4. OXIDATIVE POLYMERIZATION OF 1-AMINONAPHTHALENE AND ITS DERIVATIVES

Oligomers and polymers of 1-aminonaphthalene^{179–186} and its derivatives, such as *N*-phenyl-1-aminonaphthalene,^{187,188} 2-methyl-1-aminonaphthalene,^{189–191} 1,5-diaminonaphthalene,^{192–194} 1,8-diaminonaphthalene,¹⁹⁵ 5-amino-1-naphthol,^{196–205} 5-amino-2-naphthol,²⁰⁶ 5-amino-1,4-naphthoquinone,²⁰⁷ 2-methyl-5-amino-1,4-naphthoquinone,^{208,209} 2-(5-amino-1-naphthoxy)acetic acid,²¹⁰

2-(5-amino-1-naphthoxy)-2,2-difluoroacetic acid,²¹⁰ 3-(5-amino-1-*n*-naphthyl-oxy)-1-propanesulfonic acid²¹⁰ and sodium 4-amino-3-hydroxynaphthalene-1-sulfonate,²¹¹ have received increased attention in the past two decades. These oligomeric/polymeric materials were suggested for application in corrosion protection,^{204,212,213} sensors,^{181,182,214–216} electrocatalysts,^{194,202} adsorbents¹⁷⁹ and electrochromic devices.^{184,196,198}

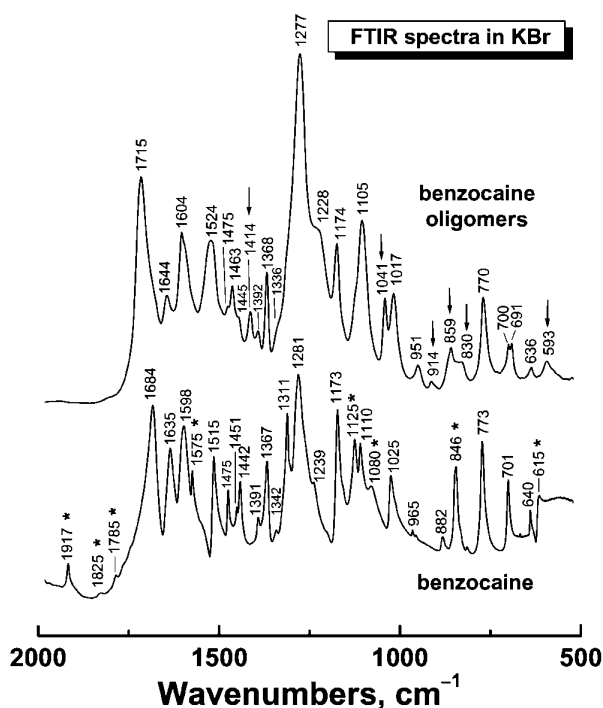


Fig. 5. FTIR spectra of benzocaine and its oligomers produced by chemical oxidative polymerization. The new bands that appeared in the spectrum of the oligomers are marked by arrows; the bands of monomer that disappeared in the spectrum of the oligomers are marked by asterisks. Reprinted¹⁷⁸ with permission. Copyright (2011) Elsevier.

Semiconducting electroactive polymeric materials that were water soluble, were synthesized by the electrochemical polymerization of sodium 4-amino-3-hydroxynaphthalene-1-sulfonate (AHNSA–Na) in aqueous solution.²¹¹ Gel-permeable chromatography (GPC) proved the presence of oligomeric chains with molar masses up to $\approx 6,300 \text{ g mol}^{-1}$ and showed that octamers to dodecamers were the dominant oligomeric species. FTIR and NMR (¹H and ¹³C) spectroscopic findings, which indicated the formation of new covalent bonds on the naphthalene ring in poly(AHNSA–Na), were correlated with the prevalent coupling modes of monomeric units determined by PM3 semi-empirical quantum-chemi-

cal computations. It was found that poly(AHNSA–Na) contained mainly N–C6 and N–C8 coupled dimer units. The paramagnetic nature of poly(AHNSA–Na) was proved by EPR spectroscopy, while the redox activity was confirmed by cyclic voltammetry. The ratio of the intensity of the two newly formed bands in the UV–vis spectrum, attributed to the polaron (delocalized poly(cation-radical)) and bipolaron form of poly(AHNSA–Na), as well as the presence of naphthoiminoquinonoid and benzenoid segments detected by FTIR and Raman spectroscopies, indicated that partly and fully oxidized bipolaron forms of poly(AHNSA–Na) prevailed. Homopolymers of AHNSA and its salts AHNSA–HCl, AHNSA–Na and AHNSA–Na₂, soluble in polar solvents, were also obtained by the standard chemical oxidative polymerization route.²¹⁷ It was shown that the use of AHNSA salts, instead of AHNSA, leads to polymeric materials with higher w_p , PDI values. The conductivity of the AHNSA polymers was in the range of 10^{-5} – 10^{-7} S cm⁻¹, poly(AHNSA–HCl) showing the highest value of 1.3×10^{-5} S cm⁻¹. The IR spectra and elemental analysis combined with MNDO-PM3 quantum chemical calculations revealed that the polymerization proceeded mainly through the oxidation of the amino group in the studied pH range, accompanied by considerable elimination of sulfonic groups. The resulting functional polymers represent polynaphthylamine-like structures with naphtho-iminoquinonoid and benzenoid N–C1, N–C5 N–C6, N–C7, and N–C8 dimer units, bearing free OH and sulfonic groups in the chains.

5. OXIDATIVE POLYMERIZATION OF ARYLDIAMINES

Oligomers and polymers of carbocyclic aryldiamines (phenylenediamines,^{107,112,125–151,218} aminodiphenylamines,^{152–163} diamionaphthalenes,^{192–195,219–223} diaminoanthraquinones,^{224–228} benzidine,^{106–114} substituted benzidines¹⁶⁴ and naphthidines²²⁹) and heterocyclic aryldiamines (diaminopyridines,^{230,231} diaminophenazines,²³² diaminoacridines²³³ and diaminocarbazoles²³⁴) have received increasing attention during the last two decades.²³⁵ Molar mass distribution measurements revealed that the products of oxidative polymerization of aryldiamines are low- to high-molar-mass oligomers rather than polymers. Aryldiamines are susceptible to oxidative polymerization *via* oxidation of one or both amino groups to give linear poly(aminoarylamines), polymers/oligomers containing phenazine units and ladder polyphenazines. Oligo/polyaryldiamines have shown tunable electroactivity,²³⁶ high permselectivity to various electroactive species,^{237,238} unique electrochromism,²³⁹ linear sensitivity of the conductivity to moisture,²⁴⁰ controlled variation of the conductivity with temperature²⁴¹ and an external electric field,²⁴² high sensibilities of polymer-modified electrodes to biosubstances at an extremely low concentration,^{243,244} good ability in detecting electro-inactive anions,²⁴⁵ pronounced electrocatalytic pro-

erties,^{246,247} effective adsorption of heavy-metal ions,^{248–252} strong adhesion to metals,²⁵³ anticorrosion ability²¹³ and high capacitance.^{254,255}

5.1. Oxidative polymerization of phenylenediamines

Polyphenylenediamines are the most frequently studied polyaryldiamines.^{107,112,125–151,218} Phenylenediamines are very susceptible to oxidative polymerization *via* the oxidation of one or both amino groups to give linear azopolymers, polyaminoanilines, ladder polyphenazines and phenazine/iminoquinonoid-unit-containing polymers. Molar mass distribution measurements revealed that polyphenylenediamines are low- to high-molar-mass oligomers rather than polymers, their molar mass being below 10,000 g mol⁻¹. Due to their complex molecular structure, oligo/polyphenylenediamines showed the unique characteristics of redox oligomers and versatile applicability in electrocatalysis, sensors and heavy metal ion removal. Mechanisms of the formation of oligo/polyphenylenediamines and their structures are still under debate.

5.1.1. Oxidative polymerization of *p*-phenylenediamine

A century ago, it was predicted that the products of a single-electron oxidation of *p*-phenylenediamine (PDA) are free radicals (Wurster dyes/salts) that may polymerize in a sufficiently concentrated solution at low temperature or in the solid state.¹²⁵ Chemical^{112,126,129,138–146,148,150,151} and electrochemical^{107,127–137} oxidative polymerizations have been widely used for the synthesis of poly(*p*-phenylenediamine) (PPDA), whereas enzyme-catalyzed oxidative polymerization has been rarely used.^{148,149} Acidic aqueous solutions were the most frequently applied polymerization media. It should be noted that dissolved aerial oxygen without any catalyst and/or co-oxidant is sufficient for the chemical oxidative polymerization of PDA. For example, PDA can polymerize in boiling aqueous acetic acid solution to semiconducting PPDA.¹⁴⁰ Depending on the synthetic route, there were several proposals for the molecular structure of PPDA, *i.e.*, a ladder structure with phenazine rings,¹²⁹ an iminoquinonoid Bandrowski base-like structure,¹⁴⁵ a linear structure with hydrazo¹⁴⁸ and azo bonds,¹³⁸ and an emeraldine-salt form of PANI.¹³²

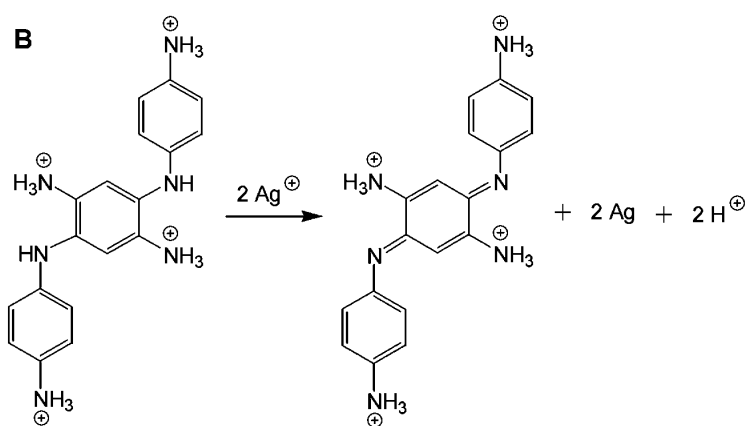
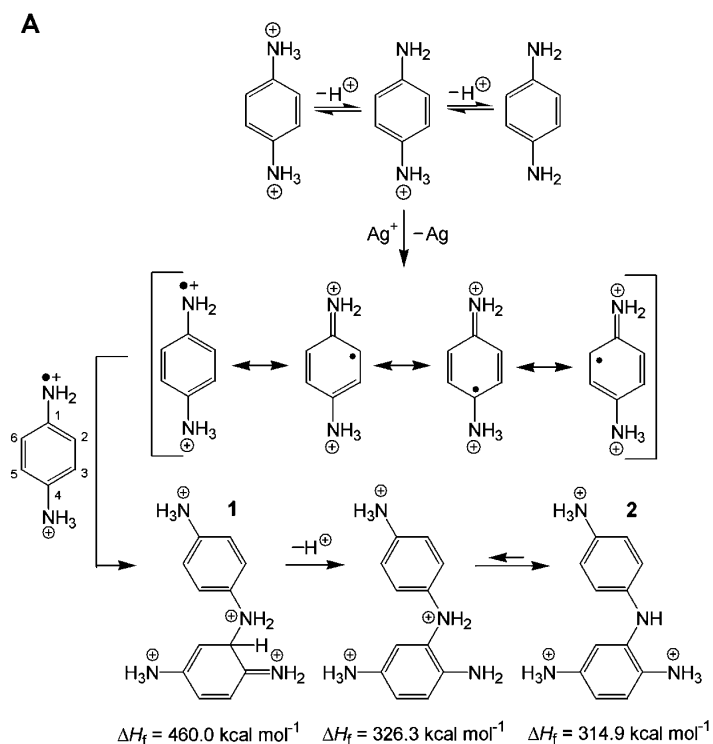
The oxidation of PDA with silver nitrate in aqueous solutions of both acetic and nitric acids, using an initial concentration [PDA] = 0.2 M and various [AgNO₃]/[PDA] mole ratios in the range from 2.5 to 7.5 was recently found to lead to the formation of highly conducting micro/nanostructured poly(*p*-phenylenediamine)–silver composites (PPDA–Ag), which significantly exceeded the conductivities of PANI–Ag analogs and commercial silver–polymer composites.²⁵⁶ The conductivity of PPDA–Ag composites synthesized in acetic acid were generally much higher than that of composites prepared in nitric acid. The highest conducting PPDA–Ag composite ($\sigma = 13,200$ S/cm) containing PPDA in

salt form was prepared in 1 M acetic acid using the mole ratio $[\text{AgNO}_3]/[\text{PDA}] = 3.75$, whereas the most conducting PPDA–Ag composite ($\sigma = 31,700 \text{ S/cm}$) containing PPDA in base form was prepared using the mole ratio $[\text{AgNO}_3]/[\text{PDA}] = 7.5$.²⁵⁶ The organic component was composed of oligomeric and polymeric fractions, their proportions varying depending on the employed concentration of AgNO_3 . In 1 M acetic acid, the formation of a true polymer fraction is marked. Molecular orbital AM1 computations, combined with the MM2 molecular mechanics force-field method and COSMO, indicated that PPDA macromolecules contain both N–C2(6) coupled PDA dimer units and Bandrowski base-like PDA trimer segments, which can exist in both the reduced (aminobenzenoid) and oxidized (iminoquinonoid) forms (Scheme 5).²⁵⁶ The quantum chemical prediction of the PDA oligomerization pathway was consistent with the results from FTIR spectroscopic analysis of the samples, which confirmed the partial transformation of 1,4-disubstituted benzene ring of monomer to 1,2,4-trisubstituted, 1,2,3,5-tetrasubstituted, and 1,2,4,5-tetrasubstituted rings in positively charged PPDA chains containing nitrate counter-ions.²⁵⁶ The FTIR and Raman spectroscopy results also indicated the presence of phenazine-like units and cation radicals in PPDA.²⁵⁶

5.2. Oxidative polymerization of diaminoacridines

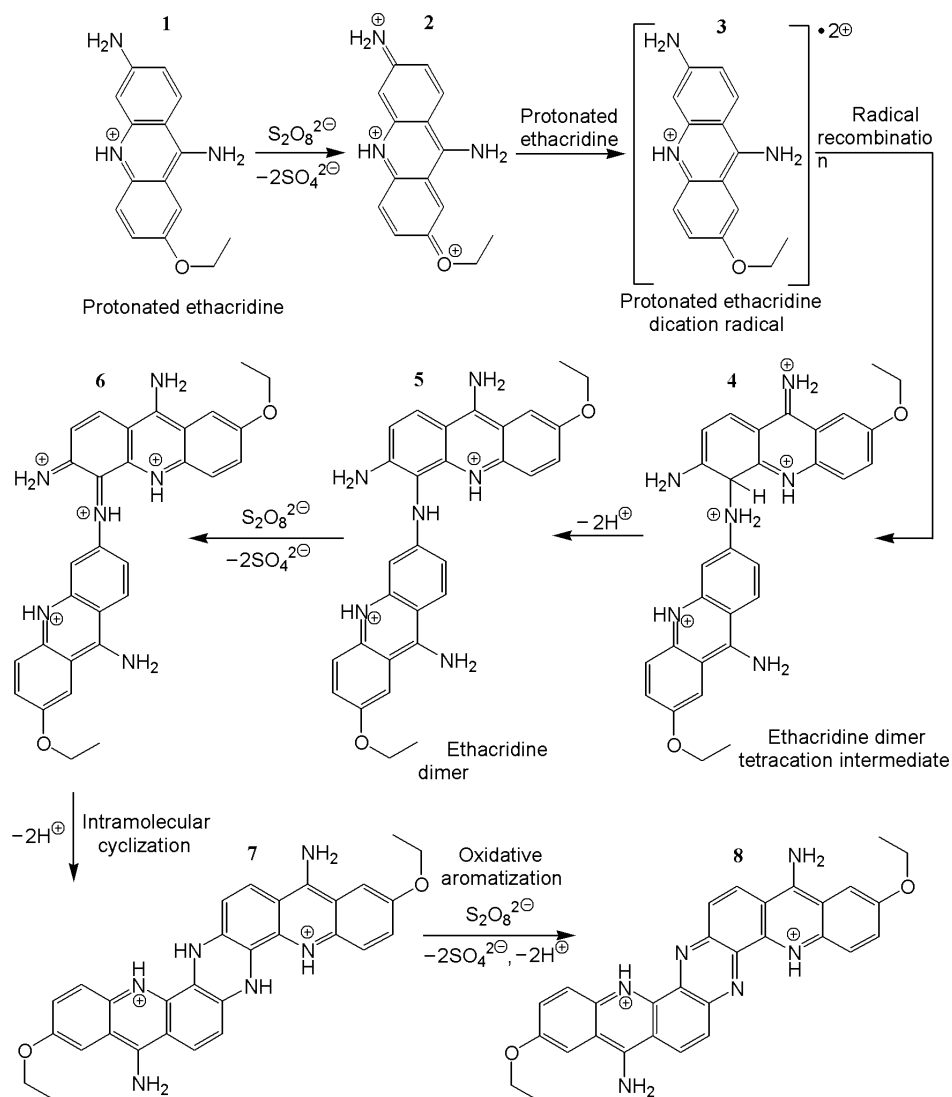
There is only one report regarding the electropolymerization of ethacridine (2-ethoxy-6,9-diaminoacridine) by potentiostatic and cyclic voltammetric methods,²³³ however, without any structural characterization of the poly(ethacridine) film at the Pt electrode. Glucose oxidase was simultaneously incorporated into the matrixes of the thin poly(ethacridine), which was developed to fabricate a glucose sensor that exhibited good stability and fast amperometric response to glucose.²³³

Electro-active paramagnetic ethacridine oligomers were recently synthesized by the oxidation of ethacridine lactate with APS in acidic aqueous solution.²⁵⁷ MALDI–TOF MS evidenced the presence of oligo-ethacridine species from dimers up to hexamers. Oligo-ethacridines protonated by both hydrochloric acid and *in situ* formed sulfuric acid, as revealed by the elemental analysis, were non-conducting ($\approx 6.5 \times 10^{-9} \text{ S cm}^{-1}$) and had fragmental and submicro/micro-layered morphology. Molecular orbital RM1 computations, combined with the MM2 molecular mechanics force-field method and COSMO, indicated that oligo-ethacridines contained N(C6)–C5 coupled the diethacridine unit as the major structural segment that can exist in both the reduced (aminobenzenoid) and oxidized (iminoquinonoid) form (Scheme 6).²⁵⁷ Quantum chemical prediction of the ethacridine oligomerization pathway was consistent with the results from FTIR spectroscopic analysis, which confirmed the oxidative transformation of the $\text{NH}_2(\text{C6})$ group of the monomer. The formation of oligomers, as well as the presence



Scheme 5. A) The oxidation of monoprotonated PDA with Ag^+ leading to the formation of $[\text{H-PDA}]^{2+}$ cation radicals and metallic Ag, followed by the recombination of $[\text{H-PDA}]^{2+}$ cation radicals and the formation of the prevalent PDA dimer in the most stable triprotonated form (**2**) through the deprotonation of the most stable N-C2(6) coupled dimer intermediate (**1**); B) formation of Bandrowski base PDA trimer. Adapted²⁵⁶ with permission.

Copyright (2011) Wiley.



Scheme 6. Oxidative dimerization of protonated ethacridine with peroxydisulfate. Reprinted²⁵⁷ with permission. Copyright (2012) Elsevier.

of both reduced and oxidized structural units in the oligomers was proved by UV-Vis spectroscopy. FTIR and Raman spectroscopies also proved the presence of phenazine-like units in the ethacridine oligomers.

6. CONCLUSIONS AND OUTLOOK

Significant progress in conducting/semiconducting and redox-active oligomers and polymers of arylamines, including the well-known polyaniline, was

achieved in the 21st century. New important quantum-chemical insights into the mechanism of polymerization of arylamines combined with the rapid development of knowledge regarding the spectroscopic characteristics of oligo/polyarylamines allowed much better elucidation of their molecular structure recently. Considerably increased understanding of the structure-properties relationship of oligo/polyarylamines opened up quite new perspectives regarding the applicability of these macromolecules in modern technology. Advances in the controlled preparation of various micro/nanostructured oligo/polyarylamines, especially polyaniline nanostructures, give today the opportunity to design new conducting/semiconducting redox-active nanomaterials with exciting properties and enhanced applicability in the fabrication of rechargeable batteries, sensors and indicators, catalysts, microwave and radar absorbing materials, non-linear optical and light-emitting devices, electron field emitters, field-effect transistors, Schottky diodes, digital memory devices, asymmetric films, membranes, supercapacitors, electrochromic devices, electromechanical actuators, electrorheological (ER) fluids, antistatic and anticorrosion coatings, fuel and solar cells.

Acknowledgment. The authors thank the Ministry of Education, Science and Technological Development of the Republic of Serbia (Contract OI 172043) for financial support.

ИЗВОД

НАПРЕДАК У ИСТРАЖИВАЊИМА ПРОВОДНИХ/ПОЛУПРОВОДНИХ И РЕДОКС-АКТИВНИХ ОЛИГОМЕРА И ПОЛИМЕРА АРИЛАМИНА

АЛЕКСАНДРА ЈАНОШЕВИЋ¹, БУДИМИР МАРЈАНОВИЋ², АЛЕКСАНДРА РАКИЋ³
и ГОРДАНА ЂИРИЋ-МАРЈАНОВИЋ³

¹Фармацеутски факултет, Универзитет у Београду, Војводе Степе 450, 11221 Београд, ²Центрохем, Вука Караџића бб, 22300 Стара Пазова и ³Факултет за физичку хемију, Универзитет у Београду, Студентски трг 12–16, 11158 Београд

У овом ревијалном раду приказан је напредак остварен у последњих неколико година у синтези, карактеризацији и примени неких проводних/полупроводних и редокс-активних олигомера и полимера ариламина. Дат је кратак приказ историјског развоја појединих области. Представљени су поступци синтезе, структура и својства полианилина, супституисаних полианилина, посебно оних добијених оксидативном полимеризацијом пара-супституисаних анилина, поли(1-аминонафталена) и његових деривата, карбоцикличних и хетероцикличних полиарилдиамина, као нпр. поли(пара-фенилендиамина) и полидиаминоакридина. Дискутован је механизам формирања наноструктура полианилина. Недавно развијени синтетички поступци за добијање једнодимензионалних наноструктура полианилина су концизно приказани, а посебна пажња посвећена је методама без темплата. Приказан је и кратак преглед актуелних и потенцијалних будућих примена олиго/полиариламина.

(Примљено 9. августа 2013)

REFERENCES

1. G. Ćirić-Marjanović, *Synth. Met.* **177** (2013) 1

2. E. Boyland, D. Manson, P. Sims, *J. Chem. Soc.* (1953) 3623
3. E. Boyland, P. Sims, *J. Chem. Soc.* (1954) 980
4. E. Boyland, P. Sims, D. C. Williams, *Biochem. J.* **62** (1956) 546
5. P. Sims, *J. Chem. Soc.* (1958) 44
6. E. Boyland, P. Sims, *J. Chem. Soc.* (1958) 4198
7. E. J. Behrman, *J. Am. Chem. Soc.* **89** (1967) 2424
8. J. T. Edward, J. Whiting, *Can. J. Chem.* **49** (1971) 3502
9. E. J. Behrman, D. M. Behrman, *J. Org. Chem.* **43** (1978) 4551
10. E. J. Behrman, *Org. React.* **35** (1988) 421
11. E. J. Behrman, *J. Org. Chem.* **57** (1992) 2266
12. E. J. Behrman, *Beilstein J. Org. Chem.* **2** (2006) (10 pages)
13. R. A. McClelland, M. J. Kahley, P. A. Davidse, G. Hadzialic, *J. Am. Chem. Soc.* **118** (1996) 4794
14. M. Trchová, I. Šeděnková, E. N. Konyushenko, J. Stejskal, P. Holler, G. Ćirić-Marjanović, *J. Phys. Chem. B* **110** (2006) 9461
15. G. Ćirić-Marjanović, M. Trchová, J. Stejskal, *J. Raman Spectrosc.* **39** (2008) 1375
16. J. Stejskal, I. Sapurina, M. Trchová, E. N. Konyushenko, *Macromolecules* **41** (2008) 3530
17. Z. D. Zujovic, L. Zhang, G. A. Bowmaker, P. A. Kilmartin, J. Travas-Sejdic, *Macromolecules* **41** (2008) 3125
18. S. P. Surwade, V. Dua, N. Manohar, S. K. Manohar, E. Beck, J. P. Ferraris, *Synth. Met.* **159** (2009) 445
19. A. Janošević, G. Ćirić-Marjanović, B. Marjanović, P. Holler, M. Trchová, J. Stejskal, *Nanotechnology* **19** (2008) 135606
20. G. Ćirić-Marjanović, V. Dondur, M. Milojević, M. Mojović, S. Mentus, A. Radulović, Z. Vuković, J. Stejskal, *Langmuir* **25** (2009) 3122
21. G. Ćirić-Marjanović, Lj. Dragičević, M. Milojević, M. Mojović, S. Mentus, B. Dojčinović, B. Marjanović, J. Stejskal, *J. Phys. Chem., B* **113** (2009) 7116
22. B. Marjanović, I. Juranić, G. Ćirić-Marjanović, *J. Phys. Chem., A* **115** (2011) 3536
23. N. Gospodinova, L. Terlemezyan, *Prog. Polym. Sci.* **23** (1998) 1443
24. J. Stejskal, P. Kratochvíl, A. D. Jenkins, *Polymer* **37** (1996) 367
25. J. Stejskal, R. G. Gilbert, *Pure Appl. Chem.* **74** (2002) 857
26. J. Ha, J. Jang, *Appl. Chem.* **9** (2005) 73
27. K. Lee, S. Cho, S. H. Park, A. J. Heeger, C.-W. Lee, S.-H. Lee, *Nature* **441** (2006) 65
28. G. Ćirić-Marjanović, *Synth. Met.* **170** (2013) 31
29. G. Ćirić-Marjanović, M. Trchová, J. Stejskal, *Collect. Czech. Chem. Commun.* **71** (2006) 1407
30. G. Ćirić-Marjanović, A. Janošević, B. Marjanović, M. Trchová, J. Stejskal, P. Holler, *Russ. J. Phys. Chem. A*, **81** (2007) 1418.
31. G. Ćirić-Marjanović, E. N. Konyushenko, M. Trchová, J. Stejskal, *Synth. Met.* **158** (2008) 200
32. G. Ćirić-Marjanović, M. Trchová, J. Stejskal, *Int. J. Quantum Chem.* **108** (2008) 318
33. E. N. Konyushenko, J. Stejskal, I. Šeděnková, M. Trchová, I. Sapurina, M. Cieslar, J. Prokeš, *Polym. Int.* **55** (2006) 31
34. E. N. Konyushenko, M. Trchová, J. Stejskal, I. Sapurina, *Chem. Pap.* **64** (2010) 56
35. J. Stejskal, I. Sapurina, M. Trchová, E. N. Konyushenko, P. Holler, *Polymer* **47** (2006) 8253

36. A. G. MacDiarmid, W. E. Jones Jr., I. D. Norris, J. Gao, A. T. Johnson Jr., N. J. Pinto, J. Hone, B. Han, F. K. Ko, H. Okuzaki, M. Llaguno, *Synth. Met.* **119** (2001) 27
37. J. Stejskal, D. Hlavatá, P. Holler, M. Trchová, J. Prokeš, I. Sapurina, *Polym. Int.* **53** (2004) 294
38. D. C. Trivedi, S. K. Dhawan, *Synth. Met.* **58** (1993) 309
39. A. Raghunathan, G. Rangarajan, D. C. Trivedi, *Synth. Met.* **81** (1996) 39
40. S. Tawde, D. Mukesh, J. V. Yakhmi, *Synth. Met.* **125** (2002) 401
41. G. N. Ćirić-Marjanović, B. N. Marjanović, M. M. Popović, V. V. Panić, V. B. Mišković-Stanković, *Russ. J. Electrochem.* **42** (2006) 1358
42. B. Marjanović, I. Juranić, S. Mentus, G. Ćirić-Marjanović, P. Holler, *Chem. Pap.* **64** (2010) 783
43. G. Ćirić-Marjanović, *Polyaniline nanostructures*, in *Nanostructured Conductive Polymers*, A. Eftekhari, Ed., Wiley, London, 2010, p. 19
44. G. Ćirić-Marjanović, I. Pašti, N. Gavrilov, A. Janošević, S. Mentus, *Chem. Pap.* **67** (2013) 781
45. S. Mentus, G. Ćirić-Marjanović, M. Trchová, J. Stejskal, *Nanotechnology* **20** (2009) 245601
46. M. Trchová, E. N. Konyushenko, J. Stejskal, J. Kovárová, G. Ćirić-Marjanović, *Polym. Degrad. Stab.* **94** (2009) 929
47. N. Gavrilov, M. Dašić Tomić, I. Pašti, G. Ćirić-Marjanović, S. Mentus, *Mater. Lett.* **65** (2011) 962
48. B. Šljukić, I. Stojković, N. Cvjetičanin, G. Ćirić-Marjanović, *Russ. J. Phys. Chem., A* **85** (2011) 2406
49. N. Gavrilov, M. Vujković, I. A. Pašti, G. Ćirić-Marjanović, S. V. Mentus, *Electrochim. Acta* **56** (2011) 9197
50. A. Janošević, I. Pašti, N. Gavrilov, S. Mentus, G. Ćirić-Marjanović, J. Krstić, J. Stejskal, *Synth. Met.* **161** (2011) 2179
51. A. Janošević, I. Pašti, N. Gavrilov, S. Mentus, J. Krstić, M. Mitrić, J. Travas-Sejdic, G. Ćirić-Marjanović, *Micropor. Mesopor. Mater.* **152** (2012) 50
52. M. Mališić, A. Janošević, B. Šljukić, I. Stojković, G. Ćirić-Marjanović, *Electrochim. Acta* **74** (2012) 158
53. N. Gavrilov, I. A. Pašti, M. Vujković, J. Travas-Sejdic, G. Ćirić-Marjanović, S. V. Mentus, *Carbon* **50** (2012) 3915
54. N. M. Gavrilov, I. A. Pašti, G. Ćirić-Marjanović, V. M. Nikolić, M. P. Marčeta-Kaninski, Š. S. Miljanić, S. V. Mentus, *Int. J. Electrochem. Sci.* **7** (2012) 6666
55. N. Gavrilov, I. A. Pašti, M. Mitrić, J. Travas-Sejdic, G. Ćirić-Marjanović, S. V. Mentus, *J. Power Sources* **220** (2012) 306
56. N. M. Gavrilov, I. A. Pašti, J. Krstić, M. Mitrić, G. Ćirić-Marjanović, S. Mentus, *Ceram. Int.* **39** (2013) 8761
57. M. Vujković, N. Gavrilov, I. Pašti, J. Krstić, J. Travas-Sejdic, G. Ćirić-Marjanović, S. V. Mentus, *Carbon* **64** (2013) 472
58. J. Huang, R. B. Kaner, *Chem. Commun.* (2006) 367
59. J. Huang, *Pure Appl. Chem.* **78** (2006) 15
60. D. Zhang, Y. Wang, *Mater. Sci. Eng., B* **134** (2006) 9
61. D. Li, J. Huang, R. B. Kaner, *Acc. Chem. Res.* **42** (2009) 135
62. M. Wan, *Macromol. Rapid Commun.* **30** (2009) 963
63. P. Liu, L. Zhang, *Crit. Rev. Solid State Mater. Sci.* **34** (2009) 75
64. C. Laslau, Z. Zujovic, J. Travas-Sejdic, *Prog. Polym. Sci.* **35** (2010) 1403

65. J. Stejskal, I. Sapurina, M. Trchová, *Prog. Polym. Sci.* **35** (2010) 1420
66. H. D. Tran, J. M. D'Arcy, Y. Wang, P. J. Beltramo, V. A. Strong, R. B. Kaner, *J. Mater. Chem.* **21** (2011) 3534
67. J. Wang, D. Zhang, *Adv. Polym. Technol.* **32** (2013) E323
68. J. Jang, *Adv. Polym. Sci.* **199** (2006) 189
69. M. Wan, *Adv. Mater.* **20** (2008) 2926
70. K. Jackowska, A. T. Bieganski, M. Tagowska, *J. Solid State Electrochem.* **12** (2008) 437
71. H. D. Tran, D. Li, R. B. Kaner, *Adv. Mater.* **21** (2009) 1487
72. C. Li, H. Bai, G. Shi, *Chem. Soc. Rev.* **38** (2009) 2397
73. Rajesh, T. Ahuja, D. Kumar, *Sens. Actuators, B* **136** (2009) 275
74. Y.-Z. Long, M.-M. Li, C. Gu, M. Wan, J.-L. Duvail, Z. Liu, Z. Fa, *Prog. Polym. Sci.* **36** (2011) 1415
75. Z. Yin, Q. Zheng, *Adv. Energy Mater.* **2** (2012) 179
76. J. Stejskal, *J. Polym. Mater.* **18** (2001) 225
77. G. Ćirić-Marjanović, I. Holclajtner-Antunović, S. Mentus, D. Bajuk-Bogdanović, D. Ješić, D. Manojlović, S. Trifunović, J. Stejskal, *Synth. Met.* **160** (2010) 1463
78. A. Janošević, G. Ćirić-Marjanović, B. Marjanović, M. Trchová, J. Stejskal, *Mater. Lett.* **64** (2010) 2337
79. A. Janošević, G. Ćirić-Marjanović, B. Šljukić Paunković, I. Pašti, S. Trifunović, B. Marjanović, J. Stejskal, *Synth. Met.* **162** (2012) 843
80. H. Ding, M. Wan, Y. Wei, *Adv. Mater.* **19** (2007) 465
81. N.-R. Chiou, L. J. Lee, A. J. Epstein, *Chem. Mater.* **19** (2007) 3589
82. H. Ding, J. Shen, M. Wan, Z. Chen, *Macromol. Chem. Phys.* **209** (2008) 864
83. Y. F. Huang, C. W. Lin, *Polymer* **50** (2009) 775
84. M. Radoičić, Z. Šaponjić, J. Nedeljković, G. Ćirić-Marjanović, J. Stejskal, *Synth. Met.* **160** (2010) 1325
85. A. Rakić, D. Bajuk-Bogdanović, M. Mojović, G. Ćirić-Marjanović, M. Milojević-Rakić, S. Mentus, B. Marjanović, M. Trchová, J. Stejskal, *Mater. Chem. Phys.* **127** (2011) 501
86. M. Radoičić, Z. Šaponjić, G. Ćirić-Marjanović, Z. Konstantinović, M. Mitrić, J. Nedeljković, *Polym. Compos.* **33** (2012) 1482
87. M. Radoičić, Z. Šaponjić, I. A. Janković, G. Ćirić-Marjanović, S. P. Ahrenkiel, M. I. Čomor, *Appl. Catal., B* **136–137** (2013) 133
88. M. Radoičić, G. Ćirić-Marjanović, Z. V. Šaponjić, M. Mitrić, Z. Konstantinović, M. Stoiljković, J. M. Nedeljković, *J. Mater. Sci.* **48** (2013) 5776
89. A. A. Rakić, M. Vukomanović, G. Ćirić-Marjanović, *Chem Pap.* in press, doi: 10.2478/s11696-013-0453-2
90. Y. Wei, W. W. Focke, G. E. Wnek, A. Ray, A. G. MacDiarmid, *J. Phys. Chem.* **93** (1989) 495
91. E. M. Geniès, P. Noël, *Synth. Met.* **46** (1992) 285
92. M. C. Gupta, S. S. Umare, *Macromolecules* **25** (1992) 138
93. W.-Y. Zheng, K. Levon *Macromolecules* **27** (1994) 7754
94. E. Pringsheim, E. Terpetschnig, O. S. Wolfbeis, *Anal. Chim. Acta* **357** (1997) 247
95. A. Malinauskas, *Ber. Bunsen Ges. Phys. Chem.* **102** (1998) 972
96. P. A. Kilmartin, G. A. Wright, *Synth. Met.* **104** (1999) 145
97. A. Gök, B. Sari, M. Talu, *Synth. Met.* **142** (2004) 41
98. H. D. Tran, I. Norris, J. M. D'Arcy, H. Tsang, Y. Wang, B. R. Mattes, R. B. Kaner, *Macromolecules* **41** (2008) 7405
99. E. M. Geniès, J. F. Penneau, M. Lapkowski, *New J. Chem.* **12** (1988) 765

100. M. Leclerc, J. Guay, L. H. Dao, *J. Electroanal. Chem.* **251** (1988) 21
101. A. Thyssen, A. Hochfeld, R. Kessel, A. Meyer, J. W. Schultze, *Synth. Met.* **29** (1989) 357
102. E. Pringsheim, E. Terpetschnig, O. S. Wolfbeis, *Anal. Chim. Acta* **357** (1997) 247
103. E. T. Kang, K. G. Neoh, K. L. Tan, *Eur. Polym. J.* **30** (1994) 529
104. P. Snauwaert, R. Lazzaroni, J. Riga, J. J. Verbist, *Synth. Met.* **16** (1986) 245
105. L. H. Dao, M. Leclerc, J. Guay, J. W. Chevalier, *Synth. Met.* **29** (1989) 377
106. Y. Wei, G. W. Jang, K. F. Hsueh, R. Hariharan, S. A. Patel, C. C. Chan, C. Whitecar, *Polym. Mater. Sci. Eng.* **61** (1989) 905
107. P. Chandrasekhar, R. W. Gumbs, *J. Electrochem. Soc.* **138** (1991) 1337
108. F. D'Eramo, A. H. Arévalo, J. J. Silber, L. Sereno, *J. Electroanal. Chem.* **382** (1995) 85
109. A. Bagheri, M. R. Nateghi, A. Massoumi, *Synth. Met.* **97** (1998) 85
110. F. D'Eramo, J. J. Silber, A. H. Arévalo, L. E. Sereno, *J. Electroanal. Chem.* **494** (2000) 60
111. D. Posadas, M. J. R. Presa, M. I. Florit, *Electrochim. Acta* **46** (2001) 4075
112. B. Rawat, S. S. Kansara, H. S. Rama, *Polym. Int.* **26** (1991) 233
113. G. M. do Nascimento, V. R. L. Constantino, M. L. A. Temperini, *J. Phys. Chem., B* **108** (2004) 5564
114. G. M. do Nascimento, P. S. M. Barbosa, V. R. L. Constantino, M. L. A. Temperini, *Colloids Surfaces, A* **289** (2006) 39.
115. J. Bacon, R. N. Adams, *J. Am. Chem. Soc.* **90** (1968) 6596
116. C. M. A. Brett, C. Thiemann, *J. Electroanal. Chem.* **538–539** (2002) 215
117. C. Thiemann, C. M. A. Brett, *Synth. Met.* **123** (2001) 1
118. A. Benyoucef, F. Huerta, J. L. Vázquez, E. Morallon, *Eur. Polym. J.* **41** (2005) 843.
119. K.-J. Huang, C.-X. Xu, W.-Z. Xie, W. Wang, *Colloids Surfaces, B* **74** (2009) 167
120. E. M. Geniès, C. Tsintavis, *J. Electroanal. Chem.* **195** (1985) 109
121. P. Snauwaert, R. Lazzaroni, J. Riga, J. J. Verbist, *Synth. Met.* **18** (1987) 335
122. A. H. Kwon, J. A. Conklin, M. Makhinson, R. B. Kaner, *Synth. Met.* **84** (1997) 95
123. K. E. Simmons, R. D. Minard, J.-M. Bollag, *Environ. Sci. Technol.* **21** (1987) 999
124. E. T. Kang, K. G. Neoh, K. L. Tan, B. T. G. Tan, *Synth. Met.* **35** (1990) 345
125. J. Piccard, *Liebigs Ann. Chem.* **381** (1911) 351
126. L. Michaelis, S. Granick, *J. Am. Chem. Soc.* **65** (1943) 1747
127. P. J. Elving, A. F. Krivis, *Anal. Chem.* **30** (1958) 1645
128. K. B. Prater, *J. Electrochem. Soc.* **120** (1973) 365
129. F. Cataldo, *Eur. Polym. J.* **32** (1996) 43
130. E. Ekinci, A. A. Karagözler, A. E. Karagözler, *Synth. Met.* **79** (1996) 57
131. J.-J. Xu, H.-Y. Chen, *Anal. Biochem.* **280** (2000) 221
132. B. Lakard, G. Herlem, S. Lakard, B. Fahys, *J. Mol. Struct. THEOCHEM* **638** (2003) 177
133. M. H. Pournaghi-Azar, B. Habibi, *J. Electroanal. Chem.* **601** (2007) 53
134. S. J. Killoran, R. D. O'Neill, *Electrochim. Acta* **53** (2008) 7303
135. M. Hébert, D. Rochefort, *Electrochim. Acta* **53** (2008) 5272
136. G. Zhang, A. Zhang, X. Liu, S. Zhao, J. Zhang, J. Lu, *J. Appl. Polym. Sci.* **115** (2010) 2635
137. S. M. Sayyah, S. S. Abd El-Rehim, M. M. El-Deeb, S. M. Kamal, R. E. Azooz, *J. Appl. Polym. Sci.* **117** (2010) 943
138. H. C. Bach, *Polym. Prepr.* **7** (1966) 576.
139. E. Tsuchida, M. Kaneko, Y. Kurimura, *Makromol. Chem.* **132** (1970) 209
140. W. Qin, X. Zhao, F. Li, *Acta Polym. Sin.* **4** (1993) 502
141. J. Prokeš, J. Stejskal, I. Krivka, E. Tobolkova, *Synth. Met.* **102** (1999) 1205

142. J. Trlica, P. Sáha, O. Quadrat, J. Stejskal, *Physica, A* **283** (2000) 337
143. T. Sulimenko, J. Stejskal, J. Prokes, *J. Colloid Interface Sci.* **236** (2001) 328
144. M.-R. Huang, Q.-Y. Peng, X.-G. Li, *Chem. Eur. J.* **12** (2006) 4341
145. R. H. Sestrem, D. C. Ferreira, R. Landers, M. L. A. Temperini, G. M. do Nascimento, *Polymer* **50** (2009) 6043
146. D. Ichinohe, K. Akagi, H. Kise, *Synth. Met.* **85** (1997) 1671
147. D. Ichinohe, T. Muranaka, T. Sasaki, M. Kobayashi, H. Kise, *J. Polym. Sci., A* **36** (1998) 2593
148. J. Shan, S. Cao, *Polym. Adv. Technol.* **11** (2000) 288
149. A. Puzari, J. B. Baruah, *React. Funct. Polym.* **47** (2001) 147
150. J.-J. Wang, J. Jiang, B. Hu, S.-H. Yu, *Adv. Funct. Mater.* **18** (2008) 1105
151. P. Bober, J. Stejskal, M. Trchová, J. Prokeš, I. Sapurina, *Macromolecules* **43** (2010) 10406
152. I. S. Yoffe, M. R. Metrikina, *Zh. Russ. Fiz.-Chim. Obsch.* **62** (1930) 1101
153. T. Hagiwara, T. Demura, K. Iwata, *Synth. Met.* **18** (1987) 317
154. Y. Ding, A. B. Padias, H. K. Hall, *J. Polym. Sci., A* **37** (1999) 2569
155. G. Ćirić-Marjanović, M. Trchová, E. N. Konyushenko, P. Holler, J. Stejskal, *J. Phys. Chem., B* **112** (2008) 6976
156. Q. Sun, Y. Deng, *Eur. Polym. J.* **44** (2008) 3402
157. K. Sasaki, M. Kaya, J. Yano, A. Kitani, A. Kunai, *J. Electroanal. Chem.* **215** (1986) 401
158. A. Kitani, J. Yano, A. Kunai, K. Sasaki, *J. Electroanal. Chem.* **221** (1987) 69
159. R. Male, R. D. Allendoerfer, *J. Phys. Chem.* **92** (1988) 6237
160. E. M. Geniès, J. F. Penneau, M. Lapkowski, A. Boyle, *J. Electroanal. Chem.* **269** (1989) 63
161. A. Petr, L. Dunsch, *J. Phys. Chem.* **100** (1996) 4867
162. A. Zimmermann, U. Künzelmann, L. Dunsch, *Synth. Met.* **93** (1998) 17
163. M. A. Cotarelo, F. Huerta, C. Quijada, R. Mallavia, J. L. Vázquez, *J. Electrochem. Soc.* **153** (2006) D114
164. G. Ćirić-Marjanović, B. Marjanović, M. Trchová, P. Holler, *Mater. Sci. Forum* **494** (2005) 357
165. S. Wang, F. Wang, X. Ge, *Synth. Met.* **16** (1986) 99
166. M. H. Reihmann, H. Ritter, *J. Macromol. Sci., A* **39** (2002) 1369
167. S. Taj, M. F. Ahmed, S. Sankarapavinasam, *J. Electroanal. Chem.* **338** (1992) 347
168. E. Ekinci, A. A. Karagozler, A. E. Karagozler, *Electroanalysis* **8** (2005) 571
169. G. Maia, H. A. Menezes, *J. Electroanal. Chem.* **586** (2006) 39
170. S. N. Vieira, L. F. Ferreira, D. L. Franco, A. S. Afonso, R. A. Gonçalves, A. G. Brito-Madurro, J. M. Madurro, *Macromol. Symp.* **245–246** (2006) 236
171. A. G. Brito-Madurro, L. F. Ferreira, S. N. Vieira, R. G. Ariza, L. R. G. Filho, J. M. Madurro, *J. Mater. Sci.* **42** (2007) 3238
172. D. L. Franco, A. S. Afonso, L. F. Ferreira, R. A. Goncalves, J. F. C. Boodts, A. G. Brito-Madurro, J. M. Madurro, *Polym. Eng. Sci.* **48** (2008) 2043
173. P. Kar, N. C. Pradhan, B. Adhikari, *J. Macromol. Sci. A* **47** (2010) 282
174. A. Kitani, K. Satoguchi, H.-Q. Tang, S. Ito, K. Sasaki, *Synth. Met.* **69** (1995) 129
175. C. Thiemann, C. M. A. Brett, *Synth. Met.* **125** (2002) 445
176. S. A. Kumar, S.-M. Chen, *Sensors Actuators, B* **123** (2007) 964
177. S. M. Sayyah, H. M. Abd-El Salam, Y. S. Wahba, *Int. J. Polym. Mater.* **54** (2005) 1133
178. B. Marjanović, I. Juranić, G. Ćirić-Marjanović, I. Pašti, M. Trchová, P. Holler, *React. Funct. Polym.* **71** (2011) 704
179. U. Riaz, S. M. Ashraf, *Chem. Eng. J.* **174** (2011) 546

180. X. Li, C. Sun, Z. Wei, *Synth. Met.* **155** (2005) 45
181. F. D'Erano, M. B. Moressi, H. Fernández, M. A. Zón, A. H. Arévalo, L. E. Sereno, A. Álvarez-Lueje, *Electrochim. Acta* **55** (2010) 4421
182. Y. Xu, Q. Xie, M. Hu, L. Nie, S. Yao, *J. Electroanal. Chem.* **389** (1995) 85
183. A. H. Arévalo, H. Fernández, J. J. Silber, L. Sereno, *Electrochim. Acta* **35** (1990) 741
184. B. K. Schmitz, W. B. Euler, *J. Electroanal. Chem.* **399** (1995) 47.
185. D. K. Moon, K. Osakada, T. Maruyama, K. Kubota, T. Yamamoto, *Macromolecules* **26** (1993) 6992
186. G. Ćirić-Marjanović, B. Marjanović, V. Stamenković, Ž. Vitnik, V. Antić, I. Juranić, *J. Serb. Chem. Soc.* **67** (2002) 867
187. S. Dong, Z. Li, *Synth. Met.* **38** (1990) 381
188. C.-H. Yang, L.-R. Huang, T.-C. Wen, S.-L. Chung, T.-L. Wang, *J. Phys. Chem., C* **111** (2007) 9227
189. G. Ćirić-Marjanović, N. Cvjetičanin, S. Mentus, J. Budinski-Simendić, I. Krakovsky, *Polym. Bull.* **50** (2003) 319
190. G. Ćirić-Marjanović, N. Cvjetičanin, S. Mentus, *Spectrosc. Lett.* **36** (2003) 151
191. G. Ćirić-Marjanović, J. Budinski-Simendić, I. Krakovsky, *Mater. Sci. Forum* **453–454** (2004) 139
192. M. Abdel Azzem, U. S. Yousef, D. Limosin, G. Pierre, *Synth. Met.* **63** (1994) 79
193. M.-C. Pham, M. Oulahyne, M. Mostefai, M. M. Chehimi, *Synth. Met.* **93** (1998) 89
194. R. Ojani, J.-B. Raoof, S. R. H. Zavvarmahalleh, *Electrochim. Acta* **53** (2008) 2402
195. N. Oyama, M. Sato, T. Ohsaka, *Synth. Met.* **29** (1989) 501
196. T. Ohsaka, M. Ohba, M. Sato, N. Oyama, S. Tanaka, S. Nakamura, *J. Electroanal. Chem. Interfacial Electrochem.* **300** (1991) 51
197. M.-C. Pham, M. Mostefai, M. Simon, P.-C. Lacaze *Synth. Met.* **63** (1994) 7
198. T. Ohsaka, M. Ohba, M. Sato, N. Oyama, S. Tanaka, S. Nakamura, *Synth. Met.* **43** (1991) 3089
199. C. P. L. Rubinger, R. L. Moreira, L. A. Cury, G. N. Fontes, B. R. A. Neves, A. Meneguzzi, C. A. Ferreira, *Appl. Surf. Sci.* **253** (2006) 543
200. C. P. L. Rubinger, R. L. Moreira, B. R. A. Neves, L. A. Cury, C. A. Ferreira, A. Meneguzzi, *Synth. Met.* **145** (2004) 147
201. E. P. Cintra, S. I. Córdoba de Torresi, *J. Electroanal. Chem.* **518** (2002) 33
202. M.-C. Pham, S. Bouallala, L. A. Lé, V. M. Dang, P.-C. Lacaze, *Electrochim. Acta* **42** (1997) 439
203. E. P. Cintra, R. M. Torresi, G. Louarn, S. I. Córdoba de Torresi, *Electrochim. Acta* **49** (2004) 1409
204. A. Meneguzzi, C. A. Ferreira, M. C. Pham, M. Delamar, P. C. Lacaze, *Electrochim. Acta* **44** (1999) 2149
205. E. P. Cintra, S. I. Córdoba de Torresi, N. Errien, G. Louarn, *Macromolecules* **36** (2003) 2079
206. M.-C. Pham, M. Mostefai, P.-C. Lacaze, L. H. Dao, *Synth. Met.* **68** (1994) 39
207. M.-C. Pham, B. Piro, E. A. Bazzaoui, M. Hedayatullah, J.-C. Lacroix, P. Novák, O. Haas, *Synth. Met.* **92** (1998) 197
208. S. Hubert, M. C. Pham, L. H. Dao, B. Piro, Q. A. Nguyen, M. Hedayatullah, *Synth. Met.* **128** (2002) 67
209. M. C. Pham, S. Hubert, B. Piro, F. Maurel, H. L. Dao, H. Takenouti, *Synth. Met.* **140** (2004) 183
210. V. George, D. J. Young, *Polymer* **43** (2002) 4073

211. G. Ćirić-Marjanović, M. Trchová, P. Matějka, P. Holler, B. Marjanović, I. Juranić, *React. Funct. Polym.* **66** (2006) 1670
212. S. Ahmad, S. M. Ashraf, U. Riaz, S. Zafar, *Prog. Org. Coat.* **62** (2008) 32
213. A. Meneguzzi, M. C. Pham, J. C. Lacroix, B. Piro, A. Adenier, C. A. Ferreira, P. C. Lacaze, *J. Electrochem. Soc.* **148** (2001) B121
214. F. D'Eramo, J. M. Marioli, A. H Arévalo, L. E. Sereno, *Talanta* **61** (2003) 341
215. R. Ojani, J.-B. Raoof, P. Salmay-Afagh, *J. Electroanal. Chem.* **571** (2004) 1
216. S.-S. Huang, H.-G. Lin, R.-Q. Yu, *Anal. Chim. Acta* **262** (1992) 331
217. G. Ćirić-Marjanović, B. Marjanović, I. Juranić, P. Holler, J. Stejskal, M. Trchová, *Mater. Sci. Forum* **518** (2006) 405
218. R. H. Sestrem, D.C. Ferreira, R. Landers, M. L. A. Temperini, G. M. do Nascimento, *Eur. Polym. J.* **46** (2010) 484
219. M. A. Rahman, M.-S. Won, N.-H. Kwon, J.-H. Yoon, D.-S. Park, Y.-B. Shim, *Anal. Chem.* **80** (2008) 5307
220. M.-S. Won, J.-H. Yoon, Y.-B. Shim, *Electroanalysis* **17** (2005) 1952
221. M. Tagowska, B. Pałys, M. Mazur, M. Skompska, K. Jackowska, *Electrochim. Acta* **50** (2005) 2363
222. A. Nasalska, M. Skompska, *J. Appl. Electrochem.* **33** (2003) 113
223. S.-Y. Honga, S.-M. Park, *J. Electrochem. Soc.* **150** (2003) E360
224. M. Gao, F. Yang, G. Zhang, L. Liu, X. Wang, *Electrochim. Acta* **54** (2009) 2224
225. F. Yakuphanoglu, B. F. Şenkal, *Synth. Met.* **159** (2009) 311
226. F. Yakuphanoglu, B. F. Şenkal, *Polym. Adv. Technol.* **19** (2008) 1193
227. M. Gao, F. Yang, X. Wang, G. Zhang, L. Liu, *J. Phys. Chem., C* **111** (2007) 17268
228. X. G. Li, H. Li, M. R. Huang, *Chem. Eur. J.* **13** (2007) 8884
229. F. D'Eramo, M. A. Zón, H. Fernández, L. Sereno, A. H. Arévalo, *Electrochim. Acta* **53** (2008) 7182
230. F. Bakhtiarzadeh, S. Ab Ghani, *Electroanalysis* **22** (2010) 549
231. B. Shentu, K. Oyaizub, H. Nishide, *J. Mater. Chem.* **14** (2004) 3308
232. G. Ćirić-Marjanović, N. V. Blinova, M. Trchová, J. Stejskal, *J. Phys. Chem., B* **111** (2007) 2188
233. J.-J. Xu, H.-Y. Chen, *Anal. Chim. Acta* **423** (2000) 101
234. M. Skompska, M. Chmielewski, A. Tarajko, *Electrochem. Commun.* **9** (2007) 540
235. X.-G. Li, M.-R. Huang, W. Duan, Y.-L. Yang, *Chem. Rev.* **102** (2002) 2925
236. G. Pierre, M. Abdel-Azzem, U. S. Yousef, *Eur. Polym. J.* **34** (1998) 819
237. S. J. Killoran, R. D. O'Neill, *Electrochim. Acta* **53** (2008) 7303
238. L. J. Murphy, *Anal. Chem.* **70** (1998) 2928
239. J. Yano, S. Yamasaki, *Synth. Met.* **102** (1999) 1157
240. K. Ogura, H. Shiigi, M. Nakayama, *J. Electrochem. Soc.* **143** (1996) 2925
241. A. Puzari, J. B. Baruah, *React. Funct. Polym.* **47** (2001) 147
242. V. N. Popok, I. A. Karpovich, V. B. Odzhaev, D. V. Sviridov, *Nucl. Instrum. Meth. Phys. Res., B* **148** (1999) 1106
243. A. A. Abdelwahab, H.-M. Lee, Y.-B. Shim, *Anal. Chim. Acta* **650** (2009) 247
244. J. C. Vidal, E. Garcia-Ruiz, J. Espuelas, T. Aramendia, J. R. Castillo, *Anal. Bioanal. Chem.* **377** (2003) 273
245. Q. Xu, C. Xu, Y. Wang, W. Zhang, L. Jin, K. Tanaka, H. Haraguchi, A. Itoh, *Analyst* **125** (2000) 1453
246. R. Ojani, J. B. Raoof, S. R. H. Zavvarmahalleh, *J. Solid State Electrochem.* **13** (2009) 1605

247. M. H. Pournaghi-Azar, B. Habibi, *J. Electroanal. Chem.* **601** (2007) 53
248. J.-J. Wang, J. Jiang, B. Hu, S.-H. Yu, *Adv. Funct. Mater.* **18** (2008) 1105
249. K. Kilian, K. Pyrzynska, *React. Funct. Polym.* **68** (2008) 974
250. M.-R. Huang, Q.-Y. Peng, X.-G. Li, *Chem. Eur. J.* **12** (2006) 4341
251. X.-G. Li, M.-R. Huang, S.-X. Li, *Acta Mater.* **52** (2004) 5363
252. M. Skompska, A. R. Hillman, *J. Chem. Soc. Faraday Trans.* **92** (1996) 4101
253. L. F. D'Elia, R. L. Ortíz, O. P. Marquez, J. Márquez, Y. Martínez, *J. Electrochem. Soc.* **148** (2001) C297
254. S. A. Hashmi, S. Suematsu, K. Naoi, *J. Power Sources* **137** (2004) 145
255. K. Naoi, S. Suematsu, A. Manago, *J. Electrochem. Soc.* **147** (2000) 420
256. G. Ćirić-Marjanović, B. Marjanović, P. Bober, Z. Rozlivková, J. Stejskal, M. Trchová, J. Prokeš, *J. Polym. Sci., A* **49** (2011) 3387
257. B. Marjanović, I. Juranić, G. Ćirić-Marjanović, M. Mojović, I. Pašti, A. Janošević, M. Trchová, P. Holler, J. Horský, *React. Funct. Polym.* **72** (2012) 25.